

## THÈSE

Pour obtenir le grade de

### **DOCTEUR DE LA COMMUNAUTE UNIVERSITE GRENOBLE ALPES**

Spécialité : **Ingénierie-matériaux mécanique énergétique  
environnement procédés production**

Arrêté ministériel : 13 mars 2017

Présentée par

**« Mariano Garrido Pacheco »**

Thèse dirigée par « **Yves Fautrelle** » et  
codirigée par « **Laurent Davoust** »

préparée au sein du **Laboratoire SIMaP EPM**  
dans l'**École Doctorale I-MEP2**

## **Electromagnetic processing of molten light alloys reinforced by micro/nanoparticles**

Thèse soutenue publiquement le « **13 mars 2017** »,  
devant le jury composé de :

**Mr, Henri, NGUYEN-THI,**

Professeur à l'Université d'Aix-Marseille, (Président)

**Mr, Jardy, Alain**

Directeur de Recherche au CNRS, (Rapporteur)

**Mr, Christian, Coddet**

Professeur à l'Université de Belfort-Monbeliard, (Rapporteur)

**Mr, Yves, Fautrelle**

Professeur à l'Université Grenoble Alpes, (Directeur de Thèse)

**Mr, Laurent, Davoust**

Professeur à l'Université Grenoble Alpes, (Co-directeur de thèse)



## Abstract

Improvement in mechanical properties of pure metals and alloys can be achieved by the introduction of ceramic particles appropriately dispersed within the material. These particles can act as nucleation sites enhancing the reduction of the crystallite (grain) size. The dispersion of these nucleant materials presents challenges due to their tendency to sediment and to agglomerate. Particles of nanometric size can also produce the improvement of mechanical properties by several reinforcement mechanisms such as Orowan or grain boundary strengthening. The use of electromagnetic stirring can provide a method to disperse particles and produce changes in the microstructure of the material. The induced stirring can increase the number of nucleation points available during solidification breaking the arms of the new formed dendrites at the solidification front. The temperature field in the molten material can be also homogenized by the action of the electromagnetic stirring. The small temperature gradient produced in the liquid metal can promote the growing of equiaxed dendrites. In this study a Bridgman type furnace has been used to produce materials containing grain refiners and reinforcement particles. The furnace has been equipped with a Bitter coil electromagnet capable to produce a travelling magnetic field (TMF). The electromagnetic stirring provides an induced flow which is used to disperse the particles and produced measurable changes in the microstructure of the materials studied. The experiments carried out were supported with numerical simulations performed by University of Greenwich and Simap laboratory. Experiments performed dispersing SiC microparticles into pure magnesium matrix showed that particle concentration patterns in the material are strongly governed by the vertical orientation of the magnetic field applied (upwards vs downwards). The observed patterns of dispersion obtained from the experiments presented a good agreement with the patterns predicted by the numerical simulation. The effects of the electromagnetic stirring in the grain refining of pure aluminium showed positive results whereas the alloys subjected to stirring presented grain coarsening which was related to the effects of the stirring in the solute present in the alloy. Experiments performed dispersing  $\text{Al}_2\text{O}_3$  particles using TMF in magnesium matrices, showed negative results in grain refining due to the reaction of the particles with the magnesium matrix. However, the reaction of the particles could provide a method to produce 'in situ' magnesium oxide particles in a pure magnesium matrix. The final part of the study was dedicated to the use of TMF electromagnetic stirring to disperse AlN nanoparticles to reinforce magnesium alloy Elektron 21. The mechanical tests performed at high temperature have shown improvements in creep resistance which can be related to the intergranular strengthening effect produced by the particles.

## Acknowledgments

First of all, I would like to express my gratitude to all the EPM technical team, Christian Garnier, Gabiel Fournier, Denis Bon, Benjamin Pichat, Ghatfan Hasan, for all the help they provided me during my work in the experimental room and also in the laboratory. Thanks for your reliable and effective work and also for your patience and support especially at the beginning of the thesis when I could barely speak French.

I would like to express my very special gratitude to Pr. Nuria Salan from UPC for all the help she provided me during my Master studies, and also for all her efforts to arrange my Master thesis presentation on time to apply for this PhD thesis. All this work would have never happened without her help.

I would like to thank the GPM2 members, Luc Salvo, Remi Daudin, Sofiane Terzi, Pierre Lhuissier and Charles Josserond for their help with the characterization of many of the samples presented in this thesis.

I would like to thank the Thermolab members, Christelle Poggi for her assistance and training provided in the chemistry room, and also to Alain Domain for his help with the production of samples.

I would like to thank my thesis director Pr. Yves Fautrelle for his scientific support during the thesis and for his sympathy and good mood during all this time which made my work easier. I would like to thank also my thesis co-director Pr. Laurent Davoust for considering me for this job and also for his help during the thesis. I would like to thank my colleague and friend Dr. Ahmed Nouri for the help that he provided me during my experimental work and especially during the preparation of my defence.

From the EPM group, I would like to thank Pr. Kader Zaidat for his effective help during the thesis, especially for his guidance during the characterization process. I would like to thank Roland Ernst for the opportunity he gave me to work in his electromagnetic stirring system which I have thoroughly enjoyed. I would like to thank Dr. Mircea Cablea for his help at the beginning of the thesis teaching me how to use and maintain VB2 furnace. I would like to thank Pr. Yves Delannoy for his help with the numerical simulation, and also to Dr. Guy Chichignoud for his help with the chemical analysis.

I would like to thank Dr. Wim Sillekens for his support during this thesis and also for his presence in my defence.

I would like to thank my family and my girlfriend, Maria, for their support during the years that took to complete this thesis.

Finally, I would like to acknowledge the economic support provided by the European Space Agency.





# List of figures

Fig 1 Exomet project partners .....	16
Fig 2 Composite Structural Weight EADS .....	19
Fig 3 Modulus of different composite and pure materials .....	20
Fig 4 AlCuMg (2080) different volume fractions .....	21
Fig 5 AlCuMg (2080) different sizes SiC .....	21
Fig 6 External fields and physical phenomena.....	22
Fig 7 Scheme of ultrasound dispersion system. Borgonovo [14] .....	23
Fig 8 Liquid shearing system for particle dispersion [16] .....	24
Fig 9 Dendrites breaking in Al 4% Cu.....	25
Fig 10 Electromagnetic stirring system.....	25
Fig 11 AC motor and polyphase energy source .....	26
Fig 12 Stages to convert an asynchronous AC motor into tubular.....	26
Fig 13 Different types of composites .....	31
Fig 14 Edge dislocation [63] .....	32
Fig 15 Screw dislocation .....	32
Fig 16 Dislocation jog .....	32
Fig 17 Particle-matrix load transfer .....	33
Fig 18 Orowan looping .....	34
Fig 19 Orowan cutting.....	34
Fig 20 Dislocation motion.....	36
Fig 21 Effect of particle pinning in grain growth.....	36
Fig 22 Nucleation of crystals .....	39
Fig 23 Free energy change balance .....	40
Fig 24 Solid particle formation .....	40
Fig 25 Contact angle .....	41
Fig 26 VB2 Vertical Bridgman .....	46
Fig 27 Crucible drawing system.....	46
Fig 28 Bitter coil detail view 2.....	46
Fig 29 Bitter coil area detail view .....	46
Fig 30 Bitter coil helical plates .....	47
Fig 31 VB2 Bitter coil.....	47
Fig 32 VB2 furnace numerical simulation .....	47
Fig 33 VB2 furnace numerical simulation .....	47
Fig 34 Upwards TMF.....	48
Fig 35 Downwards TMF .....	48
Fig 36 Quartz cell.....	49
Fig 37 Disc of material.....	49
Fig 38 Pile up of discs .....	49
Fig 39 TranSel furnace Catia V5 and picture.....	50
Fig 40 Cold crucible scheme .....	50
Fig 41 Detail view of cold crucible.....	50
Fig 42 Induction system scheme .....	50

Fig 43 Capsule containing nanoparticles .....	50
Fig 44 Magnesium sample from Transel.....	50
Fig 45 Scheme of scanning electron microscope (SEM) and picture .....	53
Fig 46 X-ray tomography system scheme.....	53
Fig 47 X-ray photographic process .....	54
Fig 48 Sample of magnesium alloy EK21 subjected to hardness test.....	55
Fig 49 TiB <sub>2</sub> microparticle.....	60
Fig 50 Al <sub>2</sub> O <sub>3</sub> microparticle.....	60
Fig 51 SiC microparticle .....	60
Fig 52 Crystal structure of the inoculant particles .....	60
Fig 53 Al 99.99% as solidified from VB2 set-up sample non-stirred.....	64
Fig 54 Al 99.99% as solidified VB2 set-up sample stirred making use of a TMF of 15 mT .	64
Fig 55 Aluminium 99 sample 1 .....	65
Fig 56 Aluminium 99.99 VB2 sample 2 .....	65
Fig 57 Aluminium 99 sample 3 .....	65
Fig 58 Broken dendrite.....	65
Fig 59 Pure aluminium produced under high temperature gradient.....	66
Fig 60 Aluminium A357 grain structure at different TMF intensities.....	67
Fig 61 Aluminium A357 not stirred.....	68
Fig 62 Detail view of non-stirred sample.....	68
Fig 63 Aluminium A357 TMF 15 mT .....	69
Fig 64 Detail view Al A357 stirred at 15mT .....	69
Fig 65 Aluminium A357 40 mT.....	69
Fig 66 stirred Al A357 at 40 mT .....	69
Fig 67 Aluminium A357 70 mT.....	69
Fig 68 Stirred Al A357 at 70 mT .....	69
Fig 69 AZ91 grain structure under natural convection with or without the applied TMF .....	70
Fig 70 Mg AZ91 grain structure of both non-stirred and stirred material using TMF .....	71
Fig 71 Summary of grain size of materials under travelling magnetic field.....	72
Fig 72 Pure aluminium with agglomerates of Al <sub>2</sub> O <sub>3</sub> particles .....	75
Fig 73 Pure aluminium 1% TiB <sub>2</sub> .....	76
Fig 74 Particles of Al <sub>2</sub> O <sub>3</sub> as observed on the surface of an aluminium sample.....	77
Fig 75 TiB <sub>2</sub> particles inside aluminium matrix .....	77
Fig 76 Sample of A357 + 1% TiB <sub>2</sub> .....	77
Fig 77 Particle engulfment .....	79
Fig 78 Cooling curve as observed aluminium A357 1% TiB <sub>2</sub> dispersed with TMF .....	81
Fig 79 Magnesium 2% SiC upwards TMF.....	82
Fig 80 Hardness map for Mg 2% SiC using upwards TMF .....	83
Fig 81 Mg SiC TMF 3D hardness map .....	83
Fig 82 Mg SiC average hardness.....	83
Fig 83 Magnesium 2% SiC Downwards TMF .....	84
Fig 84 Hardness map for Mg 2% SiC using downwards TMF .....	84
Fig 85 Mg SiC dw TMF 3D hardness map .....	84
Fig 86 Mg SiC dw average hardness.....	84

Fig 87 Particles on lower part of the sample .....	85
Fig 88 Detail view of particles .....	85
Fig 89 Scheme of cuts analysed with X-ray radiography .....	85
Fig 90 Longitudinal, downwards TMF .....	86
Fig 91 Cross sections downwards TMF .....	86
Fig 92 Longitudinal, upwards TMF .....	86
Fig 93 Cross sections upwards TMF .....	86
Fig 94 Downwards TMF .....	87
Fig 95 Upwards TMF .....	87
Fig 96 Pixel intensity.....	87
Fig 97 scheme of sampling area and isometric view (all in mm) .....	88
Fig 98 Tomography of the external area .....	88
Fig 99 Isometric plot of particles .....	88
Fig 100 Delaunay triangulation process.....	89
Fig 101 Particle size distribution external area .....	89
Fig 102 Tomography Mg SiC internal area .....	89
Fig 103 Tomography detail internal area .....	89
Fig 104 Sample of internal area .....	90
Fig 105 Particle size distribution internal area .....	90
Fig 106 Summary of particle size and average distance .....	90
Fig 107 Sample of AZ91 + 1% Al <sub>2</sub> O <sub>3</sub> particles .....	91
Fig 108 Aluminium-Manganese compound.....	92
Fig 109 Magnesium oxide particle.....	93
Fig 110 Magnesium spinel particle .....	93
Fig 111 Iron compound particle .....	94
Fig 112 DSC analysis of pure Mg and Mg EK21 with Al <sub>2</sub> O <sub>3</sub> particles.....	94
Fig 113 Pure Magnesium AZ91 .....	96
Fig 114 Pure Mg AZ91: $\beta$ phase area fraction.....	96
Fig 115 Mg AZ91 1% Al <sub>2</sub> O <sub>3</sub> .....	96
Fig 116 AZ91 1% Al <sub>2</sub> O <sub>3</sub> : $\beta$ phase area fraction.....	96
Fig 117 Mg AZ91 4% Al <sub>2</sub> O <sub>3</sub> .....	97
Fig 118 AZ91 4% Al <sub>2</sub> O <sub>3</sub> : $\beta$ phase area fraction.....	97
Fig 119 VB2 specimen scheme .....	97
Fig 120 Cross-section top view .....	97
Fig 121 AZ91 pure internal area sample.....	98
Fig 122 AZ91 pure external area sample .....	98
Fig 123 PSD Upper area.....	99
Fig 124 PSD Lower area .....	99
Fig 125 AZ91 1% Upper internal area .....	99
Fig 126 AZ91 1% Upper external area .....	99
Fig 127 PSD Upper part of the specimen.....	100
Fig 128 PSD Lower part of the specimen .....	100
Fig 129 Group of particles in Mg AZ91 + 1% Al <sub>2</sub> O <sub>3</sub> .....	101
Fig 130 Detail view of particle.....	101

Fig 131 X-ray spectrum of particle nucleus .....	101
Fig 132 Coloured enhanced particle.....	101
Fig 133 X-ray spectrum particle shell .....	101
Fig 134 Mg AZ91 + 4% Al <sub>2</sub> O <sub>3</sub> tomography .....	102
Fig 135 Mg AZ91 optical analysis .....	102
Fig 136 Number of particles detected .....	103
Fig 137 Particles average size in $\mu\text{m}$ .....	103
Fig 138 Pure Mg 18 % Al <sub>2</sub> O <sub>3</sub> .....	104
Fig 139 SEM Mg 18% Al <sub>2</sub> O <sub>3</sub> .....	105
Fig 140 SEM Mg 18% Al <sub>2</sub> O <sub>3</sub> .....	105
Fig 141 MgO Particle.....	105
Fig 142 X-ray MgO spectrometry .....	105
Fig 143 AZ91 + 2% SiC 0.1-1 $\mu\text{m}$ .....	106
Fig 144 AZ91 + 2% SiC 0.1-1 $\mu\text{m}$ sample.....	106
Fig 145 AZ91 + 2% SiC 0.1-1 $\mu\text{m}$ sample .....	106
Fig 146 Summary of Mg AZ91 grain size measurements .....	107
Fig 147 Average hardness map Mg AZ91 .....	108
Fig 148 Microhardness measured on samples of Mg AZ91 samples .....	108
Fig 149 Tensile test Mg AZ91 .....	109
Fig 150 Tensile test on a sample of AZ91 + 2% SiC 0.1-1 $\mu\text{m}$ .....	110
Fig 151 Pure Mg Ek21 and Mg EK21 0.3% AlN particles.....	114
Fig 152 Mg EK21 1% AlN and Mg EK21 1% AlN purified .....	114
Fig 153 Summary grain size Mg EK21 with different percentages of AlN particles .....	115
Fig 154 Mg EK21 - 0.3 % scale 1mm.....	115
Fig 155 Mg EK21-1% AlN scale 50 $\mu\text{m}$ .....	115
Fig 156 EDS Mg EK21 + 0.3 % AlN.....	116
Fig 157 EDS Mg EK21 1% AlN particles .....	117
Fig 158 SEM analysis and spectrometry of Mg EK21 1% AlN .....	117
Fig 159 EDS analysis of Mg EK21 1% AlN.....	118
Fig 160 X-ray spectrometry AlZr particle.....	118
Fig 161 XRD of magnesium EK21 + 1% AlN.....	119
Fig 162 Mg EK21 AlN X-ray side view .....	121
Fig 163 Mg EK21 AlN X-ray top view.....	121
Fig 164 Mg EK21 + 1% AlN tomography.....	121
Fig 165 Detail view of $\beta$ phase .....	121
Fig 166 Top view Mg EK21 + 1% AlN .....	122
Fig 167 Detail view of zirconium rich area.....	122
Fig 168 Mg EK21 + 1% AlN particles.....	122
Fig 169 Particle size distribution EK21+1% AlN .....	122
Fig 170 3D tomography of a sample of Mg EK21 0.3% aluminium .....	123
Fig 171 AlZr crystal structure .....	123
Fig 172 Mg EK21 Hardness measurements.....	126
Fig 173 Mg EK21 Microhardness measurements .....	126
Fig 174 Heating process in hot compression test at 350°C.....	127

Fig 175 Hot compression test curves Mg EK21 and Mg EK21 + AlN 350°C .....	128
Fig 176 Relationship between strain rate $\dot{\epsilon}$ vs stress $\sigma$ .....	129
Fig 177 Fitted compression curves .....	130
Fig 178 Heating process for hot compression tests .....	132
Fig 179 Hot compression test curves of Mg EK21+1% AlN at different temperatures .....	133
Fig 180 Relationship between $\ln  \dot{\epsilon} $ vs $\ln  \sigma $ .....	133
Fig 181 Relationship between $\ln  \dot{\epsilon} $ vs $\sigma$ .....	134
Fig 182 $\ln (\sinh(\alpha\sigma))$ vs $1000/T$ .....	134
Fig 183 Stress flow vs strain rate 350°C, 400°C and 450°C .....	135
Fig 184 XRD original AlN powder .....	136
Fig 185 XRD purified AlN powder .....	136
Fig 186 TEM Courtesy of Mounib [179] .....	138
Fig 187 Monophase principle 50 Hz .....	144
Fig 188 Stator .....	144
Fig 189 Asynchronous motor phase scheme .....	145
Fig 190 electric setup of the Bitter coil .....	145
Fig 191 Ideal particle and forces .....	147
Fig 192 Al-Mg phase diagram .....	148
Fig 193 Al-Zr phase diagram .....	149
Fig 194 Pneumatic particle injector .....	149
Fig 195 Visualization of the gas flow .....	150
Fig 196 Visualization of the injected particles .....	150
Fig 197 Scheme of water bench .....	151
Fig 198 High speed camera sequence of photographs: injection over free surface .....	152
Fig 199 High speed camera sequence of photographs: injection inside water .....	152
Fig 200 Scheme of furnace with injector .....	153
Fig 201 Induction furnace 4C .....	153
Fig 202 Detail view of furnace crucible area .....	153
Fig 203 Furnace in operation .....	153
Fig 204 Fluke Eurotherm .....	154
Fig 205 Electro valve .....	154
Fig 206 Electronic shutter .....	154
Fig 207 Al <sub>2</sub> O <sub>3</sub> particles .....	154
Fig 208 Detail view Al <sub>2</sub> O <sub>3</sub> .....	154
Fig 209 Al <sub>2</sub> O <sub>3</sub> particles detail view 1 .....	155
Fig 210 Al <sub>2</sub> O <sub>3</sub> particles detail view 2 .....	155
Fig 211 Al <sub>2</sub> O <sub>3</sub> particle .....	155
Fig 212 Al <sub>2</sub> O <sub>3</sub> particles detail view .....	155

## List of Tables

Table 1 Theoretical stirring speed at different magnetic field intensities .....	47
Table 2 Etching solution used to reveal grains in aluminium samples .....	51

Table 3 "Si Blue" etching solution used to reveal segregation in aluminium 357 samples .....	52
Table 4 Etching solution used to reveal grains in magnesium samples .....	52
Table 5 Aluminium A357 alloy composition.....	57
Table 6 Alloying elements and effects on magnesium alloys.....	58
Table 7 Magnesium AZ91 alloy composition.....	58
Table 8 Magnesium Elektron 21 alloy composition .....	59
Table 9 Crystal structure parameters.....	60
Table 10 Casting conditions for pure aluminium with pulling system .....	63
Table 11 Summary of grain size measurements.....	65
Table 12 Casting conditions for experiments without pulling system .....	66
Table 13 Summary of grain size measurements.....	66
Table 14 Casting conditions for experiments performed using different stirring intensities...	67
Table 15 Aluminium A357 grain size measurements .....	68
Table 16 Casting conditions for experiments performed with Mg AZ91 .....	70
Table 17 Magnesium AZ91 grain size measurements .....	70
Table 18 Magnesium Elektron 21 grain size measurements.....	71
Table 19 Casting parameters used to produce pure aluminium + 1% $\text{Al}_2\text{O}_3$ particles.....	75
Table 20 Casting parameters used to produce pure aluminium + 1% $\text{TiB}_2$ .....	75
Table 21 Grain size measurements.....	76
Table 22 Casting conditions of aluminium A357 + $\text{Al}_2\text{O}_3$ .....	76
Table 23 Aluminium A357 1% $\text{TiB}_2$ particles casting conditions .....	77
Table 24 Aluminium A357 + $\text{TiB}_2$ grain size measurements .....	78
Table 25 Pure Mg + 2% SiC casting parameters .....	82
Table 26 AZ91+ $\text{Al}_2\text{O}_3$ / SiC casting conditions.....	91
Table 27 Summary of grain size measurements of Mg AZ91 +1% and 4% $\text{Al}_2\text{O}_3$ .....	91
Table 28 Equilibrium reactions for $\text{Al}_2\text{O}_3$ with magnesium .....	94
Table 29 Composition of the alloy and $\text{Al}_2\text{O}_3$ particles .....	95
Table 30 Composition at the equilibrium.....	95
Table 31 Number of particles, volume and size in pure magnesium AZ91 .....	98
Table 32 Average interparticle distance in the central and external areas .....	99
Table 33 Number of particles and average volume/size upper and lower parts .....	100
Table 34 Average interparticle distance.....	100
Table 35 Casting parameter of pure magnesium + 18% $\text{Al}_2\text{O}_3$ particles.....	104
Table 36 Mg + 18% $\text{Al}_2\text{O}_3$ grain size measurements.....	104
Table 37 Casting parameters of magnesium AZ91 + 2% SiC .....	105
Table 38 AZ91+2% SiC: grain size measurements .....	106
Table 39 Mg EK21 casting parameters used during experiments with Mg EK21.....	113
Table 40 Mg EK21 + AlN particles grain size measurements .....	115
Table 41 Constituents used for thermodynamic calculations.....	119
Table 42 Constituents at thermodynamical equilibrium .....	119
Table 43 Constituents used for thermodynamic calculations.....	120
Table 44 Constituents at thermodynamical equilibrium .....	120
Table 45 Typical values used to calculate the mechanisms of reinforcement .....	124
Table 46 Contribution of each mechanism of reinforcement.....	125

Table 47 Strain rates applied during hot compression tests .....	127
Table 48 Fitting parameters.....	130

## Contents

Introduction .....	15
Exomet Project .....	16
Main outlines .....	17
Improving materials for aerospace applications .....	18
Matrix materials and reinforcements for aerospace applications .....	21
Light alloy nanocomposites made via field-enabled melt processing .....	22
Power ultrasound systems .....	23
Intensive liquid shearing .....	23
General overview of the production of composite materials using electromagnetic stirring .....	24
Chapter 1 .....	31
Literature review on some features of metal matrix composites .....	31
1.1 Metal matrix composites .....	31
1.2 Strengthening mechanisms in metal matrix composites .....	32
1.2.1 The shear lag theory ( Nardone and Prewo ) .....	33
1.2.2 Orowan Strengthening .....	34
1.2.3 Boundary or Hall-Petch Strengthening .....	35
1.2.4 Coefficient of Thermal Expansion .....	37
1.2.5 Sum of Contributions .....	37
1.3 Manufacturing methods of metal matrix composites (MMC) .....	38
1.3.1 Solid processes .....	38
1.3.2 Semisolid processes .....	38
1.3.3 Liquid processes .....	39
1.4 Theoretical Studies in solidification behaviour .....	39
1.4.1 Classical nucleation theory .....	40
1.5 Grain refinement using grain refining particles .....	42
1.6 Electromagnetic stirring using a travelling magnetic field .....	24
Chapter 2 .....	45
Experimental setup .....	45
2.1 Vertical Bridgman furnace VB2 .....	45
2.1.1 Characteristics and uses of VB2 electromagnetic stirring .....	46
2.1.2 VB2 furnace procedures .....	49



2.2	Cold crucible glove box furnace (Transel) .....	49
2.3	Techniques used for characterization of materials .....	51
2.3.1	Optical microscopy (OM) .....	51
2.3.2	SEM/EDS microscopy .....	52
2.3.3	X-ray Tomography .....	53
2.3.4	X-ray radiography .....	54
2.3.5	Hardness Test .....	55
2.3.6	Microindentation hardness test (microhardness).....	56
2.3.7	Hot compression test .....	56
2.3.8	Tensile test.....	56
2.4	Matrix materials used to produce metal matrix composites .....	56
2.4.1	Aluminium 99.99 % purity.....	57
2.4.2	Aluminum A357.....	57
2.4.3	Magnesium .....	57
2.4.4	Magnesium AZ91 .....	58
2.4.5	Magnesium Elektron 21 .....	58
2.5	Inoculating particles and reinforcements.....	59
Chapter 3 .....		62
Production of composite materials containing microparticles using VB2 furnace .....		62
3.1.1	Electromagnetic stirring of pure aluminium at low cooling rate and temperature gradient .....	63
3.1.2	Pure aluminium stirred using TMF and solidified at cooling rate of 0.25 K/s ..	65
3.1.3	Aluminum A357.....	66
3.1.4	Magnesium AZ91 .....	70
3.1.5	Magnesium Elektron 21 .....	71
3.1.6	Discussion on the electromagnetic stirring of pure metals and alloys .....	72
3.2	Dispersion of grain refining particles into aluminium based materials using a travelling magnetic field .....	74
3.2.1	Pure aluminium + 1% $Al_2O_3$ .....	74
3.2.2	Pure Aluminium + 1% $TiB_2$ .....	75
3.2.3	Aluminium A357 + 1 and 2% $Al_2O_3$ particles .....	76
3.2.4	Aluminium A357 + 1% $TiB_2$ particles .....	77
3.2.5	Discussion on inoculation of particles into aluminium based materials using a travelling magnetic field (TMF) .....	78

3.3	Influence of a travelling magnetic field in the dispersion of particles into magnesium materials.....	81
3.3.1	Pure magnesium + 2% in weight of silicon carbide particles (SiC).....	82
3.3.2	X-ray analysis of pure magnesium 2% SiC particles .....	85
3.3.3	Pure magnesium 2% SiC particles X-ray tomography analysis.....	87
3.3.4	Discussion on pure magnesium inoculated with SiC particles .....	90
3.4	Magnesium AZ91 inoculated with Al <sub>2</sub> O <sub>3</sub> and SiC particles .....	91
3.4.1	Magnesium AZ91 with Al <sub>2</sub> O <sub>3</sub> particles.....	91
3.4.2	X-ray tomography analysis of magnesium AZ91 1 % and 4% Al <sub>2</sub> O <sub>3</sub> .....	97
3.4.3	Pure magnesium containing 18% in weight of Al <sub>2</sub> O <sub>3</sub> particles .....	103
3.4.4	Magnesium AZ91 + 2% SiC microparticles .....	105
3.4.5	General conclusions in grain refinement using microparticles .....	106
3.4.6	Mechanical characterization of samples of magnesium AZ91 .....	107
3.4.7	Discussion on inoculation of magnesium AZ91 using Al <sub>2</sub> O <sub>3</sub> particles dispersed using a travelling magnetic field (TMF).....	110
4.1	Magnesium Elektron 21 + AlN nanoparticles .....	114
4.1.1	SEM/EDS analysis of magnesium EK21 containing AlN particles.....	116
4.1.2	Thermodynamic analysis.....	119
4.1.3	X-ray tomography of pure and inoculated magnesium Elektron 21 .....	120
	Magnesium EK21 + 0.3 % pure aluminium .....	122
4.1.4	Estimation of mechanical reinforcement of magnesium EK21 produced by dispersion of AlN nanoparticles using the classical reinforcement theories .....	124
4.1.5	Hardness and microhardness tests.....	125
4.1.6	High temperature compression tests .....	126
4.2	Nanocomposite discussion .....	136
	General Conclusion .....	141
	Short term outlooks .....	142
	Mid term outlooks .....	143
5	Appendix.....	144
	Appendix A. Electromagnetic stirring .....	144



## Introduction

The discovery and production of new materials have played an essential role in the history of our civilization leading to deep changes in our society and way of life. Their influence has been so important that anthropologists have defined cultures base on the materials they used. Neolithic was characterized by the development of the agriculture and the discovery of copper which gave way to the beginning of the Copper Age (c.4000 - 3000 B.C). Articles made of copper were commodities with a specific value. Owning objects made of copper was often considered a measure of wealth, signalling the power and status of their owner. Copper was an expensive material and relatively soft. The mix of copper with tin produced an alloy stronger than copper called bronze and its discovery gave birth to the Bronze Age (c.3000 - 1000 B. C.) in which harder and more durable tools, weapons, armors, and building materials were developed. The reduction of iron oxide leads to the production of pure iron around 2000 BC. Archeologic discoveries support the idea that at 1500 BC making and shaping iron was widely extended in Egypt. Iron tools from the same age have been found in other areas such as India and China. During those centuries it was discovered that iron could be improved when it was reheated in a furnace with charcoal. The carbon contained in this material was transferred to the iron producing improvements in its mechanical properties. This new material was called steel. The spreading of steel across Europe happened probably around 1200 BC. The Iron Age lead to products such as iron tipped plows which helped to extend the territory under cultivation. The improvements in food production lead to increase the population and the rise of towns and civilization across the European territory. The better housing and food supplies made possible by the use of stronger metals lead to better living standards for people. The development of a furnace hot enough to melt iron in China around 513 B.C. enabled the production of the world first cast iron. This material allowed the structural use of iron for the pillars of full-size pagodas. Fifteen centuries passed until the first foundry appeared in England. The use and development of steel began during the 19<sup>th</sup> century with the Industrial Revolution in Europe and North America. Developments such as the clay crucible to melt iron, the blast and the puddling furnaces during this time facilitated the mass production of steel parts such as rail tracks. The high strength of steel permitted the construction of high buildings or tiny parts for precision instruments. Steel helped to develop new modes of transport opening new ways of trade which led to massive changes in the society. This material is still widely used in construction and high strength applications. Light metal alloys based on aluminium or magnesium, and high-performance plastics appeared during the 20<sup>th</sup> century becoming important structural materials during its last decades. The combination of these materials with reinforcements of different nature gave way to a new generation of materials called composites. The use of composite materials in aerospace and automotive structures have produced great benefits in weight reduction and permitted the designs of structures not possible with traditional materials. In recent years, there has been a growing interest in the development of composites based on metallic materials reinforced

with nanoparticles. The benefits obtained with the development of these new materials could help to improve our living standards and face the greatest threat presented to our civilization, climate global warming.

## Exomet Project

Exomet is a European research project created by the European Space Agency (ESA) with the objective of producing pure metals and alloys reinforced with micro and nano particles. This four year project started in the year 2012 involving 23 international partners formed by universities and industrial companies. Grenoble INP is represented by the laboratories SIMAP EPM and GPM2 which are involved in the production and characterization of reinforced materials respectively. The materials developed in Exomet are produced using new liquid metal processing techniques coupled with external fields. These techniques are devoted to improve the microstructure of pure metals and composites materials. The final goal of the Exomet project is the enhancement of mechanical properties of these materials not reachable by conventional processing routes and compositions. The metals targeted by Exomet are magnesium and aluminium alloys. These light alloys are extensively used in aerospace applications but they can also be found in automotive and electronic parts. The methods developed during the project could be applicable to other type of materials in the future. The following figure shows the companies and organizations involved in the Exomet project.



Fig 1 Exomet project partners

The research partners participating in the Exomet project aim to produce nanocomposites using different strategies based on the following external fields: Electromagnetic fields (EM), power ultrasound (US) and high-energy liquid shearing (LS). Previous studies and prototypes have suggested the great potential of these techniques for an efficient dispersion of micro and nanoparticles. Simap EPM is the laboratory in which the work presented in this thesis has been mostly developed, participates in Exomet project producing particle reinforced materials using electromagnetic forces. The Lorentz force generated inside the liquid metal by the application of electromagnetic fields is used to introduce and disperse micro and nanoparticles. Particles are generally difficult to disperse in metallic matrices due to their tendency to settle down, to float and to form agglomerates. A powerful stirring induced by

Lorentz force can be thought as a means to improve dispersion and to avoid settling. In addition, the stirring can help to reduce porosity and produce improvements in the microstructure of the selected material. Simap EPM has developed a powerful Bitter coil configured to provide a travelling magnetic field (TMF) to produce electromagnetic stirring of metallic melted materials. Among the advantages of this type of electromagnetic field is the capacity to control accurately the melt flow direction and intensity. This thesis aims at demonstrating the feasibility of an electromagnetic approach to disperse particles of micrometric and nanometric sizes into different matrix materials.

## **Main outlines**

This manuscript presents the research carried out to disperse particles of nanometric and micrometric size in aluminium and magnesium based materials under the influence of a travelling magnetic field (TMF). The application of magnetic fields during melting and solidification of materials to produce grain refining has been studied by numerous authors. Their respective research have shown improvement in the mechanical properties of these materials using different types of techniques based on electromagnetic fields (EM), such as rotary electromagnetic stirring or pulsed magneto-oscillation [1][2][3]. However, to the author's best knowledge, very few publications are available in the literature that discusses the use of a travelling magnetic field to produce grain refinement, or to disperse microparticles and nanoparticles in metallic matrices. The current research can add a new approach to the production of particulate metal matrix composites developing a particle dispersion system based on electromagnetic fields. In addition, this manuscript will provide with knowledge about the efficiency of this type of electromagnetic stirring to improve the microstructure of pure materials and alloys. The manuscript is organized according to four chapters:

Chapter I introduces the Exomet project and the topic of metal matrix composites in the aerospace industry. The chapter presents the objectives of the research developed; provides an overview of the main techniques used to produce composite materials and introduces some literature related to metal matrix composites. The chapter also includes a description of the main theories used to explain the reinforcement of metal matrices, and presents the effects produced by the application of electromagnetic stirring during melting and solidification of materials.

Chapter II is dedicated to describe the furnaces and techniques used to produce the composite materials studied. In addition, the chapter presents a brief explanation of the methods used to characterize the materials produced.

Chapter III is divided in two parts, the first presents the results of the experimentation performed using pure materials and alloys processed under the influence of electromagnetic stirring; the second presents the results of the experiments performed dispersing  $\text{Al}_2\text{O}_3$  and  $\text{TiB}_2$  microparticles into magnesium and aluminium matrices using a travelling magnetic field.

Chapter IV presents the results of the experimentation performed dispersing nanoparticles into magnesium alloy Elektron 21 using a travelling magnetic field. The chapter finishes with the general conclusion and perspectives of the thesis.

With the joint approach, the first objective of this research is to study the dispersion of ceramic particles and their effects in the mechanical properties of aluminium, magnesium alloys and pure materials using a travelling magnetic field.

The second objective is to determine if the efficiency of grain refiner particles introduced in different materials is affected by the application of a travelling magnetic field (TMF) during their melting and solidification.

The third objective is to study the microstructural effects produced in pure metals and alloys by the application of a TMF during melting and solidification.

The fourth objective is to validate the numerical simulation developed by Greenwich University [4] of the Bitter coil TMF particle dispersion system by the experimental approach.

## **Improving materials for aerospace applications**

The aerospace industry shows a great interest in the development of light materials that can be incorporated to aircraft and other aerospace structures. These materials need to fulfill the requirements in strength and the safety standards of this industry, and at the same time producing improvements in weight reduction, damage tolerance, creep resistance, durability, and cost effectiveness. The compromise of the aerospace industry in the reduction of greenhouse carbon gasses emissions [5], considered one of the causes of global warming, makes imperative the development of aerospace vehicles with reduced fuel consumption. The replacement of heavier structural materials by lightest ones can have a direct effect in the reduction of fuel consumption and, in consequence, carbon gas emissions. The intense development of composites materials in the last decades, have provided materials with good mechanical properties and light weight. These materials have contributed to reduce weight and improve safety in aerospace related structures. Besides, the great achievements in mechanical properties attained, composites still offer a high potential for development and improvement. Composites are the result of the combination of two or more constituent

materials with significantly different physical or chemical properties. The final composite material presents characteristics different from its individual components. The material that constitutes the higher percent of the mass is called matrix, whereas the second material at low percentage is called reinforcement [6]. The materials used as matrices are usually polymers or metals, whereas the reinforcements are usually ceramics or also metals. Polymer matrix composites have been extensively developed during the last decades. They are widely used in structural and nonstructural parts of military and civil aircraft. This type of composite is made by a combination of a polymeric matrix with a reinforcement material such as carbon or aramid fibers. Fig 2 from EADS shows the evolution during 30 years of the percentage of composite materials in the structural weight of different Airbus aircrafts.

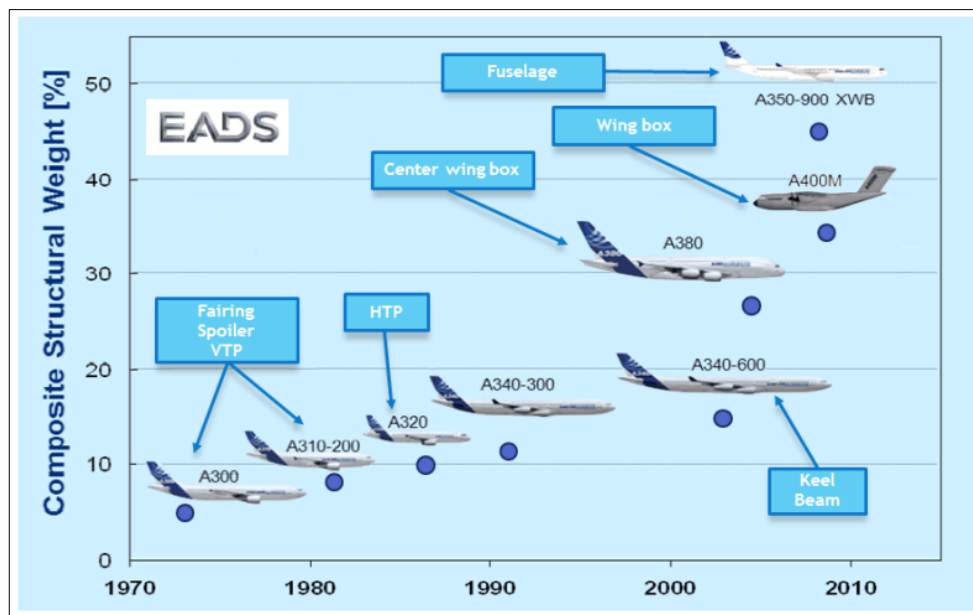


Fig 2 Composite Structural Weight EADS

For instance, structural parts traditionally made using aluminium alloys, such as landing gear doors and both horizontal and vertical tail plane, have been replaced by fibre reinforced plastic composites in the Airbus civil transport aircraft A380. Despite of the great mechanical performance provided by this type of reinforced polymers, composite materials with metallic matrices still offer some particular advantages with respect to structural ceramics or polymers. Strength and isotropy are generally higher in metallic matrices compared to organic ones. Fig 3 presents a comparison of the different modulus of some metals with respect to organic reinforced materials [7]. The values of transverse strength and axial strength that can be achieved in ceramics are extremely high compared to the rest of materials presented. On the other hand, ceramics are brittle and weak in shearing and tension. For this reason, pure ceramics are not used as structural materials in aerospace applications. However, the graph shows that a structural material such as aluminium presents a significantly better strength when is reinforced with SiC ceramic particles.



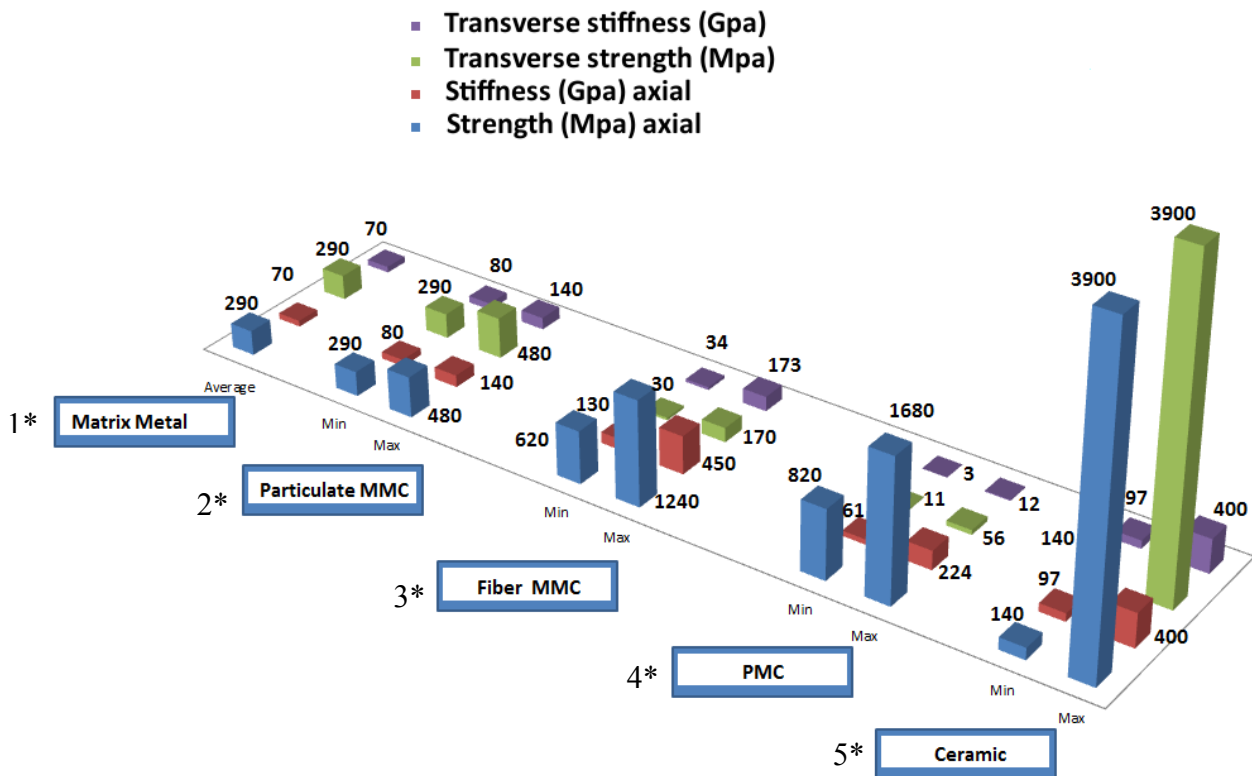


Fig 3 Modulus of different composite and pure materials

1\* Aluminium A6061. 2\* Aluminium A6061 reinforced with 0-400/0 volume fractions of SiC particulate. 3\* Aluminium A6061 reinforced with 50 % volume fractions of fibers of graphite, boron, SiC or  $Al_2O_3$ . 4\* PMC denotes a range of materials including graphite/epoxy, graphite/polymide and S-glass/epoxy. 5\* Ceramic denotes a range of materials including zirconia, SiC and  $Si_3N_4$ .

Regarding axial strength, metal matrix composites (MMCs) present high values, but still lower than advanced polymer matrix composites, which are materials highly anisotropic. The stiffness value presented by aluminum MMCs is similar to the one presented by PMCs, and higher than the one presented by unreinforced aluminum matrix. Transverse strength and stiffness is remarkable better in particulate and fiber MMCs compared to PMCS. Aircraft structures require high values of specific strength and stiffness. These properties are essential in structures in which keeping low structural weight is needed. Despite the good mechanical properties presented by MMCs, usually PMCs are more attractive for aerospace applications due to their lower density. On the other hand, the higher transverse specific strength and stiffness of MMCs make them still useful for application in which PMCs are not suitable such as landing gears. In addition, metal alloys generally offers better mechanical properties such as toughness and impact strength than organic reinforced materials. Thermal stability, very important in applications subjected to high temperatures, is generally better in metals. For all these reason, metals such as aluminium or magnesium are still extensively used in aerospace structures.

## Matrix materials and reinforcements for aerospace applications

Aluminium alloys present a relatively high tensile strength in relation to density compared to other cast alloys, such as ductile cast iron or cast steel [8]. Therefore, this material is very attractive for aerospace applications in which strength and lightness are required. In addition, aluminum alloys present good thermal, electrical conductivity, corrosion resistance and weldability. The introduction of aluminum in aircraft structures started in the 20s when the first all metal transport aircraft Junkers F13[9] entered into service. Nowadays, aluminum alloys are still widely used in structural parts for aerospace applications such as the fuel tank of the European rocket Ariane 5. Magnesium, in form of alloy, is the lightest metal used for structural parts. For instance, magnesium is present in aerospace applications such as jet engine air intakes or helicopter transmission casings. The improvement of the mechanical and thermal properties of aluminium and magnesium based composites is actively pursued by the metallurgical industry. The use of reinforcement ceramic particles of micro and nanometric size is a promising method to potentially provide composites with enhanced mechanical properties. This type of composite material containing dispersed ceramic particles is commonly classified as particulate ceramic metal matrix composite (CMMCs). During the production of CMMCs, a tradeoff in properties typically develops because high stiffness and/or strength are achieved by increasing the volume fraction of reinforcement particles in the composite. For instance, the graphs displayed in Fig 4, obtained from the studies carried out by Nikhilesh Chawla and Yu-Lin Shen [10], presents the tensile behavior of an Al-Cu-Mg (2080) matrix composite containing different volume fractions of SiC particles 5 $\mu\text{m}$  size. According to the graph, ductility can decrease significantly when higher percentages of particles are added to the composite. On the other hand, Fig 5 presents several tensile strength curves in which different particle sizes have been incorporated to the composite at a volume fraction of 20%. In this case, the tensile strength curves show that ductility in the composite is improved when particles of smaller sizes are used.

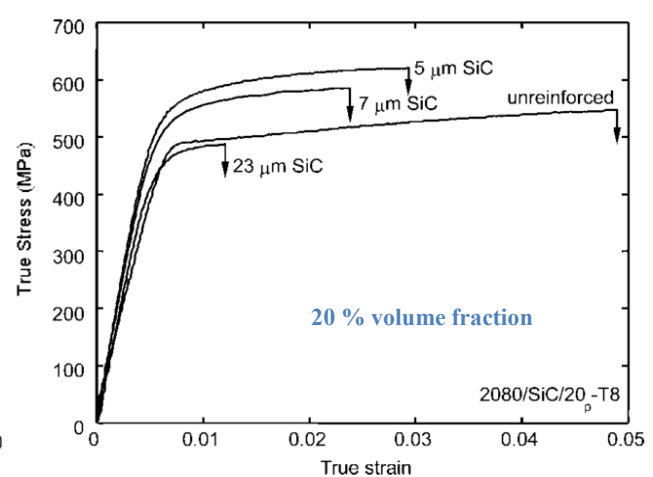
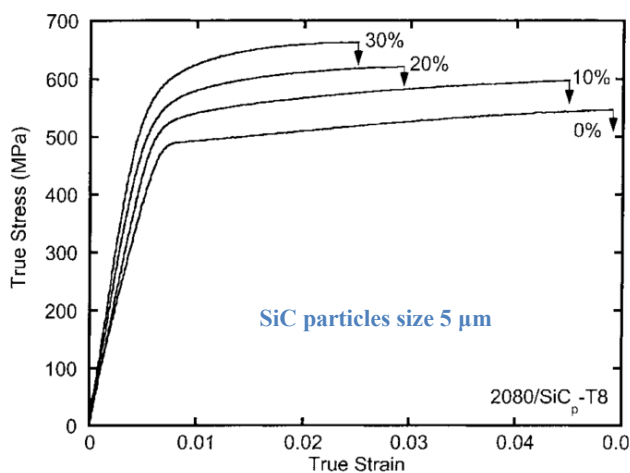


Fig 4 AlCuMg (2080) different volume fractions

Fig 5 AlCuMg (2080) different sizes SiC

Different authors have shown that in order to obtain the maximum improvement in mechanical properties of particulate reinforced composites, a good particle dispersion must be achieved [11]. For instance, Zhang [12] demonstrated that a good spatial distribution of SiC particles in an aluminium matrix particulate composite produces better results in tensile strength and hardening rate, than a composite containing particles not well dispersed.

## Light alloy nanocomposites made via field-enabled melt processing

Exomet project aims to produce ceramic metal matrix composites using techniques based on external fields such as electromagnetic stirring, power ultrasound and high energy liquid shearing. These techniques can be used to control the microstructure of alloys and also to disperse particles into metallic matrices. The following figure summarises the physical phenomena involved in each of the external fields studied:

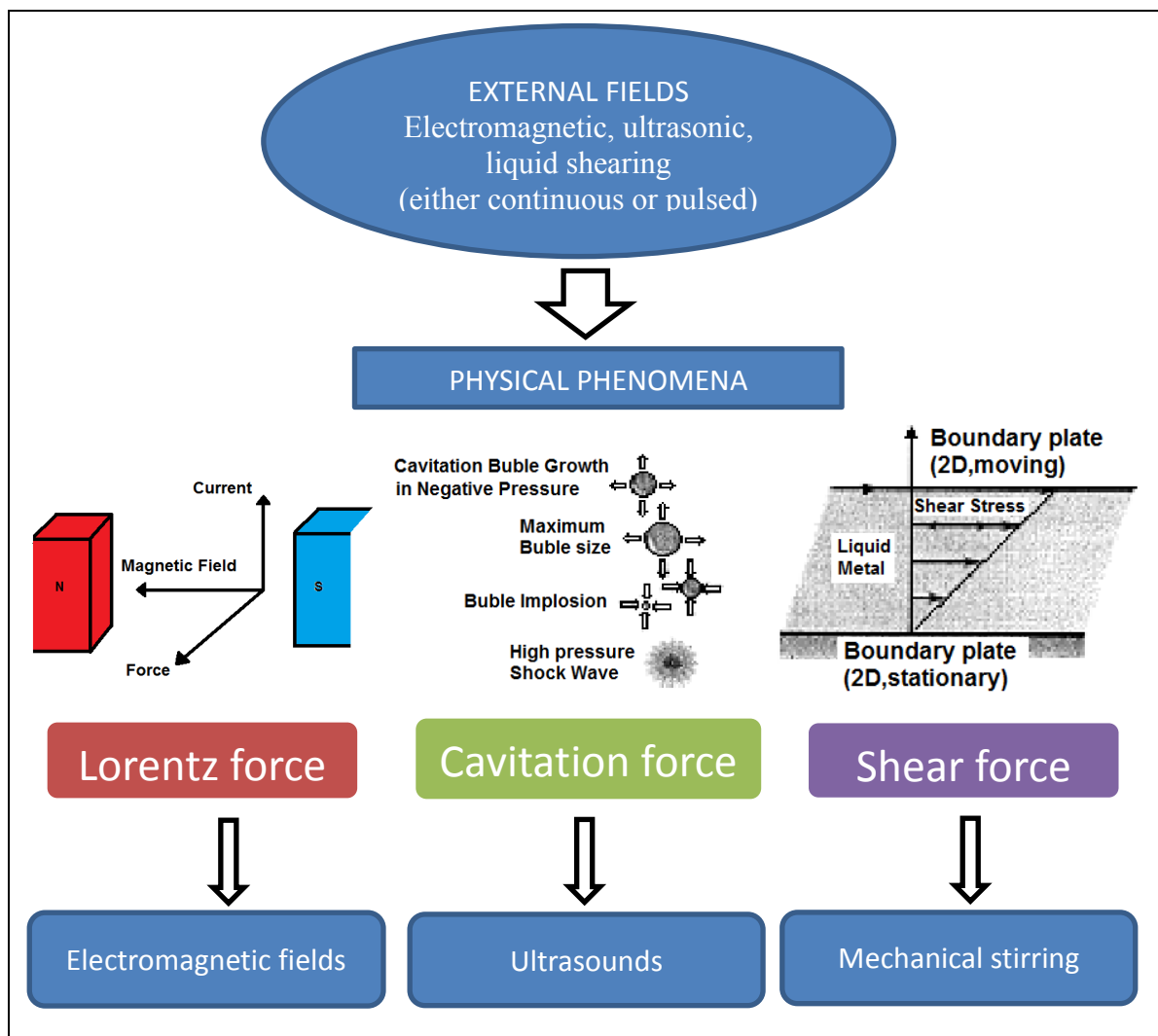


Fig 6 External fields and physical phenomena

## Power ultrasound systems

Ultrasonic waves of high intensity can generate transient cavitation and acoustic streaming in a liquid metal [13]. Ultrasounds systems can be used to disperse particles, degassing and produce grain refinement [14]. Fig 7 presents a scheme of an ultrasound dispersion system used by Borgonovo [14] to disperse nanoparticles into aluminium alloy A356. The system consists of a transducer introduced into the liquid metal which provides the ultrasound waves used to disperse the particles. A transfer tube placed over the crucible serves to introduce the particles into the melted material. Argon gas is introduced during the experiment to avoid or reduce oxidation on the free surface of the liquid metal using the gas inlet placed on the top of the crucible.

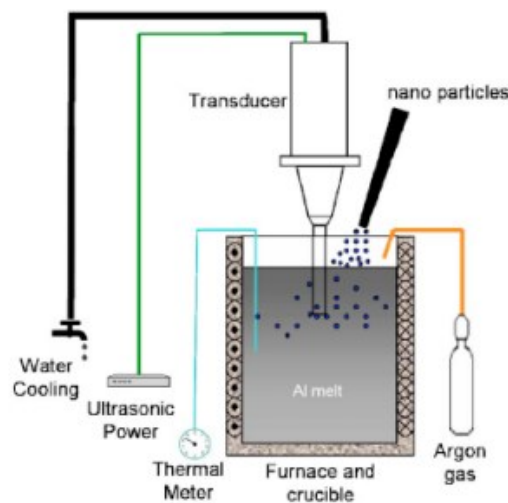


Fig 7 Scheme of ultrasound dispersion system. Borgonovo [14]

## Intensive liquid shearing

This process utilizes a mechanism such as a screw or impeller to impose a high external shear force on liquid metals, so that the conditioned melted alloy has uniform temperature, uniform chemical composition and well dispersed and completely wetted oxide particles with a fine size and narrow size distribution. The setup presented in Fig 8 utilizes a propeller to disperse particles into aluminium matrices. This system consists of a motor that drives an impeller which can be moved vertically using the position control. Particles are introduced using the transfer tube. Argon gas is introduced during the experiment using the gas inlet placed on the top of the crucible [15].

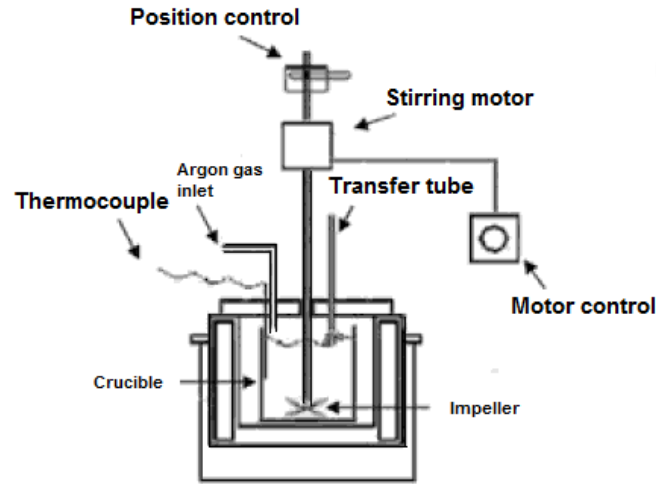


Fig 8 Liquid shearing system for particle dispersion [16]

### 1.1 Electromagnetic stirring using a travelling magnetic field

Melt stirring is a common technique used to improve the microstructure of casting materials. Electromagnetic stirring systems offer some advantages with respect to stirring systems based on ultrasound or liquid shearing, such as its contactless action on the liquid metal, and its high capacity to control accurately the forced flow. The principle of electromagnetic stirring is based on the Lorentz force induced into a liquid metal generated by an electromagnet. The electromagnetic fields applied by an electromagnet generates an induced current density ( $\mathbf{j}_{ind}$ ) called eddy current, directed in their opposite direction. The interaction between the induced current and the magnetic field ( $\mathbf{B}$ ) induces a Laplace force [16] which is used to force the liquid flow.

$$\mathbf{F}_L = \mathbf{j}_{ind} \times \mathbf{B}, (25)$$

Forcing a melt flow during solidification by electromagnetic stirring can provide with grain-refined microstructures in non-refined alloys [17][18][19]. Grain refinement due to electromagnetic stirring is produced by two mechanisms: The first is the homogenization of the temperature in the liquid metal which helps to produce equiaxed dendrites, and prevent the growth of cellular dendrites [20]. The second is related to the breaking of dendritic arms which can serve as nucleation points for new grains [21][22]. Fig 9 presents a sequence of images obtained from the work of X.Li [23] in which a primary dendrite of an Al-4%Cu peritectic alloy is broken and translated during directional solidification under strong magnetic fields. Melt agitation at the solidification front promotes dendrite fragmentation by local remelting due to changes of the local temperature and/or solute concentration. Fluid flow is also important for transporting dendrite fragments from the mushy zone into the

region ahead of the solidification front, where they act as nucleants for equiaxed grains [24] [25] [8].

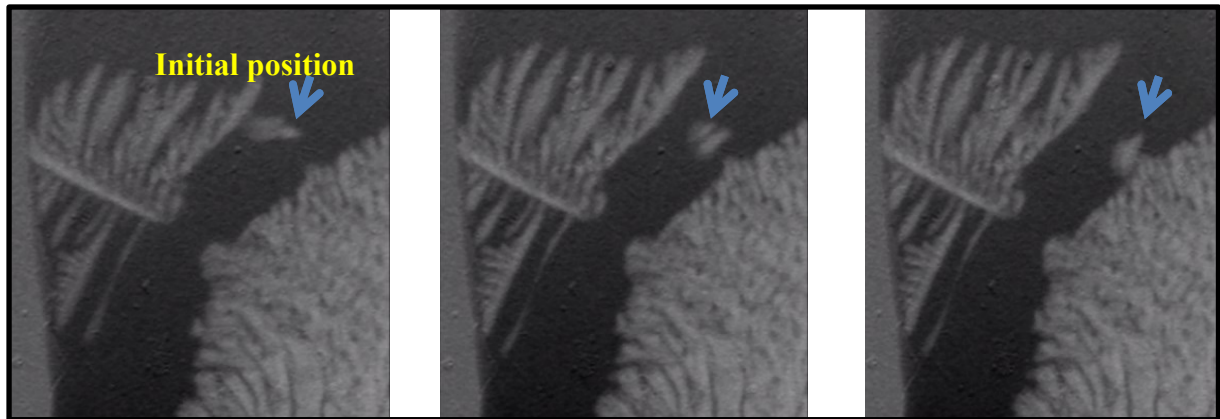


Fig 9 Dendrites breaking in Al 4% Cu

The use of electromagnetic stirring to improve the effectiveness of grain refiners dispersed into melts has been reported by several authors. For instance, studies carried out by S.Gao [26] have shown the improvement of grain refiner efficiency of  $\text{Al}_4\text{C}_3$  particles dispersed into magnesium alloys using electromagnetic stirring. The electromagnetic stirring used to produce metal matrix composites during this thesis is a vertical travelling magnetic field (TMF) based on a typical alternative current (AC) asynchronous motor. The system uses a Bitter coil surrounding a crucible in which the material is melted using resistors. A scheme of the system is presented in Fig 10.

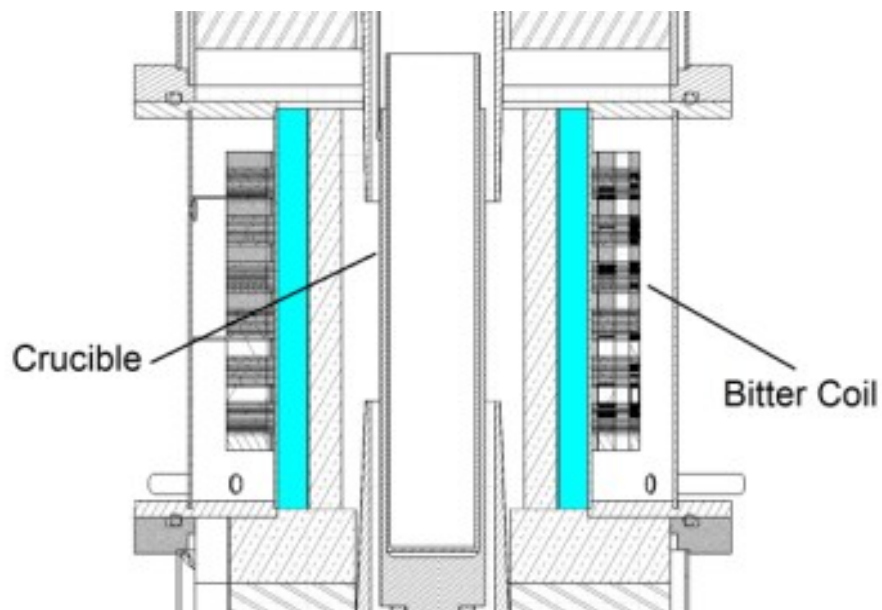


Fig 10 Electromagnetic stirring system

This type of electric motor is composed of a rotor, known as armature, and a stator containing windings connected to a poly-phase energy source, as shown in Fig 11. This configuration provides a rotating magnetic field in the stator. The speed of the rotating field is called the synchronous speed and is determined only by the frequency of the power supply and the number of poles of the machine. The magnetic field induced on the rotor provides the torque produced by the motor. In the case of the so called asynchronous AC motor, the rotor rotates at a speed slower than the synchronous speed. This type of motor can be converted into a linear or tubular motor following the stages presented in Fig 12. This type of configuration provides with a travelling magnetic field in its internal area which can be used to produce electromagnetic stirring. This technology has been already applied in the development of induction pumps designed to move liquid sodium in nuclear reactors [27]. The generalities of a travelling magnetic field stirring can be found in “**Appendix A. Electromagnetic stirring**”.

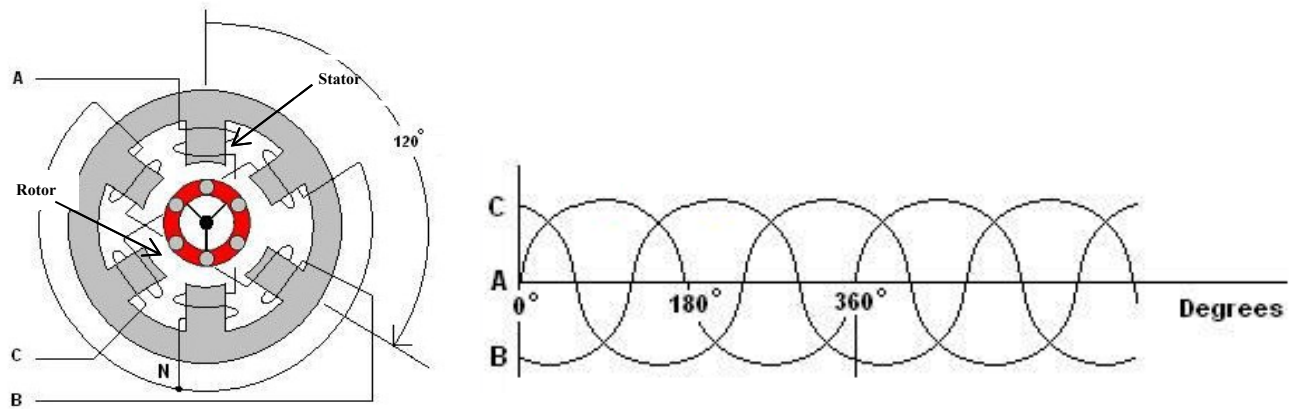


Fig 11 AC motor and polyphase energy source

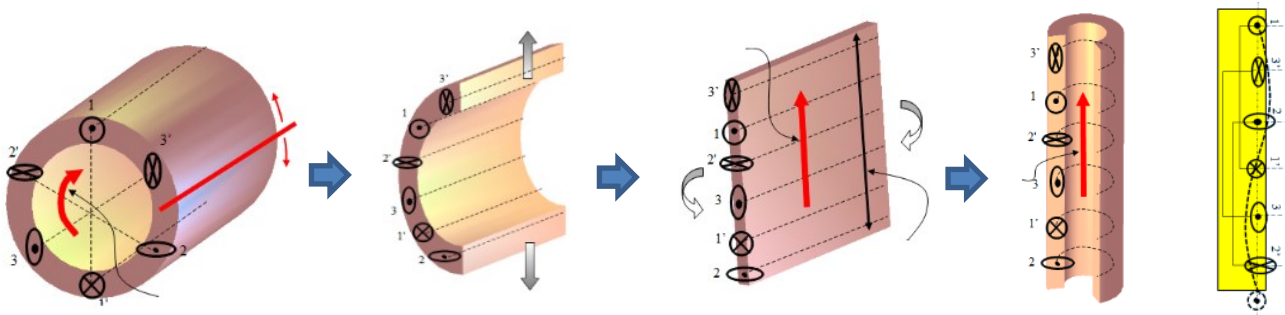


Fig 12 Stages to convert an asynchronous AC motor into tubular



## **General overview of the production of composite materials using electromagnetic stirring**

The positive effects produced on the microstructure of metals from the application of electromagnetic fields during melting and solidification has been demonstrated by several authors. Electromagnetic stirring applied by J.C Kim [28] achieved the elimination of columnar grains in the microstructure of 16 % Cr ferritic steel performed during continuous casting. Rotating electromagnetic fields have shown good results in grain refining of modified magnesium AZ91D (Y. X. JIN [29]) and promoting an equiaxial grain structure in austenitic stainless steel [30]. The application of a travelling magnetic field has been already proved as an useful tool to control macrosegregation in Al-Ni alloys during solidification [31]. In addition, electromagnetic stirring has been also applied to disperse SiC particles into steel matrices by several authors such as Zhang [32], who showed that electromagnetic stirring could provide an uniform particle dispersion. The introduction of microparticles in materials such as aluminum can promote their grain refining by increasing the number of nucleation sites available during solidification of their primary grains. Unfortunately, the efficiency of grain refining particles in aluminum and magnesium matrices is very low, for instance, generally less than 1% of  $\text{TiB}_2$  particles added to produce grain refining in aluminium are active for nucleation of  $\alpha\text{-Al}$  grains [33] [34]. Generally, the grain refining efficiency of the particles is reduced due to their tendency to agglomerate into large clusters [35] and settle at the bottom of the crucible [36]. The use of an external field to agitate the molten material could act as an effective tool to counteract the settling of the particles. Alumina particles ( $\text{Al}_2\text{O}_3$ ) are usually considered as non-desirable inclusions in aluminum alloys. They produce defects known as hard points [37] which have been related to corrosion problems and failures in parts. Therefore, the presence of these oxides in aluminium alloys is usually considered negative and should be avoided during the casting process. The Exomet project selected this type of particle considering that the efficient dispersion of alumina into aluminium casting materials could avoid the problems related with inclusions, and potentially improve its mechanical properties.  $\text{Al}_2\text{O}_3$  particles efficiently dispersed in the metallic matrix can act as nucleants producing grain refinement in the material. In addition, it is thought that a percentage of these particles will be pushed to grain boundaries where they could also help to reduce the grain size by boundary pinning [38]. The presence of  $\text{Al}_2\text{O}_3$  could also reduce the energy barrier needed for heterogeneous nucleation decreasing the undercooling needed and in consequence reducing the solidification time [39] [37]. Magnesium alloys exhibit a high strength sensitivity to grain size, and therefore their mechanical properties could be effectively improved by grain refinement [40]. The use of  $\text{Al}_2\text{O}_3$  particles could also serve to produce grain refinement of Mg-Al based alloys such as magnesium AZ91[41]. Studies performed by Shigehiro and Kiyoshi [42] showed that dispersion of  $\text{Al}_2\text{O}_3$  particles in magnesium AZ91 produced measurable changes in hardness and bending strength. Similar



results were obtained in studies performed by M. Paramsothy [43] in which  $\text{Al}_2\text{O}_3$  particles were used to reinforce magnesium hybrid alloy AZ31/AZ91, but in this case the material also presented an increase of tensile and compression strength. In addition, M. Habibnejad-Korayem [44] studied the effects of nano-sized  $\text{Al}_2\text{O}_3$  particles dispersed in pure magnesium matrix showing a significant improvement in both hardness and tensile properties. The introduction of particles inside liquid metals presents difficulties when high wetting angle is presented between the metal and the reinforcement.  $\text{Al}_2\text{O}_3$  particles are difficult to introduce in aluminum and aluminum alloys. Unsuccessful experiments to incorporate alumina particles into aluminum matrix have been reported with contact angles of  $105^\circ$  and  $97^\circ$  at  $700^\circ\text{C}$  [45][46]. It is considered that wetting of particles into metallic matrices can occur at contact angles equal or less than  $90^\circ$  [47]. Particles presenting higher contact angles would require the application of external forces to be introduced into the liquid metal. The electromagnetic stirring produced by a Bitter coil could provide the forces needed for the introduction of the particles into the molten material. In addition, a metallurgical method called superheating could help to reduce the wetting angle presented between particles and metallic matrices during electromagnetic stirring. This method consists in applying temperatures  $100^\circ\text{C}$  or higher than the melting point of the metal during casting [48].  $\text{TiB}_2$  particles are extensively used by the metallurgical industry as grain refiners of aluminum alloys [49]. They present a low wetting angle and good crystallographic match with respect to aluminum.  $\text{TiB}_2$  is usually produced ‘in situ’ in aluminum matrices during melting by the addition of titanium (Ti) and boron (B) separately or using refining rods. This method presents the advantage of the development of a clean interface between particle and matrix free of impurities or contaminants. The principal disadvantage of the ‘in situ’ method is found during the formation of particles inside the matrix. Frequently, the control of the reactions involved in their formation presents great difficulties [50], and the particles obtained forms agglomerates [51] which finish being pushed to the grain boundaries [52] during solidification.  $\text{TiB}_2$  is also available as ‘ex situ’ or already prepared microparticles. The main advantage with respect to ‘in situ’ particles is the simplicity of the production method needed to produce the composite which requires processing conditions not as critical as during the synthesis of ‘in situ’ particles [53]. However, the ‘ex situ’ refiners usually present more difficulties to be assimilated by the matrix. They frequently present an oxide layer on their surface which increase the wetting angle between particle and liquid metal [54]. The tendency to form agglomerations is also found in ‘ex situ’ particles [49]. These agglomerates, which can be of orders of magnitude larger than the individual particles, reduce the quality of the composite. The use of electromagnetic vibrations during liquid state to disperse  $\text{TiB}_2$  microparticles could help to avoid their agglomeration and increase the grain refining efficiency avoiding particle settling. The dispersion of the particles using a travelling magnetic field (TMF) applied along different directions has been studied from numerical simulations performed by Greenwich University [4]. The simulations demonstrate a strong dependency of the particle dispersion patterns on the direction of the TMF (downwards vs upwards). Experiments performed during

this thesis mixing SiC particles with pure magnesium can provide with results useful to validate the numerical simulation. Studies performed by several authors such as Janusz.L [55] have shown the capacity of SiC particles to improve the grain density of magnesium alloys such as magnesium AZ91. The dispersion of these particles using TMF could enhance their grain refinement efficiency. Magnesium alloys have shown improvement in creep resistance using reinforcements such as short fibers and particulates [56]. On the other hand, the dispersion-strengthening holds the highest potential for improvement of high-temperature properties of magnesium. For instance, authors such as H.Dieringa [57] [58] have measured the improvement in creep resistance of magnesium reinforced with SiC nanoparticles. The use of nanoparticles can produce superior performance in composites, as it was shown in the experiments performed by Y. Liu [59] in which the elastic modulus and hardness of a nanocrystalline aluminium were enhanced by its mixing with well dispersed nanoparticles of AlN. So far, the use of this type of nanoparticles to reinforce magnesium matrices has not been extensively studied. The similar lattice parameter of AlN with respect to magnesium makes this type of particle also a potential grain refiner for magnesium matrices [60]. AlN nanoparticles can potentially improve the mechanical properties of magnesium alloys at high temperatures by different reinforcement mechanisms such as Orowan pinning of dislocations or by restricting grain boundary sliding [61] [62]. The dispersion of this type of particles into a magnesium alloy Elektron 21 using the TMF could provide with knowledge of the potential of these particles to produce improvements in mechanical properties of magnesium based alloys.



# Chapter 1

## Literature review on some features of metal matrix composites

This chapter presents a review of the principal types of metal matrix composites and the main theories related to material reinforcement.

### 1.2 Metal matrix composites

Metal matrix composites (MMCs) are reinforced materials based on metallic matrices. These types of materials can be classified according to the shape of their reinforcement. The material used as reinforcement determines the principal strengthening mechanism involved in the improvement of the mechanical properties of the composite. Fig 13 presents three examples of MMCs in which three different reinforcements are depicted. The first type of composite is reinforced using fibers, usually made of carbon or glass, which produce a material highly directionally anisotropic unless they are stacked in layers placed on different direction as shown in the drawing presented. The second type of composite is reinforced using single crystals also called whiskers. These crystals grown with near zero defects are dispersed randomly in the matrix. This type of composite offers the advantage of providing similar handling and machinability than a conventional metal, and also good isotropic mechanical properties. The third type of MMC depicted is reinforced using particles of hard materials such as ceramics. The strength of this type of composite, generally called particulate normally depends on the diameter of the particles, the interparticle spacing and the volume fraction of the reinforcement. Particulate metal matrix composites are characterized by their highly isotropic mechanical properties.

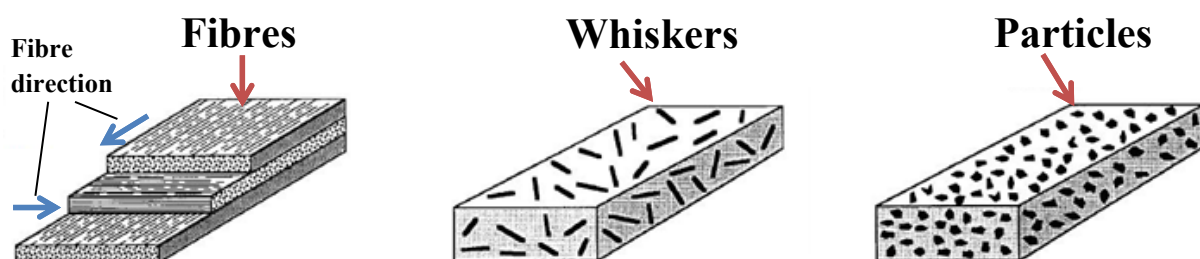


Fig 13 Different types of composites

### 1.3 Strengthening mechanisms in metal matrix composites

This section presents five strengthening theories found in literature potentially relevant to explain the mechanisms involved in the reinforcement of metal matrix composite materials using particles. But first of all it is worth clarifying what is the physical phenomenon involved in the material reinforcement. The deformation of a material is allowed by the moving of dislocations present in it. Dislocations are linear or one dimensional defects around which some of the atoms in a crystal are misaligned. There are two principal types of dislocations in materials: Edge dislocations and screw dislocations. An edge dislocation is a line imperfection caused by an extra half plane of atoms between two normal planes of atoms as shown in Fig 14 [63]. Screw dislocation is a line imperfection created by applying upward and downward shear stress to regions of a perfect crystal separated by a common plane as shown in Fig 15.

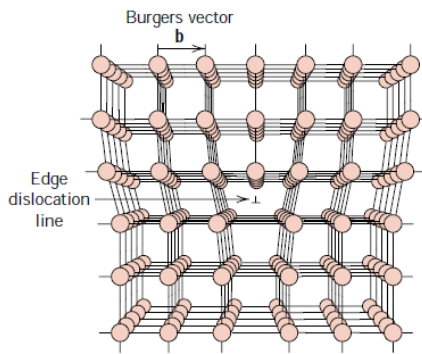


Fig 14 Edge dislocation [63]

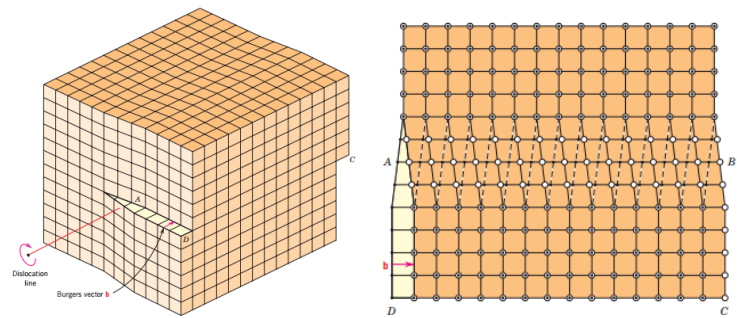


Fig 15 Screw dislocation

Dislocations interact with each other by generating stress fields in the material. The interaction between the stress fields of dislocations can impede dislocation motion by repulsive or attractive interactions which increase the yield strength of the material. Additionally, if two dislocations cross, dislocation line entanglement occurs, causing the formation of a jog which opposes dislocation motion as shown in Fig 16.

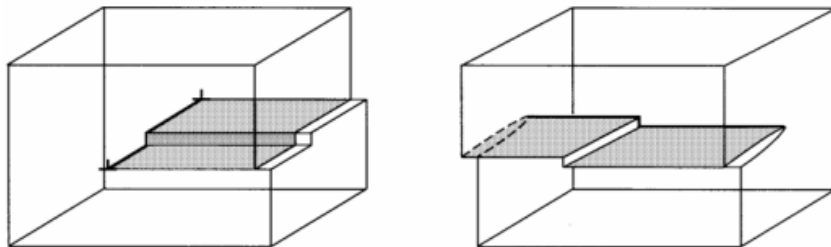


Fig 16 Dislocation jog

The dislocation density and yield strength in a material can be correlated with the following formula:

$$\Delta G_b = Gb \sqrt{\rho_{\perp}}, (1)$$

where  $G$  is the shear modulus,  $b$  is the Burgers vector and  $\rho_{\perp}$  is the dislocation density. Burgers vector represents the magnitude and direction of the lattice distortion resulting from a dislocation in a crystal lattice. In order to achieve further enhancements in mechanical properties of a material, such as tensile strength, it is necessary to introduce mechanisms to help to inhibit the movement of dislocations. One of these mechanisms of reinforcement is based on the use of particles of micrometric or nanometric size to hinder dislocation motion. A brief introduction of five strengthening theories of materials using particles is presented in the following section.

### 1.3.1 The shear lag theory

The strengthening mechanism assumed in the shear lag theory is based on the load transfer between high aspect ratio reinforcement and the matrix by means of shear stresses at the particle-matrix interface [64]. The load applied is borne partially by the particles, as shown in Fig 17.

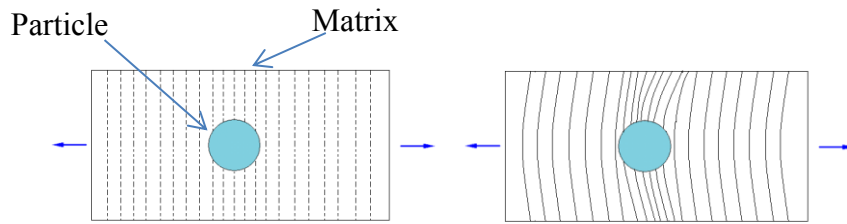


Fig 17 Particle-matrix load transfer

The equation (2) is used to predict the contribution in strengthening due to load transfer in particulate reinforced composites [65]:

$$\sigma_{cy} = \sigma_{my} \left[ V_p \left( \frac{S+4}{4} \right) + V_m \right], (2)$$

where  $V_p$  is the volume fraction of the particles,  $\sigma_{my}$  is the yield strength of the unreinforced matrix,  $\sigma_{cy}$  is the yield strength of the particulate composite,  $S$  is the aspect ratio of the particle (equal to the particle length divided by the particle thickness) and  $V_m$  is the volume fraction of matrix. In the case of equiaxed particles this equation is simplified as Eq (3).

$$\sigma_{cy} = \frac{1}{2} V_p \sigma_{my}, (3)$$

### 1.3.2 Orowan Strengthening

Hardness and yield strength can be enhanced in some metal alloys by the introduction of extremely small and uniformly dispersed particles within the original phase matrix [66]. This reinforcement method is called dispersion strengthening. Factors impeding dislocation motion, which is one of the mechanisms involved in metals yielding, can produce dramatic increases in the material's yield strength [67]. In composites containing small incoherent particles ( $<1\mu\text{m}$ ), dislocation motion can be stopped or reduced by its interaction with the particles. In the case of small impenetrable particles, a passing dislocation will bow between particles and finally pass by leaving behind an "Orowan" loop [68] as shown in Fig 18. The formation of these loops makes the dislocation motion more and more difficult. If the particles are small, the dislocations would cut through them. As a result, new surfaces (sheared particle in Fig 19) of the particle would get exposed to the matrix and the particle-matrix interfacial energy would increase.

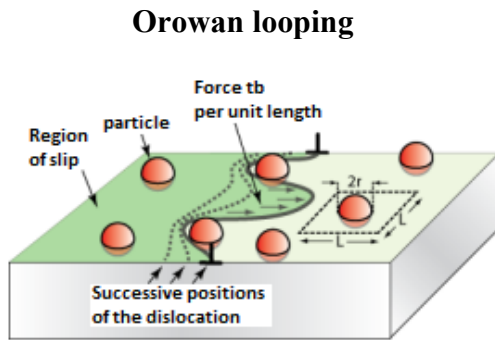


Fig 18 Orowan looping

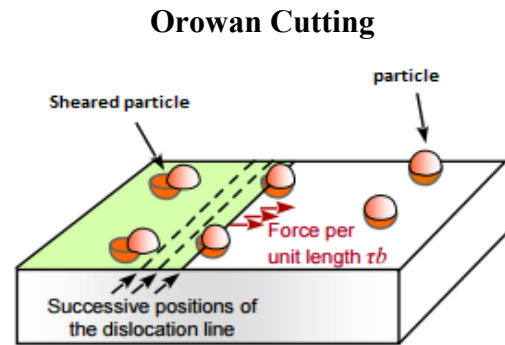


Fig 19 Orowan cutting

The Orowan effect can be expressed by the following expression:

$$f_{\text{OROWAN}} = \frac{0.13bG}{\Lambda\sigma_{ym}} \ln\left(\frac{r}{b}\right), (4)$$

$$\Lambda \sim d_p \left[ \left( \frac{1}{2V_p} \right)^{\frac{1}{3}} - 1 \right], (5)$$

Where  $V_p$  is the volume fraction of particles,  $b$  is the Burguer's vector,  $d_p$  is the particles diameter and  $G$  is the matrix shear modulus. The size, shape and amount of these particles have a direct influence in the mechanical properties of the alloy. Dispersion strengthening is

controlled by interparticle spacing in terms of the centre to centre spacing of particles. In consequence, a good dispersion of the particles is needed. Interparticle spacing can be determined by the following formula:

$$\Lambda = L - d, \quad (6)$$

$\Lambda$  is the interparticle spacing;  $L$  is the centre to centre spacing,  $d$  is the particle diameter. Due to the difficulty to measure  $\Lambda$ , for practical purpose the following relationship between the mean particle size and the volume fraction is commonly used in quantitative metallography:

$$L = \frac{1}{\sqrt{N_a}}, \quad (7)$$

If there are  $N_v$  spherical particles per unit volume, the following formula is also applied:

$$N_a = N_v \cdot d, \quad (8)$$

where  $N_a$  is the number of particles in unit area;  $N_v$  is the number of spherical particles per unit volume;  $d$  is the particle size volume fraction. The following equation (9) can be used to calculate the mean interparticle spacing ( $\Lambda$ ) if the mean particle size and the volume fraction of the particles is known. Once  $\Lambda$  is found, the Orowan's expression can be used to calculate the increase in strength in the material reinforced by the particles.

$$\Lambda = d \left( \sqrt{\frac{\pi}{6f}} - 1 \right), \quad (9)$$

The parameter  $f$  is the particle volume fraction of particles and can be calculated using the following formula:

$$f = \pi \frac{d^3}{6} N_v. \quad (10)$$

### 1.3.3 Boundary or Hall-Petch Strengthening

Plastic deformation in metals is based on the creation and motion of dislocations. Boundary or Hall\_Petch strengthening mechanism [69] is based on the impediment of the dislocations to propagate by creating crystallographic discontinuities or boundaries. When the material is stressed, dislocations tend to pile-up at the grain boundaries increasing the overall dislocation density as depicted in Fig 20. The grain boundaries act as pinning points impeding further



dislocation propagation. Small grains present short distances for atoms to move along a particular slip plane [39] and present a larger grain boundary. Hall proposed a relation between the grain size and yield stress that has been found valid for both pure metals and alloys [70]. This relation is expressed in the following equation:

$$\sigma_{pl} = \sigma_s + k_m d^{-1/2}, \quad (11)$$

where  $\sigma_{pl}$  is the proof stress of the polycrystalline specimen,  $\sigma_s$  is the resistance of the lattice to dislocation movement,  $k_m$  is the hardening factor,  $d$  is the grain diameter.

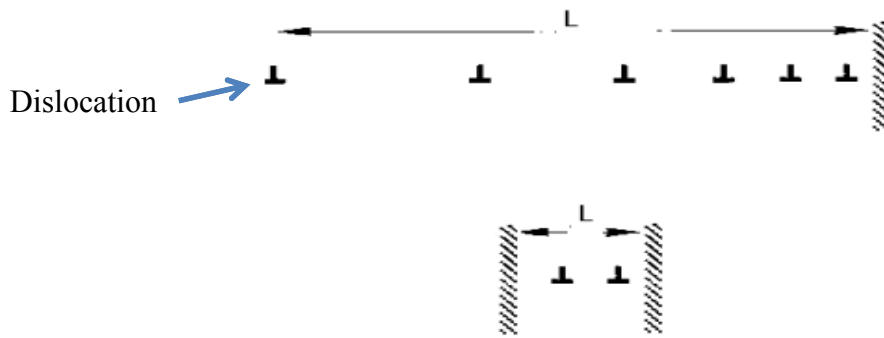


Fig 20 Dislocation motion

The introduction of particles to act as nucleants can lead to an increase of the number of grains, and to the reduction of their size. The increase of the overall grain boundary area due to the higher number of grains will help to increase the material strength. The grain size reduction can be also achieved by the interaction of particles with grain boundaries. The particles can act as pinning points retarding or stopping grain growth leading to a final refined grain structure. Fig 21 illustrates the effects produced by boundary pinning on grain size at different particle volume fractions [71].

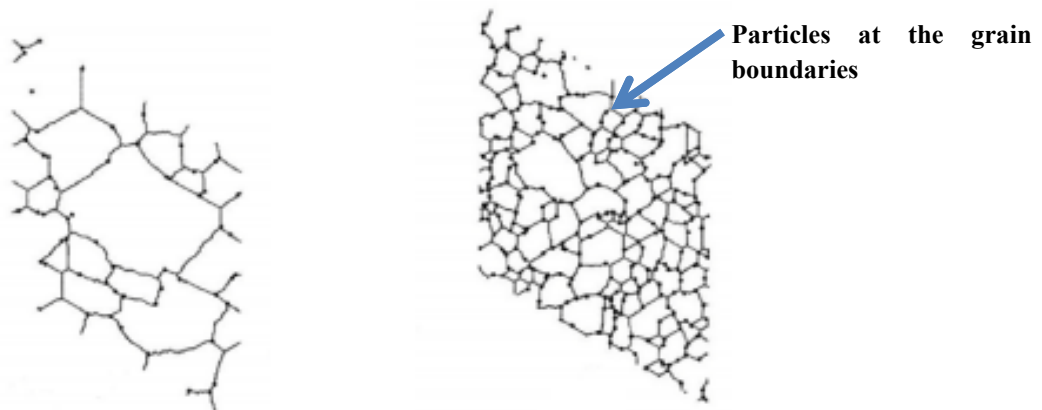


Fig 21 Effect of particle pinning in grain growth

The dependence of the pinned grain size on the volume fraction and radius of the particles could be expressed as follows [72][73][74]:

$$R = \frac{4r_p}{3V_p}, (12)$$

where  $R$  is the matrix grain radius,  $V_p$  is the volume fraction of particles added and  $r_p$  is the particle radius.

### 1.3.4 Coefficient of Thermal Expansion

Strengthening of MMC is also related to the mismatch between the thermal expansion and elastic modulus of matrix and reinforcement [75]. Plastic relaxation in the matrix can be induced by the residual stress developed due to its different coefficient of thermal expansion with respect to the reinforcement ( $\Delta CTE$ ). The stresses can induce plastic deformation in the matrix leading to the increase of dislocations density, in some cases by few orders of magnitude [76], leading to material strengthening. The tensile strength ( $\sigma_{CTE}$ ) of composite materials can be predicted by this mechanism using equation (13) [77].

$$\sigma_{CTE} = \sqrt{3\beta G_m} b \sqrt{\frac{12V_p \Delta\alpha \Delta T}{(1 - V_p) b d_p}}, (13)$$

where  $\beta$  is the strengthening coefficient equal to 1.25,  $\Delta T$  is the difference between the processing and test temperatures,  $\Delta\alpha$  is the difference between CTE values of the reinforcing nanoparticles and matrix.  $V_p$  is the volume fraction of nanoparticles,  $\alpha$  is the proportionality constant,  $b$  is the Burgers vector and  $d_p$  is the average particle diameter.

### 1.3.5 Sum of Contributions

The strength of the composite ( $\sigma_c$ ) can be evaluated by summing all the contributions related to single strengthening effects with the original yield strength of the unreinforced matrix [39] Eq. (14).

$$\sigma_c = \sigma_m + \sum_i \Delta\sigma_i, (14)$$

where  $\sigma_m$  is the yield strength value of the unreinforced matrix,  $\Delta\sigma_i$  is the yield strength of the sum of all contributions due to different strengthening effects.

## 1.4 Manufacturing methods of metal matrix composites (MMC)

This section presents some representative techniques used to manufacture metal matrix composites differentiated by the physical state of the matrix material in which a solid reinforcement is introduced.

### 1.4.1 Solid processes

In solid processes both reinforcement and matrix material are mixed in solid state. An example of this type of process is powder **blending and consolidation**. In this technique, the matrix material in form of a powder is blended with ceramic short fibres or whisker particles. The material is afterwards consolidated using hot isostatic pressing (HIP) or extrusion. Another example of solid process is based on **diffusion bonding**. This technique uses the evaporation of a matrix material which is diffused on the surface of reinforcement fibres to produce mono filament-reinforced matrix composites. This process is commonly used to produce Ti based fibre reinforced composites. In addition to the solid process presented before, there is another method to reinforce metal using fibres consisting in the use of a high power electron beam to coat the fibres by the metal itself. This technique is called **Physical vapour deposition**.

### 1.4.2 Semisolid processes

Semisolid metal processing deals with semisolid slurries in which non-dendritic solid particles are dispersed [78]. One of the most popular semisolid process used in the metallurgical industry is **Rheocasting** [79]. This process is also used to produce nanocomposites. In this case, the reinforcement particles are mixed with a semi-solid matrix using mechanical or electromagnetic stirring system. The material obtained is afterwards injected into a die without intermediate solidification. Two techniques based on semisolid process such as **Rheomoulding** and **Thixomolding** are also used to produce nanocomposites. The main difference between them is that whereas Rheomoulding use rotating screw/s to stir mechanically a metal in semisolid state, Thixomolding brings the material to semisolid state

using mostly the energy generated by shearing of pellets of material using continuously rotating screw.

### 1.4.3 Liquid processes

Liquid processes to produce composites involve the incorporation of particles into metals in liquid state [80]. Among the liquids processes adapted to the production of particle reinforced composites are: **Stir casting** and **infiltration process**. Stir casting is one of the most commercially used. In this method, pre-treated particles are introduced using a vortex created by a rotating impeller and mixed with a matrix material in liquid state. Infiltration process is a technique in which the liquid material is injected / infiltrated into the interstices of porous pre-forms made of fibres, whisker or particles to produce a composite material.

## 1.5 Theoretical Studies in solidification behaviour

The influence of the microparticles in the solidification of metals is directly related to the improvement in strength of the final material. Solidification (nucleation) is a phase transformation in which a material in liquid state passes to solid state. The emerging new phase has a lower energy than the original [81]. Nucleation occurs via the formation of small embryos of the solid phase inside the large volume of the liquid phase as shown in Fig 22. During the cooling of a liquid, nucleation will begin only after the temperature has been lowered below the equilibrium solidification (or melting) temperature  $T_m$ , this phenomenon is called undercooling.

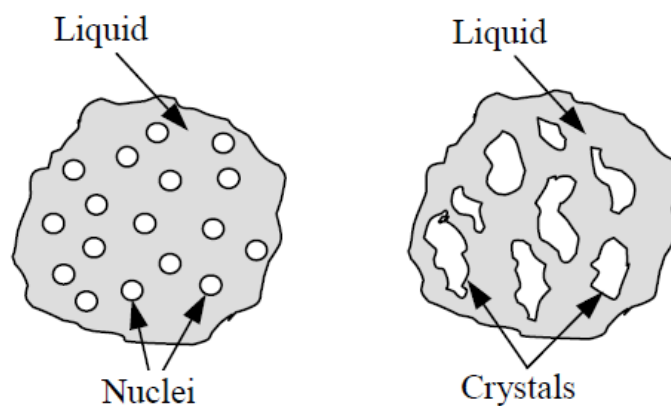


Fig 22 Nucleation of crystals

In order to understand the mechanisms involved in solidification, a brief introduction to the classical nucleation theory is presented in this section.

### 1.5.1 Classical nucleation theory

The classical nucleation theory was developed in 1930s by Becker, Döring and Volmer [82][83]. It is a phenomenological approximation based on the calculation of the free energy of formation of small clusters, by using macroscopic quantities such as surface tension and density. The first concept to understand this theory is that a liquid cooled below its melting temperature ( $T_m$ ) will have a free energy higher than the material in solid state:

$$\Delta G = G_{liquid} - G_{solid} , (15)$$

Since solidification will decrease the free energy of the system,  $\Delta G$  is said to be the driving force for the transformation.

$$\Delta G = \frac{16 \pi \sigma^3}{3 \Delta G_v^2} f(\theta) , (16)$$

where  $\sigma$  is solid-liquid interfacial energy,  $\Delta G_v$  is the difference in Gibbs free energy between solid and liquid phases and  $f(\theta)$  is the catalytic factor. The change in free energy  $\Delta G$  (a function of the internal energy and enthalpy of the system) must be negative for a transformation to occur. For the formation of a particle, the free energy change  $\Delta G(r)$  is balanced by two ‘competitive’ factors, the volume free energy and the interfacial energy due to formation of solid phase, as can be seen in the free energy change balance graph presented in Fig 23. This solidification model assumes that spherical nuclei of the solid phase are formed in the interior of the liquid as is shown in Fig 24, and also that atoms cluster together-similar to their packing in the solid phase,.

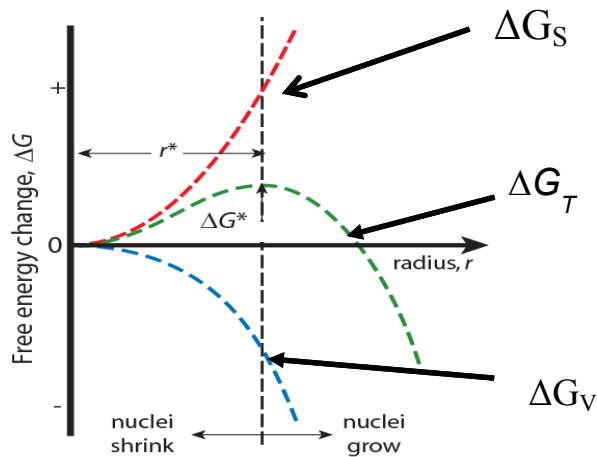


Fig 23 Free energy change balance

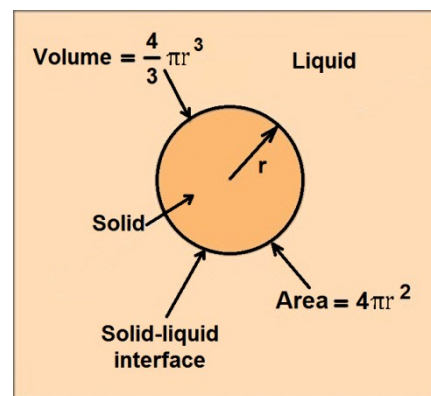


Fig 24 Solid particle formation

The process of solidification must occur by forming a small particle of solid phase. The change of Gibbs free energy when a particle of radius  $r$  form from the liquid can be calculated using the following formula:

$$\Delta G_{(T)} = \Delta G_v + \Delta G_s, (17)$$

where  $\Delta G_T$  is the total free energy to form the nucleus,  $\Delta G_v$  is the volume free energy and  $\Delta G_s$  is the surface free energy. Both energies can be calculated using the following formulas:

$$\Delta G_v = \Delta g \frac{4}{3} \pi r^3, (21) \quad \Delta G_s = 4\pi r^2 \gamma, (18)$$

$$\Delta g = -\Delta s_f \Delta T (19)$$

where  $r$  is the critical radius which is the minimum size to be achieved by atoms clustering together, before the new-phase inclusion begins to grow.  $\gamma$  is the surface tension. The critical radius can be calculated using the following formula:

$$r = \frac{-2\gamma T_m}{\Delta H_f \Delta T}, (20)$$

where  $T_m$  is the melting temperature,  $\Delta H_f$  is the latent heat of solidification;  $\Delta T$  is the difference between the melting and supercooling temperatures. This nucleation process defined as **Homogeneous** occurs spontaneously and randomly in the interior of a uniform substance. The driving force for this type of nucleation is the superheating or supercooling of the medium. Moreover, there is a second type of nucleation defined as **Heterogeneous** in which a surface serves to assist or catalyse the process. The capacity of the surface to facilitate the nucleation depends on the contact angle of the nucleus with respect to the substrate as shown in Fig 25.

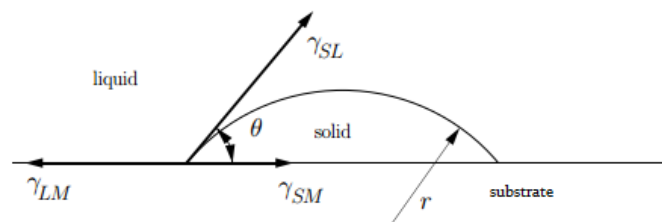


Fig 25 Contact angle

The contact angle  $\theta$  is determined by the surface energy balance using equation (21):

$$\gamma_{LM} = \gamma_{SM} + \gamma_{SL} \cos \theta, (21)$$

where  $\gamma_{LM}$  is the surface energy between the solid and liquid,  $\gamma_{SM}$  is that between the solid and the mold,  $\gamma_{SL}$  is that between the liquid and the substrate, and  $\theta$  is the contact angle. The total energy of formation of a nucleus can be calculated using the following formula:

$$\Delta G_{(r)} = \left[ \frac{4}{3} \pi r^3 \Delta G_v + 4 \pi r^2 \gamma \right] S(\theta), (22)$$

where  $S(\theta)$  is the contact angle calculated using the following expression:

$$S(\theta) = \frac{(2 + \cos \theta)(1 - \cos \theta)^2}{4}. (23)$$

Small angles will lead to a lower free energy changes and in consequence lower nucleation barrier. The critical radius of the nucleus ( $r$ ) for a heterogeneous nucleation is the same as that for a homogeneous nucleation. However, the critical volume of the nucleus is usually smaller due to the contact angle. A typical example of heterogeneous nucleation can be found between the molten metal aluminium and the crystalline crucible containing it. Heterogeneous nucleation is also affected by alloy composition, chemical and physical nature of the nucleation particles, and also by the exact solidification conditions [84].

## 1.6 Grain refinement using grain refining particles

The process of grain refining consists in reducing the crystal size of the new formed primary phase from the liquid metal using chemical, physical or mechanical methods. Grain refinement techniques are used to produce equiaxial grain structure and eliminate columnar grains in metals [85]. Improvement in hot tearing resistance and enhancement in mechanical properties are among the benefits obtained from the reduction of the grain size [86]. One of the common methods used in foundries to achieve grain refinement of metals is based on the introduction of refining particles during melting. These particles serve as nucleant for the solid phase increasing the number of grains and generally producing a decrease of the

undercooling temperature needed to start solidification [87]. In order to understand the mechanisms involved in grain refinement using particles, it is important to clarify the difference between nucleation potency and nucleation efficiency of refining particles. The nucleation potency is defined as the degree of lattice matching at the solid/substrate interface during heterogeneous nucleation [84], this crystallographic match plays an essential role in the effectiveness of the inoculants to act as nucleant [88]. The better the lattice match, the higher the nucleation potency will be. The lattice mismatch  $\xi$  can be calculated using the following equation [89]:

$$\xi = \left( \left( 1 - \frac{x_b - x_n}{x_n} \right) \right) \cdot 100\% , (24)$$

where  $\xi$  is the match index. Both  $x_b$  and  $x_n$  are crystal lattice parameters in the specified direction of the base and nucleus. When the value of index ( $\xi$ ) is closer to 100%, the more effective is the base to produce heterogeneous nucleation of the inoculated metal. On the other hand, nucleation efficiency refers to the effectiveness of a given type of solid particle to produce grain refinement, under specific physical characteristics such as particle number and size distribution; and under specific solidification conditions which depends on parameters such as the cooling rate applied [33]. Therefore, by modifying the solidification conditions, changes in the grain refiner efficiency can be achieved. According to the free growth model developed by Greer and his co-workers [90] [91], a significant grain refinement can be achieved when a high density of potent nucleation particles with an appropriate size and distribution is found inside the material. Particles of different materials, such as ceramics, can be introduced into molten materials to reinforce them, and to acts as inoculants increasing the grain density of the final material [92]. The capacity of the inoculants to serve as nucleation points is related using the free-growth model to the undercooling achieved during their dispersion into the molten material [90][93]. The ‘activation’ of the particle will take place at different cooling rates with respect to its size according to the equation (25). Small particles will need high cooling rates to be active, which could be difficult during casting of materials. The undercooling needed to activate a particle can be calculated using the following equation:

$$\Delta T_{fg} = \frac{2\sigma_{ls}}{[\Delta s]R_N} , (25)$$

where  $\Delta T_{fg}$  is the undercooling needed to activate the particle,  $\Delta s$  is the entropy of fusion per unit volume,  $R_N$  is the radius of the nucleant particle and  $\sigma_{ls}$  interfacial energy. The potency and efficiency of nucleating particles is affected by the alloy composition through adsorption



at the liquid/particle interface, and through the segregating power of the solute present in alloy which is defined as the growth restriction factor  $Q$ . The balance between latent heat production and heat extraction has an important influence in the degree of grain refinement achieved beside the size of the inoculant. The solute partitioning at the solid-liquid interface and diffusion limits the rate of latent heat produced. The growth restriction factor  $Q$  can be calculated using the following formula [94][95]:

$$Q = m (K - 1)C_0, (26)$$

where  $m$  is the liquidus slope,  $k$  is the partition coefficient, and  $C_0$  is the solute content.

# Chapter 2

## Experimental setup

This chapter presents the equipment used in this study to produce metal matrix composites (MMCs) and pure metals stirred electromagnetically. The chapter is divided in two parts: The first introduces the furnaces used to produce the materials. The second presents the techniques used to characterize the materials produced.

### 1.7 Vertical Bridgman furnace VB2

The vertical Bridgman furnace VB2, presented in Fig 26, was manufactured by the company Cyberstar. This furnace is characterized by having two distant heating elements separated by a temperature gradient controlled area. VB2 furnace is designed to produce directional solidification (DS) which is commonly used to study solidification of materials. The Bridgman technique is used to study microstructures found in the interface between solid and liquid state, and is widely used to study the columnar to equiaxed grain transition (CET). In VB2 furnace the directional solidification can be produced by two different methods: The first uses the accurate control of the heating provided by the resistors reducing gradually their temperature while maintaining the temperature gradient. The second uses a motorized withdrawing system, presented in Fig 27, to remove the crucible from the central area where the material is melted, to the lower part of the furnace maintained at lower temperature. The area between the hot and cold zones is insulated to provide an adiabatic zone designed to reduce radial temperature gradients, to decrease the sensitivity of the interface shape to thermal perturbations [96], and to reduce isotherm curvature at the melting point [97]. The hot and cold zones are equipped with graphite resistors insulated with graphite foam and water cooled. Fig 28 and Fig 29 presents a detail view of the central area in which the liquid to solid transition takes place. The crucible is insulated using graphite foam (presented in grey) and aerogel (in blue). The Bitter coil used to produce electromagnetic stirring is placed around the crucible area.

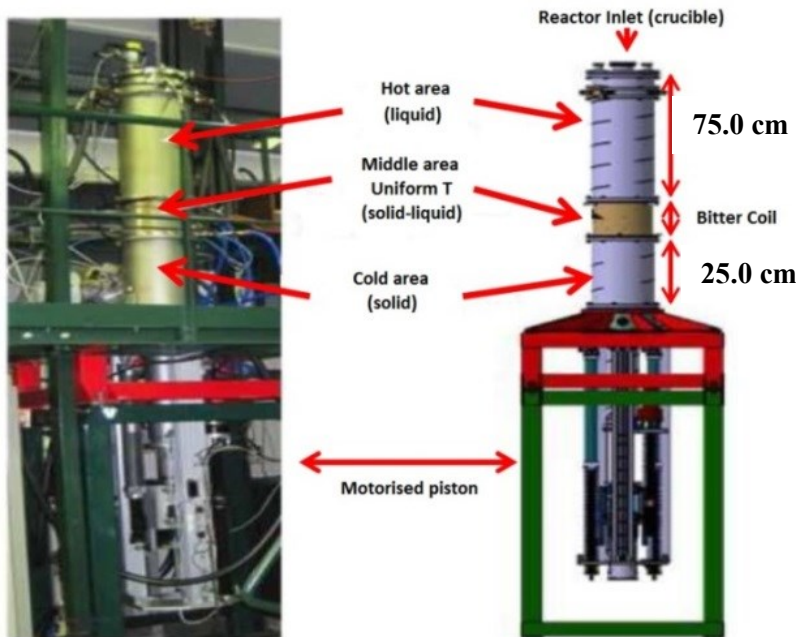


Fig 26 VB2 Vertical Bridgman

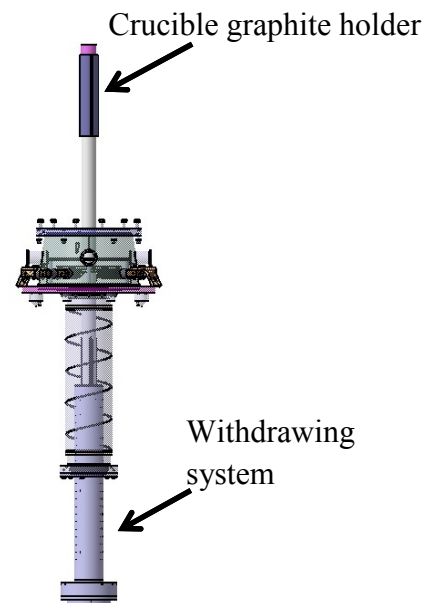


Fig 27 Crucible drawing system

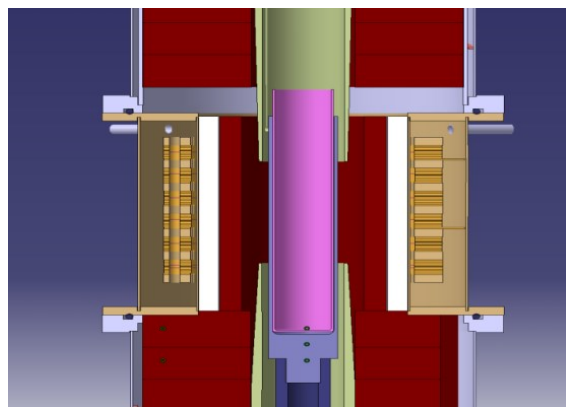


Fig 28 Bitter coil detail view 2

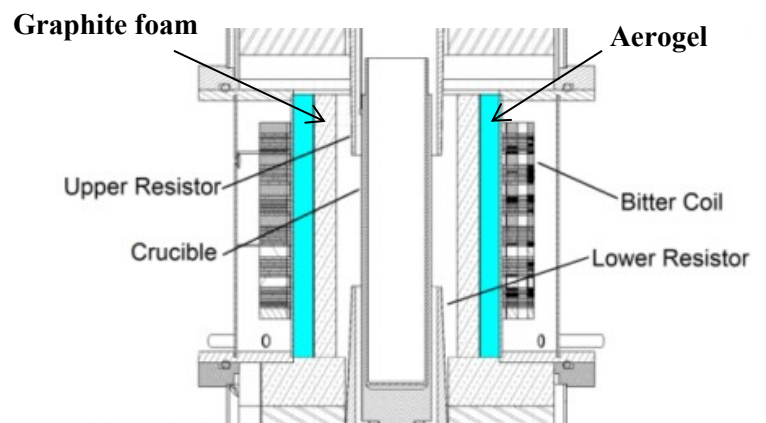


Fig 29 Bitter coil area detail view

### 1.7.1 Characteristics and uses of VB2 electromagnetic stirring

The Bitter coil electromagnet installed in VB2 can generate strong magnetic fields. Instead of coils of wire, Bitter coils are constructed using circular metal plates separated by insulating spacers stacked in a helical configuration, as shown in Fig 30. The electrical current applied to the coil flows in a helical path through the plates. The main advantage of the Bitter coil with respect to conventional electromagnetic systems is that similar stirring intensities can be produced but at reduced input of energy [24]. The Bitter coil used in VB2, shown in Fig 31, is configured to produce a travelling magnetic field (TMF) based on the principle of the asynchronous motor. The electromagnet uses an alternative current of frequency 50 Hz and produces an electromagnetic wave with a synchronism speed of 9 m/s. The method used to

calculate the speed of synchronism and metal flow speed can be found in ‘**Appendix A. Electromagnetic stirring**’. Table 1 presents the theoretical maximum stirring speeds achievable in magnesium and aluminium melted materials under two magnetic field intensities.

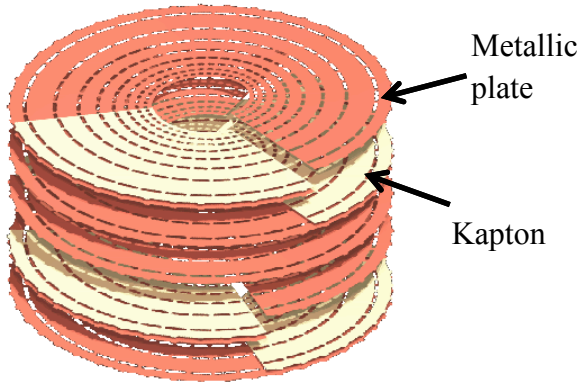


Fig 30 Bitter coil helical plates

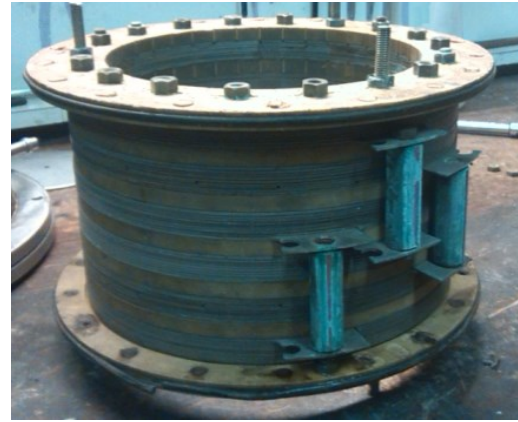


Fig 31 VB2 Bitter coil

Material	Aluminium	Magnesium
Magnetic field of 15 mT	0.022 m/s	0.04 m/s
Magnetic field of 70 mT	0.129 m/s	0.24 m/s

Table 1 Theoretical stirring speed at different magnetic field intensities

One of the effects of the electromagnetic stirring produced by a travelling magnetic is the temperature homogenization in the liquid metal. The following figures present the results of a numerical simulation of the Bitter coil area, produced by V.Bojarevics [4] using the software COMSOL Multiphysics. Fig 32 presents the temperature gradient observed in the liquid metal at the beginning of the application of a TMF oriented to upwards direction. The reduction of the temperature gradient after some seconds of the application of electromagnetic stirring can be observed in Fig 33.

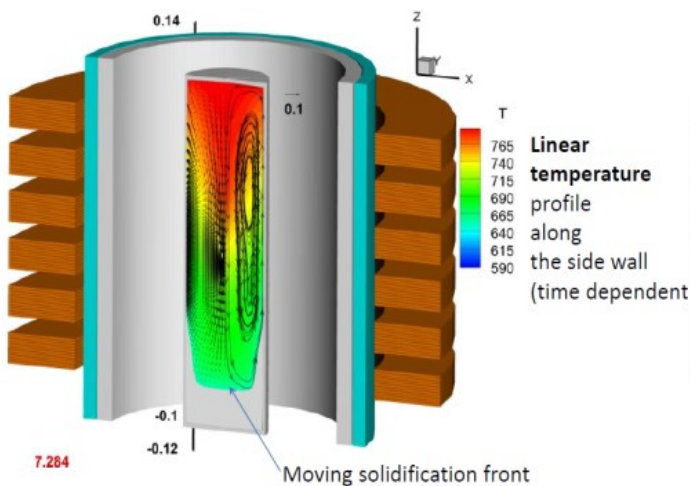


Fig 32 VB2 furnace numerical simulation

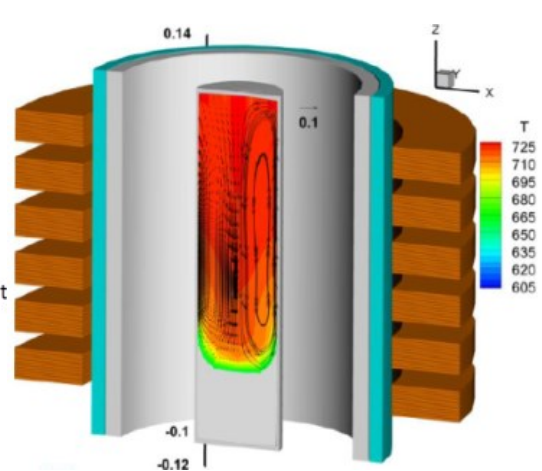


Fig 33 VB2 furnace numerical simulation

Particles introduced as reinforcement or nucleants have the tendency to settle down during casting processes. The sedimentation of particles due to gravity has a negative effect in the performance of grain refiners and reinforcement particles. The induced metal flow produced by electromagnetic stirring can be used to disperse particles and counteract their settling [98]. One of the methods used to approximate the particle settling time was developed by Stokes in 1851. This method considers the particles as spheres and assumes no interaction between them. Using the Stokes method, the calculated time to settle on the bottom of the VB2 crucible of a  $4.5\ \mu\text{m}$   $\text{Al}_2\text{O}_3$  particle placed into melted aluminium, is approximately 15 seconds. Details of the settling calculation can be found in “**Appendix C. Particle settling calculation**”. In consequence the application of electromagnetic stirring appears to be necessary in order to avoid settling of particles dispersed using this furnace. The dispersion of SiC particles of several sizes into pure magnesium using the TMF provided by VB2 has been studied using a 2D numerical simulation produced by V.Bojarevics. The results of the numerical simulation are presented in Fig 34 and Fig 35. The figures show that particle concentration patterns in the material are strongly governed by the vertical orientation of the magnetic field applied (upwards vs downwards). The shape of the solidification front, which plays an important role in the particle engulfment by the matrix material, is also affected by the orientation of the magnetic field [99]. The solidification front developed using upwards travelling magnetic field presents a concave shape. The numerical simulation shows that this type of solidification front produces a fast entrapment of the particles at the bottom of the specimen. On the other hand, the numerical simulation shows that a solidification front with a central convex shape is generated when downwards TMF is applied. This type of solidification front delays the assimilation of the particles and enhances the concentration of the particles on the upper part of the specimen. The numerical simulation also shows that larger particles ( $>10\ \mu\text{m}$ ) which are more sensitive to the buoyancy and EM force effects [100] [101], present a high tendency to be rejected to the edges of the specimen.

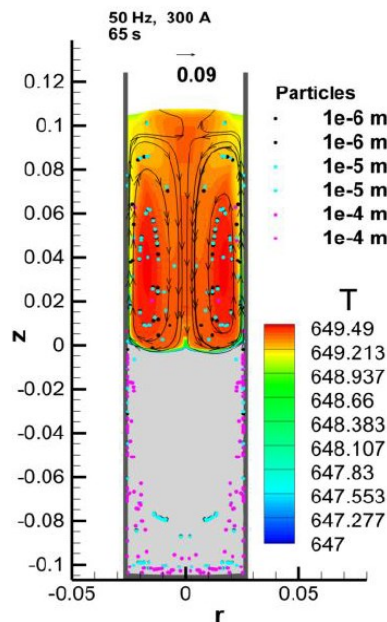


Fig 34 Upwards TMF

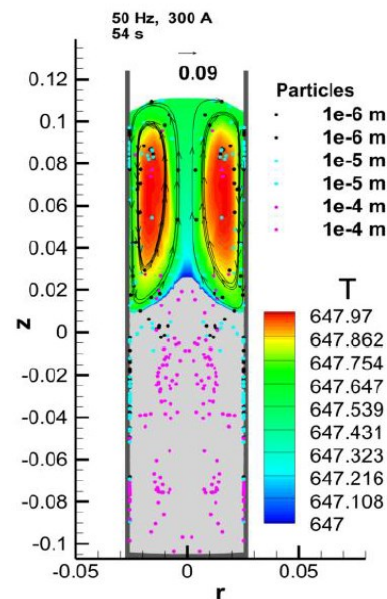


Fig 35 Downwards TMF



## 1.7.2 VB2 furnace procedures

The samples produced in VB2 furnace are melted inside crucibles made of different materials. In the case of melting aluminium, the crucible used is made of quartz (presented in Fig 36) which is protected with a layer of boron nitride (pink surface) to avoid its reaction with the melted material. On the contrary, magnesium or magnesium alloys are melted using a crucible made of steel which presents a low reactivity with magnesium. The materials to be melted are machined in form of discs with a shallow side, shown in Fig 37, in which microparticles are introduced. The discs are piled up, as shown in Fig 38, and introduced into the quartz or graphite crucible, which is finally placed into a graphite holder, shown in Fig 27 (page 46).



Fig 36 Quartz cell



Fig 37 Disc of material



Fig 38 Pile up of discs

## 1.8 Cold crucible glove box furnace (Transel)

The furnace TranSel, presented in Fig 39 allows a safe introduction of nanoparticles into selected matrix materials. Transel furnace is equipped with an induction heated water cooled crucible made of copper, also commonly called ‘cold crucible’. The wall of this type of crucible consists of a ring formed by several closed water cooled sectors fixed on a bottom plate as shown in Fig 40 and Fig 41. The induction coil around the crucible is connected to an oscillating circuit, shown in the scheme presented in Fig 42, feed by an induction generator capable to generate a medium frequency alternating current to drive the coil. The typical frequencies used to melt magnesium range from 8 to 14 KHz with a power level of 8 to 14 kilowatts. The induced currents inside the crucible sectors produce an alternating magnetic field in the material placed inside the crucible. The material is melted by the heat generated by the ohmic losses of the alternating field [102]. Among the advantages obtained by the use of this type of furnace are the visual control of the melt, and the capacity to add manually particles and other materials into the crucible during the melting process. The lack of insulation around the crucible area facilitates the removal of particles that could ‘escape’ from

the melt avoiding possible permanent contamination of the furnace. The temperature of the melt is controlled using two thermocouples type C placed inside the crucible. The experiments are performed under argon atmosphere.

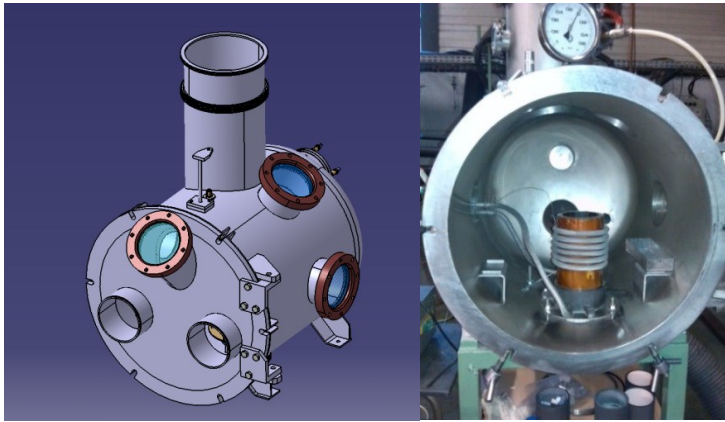


Fig 39 TranSel furnace Catia V5 and picture

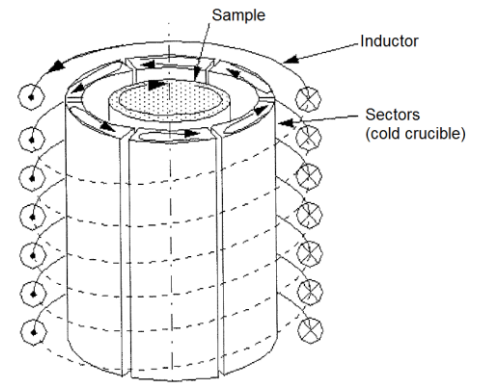


Fig 40 Cold crucible scheme



Fig 41 Detail view of cold crucible

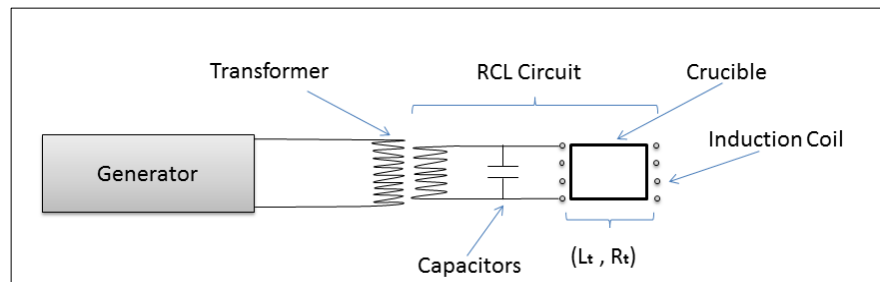


Fig 42 Induction system scheme

Nanoparticles are introduced into the molten matrix material used as a matrix for the composite inside capsules, as the one shown in Fig 43, made of the same matrix material. The high bulk density of the particles makes necessary the use of several capsules to obtain a standard percentage in weight of 1% of reinforcement. An example of the final specimen obtained using TranSel furnace is presented in Fig 44.

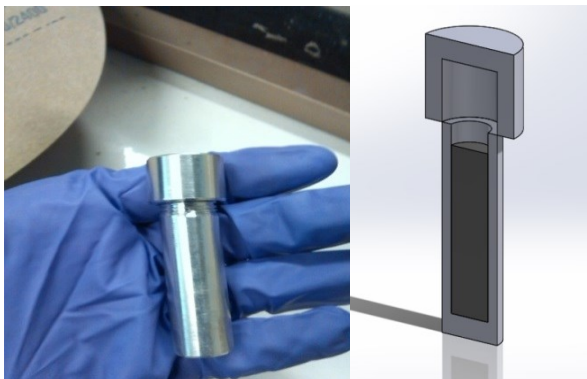


Fig 43 Capsule containing nanoparticles



Fig 44 Magnesium sample from TranSel

## 1.9 Techniques used for characterization of materials

This section presents a brief introduction of the different techniques used for the characterization of the materials produced during this thesis. Optical and SEM microscopy are the main the techniques used to analyze visually their microstructure, whereas the principal techniques used for their chemical analysis are X-ray spectrometry and EDS mapping. In the case of particle dispersion, this is studied using X-ray tomography and X-ray radiography. Regarding the mechanical properties of the materials produced, these are studied using standard mechanical testing.

### 1.9.1 Optical microscopy (OM)

Optical microscopy (OM) is commonly used to study the microstructure of materials. Images obtained with this technique can be used to measure accurately the average grain size presented by metallic samples. The optical microscope used in this study is a model Axio Imager 2. The samples to be analysed are mounted in epoxy resin and ground using rotating discs of abrasive paper of silicon carbide flushed with water. The grinding is performed in stages in which finer papers are used successively. The process starts using coarsest paper grade 80P, and finishes with the finest paper 1200P. Afterwards, the samples are polished using discs covered with soft cloth impregnated with a diamond polishing suspension. The polishing process is performed using liquid suspensions containing diamonds of size 9  $\mu\text{m}$ , 3 $\mu\text{m}$ , and 1 $\mu\text{m}$ . These liquid suspensions are applied consecutively into different polishing steps. In order to facilitate the visualization of the microstructure, the samples are etched through selective chemical attack using different reagents. Table 2 presents the composition of the reagent applied to reveal the grain structure on samples of pure aluminium and aluminium alloys. The etching procedure consists in the immersion of the polished sample maintained at a temperature of 60°C into the etching solution during 60s. Afterwards, the specimen is dried blowing argon on its surface.

Substance	Amount
CH <sub>4</sub> O (Methanol)	25ml
HCl (Hydrochloric Acid)	64.5 ml
HNO <sub>3</sub> (Nitrid Acid)	38.25 ml
HF (Hydrofluoric acid)	10 ml

Table 2 Etching solution used to reveal grains in aluminium samples



The etching solution presented in Table 3 is used to study segregation in samples of aluminium A357. In this case, etching is performed immersing the sample into the solution during 20 s.

Substance	Amount
H <sub>2</sub> O	90 ml
CrO <sub>3</sub> (Chromium trioxide)	2 g
H <sub>2</sub> SO <sub>4</sub> (Sulfuric acid)	4 ml
HF (Hydrofluoric acid)	4 ml

Table 3 "Si Blue" etching solution used to reveal segregation in aluminium 357 samples

Table 4 presents the etching solution used to reveal the grain structure on samples of pure magnesium and magnesium alloys. The etching procedure is the same than the one used for aluminium, but in this case the magnesium sample is immersed into the etching solution only during 20 s.

Substance	Amount
H <sub>2</sub> O	10 ml
C <sub>2</sub> H <sub>6</sub> O (Ethanol)	100 ml
C <sub>2</sub> H <sub>4</sub> O <sub>2</sub> (Acetic Acid)	5 ml
C <sub>6</sub> H <sub>3</sub> N <sub>3</sub> O <sub>7</sub> (Picric acid)	5 g

Table 4 Etching solution used to reveal grains in magnesium samples

The average grain size of a representative number of grains on each sample is measured manually using the software AxioVision SE64.

## 1.9.2 SEM/EDS microscopy

Scanning electron microscopy (SEM) is extensively used during this study to analyse the distribution of the reinforcement particles in the MMCs produced. An electron gun and several electromagnetic lenses are installed inside the SEM column. Operating under vacuum conditions, electrons are accelerated to energies in the range of 1 to 40 keV by the electron gun producing a fine electron beam. This beam is focused using the electron lenses and scanned across the surface of the specimen with the help of scanning coils. A signal in form of electromagnetic radiation is emitted by each point of the specimen struck by the electrons. Some of this radiation, usually secondary (SE) and/or backscattered electrons (BSE), is collected by a detector and the resulting signal is amplified and displayed on a computer monitor producing a topographic image of the sample surface. The model of SEM microscope

used for the analysis of the samples presented in this thesis is a CMTC-LEO S440-MEB W. This microscope is equipped with an X-ray energy dispersive spectrometer which is used to analyse the composition of precipitates, phases and reaction products present in the material studied. The scheme and picture showing the main components of the SEM microscope are presented in Fig 45.

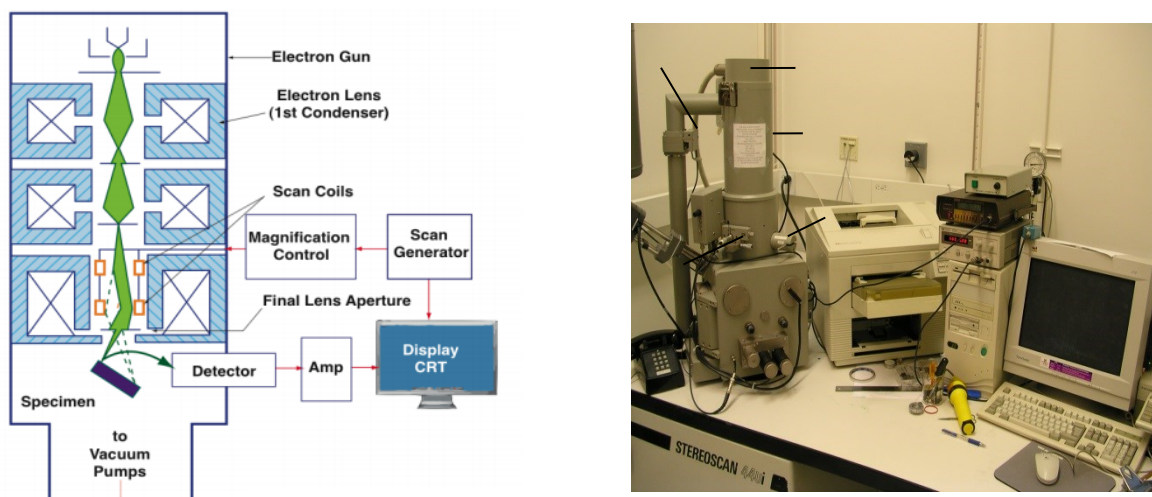


Fig 45 Scheme of scanning electron microscope (SEM) and picture

### 1.9.3 X-ray Tomography

X-ray tomography is a technique used to reveal the internal structure of materials by the reconstruction of projected images taken at different angles of the object studied using an X-ray beam [103]. Fig 46 presents a scheme of the tomography system used to analyse the materials produced during this study. The sample is placed on a plate which is rotated during the test in order to obtain radiographs from all its angles.

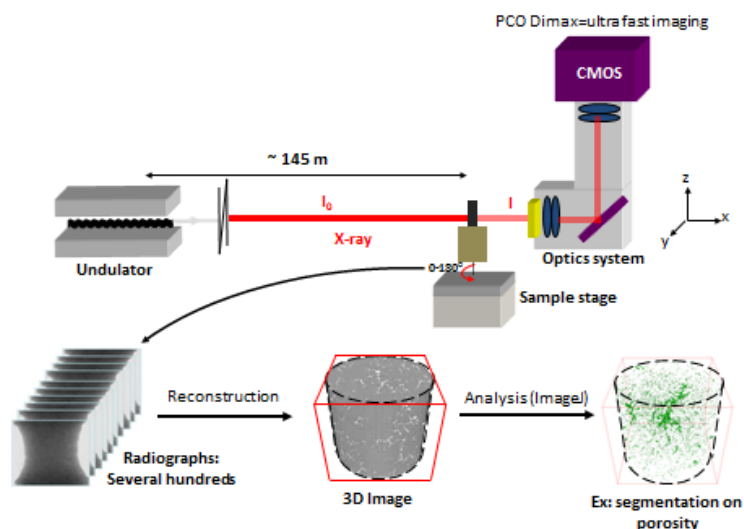


Fig 46 X-ray tomography system scheme

The X-rays transvers the object studied and are collected using a detector placed behind it. These X-rays collected are attenuated after traversing the object by energy absorption. This energy is represented mathematically using the Beer Lambert equation presented in eq (27) [104]:

$$I = I_0 \exp (-\mu t), (27)$$

where  $I$  is the X-ray beam intensity after passing through the object,  $I_0$  is the X-ray beam energy at the source,  $t$  is the thickness of the object in the direction of the X-ray beam,  $\mu$  is the X-ray linear attenuation coefficient of the material. The net intensity  $I$  of the X-ray beam emerging out of the object is used to determine the gray level value of each pixel used in each projection image. The 2D projection images are afterwards combined together to reconstruct the 3D volume of the specimen using a technique known as filtered back-projection. The tomographic analysis presented in this thesis is carried out in the facilities of ESRF (European Synchrotron Radiation Facility) and GPM2 laboratory. The 3D volumes obtained are processed using the image analysis software ImageJ which allows the measurement of the particle number density, the size of the particles or agglomerates, and their average interparticle distance.

#### 1.9.4 X-ray radiography

X-ray radiography is a very versatile nondestructive technique used in industry and research to provide images of the internal structure of materials. Photographic records are obtained using highly penetrating X-rays impacting onto sensitive films after passing through objects. Fig 47 presents a scheme of the photographic process.

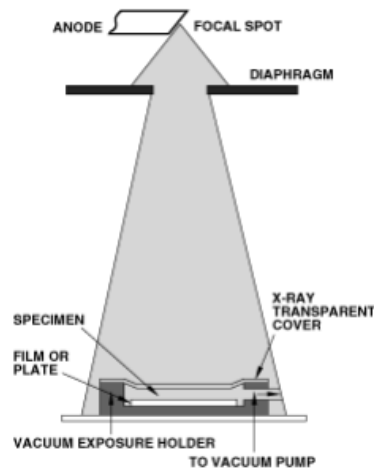


Fig 47 X-ray photographic process

X-ray absorption depends on the spectrum and energy of the rays, and also on the composition and thickness of the investigated object. Absorption using monochromatic X-rays, relates to the exponential function of the negative product of the specimen thickness and absorption coefficient. If X-rays with incident intensity  $I_0$  penetrate a material of layer thickness  $d$ , then the intensity behind the layer is given by:

$$I = I_0 e^{-\mu(\lambda)d}. \quad (28)$$

The quantity  $\mu$  is called the linear attenuation coefficient, which is dependent on the wavelength  $\lambda$  of the primary radiation and the atomic number  $Z$ . The latter is a function of the X-ray wavelength and the atomic number of the atoms of the specimen. During this study X-ray radiography has been used to analyse the dispersion of SiC particles in samples of pure magnesium.

### 1.9.5 Hardness Test

Hardness is a measure of the resistance of a material to plastic deformation and indentation when a compressive force is applied. The material hardness is influenced by different factors such as grain size, material microstructure, strain hardening, or the presence of particles. The hardness tests presented during this study are performed using a Rockwell superficial hardness tester Indentec 8150 LK Digital, in which a standard load of 60 Kgf is applied. The penetrator used is a Brinell 1/16" ball (HR15T). This test is performed to produce hardness maps of the samples by measuring hardness at different points along the longitudinal section of the specimen produced in VB2. The map is produced with the help of lines drawn on the specimen which are used to guide the measurements, shown in Fig 48. The measurements are performed at crossing points between the horizontal and vertical lines along the length of the specimen.

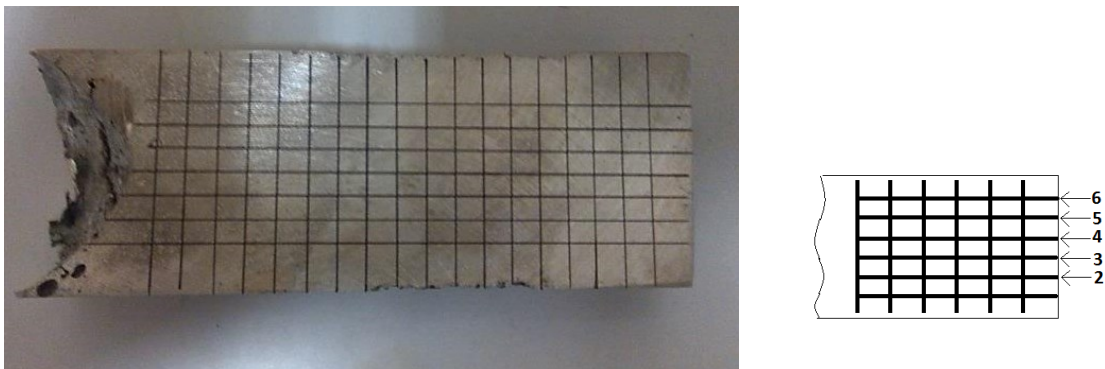


Fig 48 Sample of magnesium alloy EK21 subjected to hardness test

### **1.9.6 Microindentation hardness test (microhardness)**

Microindentation hardness test, also called microhardness test is widely used to study fine scale changes in hardness. This test is performed to analyse the materials produced in this thesis using in a Wilson Tukon 1202 model with a load of 100 gf. Microhardness is useful to detect the presence of particles inside the grains which have been related to the increase of hardness in reinforced materials.

### **1.9.7 Hot compression test**

The creep performance at high temperatures of different materials can be studied using hot compression tests. This type of thermomechanical test can provide with knowledge of the flow behavior in workpieces under different operating conditions. The data obtained can be used to determine the constitutive equations of the material studied. These equations relate plastic stress to variables such as strain, strain rate and temperature. The information obtained with the equations can serve to guide or to improve the efficiency of forming processes such as hot working, rolling, extrusion and also forging [105]. Hot compression tests can help to understand the effects produced by nanoparticles on the mechanical properties of materials subjected to high temperatures. Hot compression tests presented in this thesis are performed using a hot compression testing machine, model referred as an Instron Industrial Series 300DX system jointly used with a Model SF-16 split furnace.

### **1.9.8 Tensile test**

Tensile test provides information about the strength of materials under tension. The tensile testing machine slowly exerts an axial pull to a standard test specimen gripped at both ends. During this process, the elongation of the gauge section is recorded against the applied force obtaining stress-strain curves. These curves are an important visual tool to reveal mechanical properties of a material such as the Modulus of Elasticity. Tensile tests presented in this thesis are performed using a universal tensile test machine AG-Xplus Series with a maximum load of 20 KN.

## **1.10 Matrix materials used to produce metal matrix composites**

The leaders of the Exomet project narrowed the number of alloys systems to be investigated. The materials selected are: Aluminum 99,99 % purity, aluminum A357, pure magnesium,

magnesium AZ91 and magnesium EK21. This section presents a brief introduction of these materials.

### 1.10.1 Aluminium 99.99 % purity

High purity aluminum is normally used only for nonstructural applications such as capacitor plates [106]. Beyond its interesting properties such as high conductivity, the lack of strength and stiffness makes this material not attractive for structural applications. Pure aluminium usually presents a columnar crystal structure independently of the crystal lattice. This latter structure can be eliminated by inoculation of the metal; controlling the heat removal rate from the casting or using external fields such as electromagnetic fields [92]. Copper is widely used as the principal material for electric conduction in industrial and aerospace applications. Despite the good conductivity of this material, its density is three times higher than the one of aluminum [107] and in consequence, copper cables are generally heavy. Improvements in the mechanical properties of pure aluminium using reinforcement particles could provide a light conductive material offering possibly an alternative to copper cables.

### 1.10.2 Aluminum A357

This aluminum alloy is part of the A300 series which are widely used in automobile and aerospace industry [108]. Aluminum A357 offers an excellent castability and provides a range of attractive mechanical properties. It is characterized by the presence of silicon and magnesium in its composition. The silicon provides good fluidity during casting while magnesium is used to increase strength after heat treatment. The microstructure of aluminum A357 consists in an aluminum solid solution containing hard precipitates of silicon. The chemical composition of aluminium A357 is listed in Table 5 obtained from reference [109].

Mg	Si	Cu	Fe	Ti	Mn	Zn	Al
0.481	0.001	0.143	0.123	0.123	0.005	<0.001	Balance

Table 5 Aluminium A357 alloy composition

### 1.10.3 Magnesium 99.99 % purity

Magnesium and magnesium alloys are characterized by their light weight and a high damping capacity [110]. The crystal structure of magnesium is hexagonal closed packed (HCP). The slippage of the atoms in this structure is more difficult with respect to other crystalline structures such as face centered-cubic (FCC) presented by aluminium. Magnesium presents a

lower ductility than aluminium and therefore, it is used mainly as casting material. Magnesium alloys have a larger Hall-Petch coefficient than aluminium alloys [111], in consequence, their mechanical properties can be highly improved by grain refinement. The major alloying elements and their effects in magnesium alloys are presented in Table 6 [112].

Substance	Effect
Aluminium	Provides hardness and strength at room temperature, widens the freezing range and makes the alloy easier to cast
Zinc	Provides strength but increase microporosity, reduces corrosion resistance
Manganese	Helps in offsetting effect of trace element on corrosion and provide toughness. To certain extent reduces micro galvanic corrosion resistance
Silver	Provides strength but reduces corrosion resistance
Neodymium	Increase elevated temperature properties, assists in castability
Rare Earths	Improves room and elevated temperature mechanical properties
Zirconium	Works as a grain refiner

Table 6 Alloying elements and effects on magnesium alloys

#### 1.10.4 Magnesium AZ91

This is a typical cast alloy commonly used for 3D shape castings. Magnesium AZ91 contains 9% of aluminium in its composition. This element is added to increase the mechanical properties and corrosion resistance of the alloy [113][114]. The basic microstructure of magnesium alloy AZ91 consists of solid solution matrix of  $\alpha$  Mg base surrounded by  $Mg_{17}Al_{12}$   $\beta$  phase. The zinc present in its composition, usually is found forming the intermetallic compound  $Mg_{17}(Al,Zn)_{12}$  precipitated near grain boundaries [115]. Magnesium AZ91 also contains manganese in its composition which is added to improve corrosion resistance by forming iron compounds. Magnesium AZ91 is susceptible to heat treatments and presents a high strength, good flow characteristics and die-filling abilities [112]. The composition of this alloy is given in table 7.

Al	Zn	Mn	Si	Cu	Fe	Be	Mg
8.25	0.63	0.22	0.035	0.003	0.014	0.002	Balance

Table 7 Magnesium AZ91 alloy composition

#### 1.10.5 Magnesium Elektron 21

Magnesium Elektron 21 is a new high strength fully heat treatable magnesium based casting alloy designed to be used at temperatures up to 200 °C. This alloy has excellent corrosion resistance and improved castability. It is used mainly in motorsport and aerospace applications due to its superior mechanical properties. The composition of Mg EK21 contains

neodymium and gadolinium. Neodymium improve tensile strength at high temperatures and also helps to reduce porosity [116]. This alloy offers potential for precipitation strengthening due to the decrease in solubility of both neodymium and gadolinium when cooling. Zinc is added to achieve precipitation strengthening, and to improve strength while maintaining ductility. The zirconium present in the alloy contributes to obtain a fine grain structure and improves its mechanical properties at an ambient temperature, castability and corrosion resistance. The composition of this alloy is presented in table 8.

<b>Gd</b>	<b>Nd</b>	<b>Zr</b>	<b>Zn</b>	<b>Mn</b>	<b>Fe</b>	<b>Ag</b>	<b>TRE</b>	<b>Mg</b>
1.2	2.7	0.49	0.4	0.001	0.003	0.01	4.2	Balance

Table 8 Magnesium Elektron 21 alloy composition

### 1.11 Inoculating particles and reinforcements

Four types of particles were selected by Exomet project to serve as grain refiners and reinforcement of matrix materials based on aluminium and magnesium. The first type of ceramic particle is  $TiB_2$  which is a material with relatively high strength, melting point, hardness and wear resistance [117].  $TiB_2$  presents a crystal mismatch with respect to aluminium of only 4.5%, and is practicable insoluble in it [45]. These properties make  $TiB_2$  particle a very good grain refiner for aluminium and aluminium alloys. The average size of the  $TiB_2$  particles used to inoculate aluminium matrices in this study is 8.5  $\mu m$ . Fig 49 presents a sample of  $TiB_2$  particle. The second type of ceramic particle used as grain refiner is alumina ( $Al_2O_3$ ) with an average size of 4.5  $\mu m$ . A sample of  $Al_2O_3$  particle is presented in Fig 50. These particles present good stability and high temperature resistance in aluminium matrices [118]. The improvement of the mechanical performance of magnesium matrices containing  $Al_2O_3$  particles has been observed by several authors such as Kawamori [42], but its capacity as grain refiners for magnesium has not been extensively studied. The third type of ceramic particle used is made of SiC with a size ranging from 0.1 to 1  $\mu m$ . A sample of SiC particle is presented in Fig 51. This type of particle presents a high stability in magnesium matrices, and at the crystallographic orientation relationship  $(1010)_{Mg} // (0001)_{SiC}$ , SiC particles (6Ha type)) presents a lattice mismatch of only 2.3% with respect to primary phase ( $\alpha$ -Mg) [119]. This low lattice mismatch makes SiC potential grain refiners for magnesium matrices. Finally, particles of aluminium nitride (AlN) are used as reinforcement in this study for magnesium alloy Elektron 21. These nanoparticles present a size ranging from 30 to 40 nanometers. The effects of AlN nanoparticles in the mechanical properties of magnesium matrices have been measured by different authors. For instance, Paramsothy [120] achieved the increase of tensile strength of an hybrid magnesium alloy AZ91/ZK60A using AlN particles as reinforcement. In addition, the low crystal lattice mismatch of the AlN with respect to magnesium crystal



lattice makes this type of particle a potential grain refiner. Fig 52 depicts the crystal structure of the particles used during the study as grain refiners or reinforcements.

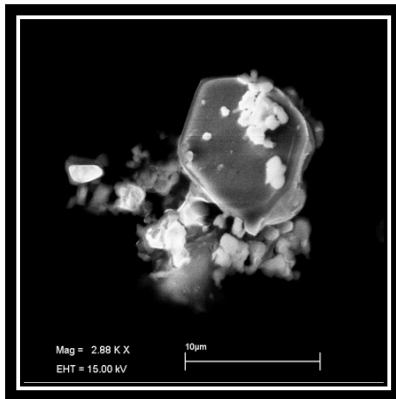


Fig 49 TiB<sub>2</sub> microparticle

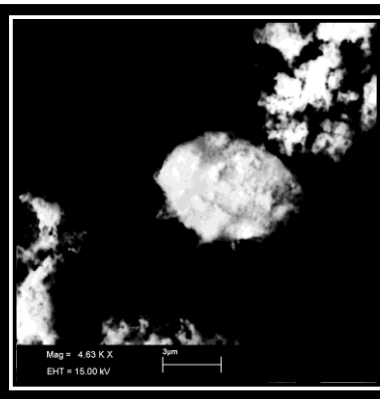


Fig 50 Al<sub>2</sub>O<sub>3</sub> microparticle

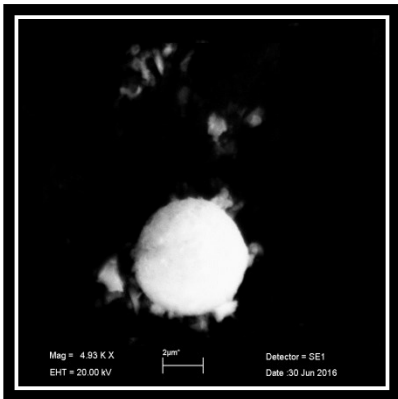


Fig 51 SiC microparticle

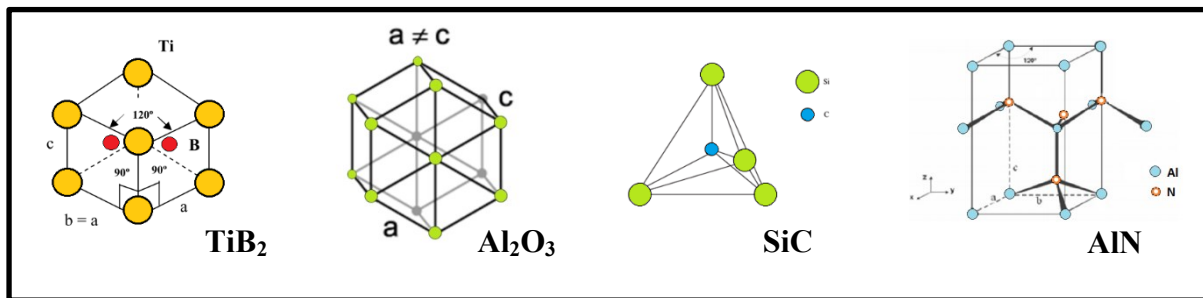


Fig 52 Crystal structure of the inoculant particles

Table 9 presents a summary of the characteristics presented by the particles used as nucleant and reinforcement.

Particle	Melting point °C	Crystal lattice	Parameters of crystal lattice (Å)	Lattice parameter Mismatch Al%	Lattice parameter mismatch Mg%
$\alpha$ -Al <sub>2</sub> O <sub>3</sub>	2000	Hexagonal	a = 4.785 c = 12.991	c = 4.6 % [121]	-----
TiB <sub>2</sub>	2900	Hexagonal C32	a = 3.02 3.25 [33]	b = *4.2% [34]	5.6% [122]
SiC	2829[123]	Wurtzite	a = 3.073 b = 10.053[124]	-----	**3.96[125]
AlN	3273[126]	Rocksalt	a = 3.189 c = 4.982	-----	3.4 [127]

Table 9 Crystal structure parameters

Rocksalt: The rock-salt crystal structure is characterized by having each atom surrounded by six nearest neighbours, with octahedral geometry. Wurtzite crystal lattice is a type of hexagonal crystal system. \* Along closed packed direction 660°C\*\*. The lattice mismatch between (111) crystal face of  $\beta$ -SiC and (0001) crystal face of  $\alpha$ -Mg is only 3.96%.

## Chapter 3

# Production of composite materials containing microparticles using VB2 furnace

This chapter presents the results of the experiments performed using VB2 furnace to produce ceramic particle-reinforced metal matrix composites (CMMC). The ceramic particles were dispersed using the electromagnetic stirring produced by the Bitter coil installed in VB2 furnace. The application of stirring during metal melting can produce changes in the microstructure of the solidified material as it was explained previously in section 1.3. The first part of this chapter presents the effects in the microstructure of pure materials and alloys produced by the use of electromagnetic stirring during their casting process. The second part of the chapter presents a series of experiments dedicated to the introduction and dispersion of  $\text{TiB}_2$  and  $\text{Al}_2\text{O}_3$  microparticles into aluminium and magnesium matrices using electromagnetic stirring. These microparticles are dispersed with the objective of producing exogenous inoculation in the material leading to grain refinement. These experiments also aim to reveal the influence of electromagnetic stirring on the grain refining efficiency of  $\text{TiB}_2$  particles, and to confirm the capacity of  $\text{Al}_2\text{O}_3$  particles to serve as grain refiners for aluminium and magnesium matrices.

### 2.1.1 Electromagnetic stirring of pure aluminium at low cooling rate and temperature gradient

Two samples of pure aluminium were melted and solidified in VB2 furnace using the parameters presented in Table 10. The objective of the experiments is to show the capacity of a travelling magnetic field to produce an equiaxial structure in pure aluminium solidified under columnar grain growth casting conditions. Two specimens were directionally solidified from bottom to top using the pulling system of the furnace in order to extract them from the hot zone to the cold zone at a speed of 0.6 mm/ minute. The first sample was solidified under natural convection, whereas the second sample was solidified under the effects of the stirring produced by a travelling magnetic field of 15 mT oriented to downwards direction.

Max T K	Time (max T) min	Cooling rate K/s	T Gradient K/m
973	600	0.05	8

Table 10 Casting conditions for pure aluminium with pulling system

It is important to clarify that pure metals do not form equiaxed crystals naturally, since constitutional undercooling cannot occur without solute rejection in the absence of alloying elements [128]. In pure substances, only thermal instabilities must be considered [129]. Two types of solidification can occur in a pure metal. In the first type, the solidification starts from the mold surface towards the liquid with the temperature decreasing continuously from the liquid to the solid. For this type of solidification, the thermal gradient is considered positive. The thermal instabilities required to drive the process of moving the interface S/L finds a high temperature in the bulk liquid stopping the growth of any perturbation on the growing surface. In this case, the solidification leads to a planar surface. In the second type of solidification, the liquid bulk became highly undercooled and solidification starts on nuclei formed away from the interface. In this case, the thermal gradient is considered negative. The growth conditions in the liquid are homogeneous isotropic, crystals will have a spherical shape and their growth will generate equiaxed grains. Thermal instabilities in the growing crystal surface will find an undercooling environment leading to a final dendritic pattern. Therefore, in pure aluminium only thermal instabilities can provide with two types of possible patterns: Planar when the thermal gradient is positive or dendritic equiaxed when the thermal gradient is negative. Fig 53 shows the longitudinal section of the specimen solidified under natural convection using the pulling system. The sample presents mainly a columnar grain structure with an equiaxial transition (CET) found at approximately 50 mm from the bottom of the sample. Fig 54 shows the longitudinal section of the specimen solidified under a forced convection using a TMF of 15 mT. This material was also extracted from the hot zone using the pulling system. The sample presents an equiaxial grain structure with an average size of 4.5 mm.

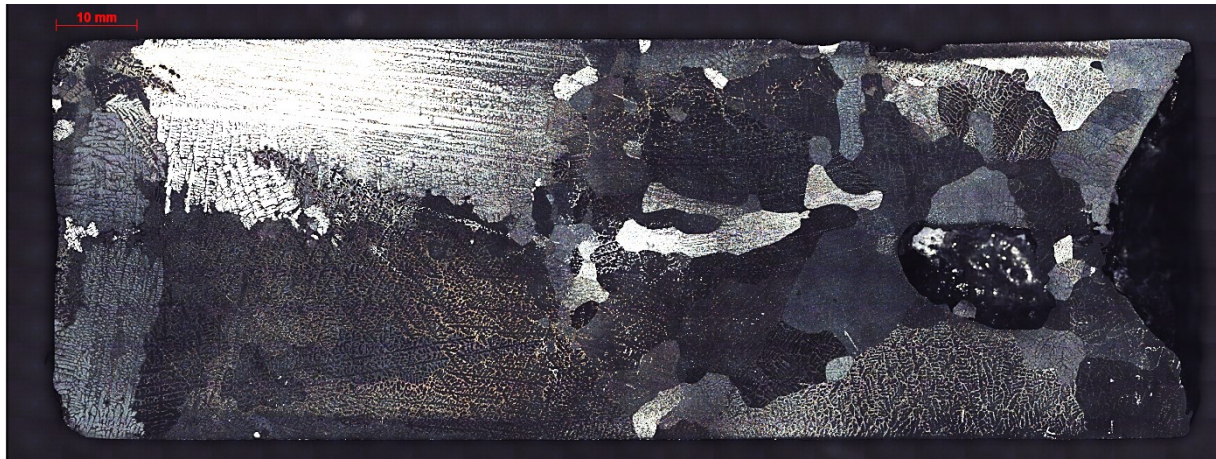


Fig 53 Al 99.99% as solidified from VB2 set-up sample non-stirred

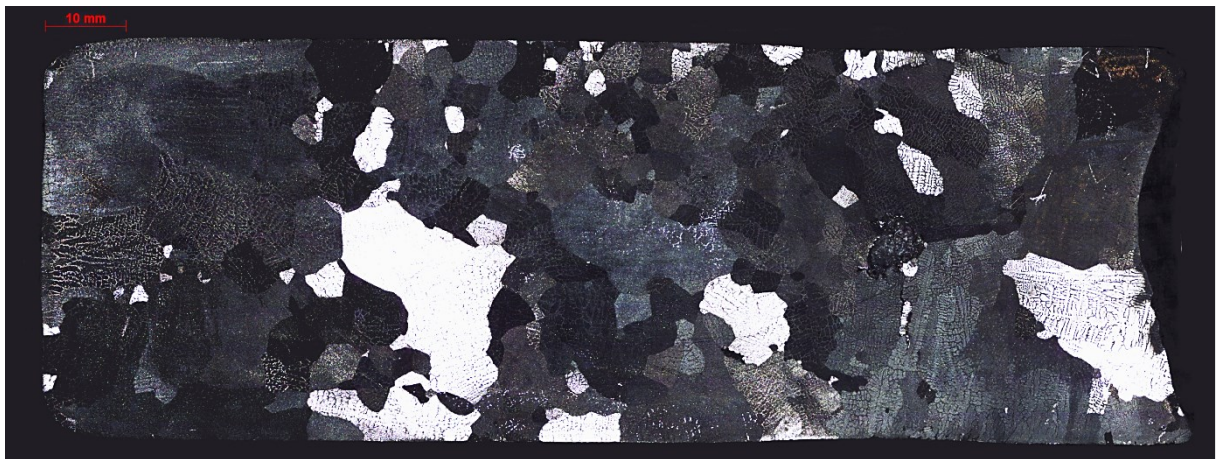


Fig 54 Al 99.99% as solidified VB2 set-up sample stirred making use of 15 mT TMF

Both samples were studied using optical microscopy with the objective to analyse their dendritic structure, and to measure the average secondary dendrite arm spacing presented in the material. The latter parameter is defined as the distance between developed secondary dendrite arms. A finer distance between secondary arms is desirable to improve mechanical property performance of metallic materials such as ductility [130] [131]. The arm spacing is directly controlled by the cooling rate applied during solidification. Therefore, its measurement can reveal the influence of the TMF in the cooling rate. Two samples used to measure primary and secondary arm spacing in the material solidified under natural convection are shown in Fig 55 and Fig 56. A detailed view of an equiaxial grain observed in the material stirred using the TMF is presented in Fig 57. A broken dendrite found near the bottom of the specimen is presented in Fig 58.



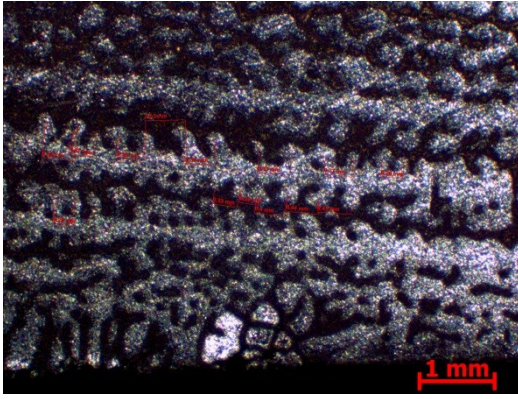


Fig 55 Aluminium 99 sample 1

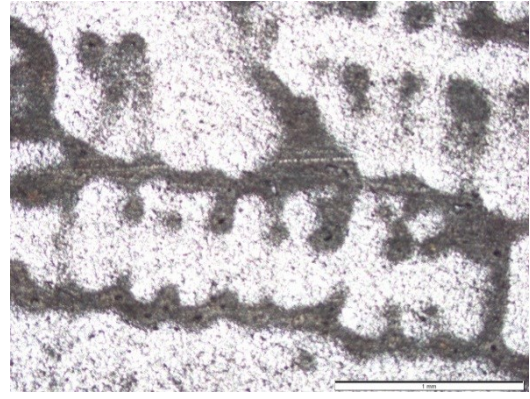


Fig 56 Aluminium 99.99 VB2 sample 2

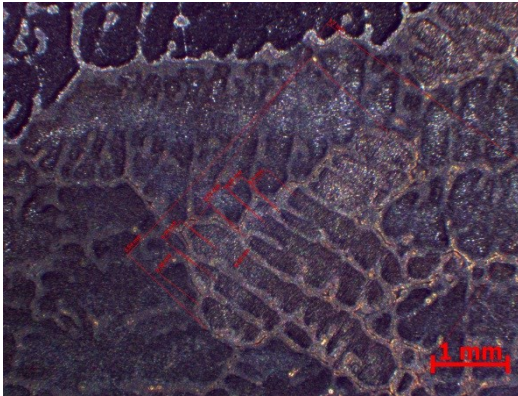


Fig 57 Aluminium 99 sample 3

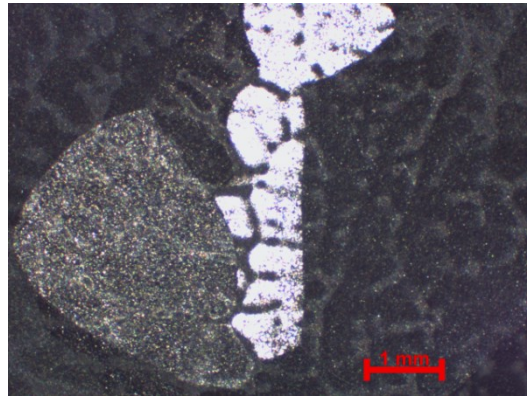


Fig 58 Broken dendrite

A summary of the measurements performed on grain size and arm spacing is finally presented in table 11.

Measurement	No TMF	TMF 15 mT
Mean grain size ( $\mu\text{m}$ )	31	6.95
Minimum/maximum size (mm)	60/10	3.18/11.7
Standard deviation	2.5	2.66
$\lambda_1$ (mm) Primary arm spacing	0.29	Not possible
$\lambda_2$ (mm) Secondary arm spacing	0.34	0.32

Table 11 Summary of grain size measurements

### 2.1.2 Pure aluminium stirred using TMF and solidified at cooling rate of 0.25 K/s

Two samples of pure aluminium were melted and solidified using VB2 furnace using the casting parameters presented in Table 12. In this case, the cooling rate during solidification was set to 0.25 K/s which is typical for metallurgical processes such as casting [132].

Max T K	Time ( max T) min	Cooling rate K/s	T Gradient K/m	Magnetic field mT
1073	60	0.25	666	15

Table 12 Casting conditions for experiments without pulling system

The first material was processed under natural convection, whereas the second was subjected to electromagnetic stirring of 15 mT intensity. In both cases, the specimen was cooled down decreasing the whole temperature of the VB2 heating elements. A sample taken from each material is presented in Fig 59. The specimen produced under natural convection presents an average grain size of 2.8 mm, whereas the average grain size measured on the stirred material is 4 mm. Both samples present an equiaxial grain structure. A summary of the grain size measurements performed on both samples can be found in Table 13.

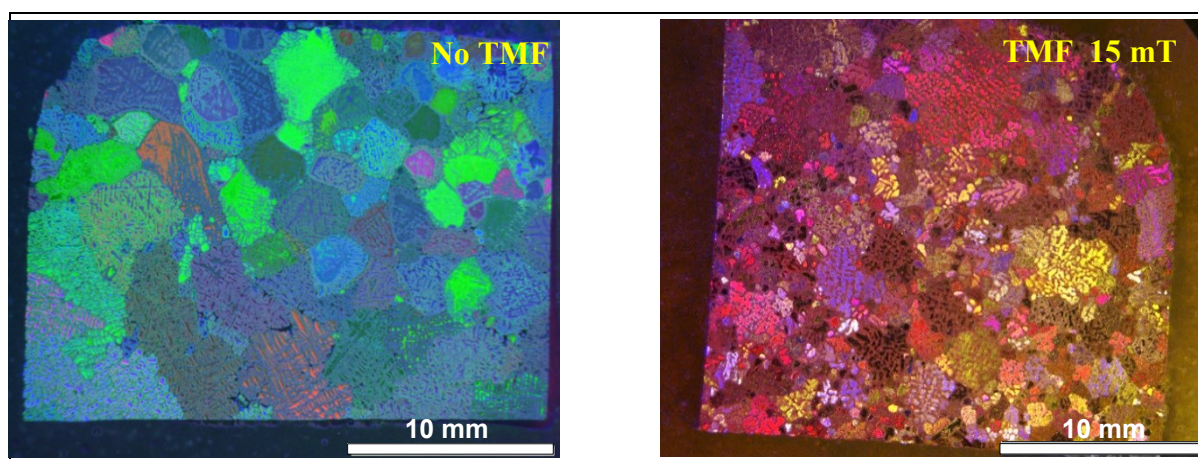


Fig 59 Pure aluminium produced under high temperature gradient

Measurement	TMF 15 mT	No TMF
Mean grain area (mm <sup>2</sup> )	2.8	8.34
Mean grain size (mm)	2.4	4.0
Minimum /maximum grain area (mm <sup>2</sup> )	0.04 / 3.2	3.20/13.63
Minimum /maximum grain length (mm)	1.2 /4.1	1.96/6.65
Standard deviation (area)	2.19	3.41
Standard deviation (grain size)	0.28	1.25
Number of grains measured	45	45

Table 13 Summary of grain size measurements

### 2.1.3 Aluminum A357

The effects of a travelling magnetic field during melting and solidification of aluminium alloy A357 were studied producing three specimens under different electromagnetic fields intensities. A fourth specimen produced to serve as reference material was solidified under



natural convection. The casting parameters use to produce the samples are presented in Table 14. A sample of each material is presented in Fig 60. The totality of the samples presents an equiaxial grain structure. The reference material presents an average grain size of 2 mm, whereas the material stirred using a travelling magnetic field of 15 mT, presents an average grain size of 3 mm. The materials stirred at 45 and 70 mT presents an average grain size of 2.27 mm and 1.98 mm respectively. The TMF was oriented to downward direction in all the cases. A summary of the grain size measurements performed can be found in Table 15.

Max T K	Time ( max T) min	Cooling rate K/s	T Gradient K/m	Magnetic field mT
1073	60	0.25	666	15-45-70

Table 14 Casting conditions for experiments performed using different stirring intensities

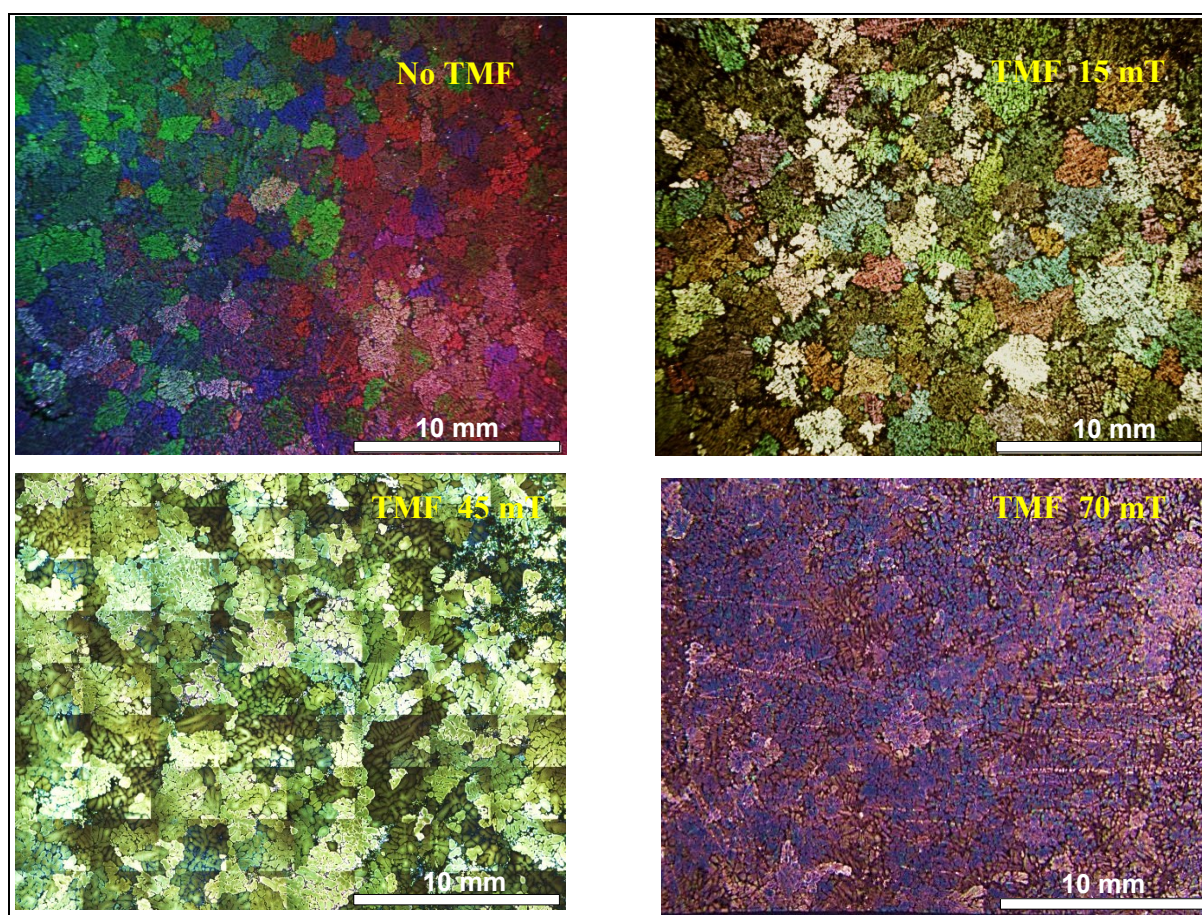


Fig 60 Aluminium A357 grain structure at different TMF intensities



Measurement	No TMF	15 mT	45 mT	70 mT
Mean grain area (mm <sup>2</sup> )	2.23	4.58	2.49	2.23
Mean grain size (mm)	2.0	3.02	2.27	1.98
Minimum /maximum grain area (mm <sup>2</sup> )	0.8/6.93	1.45/7.94	0.03/7.05	0.45/5.21
Minimum /maximum grain length (mm)	1.36/4.26	1.52/4.3	0.99/3.6	0.80/3.88
Standard deviation (area)	1.14	1.79	1.50	1.33
Standard deviation (grain size)	0.54	0.72	0.64	0.717
Number of grains measured	48	26	20	26

Table 15 Aluminium A357 grain size measurements

In order to understand the effects produced by a travelling magnetic field in the microstructure and distribution of the eutectic phase present in the alloy, several horizontal cross sections taken from the specimen obtained from VB2 were analysed. The first sample presented in Fig 61 was taken from the material processed under natural convection. The red arrows indicate the direction of the solidification front view from the top of the horizontal cross section. The sample presents a high level of porosity and a dendritic structure characterised by the presence of wide eutectic areas, shown in Fig 62.

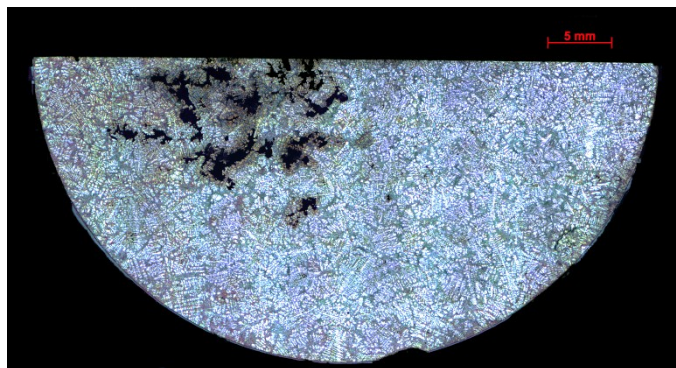


Fig 61 Aluminium A357 not stirred

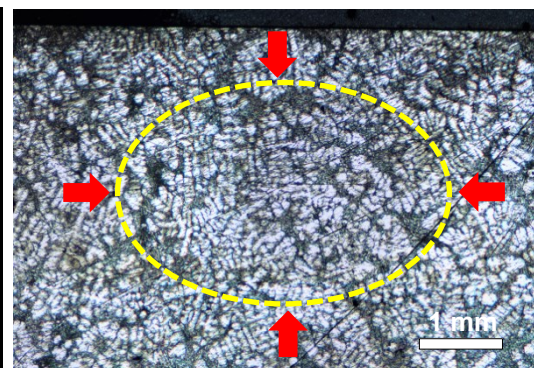


Fig 62 Detail view of non-stirred sample

The second sample presented in Fig 63 was obtained from the specimen processed using a TMF of 15 mT. This material presents a lower level of porosity with respect to the non-stirred material and its microstructure presents a more compacted dendritic structure as shown in Fig 64.

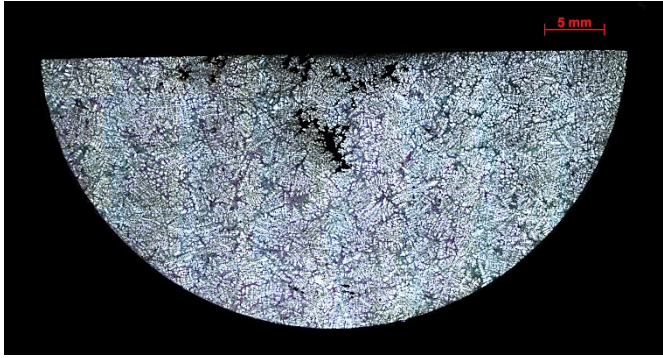


Fig 63 Aluminium A357 TMF 15 mT

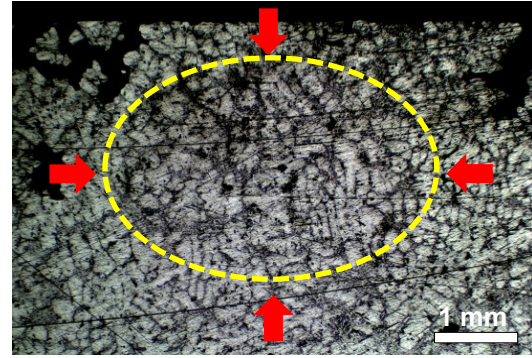


Fig 64 Detail view Al A357 stirred at 15mT

Finally, two samples were obtained from materials produced under TMF intensities of 40 and 70 mT. The samples, etched using ‘Si-Blue’ solution, are displayed in Fig 65 and Fig 66. These materials present a compacted dendritic structure and signs of concentrated eutectic areas on the centre of each sample as shown in Fig 67 and Fig 68. As a matter of fact, the application of a downwards TMF provides a forced convection against the direction of the natural convection. This stirring enhanced the rejection of solute rich in silicon towards the central area of the sample as demonstrated from the analysis of the cross sections. This excess of solute can produce a segregation channel and promote a more compacted dendritic structure.

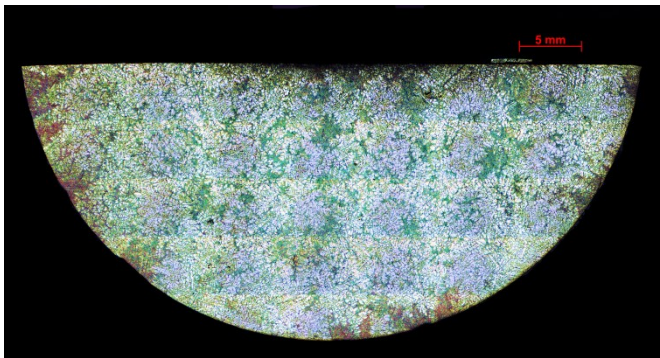


Fig 65 Aluminium A357 40 mT



Fig 66 stirred Al A357 at 40 mT

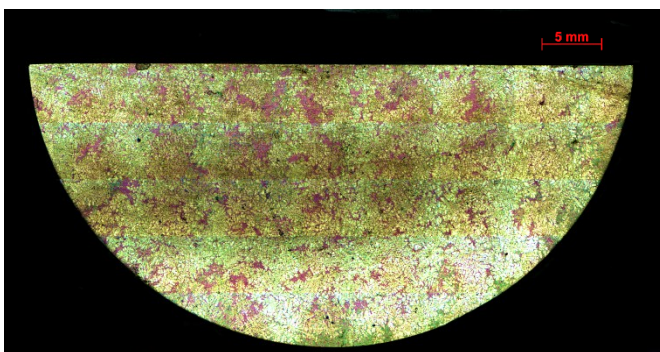


Fig 67 Aluminium A357 70 mT

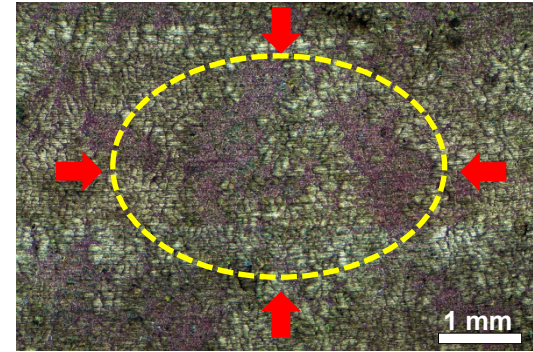


Fig 68 Stirred Al A357 at 70 mT



### 2.1.4 Magnesium AZ91

The effects on the microstructure caused by a travelling magnetic field applied during melting and solidification of magnesium AZ91 were studied producing a specimen stirred using a TMF of 15 mT intensity, and a reference material produced with the same casting condition presented in table 16, but melted and solidified under natural convection.

Max T K	Time ( max T) min	Cooling rate K/s	T Gradient K/m	Magnetic field mT
1073	60	0.25	666	15

Table 16 Casting conditions for experiments performed with Mg AZ91

The sample stirred using TMF presents an average grain size of 0.88 mm, whereas the non-stirred sample presents an average grain size of 0.96 mm. A dendritic equiaxial grain structure was observed in both situations. For each material, a representative cross-section of a solidified sample is presented in Fig 69. A summary of grain size measurements can be found in Table 17. Grain refining is not particularly made evident analysing the images obtained. No signs of segregation were detected during the analysis of the samples.

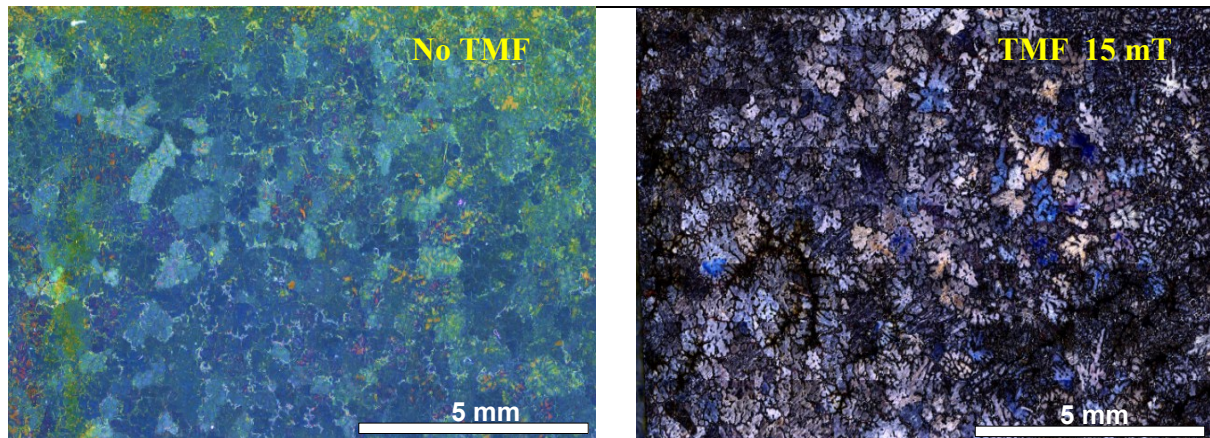


Fig 69 AZ91 grain structure under natural convection with or without the applied TMF

Measurement	No TMF	TMF 15 mT
Mean grain area (mm <sup>2</sup> )	0.44	0.54
Mean grain size (mm)	0.88	0.96
Minimum /maximum grain area (mm <sup>2</sup> )	0.06 /1.61	1.21/0.13
Minimum /maximum grain length (mm)	0.34/1.86	0.42/1.42
Standard deviation (area)	0.31	0.25
Standard deviation (grain size)	0.34	0.25
Number of grains measured	40	32

Table 17 Magnesium AZ91 grain size measurements

### 2.1.5 Magnesium Elektron 21

The effects of the electromagnetic stirring applied during melting and solidification of magnesium alloy EK21 were studied producing two specimens under the same casting conditions used for magnesium AZ91 (table 18). The samples are presented in Fig 70. The sample produced without stirring (on the left in the figure) presented an average grain size of 0.40 mm. The sample stirred during melting and solidification (on the right in the figure) was produced applying a travelling magnetic field of 15 mT intensity. The stirred sample presents an average size of 0.31mm. In both cases, the material presents an equiaxial grain structure. A summary of the grain size measurements can be found in table 18.

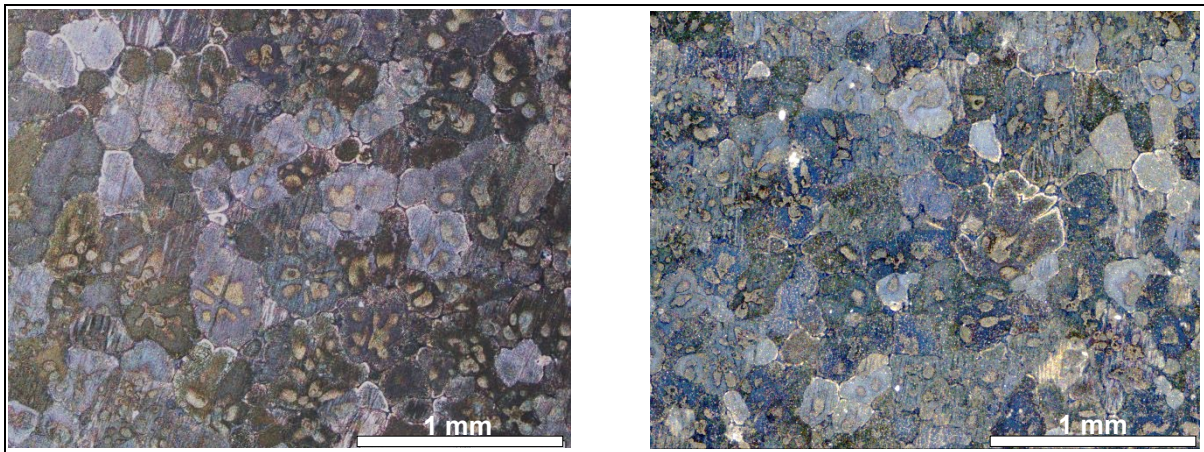


Fig 70 Mg AZ91 grain structure of both non-stirred and stirred material using TMF

Measurement	No TMF	TMF 15 mT
Mean grain area (mm <sup>2</sup> )	0.093	0.060
Mean grain size (mm)	0.40	0.31
Minimum /maximum grain area (mm <sup>2</sup> )	0.03/0.19	0.013/0.157
Minimum /maximum grain length (mm)	0.23/0.63	0.137/0.632
Standard deviation (area)	0.043	0.033
Standard deviation (grain size)	0.098	0.097
Number of grains measured	45	45

Table 18 Magnesium Elektron 21 grain size measurements

## Summary of the results

The calculated average grain size of the samples of pure aluminium and magnesium alloys produced has been listed on the graph presented in Fig 71. The average grain size of pure aluminium stirred with the TMF decreased by approximately 50 % with respect to the non-stirred material, showing a clear effect of electromagnetic stirring in grain size. In the case of aluminium alloy A357, the application of TMF did not produce any significant effects on the average grain size of the material. The travelling magnetic field applied during the processing of magnesium alloys AZ91 did not produced any signs of grain refinement, whereas the TMF applied during the processing of magnesium alloy EK21 produces a grain size reduction of 25% with respect to the same material produced without electromagnetic stirring.

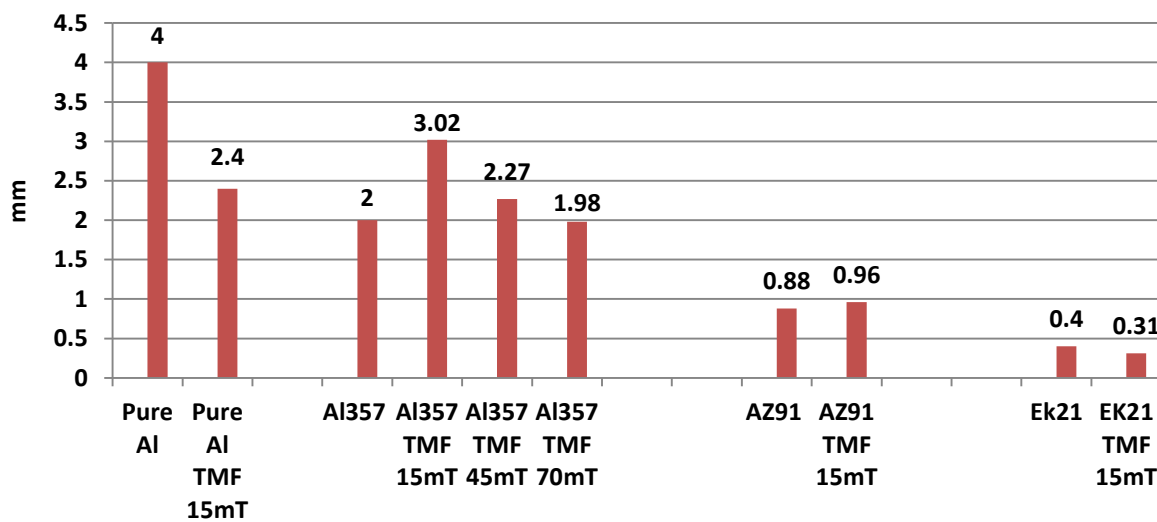


Fig 71 Summary of grain size of materials under travelling magnetic field

### 2.1.6 Discussion on the electromagnetic stirring of pure metals and alloys

The experiments performed to produce grain refinement on pure aluminium metal using electromagnetic stirring demonstrated grain refinement. The experiment performed using pure aluminium directionally solidified under low temperature gradient and slow pulling velocity produced a specimen with a columnar grain structure. On the contrary, using the same casting conditions under electromagnetic stirring, the material presented an equiaxial grain structure. The electromagnetic stirring applied during melting and solidification could have enhanced the thermal instabilities inside the material promoting the development of equiaxial dendrites. In addition, the broken dendrites detected during optical analysis, support the idea that grain refining is also related to the increase of nucleation points produced from dendrites breaking-up at the solidification front due to forced flow. The study of dendrite arm spacing of both

materials showed that forced convection did not produce changes in the cooling rate during the experiment. This increase could have been related to the enhancement of heating exchange with the walls of the crucible due to the stirring as observed by other authors such as B.Hamri [133]. The grain refinement of pure aluminium using TMF was confirmed with the experiment performed under high temperature gradient and cooling rate. The material stirred presented grains 50 % smaller than aluminium produced under natural convection. In the case of aluminium alloy A357 the application of electromagnetic stirring did not produce significant grain refinement. The grain refinement of a material is generally related to the thermal conditions presented in the system [134]. For instance, studies performed by M. Krupiński [135] on Al-Si base alloy showed that cooling rate has a direct relation with crystallization kinetics. In addition, in alloys the solute released during solidification produces constitutional undercooling which plays an important role in the process of grain refinement [136]. The decrease of melting point due to the solute released plays an essential role for the survival of new ‘crystals embryos’ formed during solidification. In the case of an alloy, during the solidification process, the released solute pile up ahead of the interface due to the smaller solubility of the solid when the distribution coefficient, which describes the difference in the composition at the growing interface, is less than unity [137]. This excess of solute is accumulated in an enriched boundary layer ahead of the interface [138]. Electromagnetic stirring can eliminate the solute barrier around the growing dendrites reducing or stopping constitutional undercooling and in consequence reducing the nucleation capacity of the melt. Without the presence of solute, the new ‘crystal embryos’ formed could have been remelted by the latent heat of formation. For instance, the material processed under low intensity TMF showed an average grain size bigger than the material melted without electromagnetic stirring. This effect on the grain size at low TMF stirring was mentioned by Zaidat [139] with the application of a travelling magnetic fields in the range of 10 to 30 mT on the solidification of aluminium 7% silicon alloy. On the other hand, the grain size observed in our alloy experienced a reduction when higher intensities were applied until returning to the original size at 70 mT. In the current case, the experiments performed under different electromagnetic stirring applied downwards direction indicate that the greatest grain growth happens at the electromagnetic intensity of 15 mT. This effect was also observed by Zaidat [139] who suggested that the solute removal find its greater effects at this value. The cross sections show some wide areas of eutectic concentrated on the centre of the samples electromagnetically stirred and some small areas on the external areas. The samples also show a more compact dendritic structure with respect to the material produced under natural convection. These results support that downwards electromagnetic stirring produces the removal of solute during solidification which was directed mainly to the central areas of the samples creating a more compacted dendritic structure in the alloy. In the case of magnesium alloy AZ91 stirred at the electromagnetic intensity of 15mT, the grain structure presents similar results with respect to aluminium alloy A357. The results could also be related to the solute removal with subsequent elimination of constitutional undercooling, not compensated by the thermal

cooling provided by the furnace. In both magnesium and aluminium cases, future analysis of the macrosegregation observed in the samples could help to establish clearly the influence of the TMF in the solute removal. In the case of magnesium EK21, the material processed using TMF demonstrates grain refinement. This magnesium alloy contains zirconium in its composition which is present as dissolved and forming particles as well. The zirconium particles can serve as nucleation sites whereas dissolved zirconium can act as a growth restriction factor. The growth restriction factor of zirconium was found to be the highest among all the elements that promote grain refinement in magnesium and magnesium alloys. Strong nucleants require lower degree of undercooling for their 'activation' and therefore their effects would be noticeable at low level of solute. Therefore, in this case the reduction of constitutional undercooling due to solute removal could be not enough to eliminate the grain refiner effect of zirconium. Consequently, the reduction of grain size observed can be related to other factors such as the good dispersion of the zirconium particles, which have a natural tendency to sediment at the bottom of the crucible during casting reducing its efficiency as grain refinement.

## **2.2 Dispersion of grain refining particles into aluminium based materials using a travelling magnetic field downwards direction**

This section presents the results of the experiments performed dispersing grain refiner microparticles into pure aluminium and aluminium alloy A357 using the travelling magnetic field provided by VB2 furnace. The solidification of both materials is carried out using the control of VB2 heating elements.

### **2.2.1 Pure aluminium + 1% $\text{Al}_2\text{O}_3$**

Four experiments were performed to disperse  $\text{Al}_2\text{O}_3$  particles into pure aluminium using the casting parameters presented in table 19 and following the procedure presented in chapter 1.7.2. The first experiment was performed using a maximum temperature of 1073 K. The specimen obtained is presented inside the quartz crucible used during the experiments in Fig 72. The image shows particles agglomerated on the top of the solidified material, indicated with a yellow arrow. Three more experiments were performed to disperse the particles but the casting temperature was increased to superheating levels with the objective to facilitate the engulfment of the particles by the aluminium matrix. These experiments also failed to produce the engulfment of the particles which were found also on the top of the solidified sample.



Max T K	Time max T min	Cooling rate K/s	T Gradient K/m	TMF mT	% Weight
1073	60	0.25	600	15	1
1373/1273	60	0.25	600	15	2
1593	60	0.25	600	15	3

Table 19 Casting parameters used to produce pure aluminium + 1% Al<sub>2</sub>O<sub>3</sub> particles



Fig 72 Pure aluminium with agglomerates of Al<sub>2</sub>O<sub>3</sub> particles

### 2.2.2 Pure Aluminium + 1% TiB<sub>2</sub>

Two experiments were performed to disperse TiB<sub>2</sub> particles into pure aluminium using the travelling magnetic field provided by VB2. The casting parameters used to produce the materials are presented in table 20.

Max T K	Time max T min	Cooling rate K/s	T Gradient K/m	TMF mT	% Weight
1073	60	0.25	600	15	1
1073	60	0.25	600	15	1

Table 20 Casting parameters used to produce pure aluminium + 1% TiB<sub>2</sub>

The dispersion of TiB<sub>2</sub> particles into pure aluminium was achieved. Fig 73 presents a sample of the composite material obtained in which an equiaxial grain structure is observed. The average grain size measured is 2.8 mm which is very similar to the average grain size obtained in the pure material electromagnetically stirred presented in section 2.1.2. Table 21 presents a summary of the grain size measurements performed.



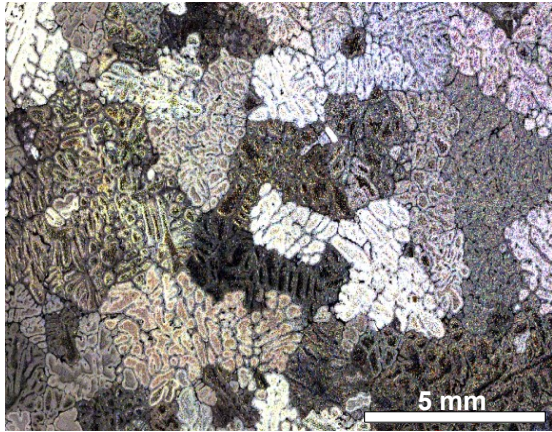


Fig 73 Pure aluminium 1% TiB<sub>2</sub>

Measurement	
Mean grain area mm <sup>2</sup>	4.13
Mean grain size mm	2.8
Minimum /maximum grain area (mm <sup>2</sup> )	0.32/15.21
Minimum /maximum grain length (mm)	0.77/5.85
Standard deviation (area)	3.2
Standard deviation (grain size)	1.23
Number of grains measured	25

Table 21 Grain size measurements

### 2.2.3 Aluminium A357 + 1 and 2% Al<sub>2</sub>O<sub>3</sub> particles

Three experiments were performed with the objective of dispersing Al<sub>2</sub>O<sub>3</sub> particles into aluminium alloy A357 using the casting parameters presented in table 22.

Max T K	Time max T min	Cooling rate K/s	T Gradient K/m	TMF mT	% Weight
1073/1273	60	0.25	666	15	2
1073	60	0.25	666	70	1

Table 22 Casting conditions of aluminium A357 + Al<sub>2</sub>O<sub>3</sub>

The dispersion of the particles into samples of aluminium A357 was unsuccessful. The particles were not engulfed by the matrices even with the application of a TMF of 70 mT intensity. Superheating temperature was applied in one of the experiments to help to introduce the particles obtaining negative results. Two samples are presented in Fig 74 in which particles can be observed on the surface of the material (some of them indicated with black arrows). The materials also presented a high level of porosity in the matrix.

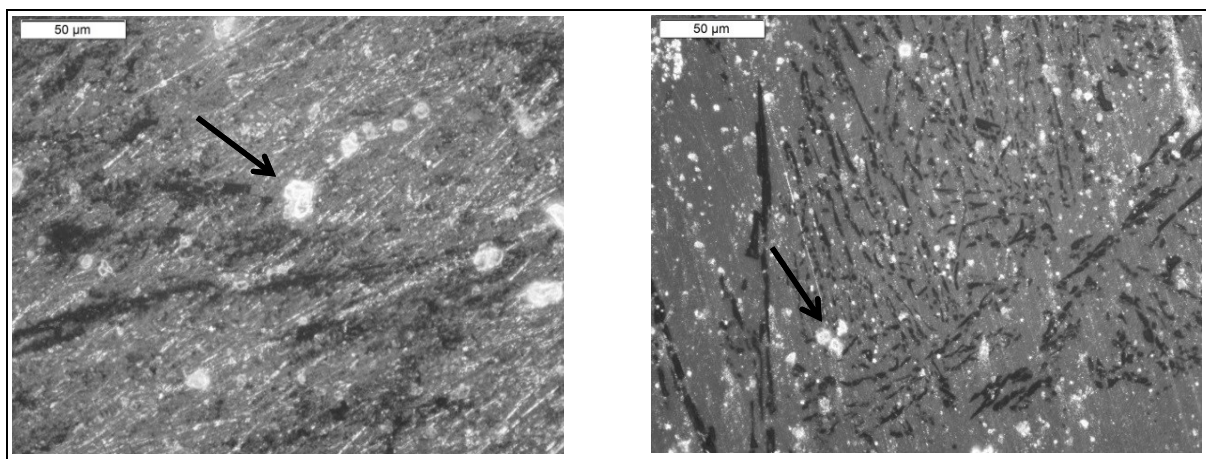


Fig 74 Particles of  $\text{Al}_2\text{O}_3$  as observed on the surface of an aluminium sample

## 2.2.4 Aluminium A357 + 1% $\text{TiB}_2$ particles

Particles of  $\text{TiB}_2$  were dispersed into a sample of aluminium A357 using a TMF intensity of 70 mT and the casting parameters presented in Table 23.

Max T K	Time max T min	Cooling rate K/s	T Gradient K/m	TMF mT	% Weight
1073	60	0.25	666	70	1

Table 23 Aluminium A357 1%  $\text{TiB}_2$  particles casting conditions

Fig 75 presents a  $\text{TiB}_2$  particle embedded in the aluminium matrix, which is an evidence of the good wetting between the particles and aluminium. The grain structure observed in the inoculated material is equiaxial, as shown in the sample presented in Fig 76. The average grain size measured is 2.14 mm. A summary of the grain size measurements performed can be found in Table 24.

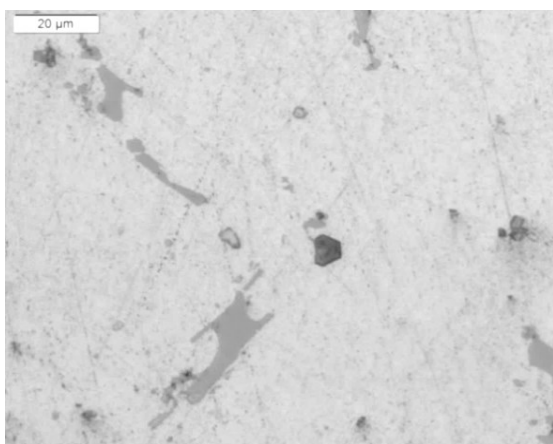


Fig 75  $\text{TiB}_2$  particles inside aluminium matrix

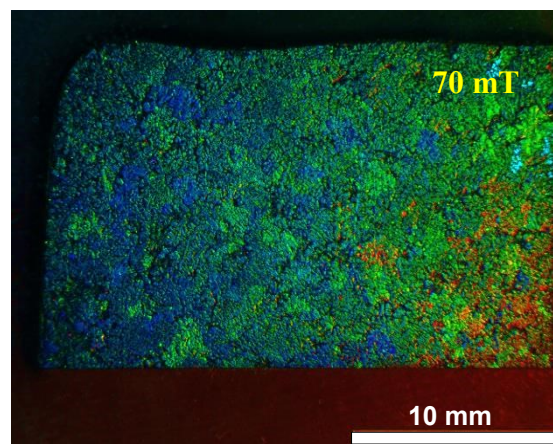


Fig 76 Sample of A357 + 1%  $\text{TiB}_2$

Measurement	
Mean grain area mm <sup>2</sup>	2.53
Mean grain size mm	2.14
Minimum /maximum grain area (mm <sup>2</sup> )	0.56/6.37
Minimum /maximum grain length (mm)	0.94/3.42
Standard deviation (area)	1.47
Standard deviation (grain size)	0.67
Number of grains measured	25

Table 24 Aluminium A357 + TiB<sub>2</sub> grain size measurements

### 2.2.5 Discussion on inoculation of particles into aluminium based materials using a travelling magnetic field (TMF)

Experiments devoted to the dispersion of Al<sub>2</sub>O<sub>3</sub> microparticles in both pure aluminium and aluminium A357 were unsuccessful due to the great difficulties for engulfing the particles into the liquid matrix. At the end of the experiments, the particles were focused along the internal wall of the crucible and at the surface of the solidified metals. The wetting angle between the Al<sub>2</sub>O<sub>3</sub> particle and the liquid aluminium can be as high as 150° at 1000°C [4]. Spontaneous mixing of the particles with liquid aluminum is therefore not possible and external forces should be applied to introduce the particles. In addition, the free surface of the liquid aluminium generally presents a thick layer of aluminium oxide which acts as a barrier avoiding the engulfment of the particles by the matrix. The minimum shear stress to be exerted on a liquid in order to entrap a particle against the surface tension of the liquid surface can be represented using a dimensionless parameter called the capillary number Ca:

$$Ca = \frac{\mu \cdot v \cdot l}{\sigma \delta}, (29)$$

where  $\mu$  is the Newtonian viscosity (3~ Pa·s),  $v$  is the liquid velocity,  $l$  is the particle size,  $\sigma$  is the surface tension (N/m) and  $\delta$  is the shear thickness (crucible radius). The capillarity number is negligibly small which explains why the particles remain along the side wall of the crucible. A second dimensionless number relevant here is the Weber number [140], defined as the ratio of inertia to the surface tension. The Weber number is used to determine a phenomenon called the entrainment limit. Using Eq. (30), a Weber number equals 1 or higher will mean that particle will get through the liquid. The larger it is, the easier the particle will be introduced under the effect of its own inertia.

$$We = \frac{\rho \cdot v^2 \cdot l}{\sigma}, (30)$$

where  $\rho$  is the fluid density ( $\text{kg/m}^3$ ),  $v$  is the fluid velocity,  $l$  is the characteristic length (m) or particle diameter and  $\sigma$  is the surface tension (N/m). Aluminium alloy A357 presents a surface tension value of 0.844 N/m [141] and a density of 2.36  $\text{kg/m}^3$  [5] [142]. Using this approximation, the calculated minimum velocity needed for the incorporation of  $\text{Al}_2\text{O}_3$  particles of 4.5  $\mu\text{m}$  into the liquid aluminum is 280 m/s. Considering the capillary number, the minimum velocity is even found larger,  $v \sim 1000$  m/s. Another consideration used to determine the interfacial force needed to engulf the particles is developed by G.Kaptay [143], essentially based on the interfacial forces acting upon a spherical particle fully wetted by the liquid metal. In this case the following equation should be applied [7]:

$$F_{(l/g)} = 2 \cdot \pi \cdot R \cdot \sigma_{lg} \cdot \left( 1 + \cos \theta - \frac{x}{R} \right). \quad (31)$$

Where  $\sigma_{lg}$  is the surface tension of the melted metal,  $\theta$  is the contact angle between melted metal and the ceramic particle in vacuum,  $R$  is the radius of the particle and  $x$  is the depth at which the particle is situated with respect to the liquid surface. The interfacial force  $F_{(l/g)}$  is zero if no forces are needed to introduce the particles into the liquid metal. The maximum temperature reached during the experiments performed is 1273 K. The wetting angle between  $\text{Al}_2\text{O}_3$  particle and liquid aluminum at such temperature has been reported to be higher than  $150^\circ$  [46]. Therefore, mechanical forces should be applied against the interfacial force. The value of the energy needed can be calculated integrating Eq 32 from  $x=x_{eq}$  (equilibrium depth of immersion) to  $x=2R$  as shown in Fig 77 [144]:

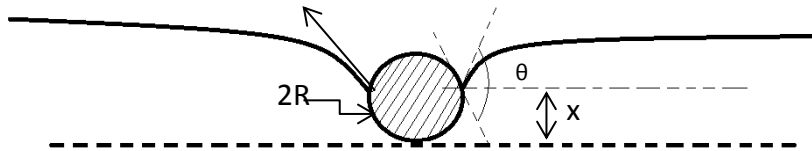


Fig 77 Particle engulfment

$$E_{c(g-l)} = \int_{x_{eq}}^{2R} F_{c(l/g)} \cdot dx = R^2 \cdot \pi \cdot \sigma_{lg} \cdot (1 - \cos \theta)^2, \quad (32)$$

The value of  $F_c$  (l/g) obtained for perfect spherical ceramic particle of diameter  $45 \times 10^{-6}$  m introduced into aluminium A357 is  $53.6 \times 10^{-4}$  N·m. Therefore, enough kinetic energy should be applied to the particle so as to overcome this mechanical energy needed to compensate the interfacial force. The following expression developed by Vreeling et al. [145] can be used to obtain the critical velocity  $V_{c,cr}$  needed to achieve the minimum kinetic energy required to introduce the particles:

$$V_{c,cr} \geq (1 - \cos \theta) \cdot \sqrt{\frac{3 \cdot \sigma_{lg}}{2 \cdot R \cdot \rho_c}}, \quad (33)$$

For aluminum A357 at 1273 K, the minimum velocity obtained using this formula is 7 m/s. The calculations performed, using different approximations, to determine the minimum speed to be attained by the particles to overcome the surface energy of liquid aluminium, shows unrealistic stirring velocities far beyond the capacities of the electromagnetic stirring provided by the Bitter coil. In consequence, the  $Al_2O_3$  particles are not engulfed by the liquid metal and finish on the surface of the solidified material. In the case of  $TiB_2$  particles, the particles are successfully introduced in both pure aluminium and aluminum alloy A357 using the TMF, but no grain refinement is detected for both materials. The application of forced convection due to electromagnetic stirring, as mention in section 3.1.6, could have negative effects in grain growth. In the case of aluminium A357, the solute present in the alloy is responsible of constitutional undercooling during solidification which plays an important role in the activation of the grain refining particles [146]. Several theories have been developed to relate the grain refining capacity of  $TiB_2$  particles to the formation of  $Al_3Ti$  on their surface. The titanium present in the composition of A357 can create a layer of  $Al_3Ti$  over the surface of the  $TiB_2$  particles which is critical for the nucleation capacity of the particles. The lattice misfit between  $Al_3Ti$  and aluminium is only 0.09, which is smaller than the misfit presented between aluminium and  $TiB_2$ . The forced convection could transport the  $TiB_2$ , particles covered by this layer of  $Al_3Ti$  to the hottest areas of the metal bath destroying this layer [90][147]. In addition to the effects produced by the solute, another factor such as the cooling rate can play an important role in the activation of the particles. The classical nucleation theory, presented in chapter 1, establish a direct relation between the activation of a grain refiner and the cooling rate of the melt. The thermal undercooling which is the heat removed from the interface regions, either by convection in the molten metal or by conduction through the mold depends on the cooling rate. The maximum cooling rate provided by VB2 is 0.20-0.25 K/s. Fig 78 depicts the cooling rate measured in VB2 during the solidification of aluminium A357 containing 1% of  $TiB_2$  particles dispersed using the TMF.

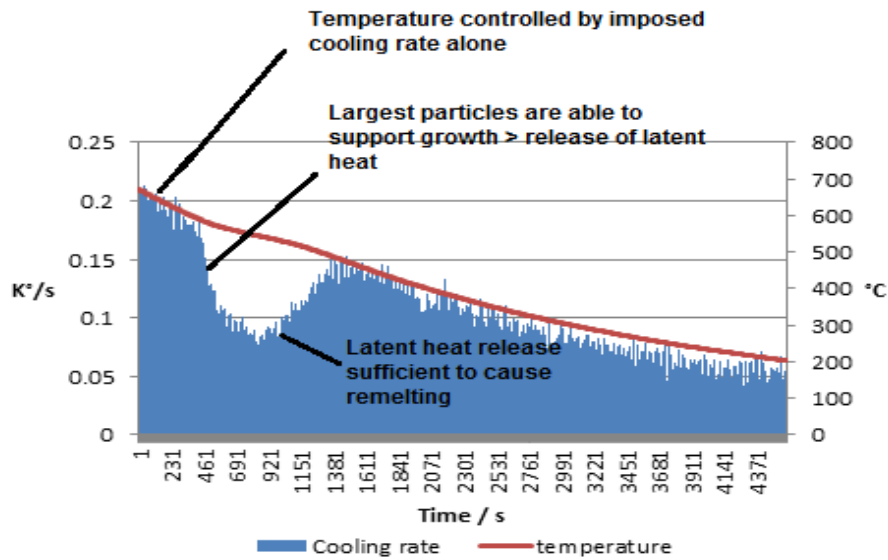


Fig 78 Cooling curve as observed aluminium A357 1% TiB<sub>2</sub> dispersed with TMF

It can be observed that the cooling rate decreased until less than 0.1 K/s during the transition from liquid to solid state. The recalescence observed due to the latent heat released into the system during grain growth can be high enough to stop the initiation of new grains [148]. The removal of solute responsible for constitutional undercooling and the low thermal undercooling could reduce or cancel the capacity of high potency particles to produce grain refinement [149].

### 2.3 Influence of a travelling magnetic field in the dispersion of particles into magnesium materials

This section presents the results of the experiments performed dispersing microparticles into pure magnesium and magnesium alloy AZ91. In the case of pure magnesium, SiC microparticles were dispersed with the objective of showing the different particle dispersion patterns obtained when a TMF at different vertical orientations is applied. The second part of the section presents a series of experiments performed dispersing microparticles of Al<sub>2</sub>O<sub>3</sub> and SiC into magnesium alloy AZ91 using the TMF. In this case, the objective is to study the effects produced by the particles in grain size and mechanical properties of the alloy. The characterization of magnesium AZ91 containing Al<sub>2</sub>O<sub>3</sub> particles revealed the high reactivity of the particles with the magnesium matrix. The reaction of the particles with magnesium produces particles of magnesium oxide and release aluminium into the magnesium matrix. These results suggest that a method to produce an aluminium rich magnesium alloy can be developed by using the reaction of the particles with pure magnesium. In order to confirm it, a specimen was produced in VB2 furnace mixing particles of Al<sub>2</sub>O<sub>3</sub> with pure magnesium. The results obtained are presented in the last part of the section.



### 2.3.1 Pure magnesium + 2% in weight of silicon carbide particles (SiC)

The dispersion of SiC particles into pure magnesium using travelling magnetic field (TMF) was studied using numerical simulations presented in section 1.7.1. These simulations showed that particle concentration patterns in the specimen are strongly governed by the vertical orientation of the magnetic field applied (upwards vs downwards). In order to confirm the predictions of the numerical simulation, two experiments were performed dispersing SiC particles into pure magnesium matrices using the TMF provided by VB2 furnace. The samples are produced using the casting parameters presented in table 25.

Max T	Time max T min	Cooling rate k/S	Gradient K/m	TMF mT	Particles size $\mu\text{m}$	% Weight
1073 K	60	0.25	666	15	0.1-1	2

Table 25 Pure Mg + 2% SiC casting parameters

#### 2.3.1.1 Hardness map of sample containing particles dispersed using upwards TMF

The characterisation of the samples obtained from the experiments begins with the production of hardness maps. The measurements are obtained from the longitudinal section obtained from the central axis of the specimens produced in VB2 furnace. The maps are used to reveal areas of high concentration of particles and the effect produced by the particles in the material hardness. The longitudinal section of the sample of pure magnesium containing 1% of SiC particles dispersed using upwards TMF is presented in Fig 79. The sample presented an equiaxial grain structure with an average grain size of 2 mm.

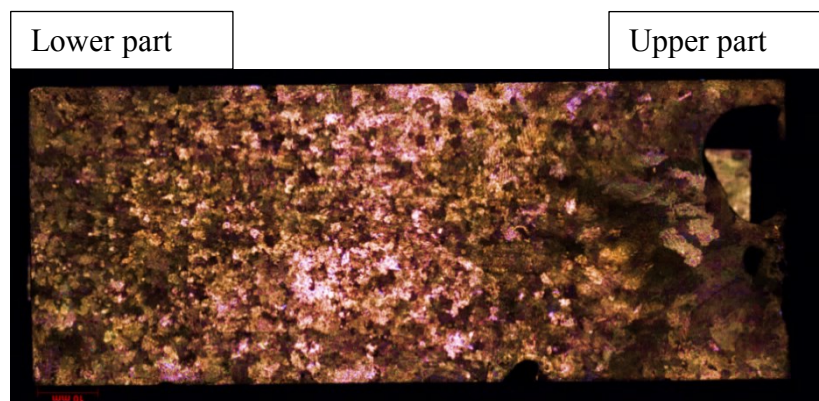


Fig 79 Magnesium 2% SiC upwards TMF

A Brinell hardness map of the sample produced using 260 points of measurement along its total length is presented in Fig 80. The data obtained shows that hardness values are higher on the lower part of the sample. A 3D view of the hardness map is presented in Fig 81. Finally, the average hardness curve measured along the sample is displayed in Fig 82. The curve is created using the average of the 10 measurements performed along the width of the sample every 4 mm. The tendency line displayed in the graph shows a higher hardness value on the lower part of the specimen.

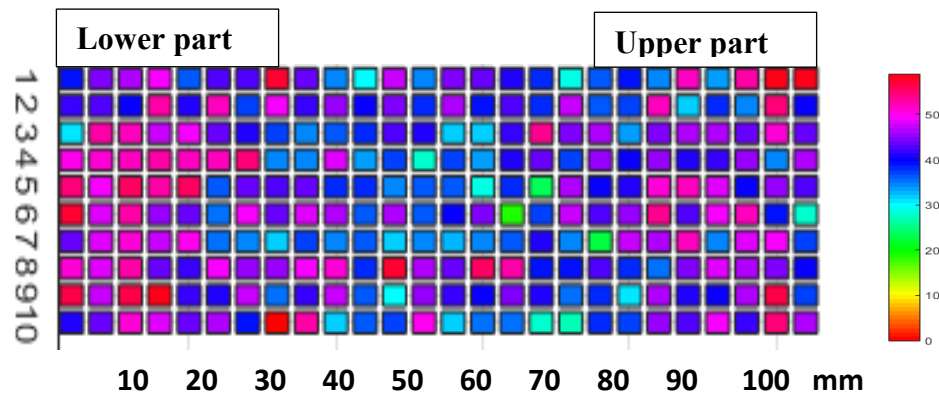


Fig 80 Hardness map for Mg 2% SiC using upwards TMF

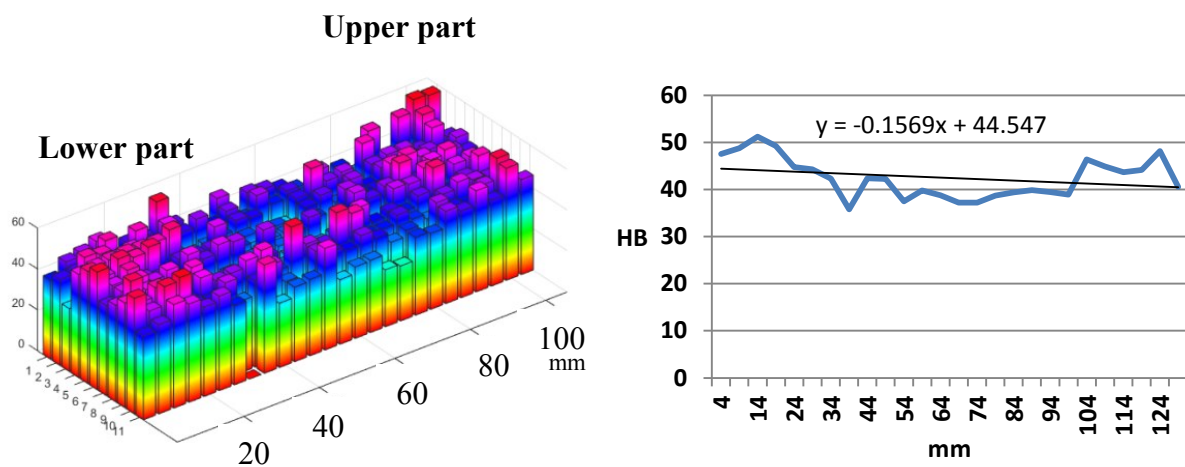


Fig 81 Mg SiC TMF 3D hardness map

Fig 82 Mg SiC average hardness

### 2.3.1.2 Hardness map of sample containing particles dispersed using downwards TMF

The longitudinal section of a sample of pure magnesium containing 1% of SiC particles dispersed downwards TMF is presented in Fig 83. The grain structure is mainly equiaxial but some elongated equiaxial grains were observed on the lower part of the sample. The average grain size measured in this case is 3 mm.



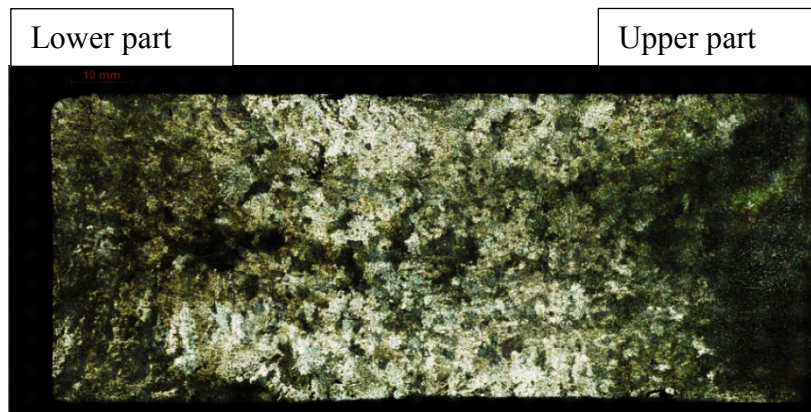


Fig 83 Magnesium 2% SiC Downwards TMF

The Brinell hardness map of the specimen is presented in Fig 84. The map shows that hardness is higher towards the central area. The 3D view of the hardness map is presented in Fig 85. The curve displayed in Fig 86 is created using the average hardness measured along the specimen, as already explained in the previous section. The material presents a more homogenous hardness value along its total length.

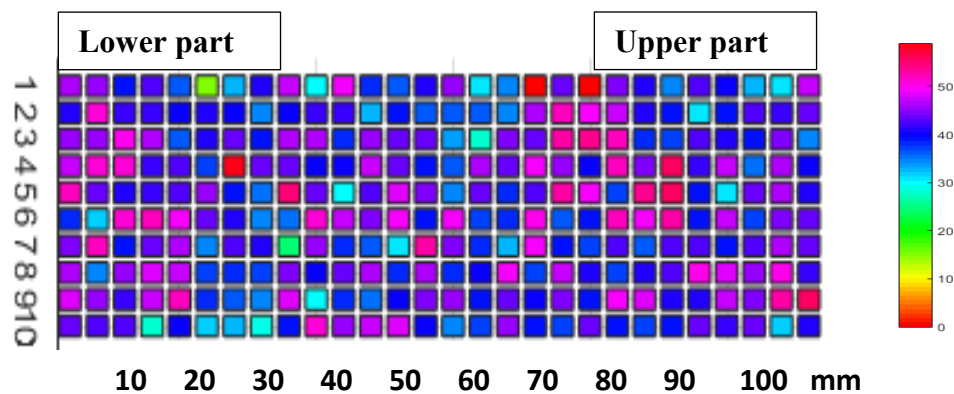


Fig 84 Hardness map for Mg 2% SiC using downwards TMF

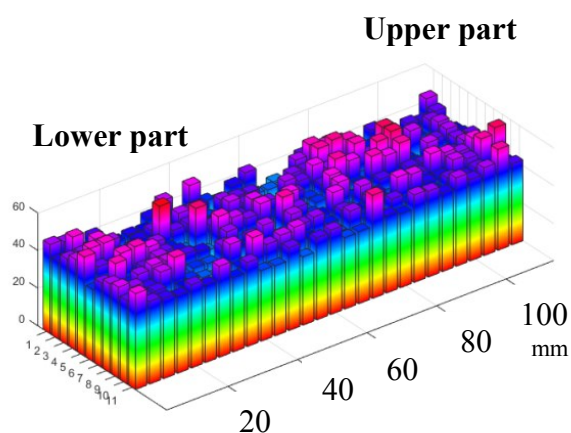


Fig 85 Mg SiC dw TMF 3D hardness map

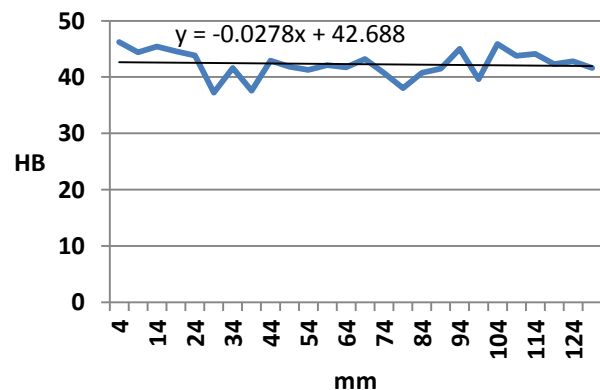


Fig 86 Mg SiC dw average hardness

A detail view of the lower part of the sample is presented in Fig 87. Areas rich in particles of average size 40  $\mu\text{m}$  are easily identifiable on the edges and within the elongated grains of the sample. Fig 88 presents a detail view of the central area in which particles can be observed inside and between magnesium grains.

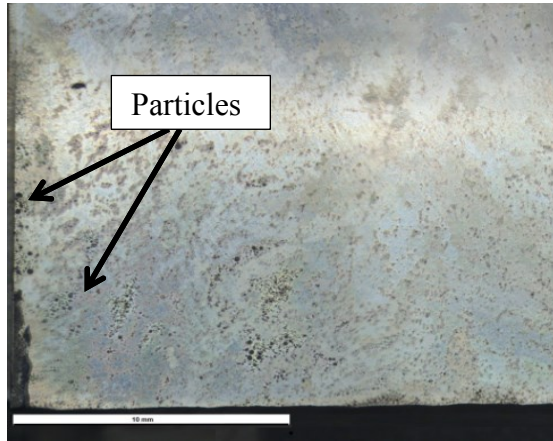


Fig 87 Particles on lower part of the sample



Fig 88 Detail view of particles

### 2.3.2 X-ray analysis of pure magnesium 2% SiC particles

The second technique used to analyse the dispersion particle dispersion of SiC particles in magnesium is X-ray radiography. The particle dispersion patterns obtained using opposite vertical orientation of the TMF to disperse the particles are analysed using 2D images obtained from this technique. X-ray radiography is performed on a sample taken from the centre of the vertical cross-section of a specimen obtained from VB2. The specimen is cut in two halves to obtain this sample. From each of the halves nine specimens are taken from their horizontal cross-section to be analysed. The whole process is summarized in the scheme presented in Fig 89.

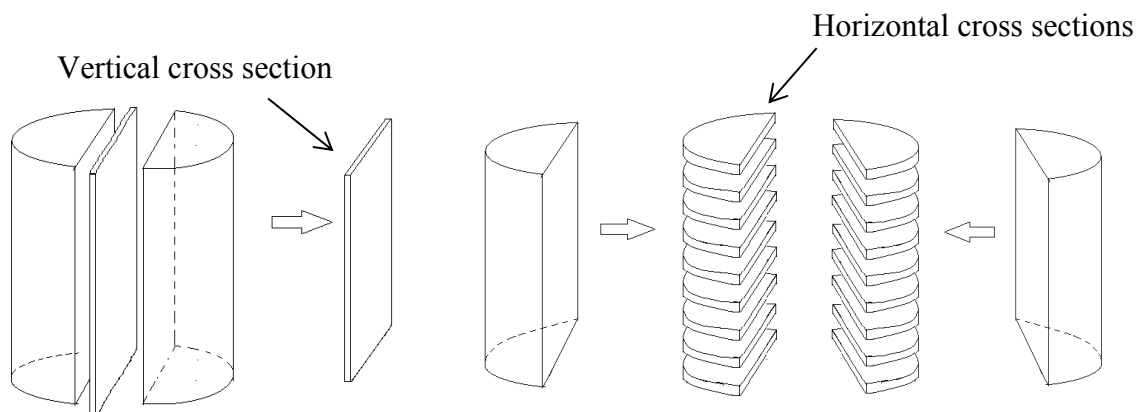


Fig 89 Scheme of cuts analysed with X-ray radiography

The radiographies obtained are converted into binary images using the software ImageJ with the objective to facilitate their analysis. The longitudinal section of the material stirred using downwards TMF is presented in Fig 90. The processed image shows the particle concentration patterns on the total length of the sample. The radiographies of the transversal sections taken every 15 mm along the length of the specimen are presented in Fig 91. The sections displayed shows the particles mostly concentrated near their edges. Fig 92 presents the longitudinal sections obtained from the material stirred using upwards TMF. In this case, particles can be observed highly concentrated on the lower part of the sample. The transversal sections of this specimen are presented in Fig 93. In this case, particles were found on the total area of the sections.

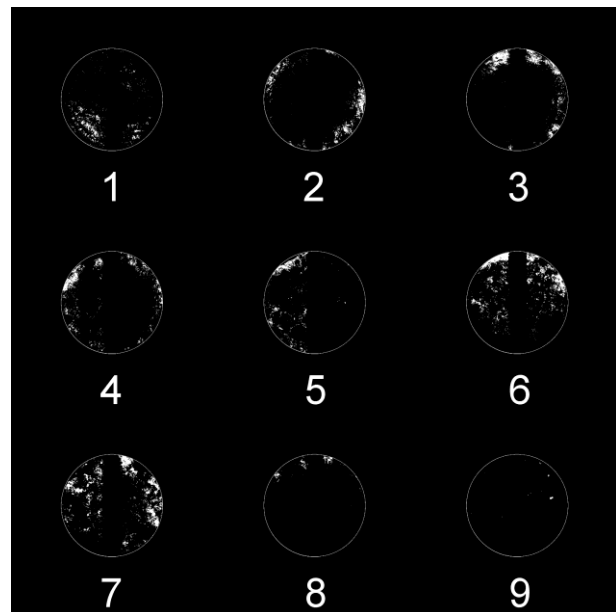
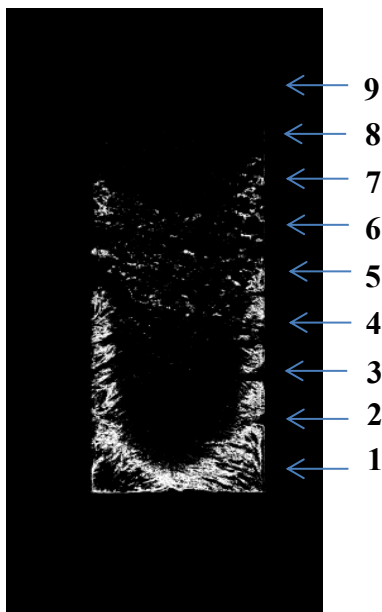


Fig 90 Longitudinal, downwards TMF

Fig 91 Cross sections downwards TMF

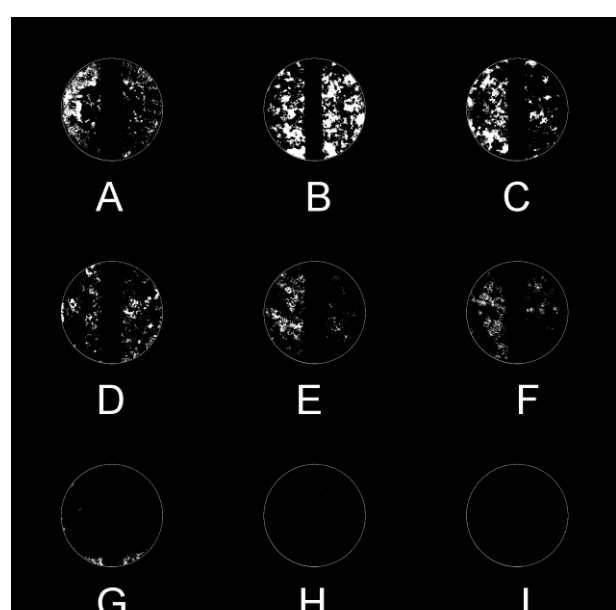
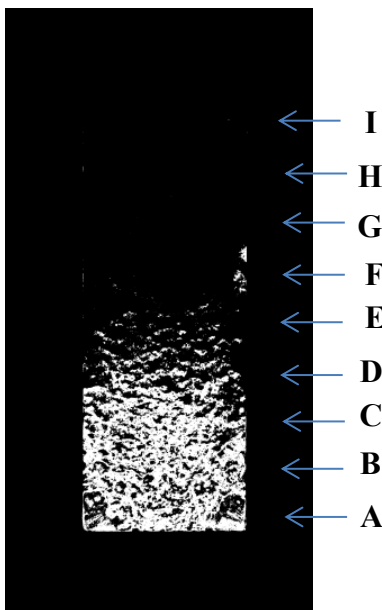


Fig 92 Longitudinal, upwards TMF

Fig 93 Cross sections upwards TMF

In order to give a 3-D view of the particle dispersion, two isometric views were produced using the transversal sections of both materials. The specimen produced using upwards TMF is presented in Fig 94; whereas the specimen produced using downwards TMF is presented in Fig 95. The mean brightness intensity measured on each cross section of both stirred materials is presented on the 2D graph displayed in Fig 96. The brightness profile is more homogeneous on the sample stirred with downwards TMF. The results obtained from X-ray radiography support that better particle dispersion is obtained using downwards TMF.

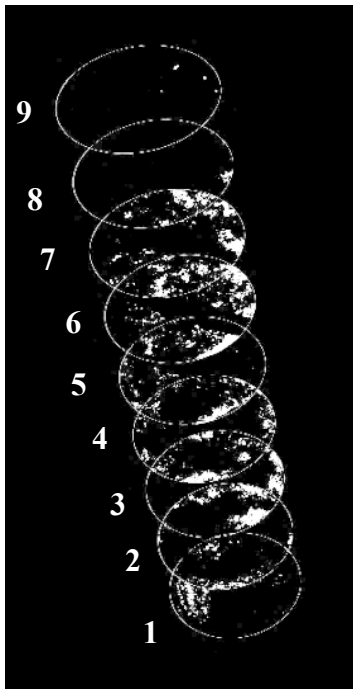


Fig 94 Downwards TMF

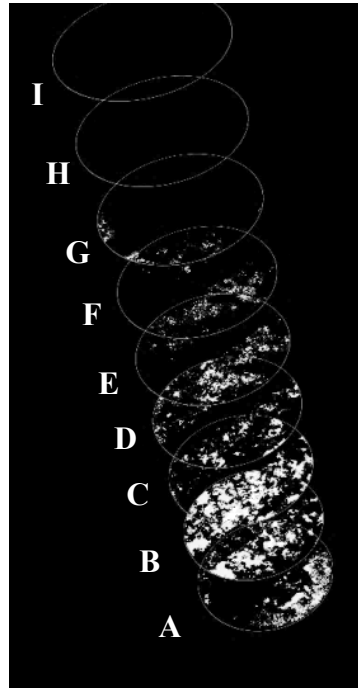


Fig 95 Upwards TMF

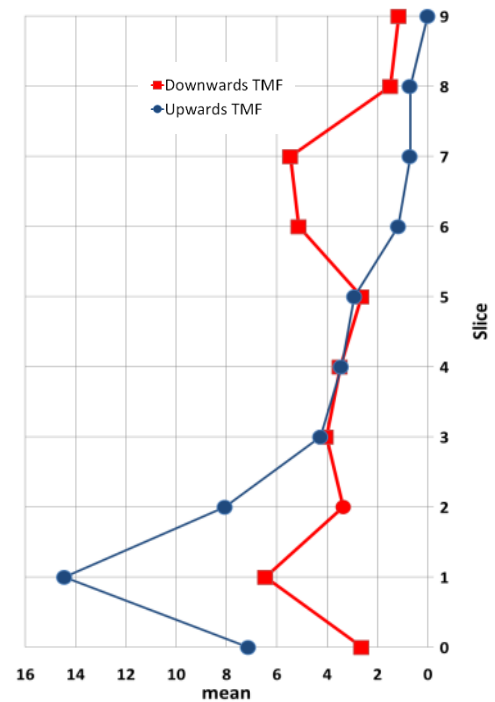


Fig 96 Pixel intensity

### 2.3.3 Pure magnesium 2% SiC particles X-ray tomography analysis

The third technique used to analyse the dispersion of SiC particles into pure magnesium is X-ray tomography. Information about the particle size distribution and interparticle average distance in the matrix material can be calculated using the images obtained using this technique. Tomography analysis is performed on samples obtained at different distances from the central axis of the specimen, as specified in the scheme presented in Fig 97. The samples studied have a volume of  $0.10 \text{ mm}^3$ . The tomographic images are performed using an X-ray beam energy of 40 KV and an exposition time of 5s.

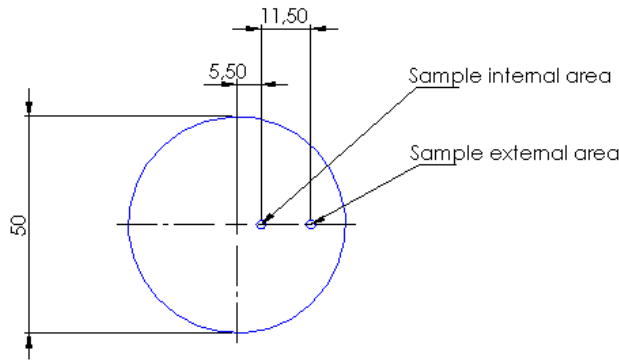


Fig 97 scheme of sampling area and isometric view (all in mm)

## X-ray tomography of sample obtained from external area of VB2 specimen

The tomography of a sample obtained from the external area of a specimen obtained from VB2 furnace is presented in Fig 98. SiC particles can be observed well dispersed inside the volume. Using the software imageJ plugin 3D object counter [150], the position in the space of the centroid of each particle is measured and displayed in the isometric view presented in Fig 99. A Matlab code based on Delaunay triangulation has been developed to calculate the average interparticle distance using the position of the centroid of each particle. Details of the code can be found in “**Appendix B. Interparticle distance calculation**”. Fig 100 presents graphically the triangulation process performed. Finally, using the software ImageJ, measurements of the particle volume and the particle size distribution are obtained. The average interparticle distance calculated is  $45.42 \mu\text{m}$  and the average particle volume is  $414 \mu\text{m}^3$ . Considering the particles as spheres, the average size calculated is  $16 \mu\text{m}$ . The particle size distribution (PSD) curve is obtained from 4 samples taken from the external area of the specimen. Finally, the curve of probability, presented in Fig 101, shows that the particle size more often observed is approximately  $15 \mu\text{m}$ .

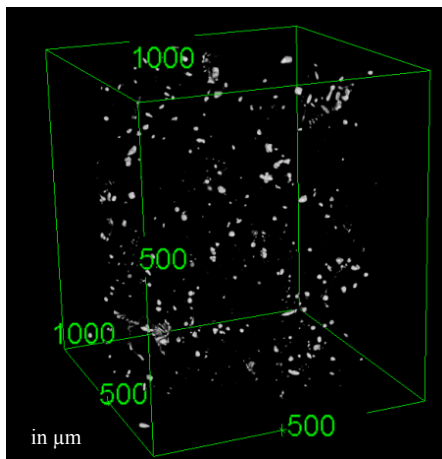


Fig 98 Tomography of the external area

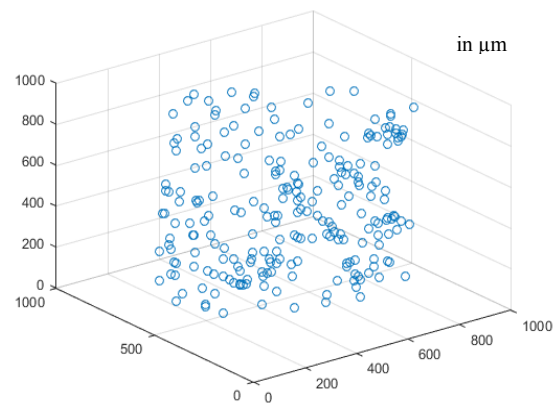


Fig 99 Isometric plot of particles



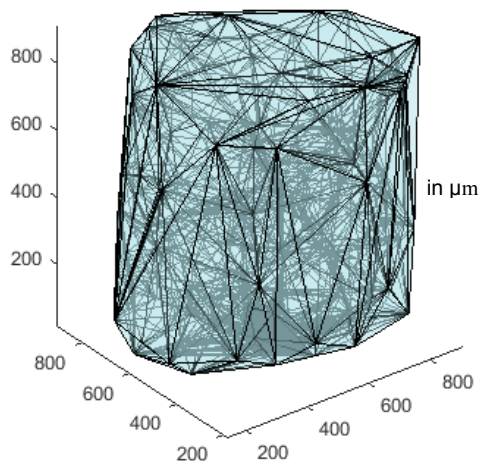


Fig 100 Delaunay triangulation process

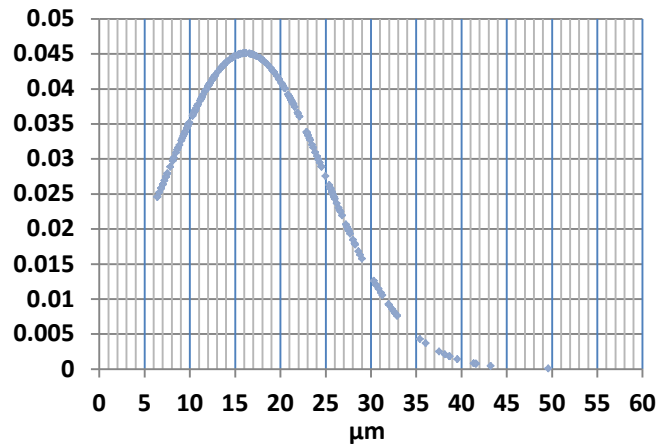


Fig 101 Particle size distribution external area

### X-ray tomography of sample obtained from central area of VB2 specimen

A sample obtained from the central area of a specimen obtained from VB2 furnace is presented in Fig 102. These images show a high concentration of SiC particles in clusters like structures. Mixed and surrounding them, polygonal particles in white colour were identified as silicon impurities. An area from this volume rich in particles (indicated with a red arrow in Fig 103 and presented in Fig 104) was analysed with the objective of determining the average interparticle distance and average volume of the particles present in the sample. The average interparticle distance and average particle volume calculated are  $6.48 \mu\text{m}$  and  $56.3 \mu\text{m}^3$  respectively. Taking the particles as spheres the average size calculated is  $8.7 \mu\text{m}$ . The particle size distribution is obtained using the measurements obtained from tomographic images of four samples taken from the central area of the specimen. The curve of probability, presented in Fig 106, shows that the particle size more often observed is approximately  $9 \mu\text{m}$ .

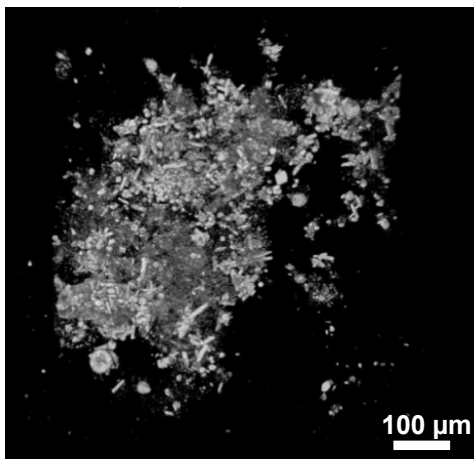


Fig 102 Tomography Mg SiC internal area

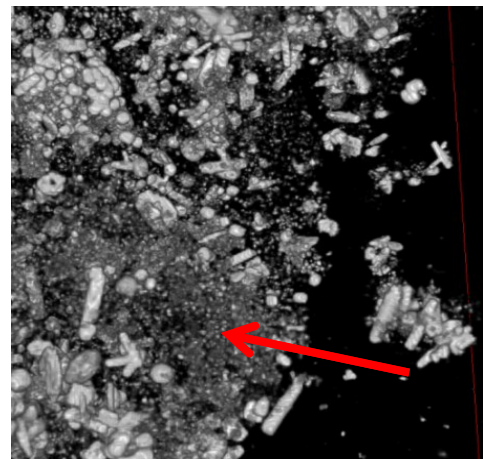


Fig 103 Tomography detail internal area

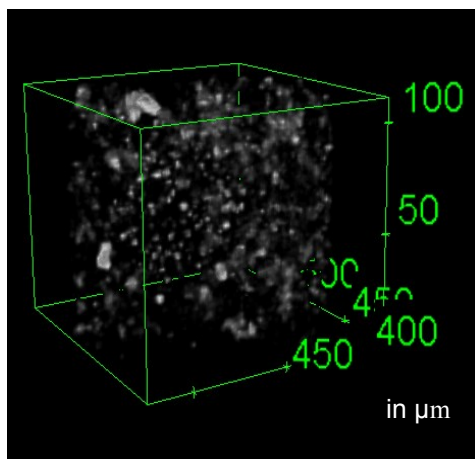


Fig 104 Sample of internal area

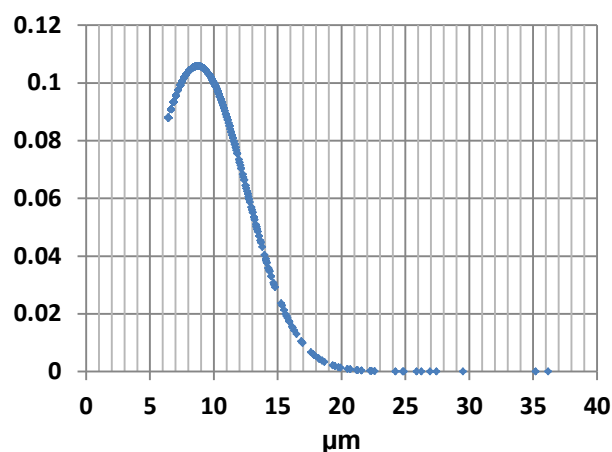


Fig 105 Particle size distribution internal area

### 2.3.4 Discussion on pure magnesium inoculated with SiC particles

The experiments performed using VB2 furnace to disperse SiC microparticles into pure magnesium matrix using a travelling magnetic field, show that particle dispersion is governed by the direction of the travelling magnetic field applied. The results also show a fair agreement between the observed patterns of dispersion, and the patterns predicted by the numerical simulation presented in section 2.1.1. A summary of the results is presented in Fig 106. Tomography revealed that particles found near the crucible walls were 83.9 % bigger than particles found in the central area of the specimen. The electromagnetic forces induced inside the melted metal have the tendency to push the particles to the external areas of the sample. This effect could be related to the higher sensibility of larger particles to buoyancy and EM force effects [100][101]. This effect was also observed in the numerical model performed by Greenwich University. It is also found that downwards TMF enhanced macrosegregation on the central area of the specimen where high concentration of silicon impurities is observed.

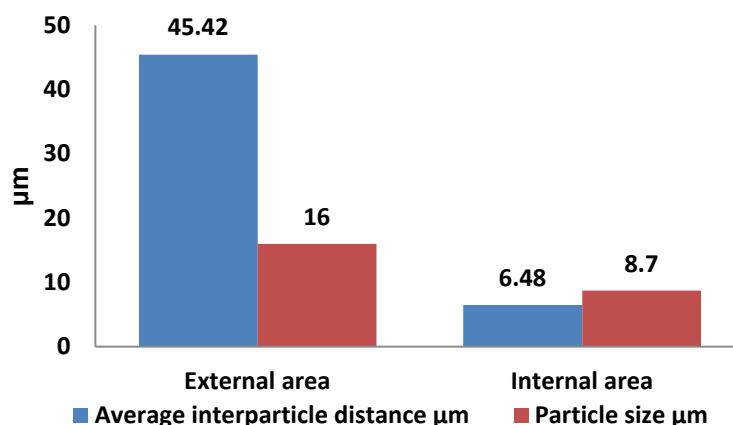


Fig 106 Summary of particle size and average distance

## 2.4 Magnesium AZ91 inoculated with Al<sub>2</sub>O<sub>3</sub> and SiC particles

This section presents the results of the experiments performed dispersing Al<sub>2</sub>O<sub>3</sub> and SiC microparticles into magnesium alloys.

### 2.4.1 Magnesium AZ91 with Al<sub>2</sub>O<sub>3</sub> particles

Two samples of magnesium AZ91 containing 1% and 4% in weight of 4.5 µm size Al<sub>2</sub>O<sub>3</sub> particles were produced using VB2 furnace. The casting parameters used to produce them are presented in Table 26.

Max T K	Time (max T) min	Cooling rate K/s	T Gradient K/m	Magnetic field mT	% Weight
1073	60	0.25	666	15	1

Table 26 AZ91+ Al<sub>2</sub>O<sub>3</sub>/ SiC casting conditions

Cross-sections of two typical solidified samples are presented in Fig 107. In both cases, the alloy exhibits a dendritic equiaxial grain structure. Table 27 presents a summary of the grain size measurements performed on both materials

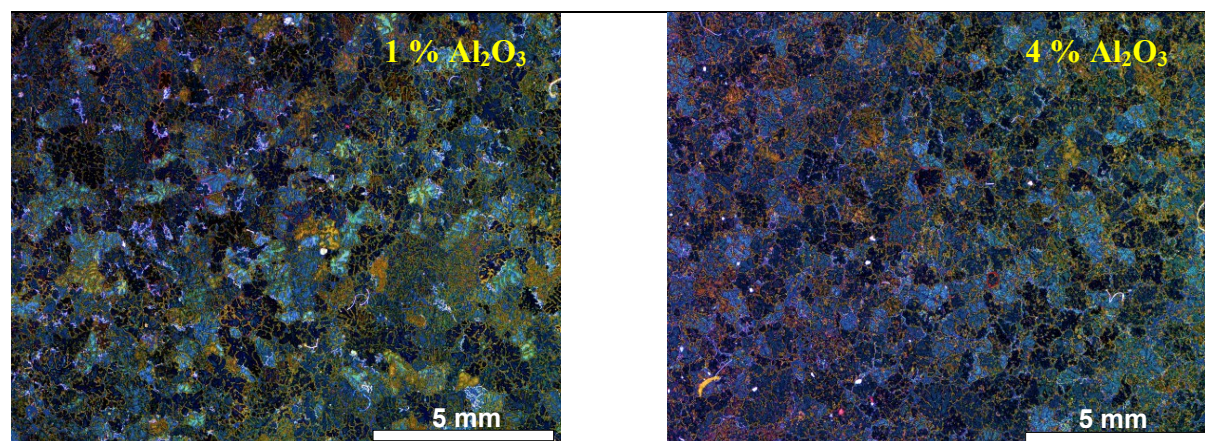


Fig 107 Sample of AZ91 + 1% Al<sub>2</sub>O<sub>3</sub> particles

Measurement	1% Al <sub>2</sub> O <sub>3</sub>	4% Al <sub>2</sub> O <sub>3</sub>
Mean grain area (mm <sup>2</sup> )	0.23	0.31
Mean grain size (mm)	0.63	0.75
Minimum /maximum grain area (mm <sup>2</sup> )	0.08/0.39	0.09/1.85
Minimum /maximum grain length (mm)	0.35/0.91	0.43/1.63
Standard deviation (area)	0.12	0.31
Standard deviation (grain size)	0.08	0.23
Number of grains measured	50	57

Table 27 Summary of grain size measurements of Mg AZ91 +1% and 4% Al<sub>2</sub>O<sub>3</sub>.



## SEM and X-ray spectrometry analysis of magnesium AZ91 with 1% Al<sub>2</sub>O<sub>3</sub>

The SEM analysis, supported by X-ray spectrometry, is performed on samples of Mg AZ91 1% Al<sub>2</sub>O<sub>3</sub> to analyse the dispersion of Al<sub>2</sub>O<sub>3</sub> particles. During SEM analysis several types of particles were found which are presented in this section.

### Aluminium- Manganese compound: Al<sub>8</sub>Mn<sub>5</sub>

Aluminium-Manganese compounds Al<sub>8</sub>Mn<sub>5</sub> are widely made evident from SEM analysis. Fig 108 presents two hexagonal particles inside the  $\alpha$ -Mg phase and their X-ray spectrum. This intermetallic particle is commonly found in this type of alloy due to the presence of manganese in its composition. This element is added to improve the corrosion resistance of the alloy removing iron by forming compounds with it. Some authors such as Cao et al.[111] suggest that AlMn compounds are effective heterogeneous nucleation sites for the grain refinement of  $\alpha$  Mg grains. On the contrary, the work of authors such as Y.Wang [151] shows the low potential of these particles to serve as grain refiners. Moreover, increase of grain size resulting from the addition of Mn to Mg-Al alloys is observed by Easton et al.[152]. Therefore, the effectiveness of these particles as grain refiners is still under debate.

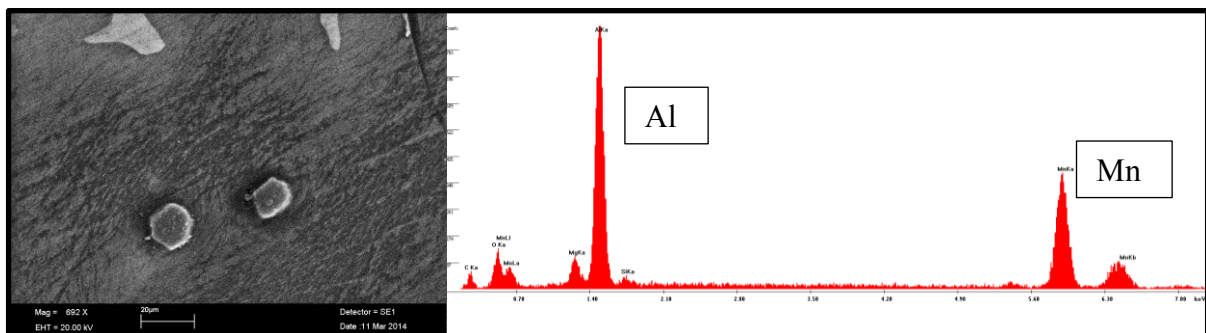


Fig 108 Aluminium-Manganese compound

### Magnesium oxide particles: MgO

Particles of MgO are made evident during the analysis. The particles are found mostly inside the grains and near the eutectic. The presence of these particles should be related to the reaction of Al<sub>2</sub>O<sub>3</sub> particles with the magnesium matrix. A sample of MgO particle and its X-ray spectrum is presented in Fig 109.

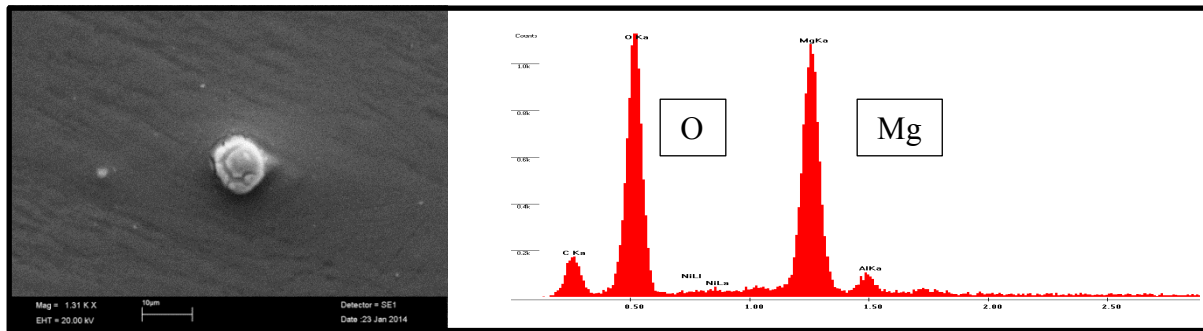


Fig 109 Magnesium oxide particle

## Magnesium spinel particles: $\text{MgAl}_2\text{O}_4$

The formation of spinel particles ( $\text{MgAl}_2\text{O}_4$ ) in magnesium matrix is energetically favourable at 700 K ( $-205.6$  kJ/mol). It preferentially forms at areas where aluminium has diffused out from the Mg matrix and reacted with oxygen [153] [154]. SEM analysis identified several particles of spinel as the one presented in Fig 110.

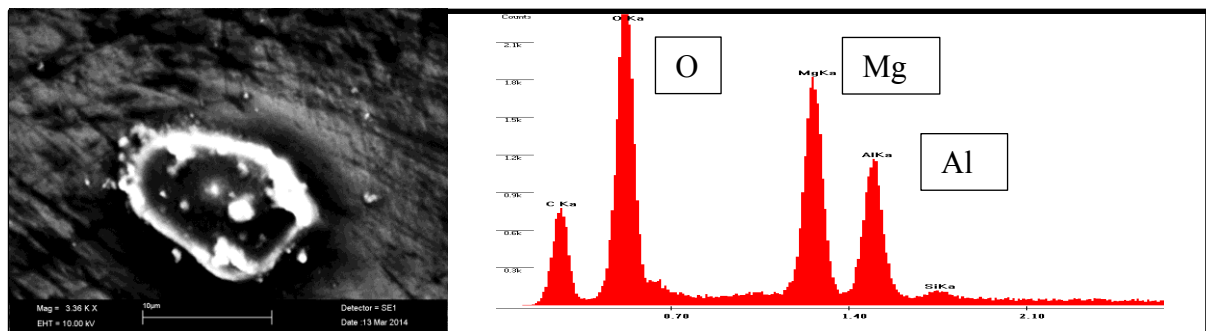


Fig 110 Magnesium spinel particle

## Manganese --Iron compounds

A small amount of iron compounds is found during the analysis of the material. Fig 111 presents a sample found within the magnesium matrix. Iron (Fe) is always present in magnesium alloys as an impurity, thereby decreasing their corrosion resistance [155]. The presence of sufficient iron modifies the manganese-aluminium compounds to very hard manganese-aluminum-iron [156] compounds. These type of compounds has been suggested as potent sites for heterogeneous nucleation of  $\alpha$ -Mg grains by authors such as Tamura et al.[157] who related superheating grain refinement with their presence. In the current study no evidence of grain refinement due to the presence of these particles has been found.

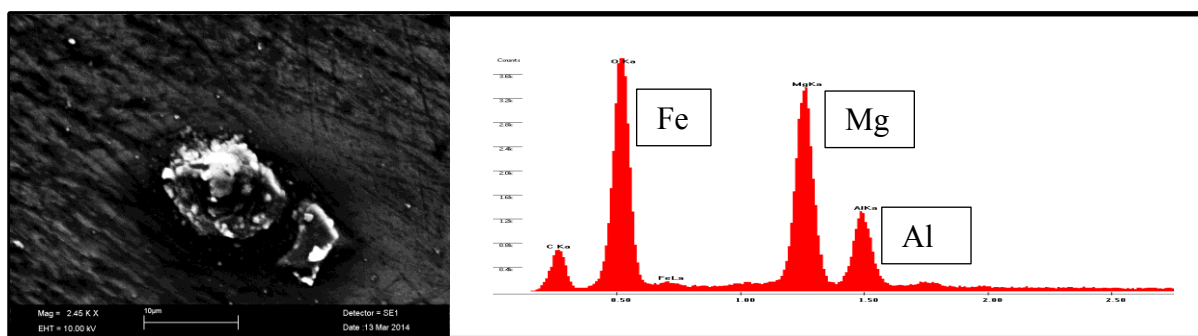


Fig 111 Iron compound particle

The SEM analysis and X-ray spectrometry performed on samples of magnesium AZ91 1%  $\text{Al}_2\text{O}_3$  did not revealed the presence of  $\text{Al}_2\text{O}_3$  particles. This type of particle is usually incorporated into magnesium matrices via semisolid or solid processes in order to avoid reactions between particles and matrix materials. In the current study, the introduction of the particles is carried out in liquid state. In consequence, reaction products are expected. Thermodynamic calculations based on minimization of Gibbs energy are presented in table 28. The equilibrium reactions shows the high tendency of the  $\text{Al}_2\text{O}_3$  particles to react with magnesium matrices producing reaction products such as magnesium spinel [154]. In addition, the calculations show that pure aluminium will be also released in the magnesium matrix.

$\text{Al}_2\text{O}_{3(s)} + 3 \text{Mg}_{(s)} \rightarrow 3\text{MgO}_{(s)} + 2\text{Al}_{(l)}$	$\Delta F_{1000\text{K}} = -76.63 \text{ KJ mol}^{-1}$
$3 \text{Mg}_{(l)} + 4\text{Al}_2\text{O}_{3(s)} \rightarrow 3\text{MgAl}_2\text{O}_{4(s)} + 2\text{Al}_{(l)}$	$\Delta F_{1173\text{K}} = -202.8 \text{ KJ mol}^{-1}$ [158]
$\text{MgO}_{(s)} + \text{Al}_2\text{O}_{3(s)} \rightarrow \text{MgAl}_2\text{O}_{4(s)}$	$\Delta F_{1000\text{K}} = -47 \text{ KJ mol}^{-1}$

Table 28 Equilibrium reactions for  $\text{Al}_2\text{O}_3$  with magnesium

Differential scanning calorimetry (DSC) was performed by Mounib [159] using samples of pure magnesium and magnesium EK21 reinforced with  $\text{Al}_2\text{O}_3$  particles. The results, displayed in Fig 112, confirmed the reaction between the particles and magnesium showing a strong exothermic peak at 520°C.

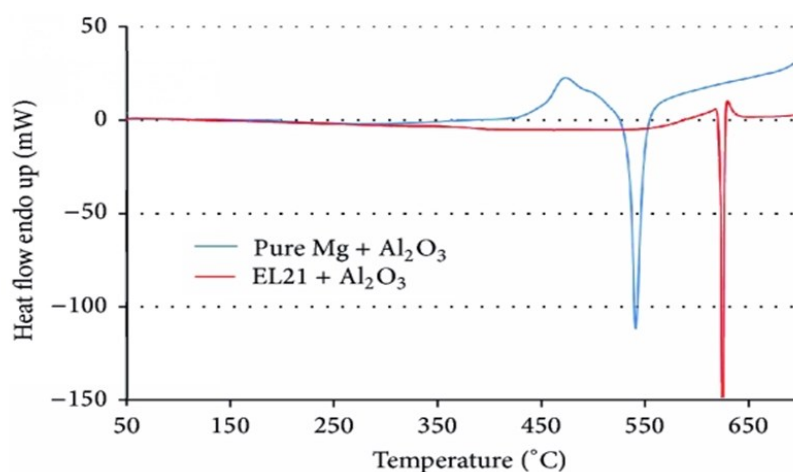


Fig 112 DSC analysis of pure Mg and Mg EK21 with  $\text{Al}_2\text{O}_3$  particles

In order to determine the constituents in the equilibrium obtained from the reaction of the particles with the magnesium matrix, a calculation was performed using the thermochemical software FactSage. The initial composition of the magnesium alloy AZ91 used for the calculations is presented in Table 29. The temperature selected for the simulation was set to 1000 K. The results obtained are displayed in Table 30.

Stream Constituents	Mg	Al	Zr	Mn	Si	Cu	Fe	Be	Zn	Al <sub>2</sub> O <sub>3</sub>
Amount/gram	3.78	0.3	0.4	10	1	4.68E-05	25E-04	22E-04	9.6E-03	0.0098

Table 29 Composition of the alloy and Al<sub>2</sub>O<sub>3</sub> particles

Constituents	Mg <sub>(liquid)</sub>	Al <sub>liquid</sub>	MgO <sub>(solid)</sub>	Mn <sub>3</sub> Si <sub>(solid)</sub>	Zn <sub>(liquid)</sub>	Al <sub>(solid)</sub>
Equilibrium gram	3.75	0.461	0.1202	1.25E-03	9.6E-03	0

Table 30 Composition at the equilibrium

The results show that 100 % of the Al<sub>2</sub>O<sub>3</sub> particles will be converted into reaction products at 1000°K. Moreover, magnesium oxide not present as initial compound will be found in the composition at the equilibrium, as it was predicted by the previous equilibrium reactions. MgO particles has been used to reinforce magnesium alloys by different authors [160]. These particles have been proposed as grain refiners for magnesium matrices. The crystal match of MgO with Mg along the magnesium crystal plane (0002) ( $d = 0.2617$  nm) and magnesium crystal plane (111) ( $d=0.2445$  nm)  $[1\ 1\ 0]_{\text{Mg}} \parallel [1\ 1\ \bar{0}]_{\text{MgO}} : (0\ 0\ 0\ 2)_{\text{Mg}} \parallel (1\ 1\ \bar{0})_{\text{MgO}}$  presents a crystallographic disregistry of about 5.46 % [111]. Therefore, the potency of the MgO particles issued from the chemical reaction of the Al<sub>2</sub>O<sub>3</sub> particles with magnesium to act as nucleation sites is very high. In consequence, these particles could potentially produce grain refining in the material. The equilibrium reactions between Al<sub>2</sub>O<sub>3</sub> and magnesium show also aluminium as reaction product. This aluminium, released into the matrix, changes the composition of the alloy, which can lead to changes in its microstructure. For instance, in order to introduce 4% in weight of particles in 600g specimen of magnesium AZ91, an amount of 24 g of Al<sub>2</sub>O<sub>3</sub> particles is needed. Taking into account the complete reaction of the particles, the aluminium released into the matrix can be calculated using the following formula:

$$\% \text{ Element} = \frac{(n^{\circ} \text{ atoms}) \text{ atomic mass}}{\text{atomic mass compound}} \times 100, (34)$$

where the atomic mass calculated for  $\text{Al}_2\text{O}_3$  is 102. The percentage of aluminium in the compound is 52.99% meaning an amount of aluminium released of approximately 12.7 g. Pure magnesium alloy AZ91 contains 9% of aluminium in its composition. The aluminium released by the dissolution of the particles will increase this percentage up to 11.11%. The following images present samples of magnesium AZ91 containing different percentages in weight of  $\text{Al}_2\text{O}_3$  particles. The optical images are converted into binary format in order to improve the visualization of the  $\text{Mg}_{17}\text{Al}_{12}$   $\beta$  phase presented in the alloy. Measuring the percentage of white pixels with respect to black ones in each picture, the area fraction composed by the intermetallic  $\beta$  phase  $\text{Mg}_{17}\text{Al}_{12}$  can be calculated. The analysis of the images presented in Figs 113-118 shows that  $\beta$  phase in the material containing 4% of  $\text{Al}_2\text{O}_3$  particles increase by 9% with respect to the original material.

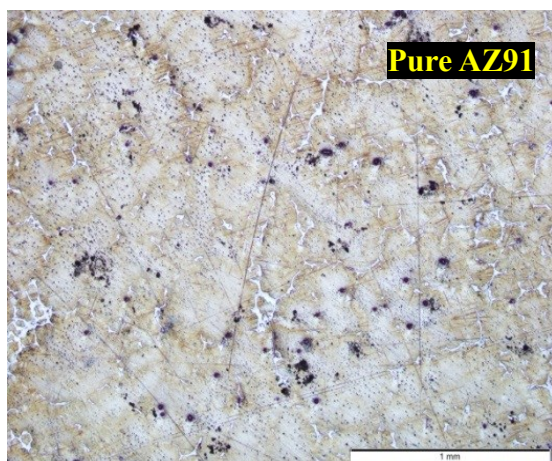


Fig 113 Pure Magnesium AZ91

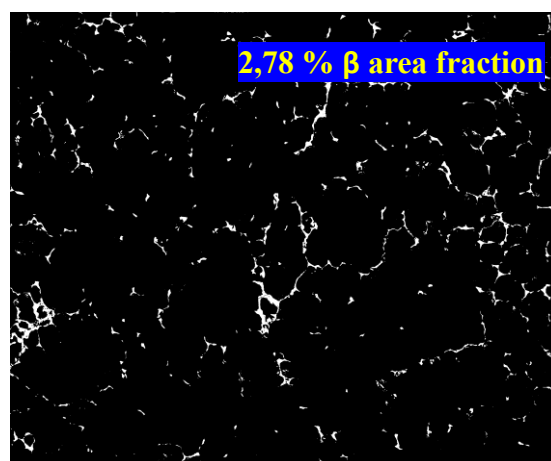


Fig 114 Pure Mg AZ91:  $\beta$  phase area fraction

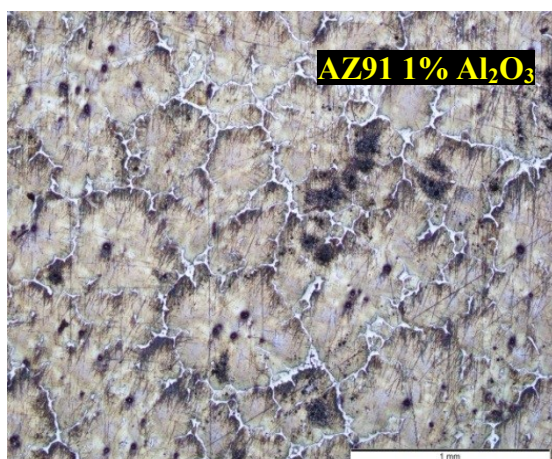


Fig 115 Mg AZ91 1%  $\text{Al}_2\text{O}_3$

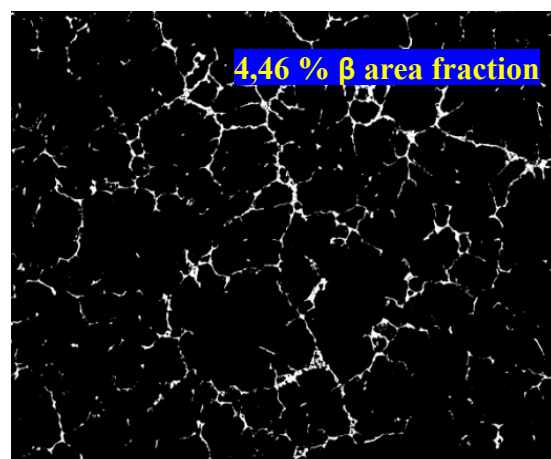


Fig 116 AZ91 1%  $\text{Al}_2\text{O}_3$ :  $\beta$  phase area fraction



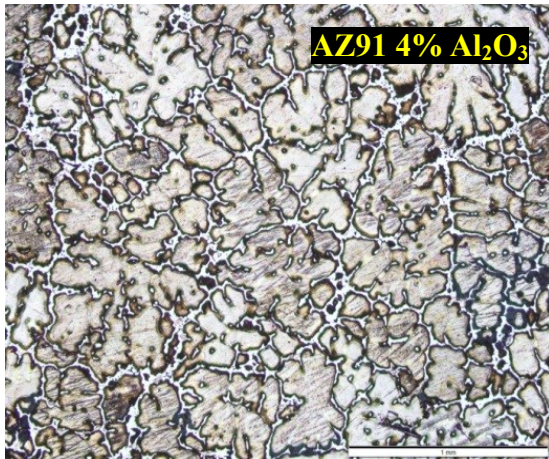


Fig 117 Mg AZ91 4%  $\text{Al}_2\text{O}_3$

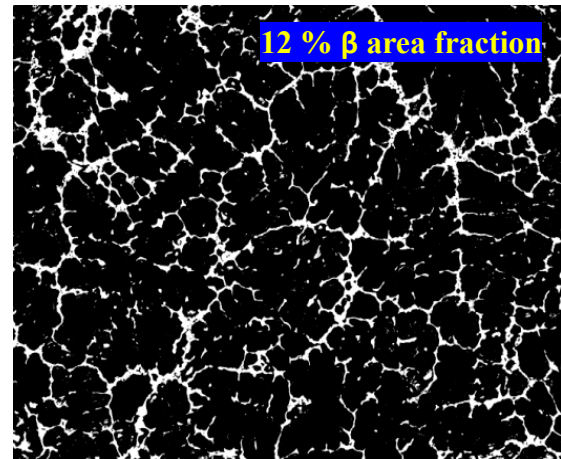


Fig 118 AZ91 4%  $\text{Al}_2\text{O}_3$ :  $\beta$  phase area fraction

## 2.4.2 X-ray tomography analysis of magnesium AZ91 1 % and 4% $\text{Al}_2\text{O}_3$

X-ray tomography was performed on samples of pure magnesium AZ91 and magnesium AZ91 containing different percentages in weight of  $\text{Al}_2\text{O}_3$  particles dispersed using a downwards TMF of 15 mT. The objective pursued with this test is the analysis of the particle dispersion in the materials. The samples are taken from both upper and lower parts of specimens obtained from VB2 furnace, at different distances from its vertical axis, as shown in Fig 120 and Fig 121. The samples have a volume of  $0.10 \text{ mm}^3$ . The tomography is performed using an X-ray energy beam of 40 KV, and an exposition time of 5s following the procedure presented in section 2.3.3. 3D volumes of the samples are obtained assembling the 2D images obtained from X-ray tomography. The analysis of the 3D volumes using the software imageJ provided information on the number of particles, their average interparticle distance and the particle size distribution (PSD) in the material.

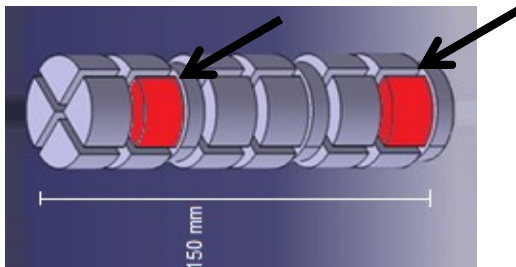


Fig 119 VB2 specimen scheme

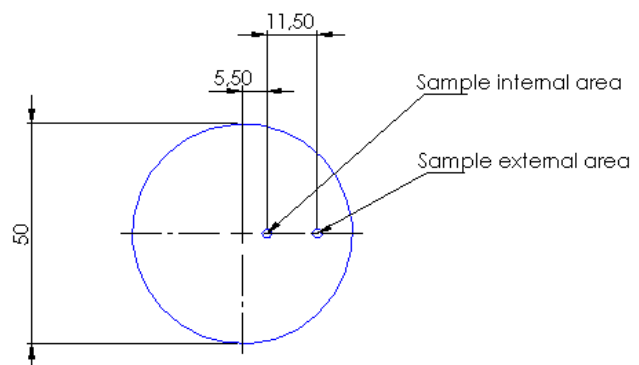


Fig 120 Cross-section top view

## Pure Magnesium AZ91

This section presents the results of the tomography analysis performed on samples of pure magnesium AZ91 processed without electromagnetic stirring. The previous SEM and optical microscopy analysis of this material showed the presence of intermetallic compound particles containing manganese. The dispersion of these compounds on the upper part of the specimen can be observed in the 3D view presented in Fig 121 and Fig 122.

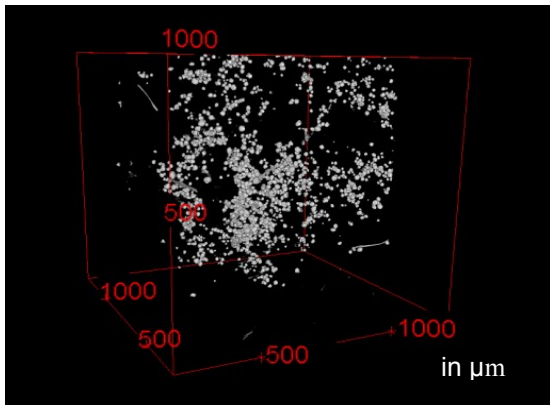


Fig 121 AZ91 pure internal area sample

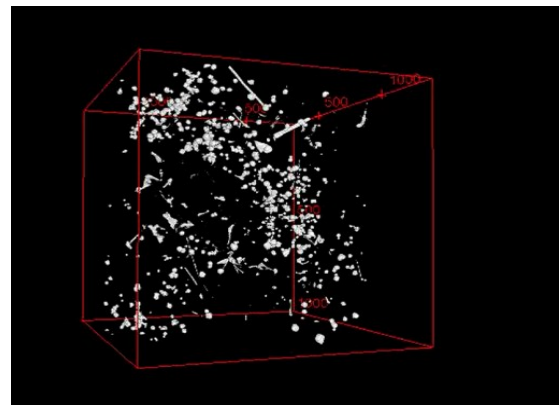


Fig 122 AZ91 pure external area sample

The number of particles counted on the upper and lower parts of the VB2 specimen analysed is presented in Table 29.

Measurement	Number of particles		Average volume and size ( $\mu\text{m}^3$ ) / ( $\mu\text{m}$ )	
	Central	External	Central	External
Upper Part	79	89	512/9.9	441/9.4
Lower Part	2553	484	1972/15.5	1914/15.45

Table 31 Number of particles, volume and size in pure magnesium AZ91

The particle size distribution (PSD) detected in the sample is presented in Fig 123 and Fig 124. The curves of probability show that the particle size more frequently found is approximately 36  $\mu\text{m}$  on the upper and lower part of the specimen. The particle size most frequently detected in both internal and external areas is also 36  $\mu\text{m}$ . The average interparticle distance measured in upper and lower areas of the specimen is summarized in Table 32.

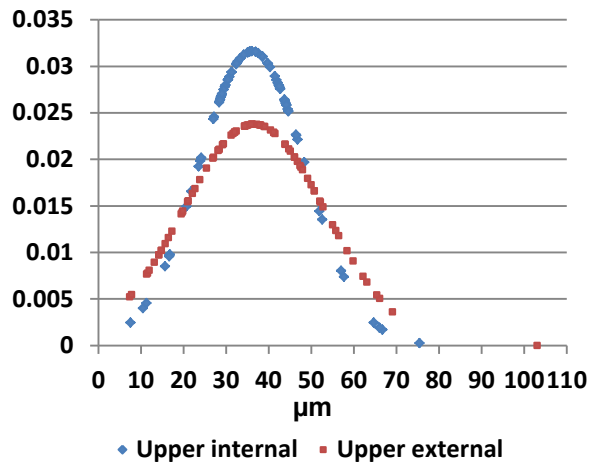


Fig 123 PSD Upper area

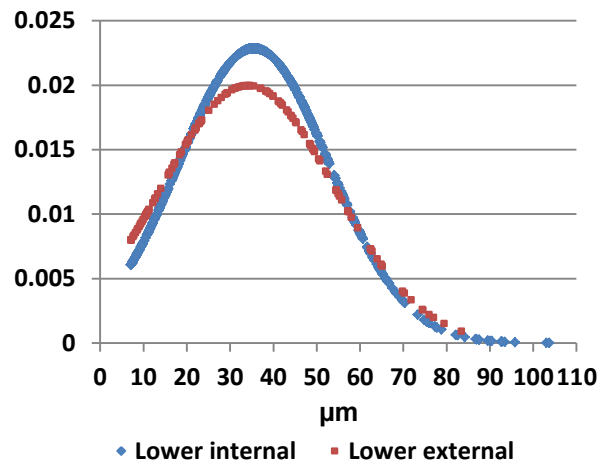


Fig 124 PSD Lower area

Average distance $\mu\text{m}$	Central area	External area
Upper Part	39.24	29
Lower Part	39.85	32.8

Table 32 Average interparticle distance in the central and external areas

### Magnesium AZ91 1% $\text{Al}_2\text{O}_3$

Tomography analysis was performed on samples of magnesium AZ91 containing 1% in weight of  $\text{Al}_2\text{O}_3$ . The dispersion of the particles can be observed in two representative tomographic volumes, presented in Fig 125 and Fig 126, obtained from the upper part of a VB2 specimen.

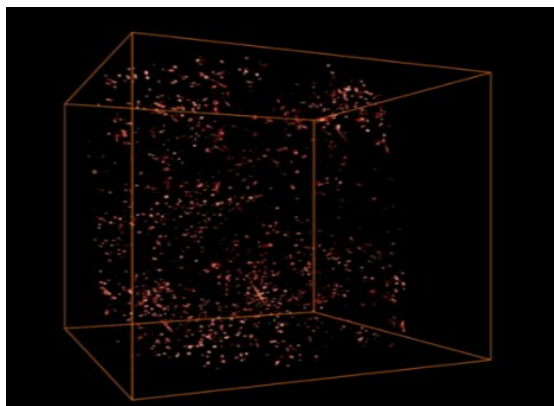


Fig 125 AZ91 1% Upper internal area

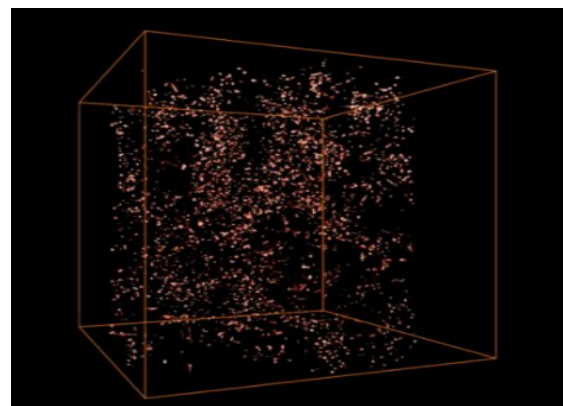


Fig 126 AZ91 1% Upper external area



The number and size of the particles detected in the tomographic volumes are measured following the same procedure used for pure magnesium AZ91. Table 33 presents a summary of the measurements. The average interparticle distances calculated on the central and external area are presented in table 34.

Measurement	Number of particles		Average volume and size ( $\mu\text{m}^3$ ) / ( $\mu\text{m}$ )	
	Central	External	Central	External
Upper Part	719	790	398/7.7	399/7.3
Lower Part	2553	4845	208/5.5	553/7.4

Table 33 Number of particles and average volume/size upper and lower parts

Average distance $\mu\text{m}$	Central area	External area
Upper Part	62	51.5
Lower Part	24.13	42.73

Table 34 Average interparticle distance

The particle size distribution detected on the upper and lower parts of the specimen is presented in Fig 127 and 128. The curves of probability show that the particle sizes more frequently found are 22 and 20  $\mu\text{m}$  on the upper part internal and external areas respectively. On the other hand the curves of probability produced from the analysis performed on the lower part of the specimen, show that the particle sizes more frequently found are 14 and 22  $\mu\text{m}$  and in both internal and external areas respectively.

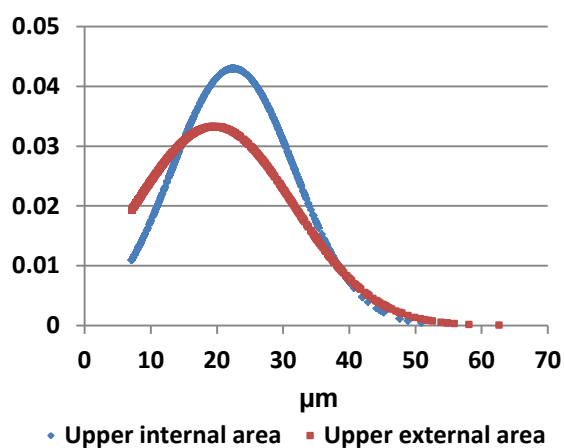


Fig 127 PSD Upper part of the specimen

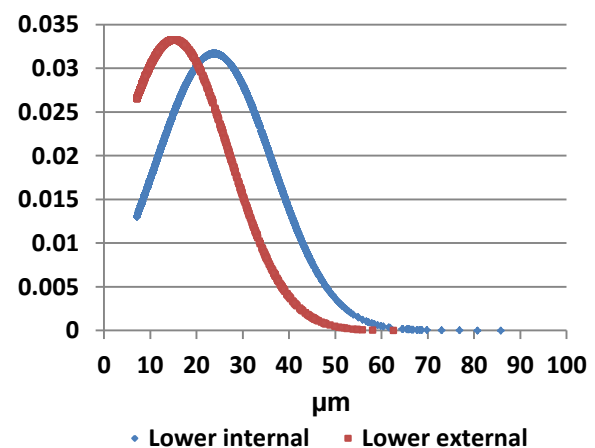


Fig 128 PSD Lower part of the specimen

A general view of a sample analysed with tomography is displayed in Fig 129. This sample present several particles dispersed within its microstructure. A detail view of one of the particles, presented in Fig 130 shows a difference between its core and external shell. This can be clearly seen in the colour enhanced particle presented in Fig 132. The X-ray spectrometry analysis presented in Fig 131 and 133 revealed that the particle is formed by a nucleus of MgO surrounded by a layer of AlMn. This result suggests that MgO particles serve as nucleant for this type of intermetallic compound. Manganese is present in the composition of magnesium AZ91 to enhance its corrosion resistance and is usually found in the forms of  $\text{Al}_8\text{Mn}_5$  or  $\text{Al}_8(\text{Mn}, \text{Fe})$  intermetallic compounds [151].

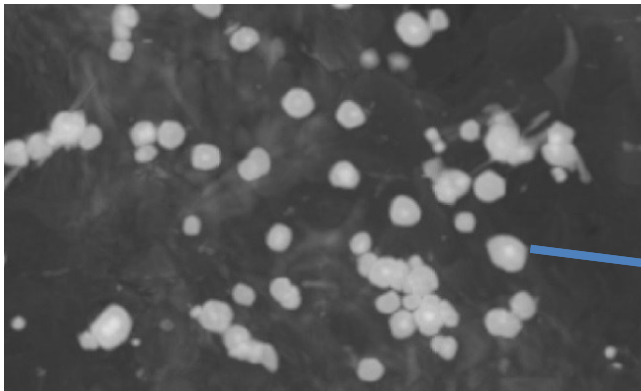


Fig 129 Group of particles in Mg AZ91 + 1%  $\text{Al}_2\text{O}_3$

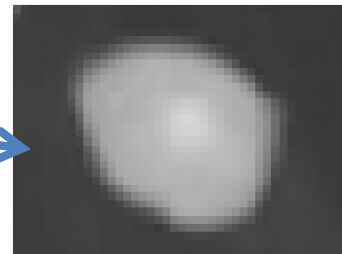


Fig 130 Detail view of particle

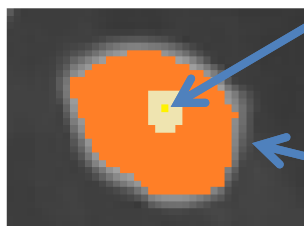


Fig 132 Coloured enhanced particle

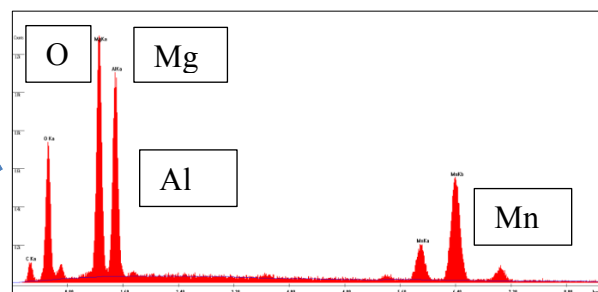


Fig 131 X-ray spectrum of particle nucleus

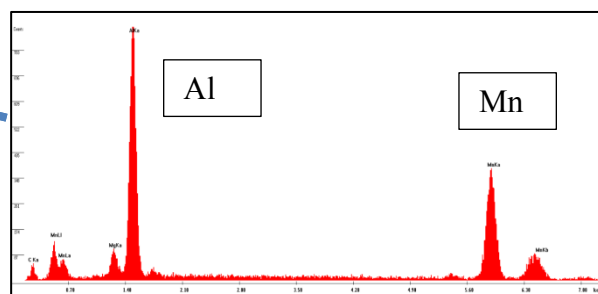


Fig 133 X-ray spectrum particle shell

The thermodynamic calculations based on Gibbs energy, presented in chapter 3.4.1, demonstrate the high tendency of the  $\text{Al}_2\text{O}_3$  particles to react with magnesium matrices producing MgO and pure Al. Magnesium oxide particles have been used by different authors to reinforce magnesium alloys, also several studies have shown that particles of MgO can act as nucleants for intermetallic particles [158]. Fan [111] calculated that atomic mismatch along the closely packed directions Mg [1 1 0] and  $\text{Al}_8\text{Mn}_5$  [1 -2 1 0] is 5.80%. This value makes MgO particles to be potent nucleants for  $\text{Al}_8\text{Mn}_5$  intermetallics [111]. The analysis performed to find the number of intermetallic particles, and their size distribution in the material containing  $\text{Al}_2\text{O}_3$  particles shows that their number increase, and their average size decrease with respect to the particles found in pure magnesium AZ91. Similar results were found by Fan who studied the effects of a strong mechanical stirring on magnesium AZ91D reinforced with MgO particles. In the current case, the reduction in size and increase in number of  $\text{Al}_8\text{Mn}_5$  particles can be related to the electromagnetic stirring and the nucleant capacity of the magnesium oxide particles.

### Magnesium AZ91 4% $\text{Al}_2\text{O}_3$

A sample of magnesium AZ91 + 4%  $\text{Al}_2\text{O}_3$  was analysed using X-ray tomography. This specimen revealed a structure containing needle-like intermetallics of  $\text{Al}_8\text{Mn}_5$  (Fig 134). These particles can be also observed during optical analysis, as shown in the sample presented in Fig 135.

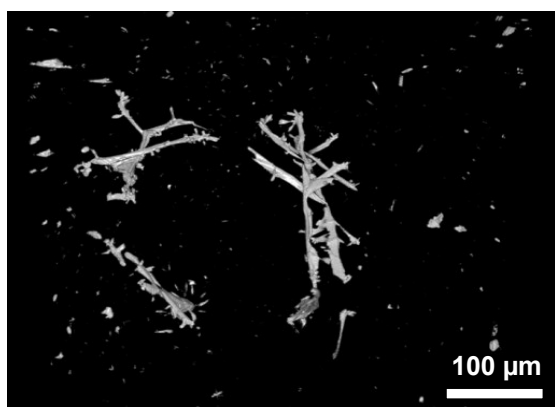


Fig 134 Mg AZ91 + 4%  $\text{Al}_2\text{O}_3$  tomography

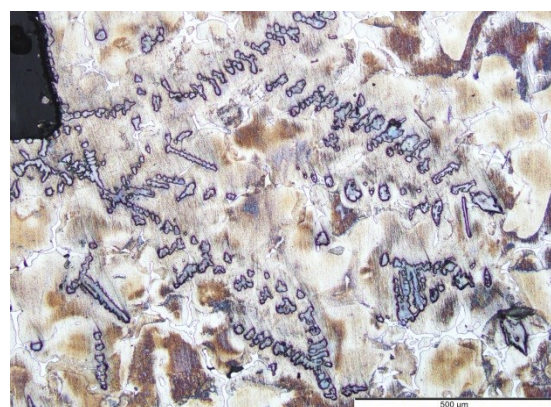


Fig 135 Mg AZ91 optical analysis

The formation of this type of particles could be the result of coalescence between  $\text{Al}_8\text{Mn}_5$  intermetallic particles which nucleated on magnesium oxide particles. The MgO particles present in the alloy proceed probably from the reaction of the  $\text{Al}_2\text{O}_3$  with the magnesium matrix as it was explained in section 3.4.1.

## Concluding remarks and summary of the X-ray tomography results

The analysis of the inoculated materials did not show any signs of  $\text{Al}_2\text{O}_3$  particles within the matrix. Instead the presence of different precipitates such as  $\text{MgO}$  particles, predicted by the thermodynamic analysis, and the increase of aluminium in the composition of the alloy were observed. These results support the idea that a chemical reaction between the particles with the magnesium matrix took place. The addition of  $\text{Al}_2\text{O}_3$  particles did not produce any considerable signs of grain refinement. However, the number of  $\text{Al}_8\text{Mn}_5$  intermetallic particles increases in the material containing  $\text{Al}_2\text{O}_3$  particles. These particles show an average size 10 to 70 % smaller than the intermetallic particles detected in the unreinforced material. The results of the measurements performed to detect the number and size of the intermetallic particles present in samples of pure magnesium AZ91, and magnesium AZ91+1%  $\text{Al}_2\text{O}_3$  are summarized in Fig 136 and Fig 137.

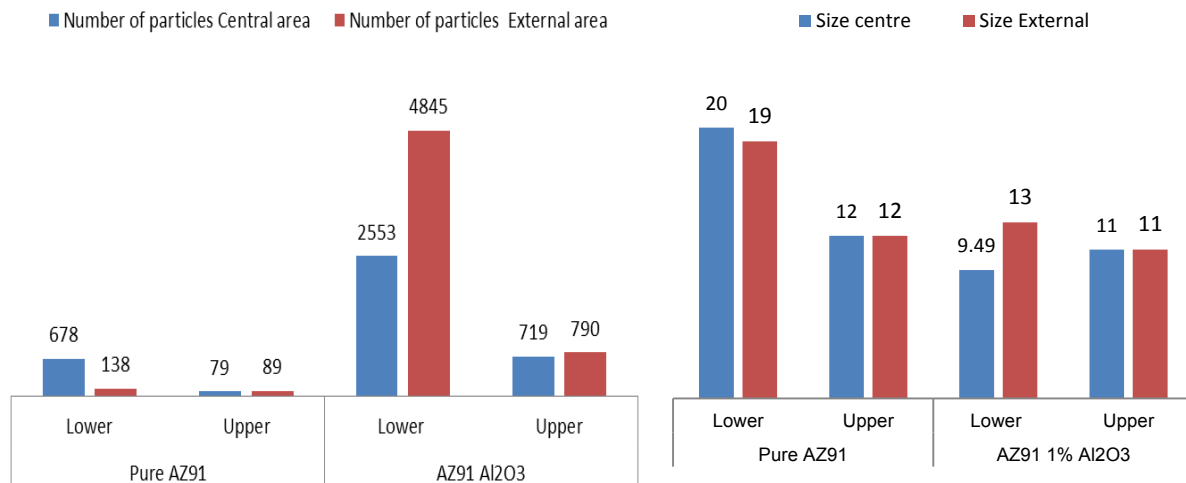


Fig 136 Number of particles detected

Fig 137 Particles average size in  $\mu\text{m}$

### 2.4.3 Pure magnesium containing 18% in weight of $\text{Al}_2\text{O}_3$ particles

This section focuses on the feasibility of a process based on the reaction between  $\text{Al}_2\text{O}_3$  particles with magnesium to produce aluminium rich magnesium alloy. The alloy obtained will be also rich in  $\text{MgO}$  particles, produced ‘in situ’, and dispersed using the TMF provided by VB2 furnace. The alloy produced to test the process contains a percentage in weight of aluminium of 9%, which is the same of Mg AZ91. In order to reach the percentage of aluminium required, a percentage in weight of particles of 18% is mixed with magnesium. The aluminium released by the reaction between the particles and the matrix is accompanied by the production of  $\text{MgO}$  particles. The lack of manganese in the material facilitates the

detection of MgO particles. Table 35 presents the casting conditions used during the experiment.

Max T K	Time (max T) min	Cooling rate K/s	T Gradient K/m	TMF mT	Particles	% Weight
1073	60	0.25	666	70	Al <sub>2</sub> O <sub>3</sub>	18

Table 35 Casting parameter of pure magnesium + 18% Al<sub>2</sub>O<sub>3</sub>

A sample of the alloy produced is presented in Fig 138. The material presents an equiaxial grain structure with an average grain size of 2.2 mm. Table 36 presents a summary of the grain size measurements performed on this material.

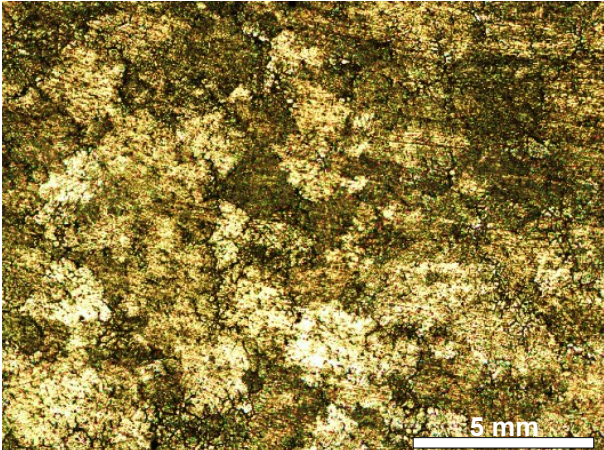
	Measurement	
	Mean grain area (mm <sup>2</sup> )	2.2
	Mean grain size (mm)	2.2
	Minimum /maximum grain area (mm <sup>2</sup> )	0.7/5.3
	Minimum /maximum grain length (mm)	1.23/3.51
	Standard deviation (area)	1.28
	Standard deviation (grain size)	0.68
	Number of grains measured	48

Fig 138 Pure Mg 18 % Al<sub>2</sub>O<sub>3</sub>

Table 36 Mg + 18% Al<sub>2</sub>O<sub>3</sub> grain size measurements

### SEM and X-ray spectrometry analysis of pure magnesium+ 18% Al<sub>2</sub>O<sub>3</sub> microparticles

The analysis of several samples of magnesium 18% Al<sub>2</sub>O<sub>3</sub> using SEM microscopy revealed a microstructure composed by an alpha magnesium matrix and a  $\beta$  phase composed by the intermetallic compound Mg<sub>17</sub>Al<sub>12</sub>. A general view of the microstructure obtained by backscattered electrons is presented in Fig 139 and Fig 140. In both images, particles can be seen as black dots well dispersed within the matrix and next to the  $\beta$  phase. A detail view of one of the particles is presented in Fig 141. X-ray spectrometry presented in Fig 142, confirmed that the composition of the particle is MgO. The calculated average size of the particles detected is 5  $\mu$ m.



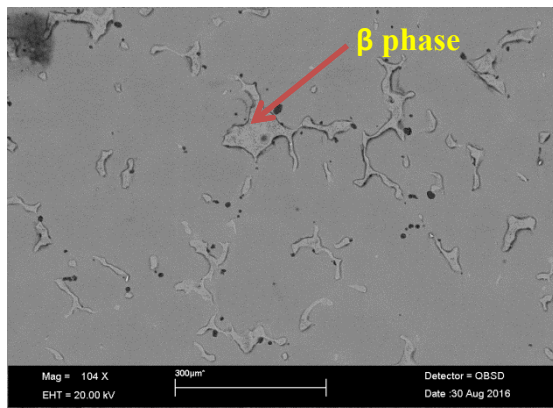


Fig 139 SEM Mg 18% Al<sub>2</sub>O<sub>3</sub>

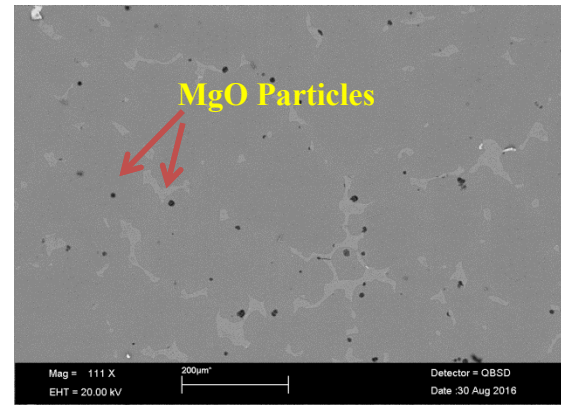


Fig 140 SEM Mg 18% Al<sub>2</sub>O<sub>3</sub>

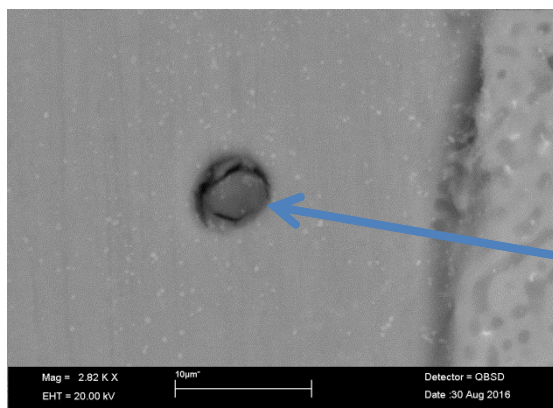


Fig 141 MgO Particle

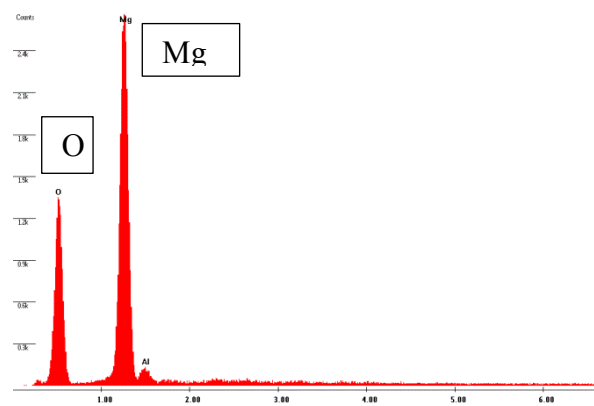


Fig 142 X-ray MgO spectrometry

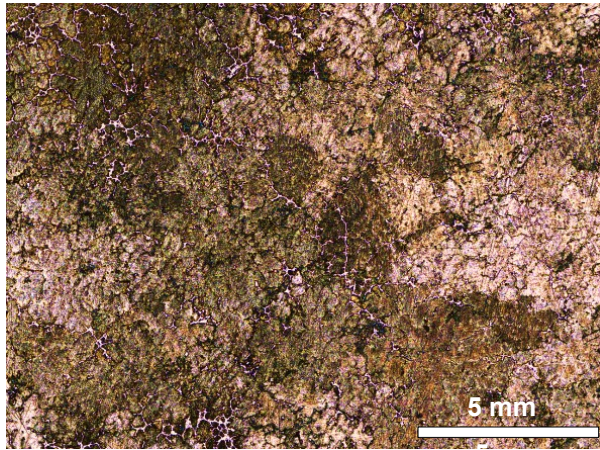
The detection of magnesium oxide particles within the magnesium matrix demonstrate the feasibility of the process, and confirm that the production of an aluminium rich magnesium alloy can be achieved by the dissolution of Al<sub>2</sub>O<sub>3</sub> particles into pure magnesium matrix.

#### 2.4.4 Magnesium AZ91 + 2% SiC microparticles

Microparticles of SiC size ranging from 0.1 to 1  $\mu$ m were dispersed in magnesium alloy AZ91. The amount of particles was equivalent to 2 % in weight of the specimen. The microparticles were dispersed using a TMF of 70 mT intensity. Table 37 presents the casting parameters used to produce the inoculated material. The optical analysis performed on samples of the material revealed an average grain size of 2 mm, and an equiaxial grain structure as shown in Fig 143. A summary of the grain size measurements performed can be found in Table 38.

Max T K	Time (max T) min	Cooling rate K/s	T Gradient K/m	TMF mT	Particles	% Weight
1073	60	0.25	666	70	SiC	2

Table 37 Casting parameters of magnesium AZ91 + 2% SiC



Measurement	
Mean grain area (mm <sup>2</sup> )	2.1
Mean grain size (mm)	2.0
Minimum /maximum grain area (mm <sup>2</sup> )	0.76/4.63
Minimum /maximum grain length (mm)	3.09/1.29
Standard deviation (area)	1.16
Standard deviation (grain size)	0.61
Number of grains measured	20

Fig 143 AZ91 + 2% SiC 0.1-1 μm

Table 38 AZ91+2% SiC: grain size measurements

The optical analysis of the sample shows particles well dispersed within the magnesium phase. Fig 144 presents a sample in which several particles (indicated with black arrows) can be seen near the  $Mg_{17}Al_{12}$   $\beta$  phase. The material also presented some areas of porosity as shown in Fig 145.

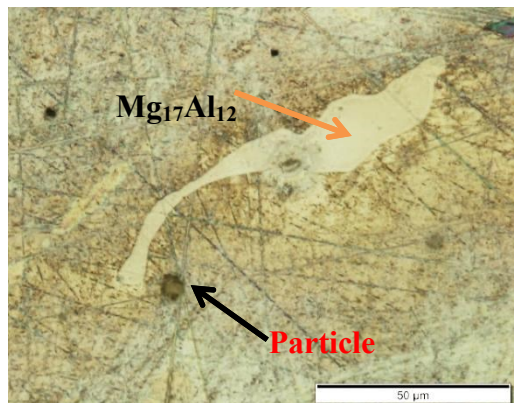


Fig 144 AZ91 + 2% SiC 0.1-1μm sample

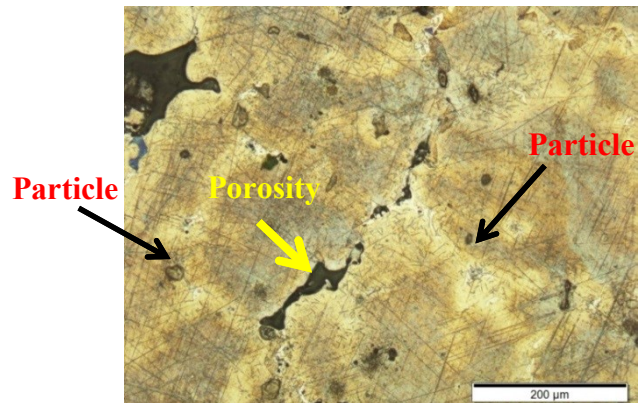


Fig 145 AZ91 + 2% SiC 0.1-1μm sample

The results confirm the stability of the SiC particles in the magnesium matrix, and revealed no signs of grain refining as in the case of the material reinforced with  $Al_2O_3$ .

## 2.4.5 General conclusions in grain refinement using microparticles

The graph presented in Fig 146 summarizes the average grain size measurements performed on samples of pure and inoculated magnesium AZ91. The graph shows a grain size reduction with respect to the pure alloy of approximately 28 % and 14% on samples containing 1% and 4 % in weight of  $Al_2O_3$  particles respectively. The graph also displays the value of the grain



size measured on a sample containing 3% in weight of pure aluminium, which is the equivalent amount released by the reaction between the  $\text{Al}_2\text{O}_3$  particles with the magnesium matrix in the sample containing 1% in weight of particles. This material presents a similar grain size with respect to the inoculated materials. Finally, the material in which particles of SiC were dispersed presents the biggest grain size with respect to the materials containing  $\text{Al}_2\text{O}_3$  particles. Based on the results displayed in the summary graph, it can be concluded that only the addition of  $\text{Al}_2\text{O}_3$  particles produced a slight reduction in grain size with respect to the pure alloy.

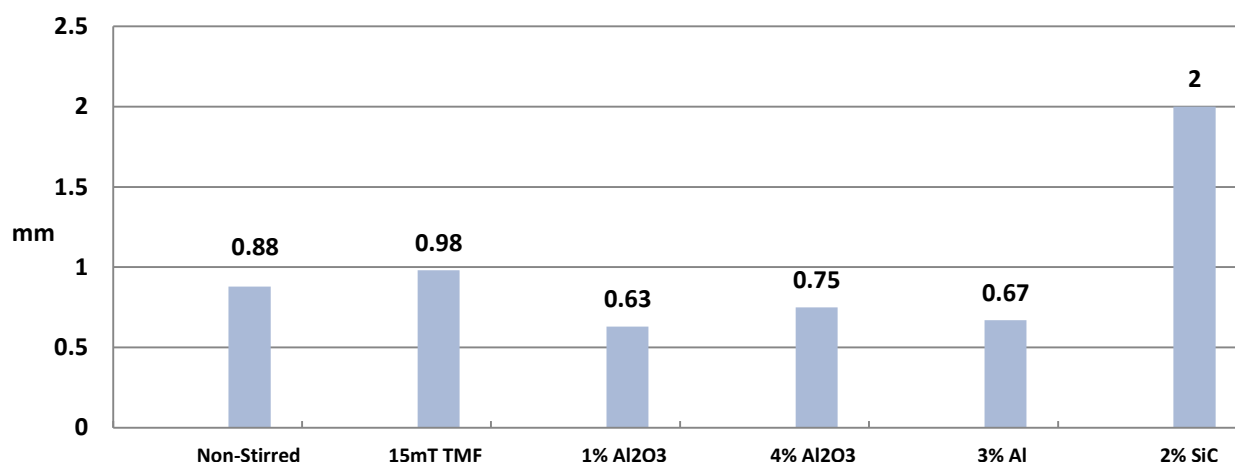


Fig 146 Summary of Mg AZ91 grain size measurements

## 2.4.6 Mechanical characterization of samples of magnesium AZ91

This section presents the results of the mechanical characterization performed on samples of magnesium AZ91 reinforced with microparticles of  $\text{Al}_2\text{O}_3$  and SiC.

### Hardness test and micro indentation (micro hardness)

Hardness test can provide with an indication of the effects produced by the particles in the resistance to deformation presented by the material. This test is also useful to determine the efficiency of the electromagnetic stirring to disperse microparticles. The average hardness of the specimen obtained from VB2 is measured along the centre of its longitudinal section using 260 measurement points (as explained in section 2.3.5). A linear graph depicted in Fig 147 presents the results of the measurements perfo

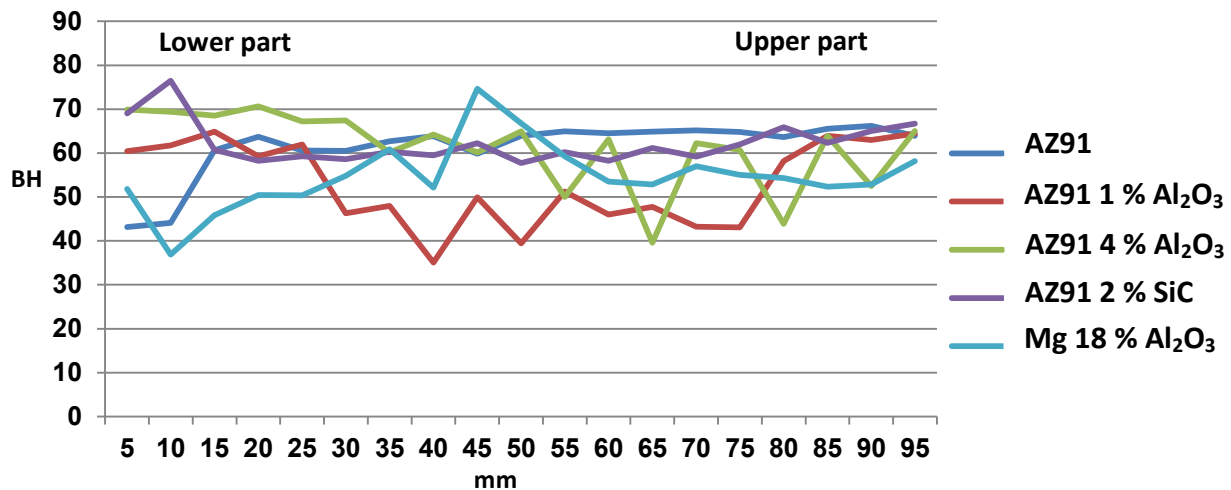


Fig 147 Average hardness map Mg AZ91

The graph shows that Brinell hardness in pure magnesium AZ91 present a value of approximately 62 along the total length of the specimen. On the contrary, the two samples of magnesium alloy AZ91 reinforced with Al<sub>2</sub>O<sub>3</sub> present hardness values well below the one of pure magnesium AZ91. The lower hardness value measured can be related to the high level of porosity observed in these materials. Only in the case of MgAZ91+ 4% Al<sub>2</sub>O<sub>3</sub>, some areas of high hardness values were detected on the lower part of the specimen. Magnesium AZ91 reinforced with SiC particles presents hardness values similar to pure magnesium AZ91 along the sample, but also presents a peak of hardness on the lower part of the specimen, which can be related to a high concentration of particles on this area produced by sedimentation. Finally, pure magnesium reinforced with 18% in weight of Al<sub>2</sub>O<sub>3</sub> particles presents hardness values similar to magnesium AZ91. This material also presents low hardness values on the lower part of the specimen which can be related to a high level of porosity observed in this area. A bar graph presented in Fig 148 summarizes the results of the microhardness tests performed. The results show a general decrease in hardness on the materials containing particles with respect to the pure material.

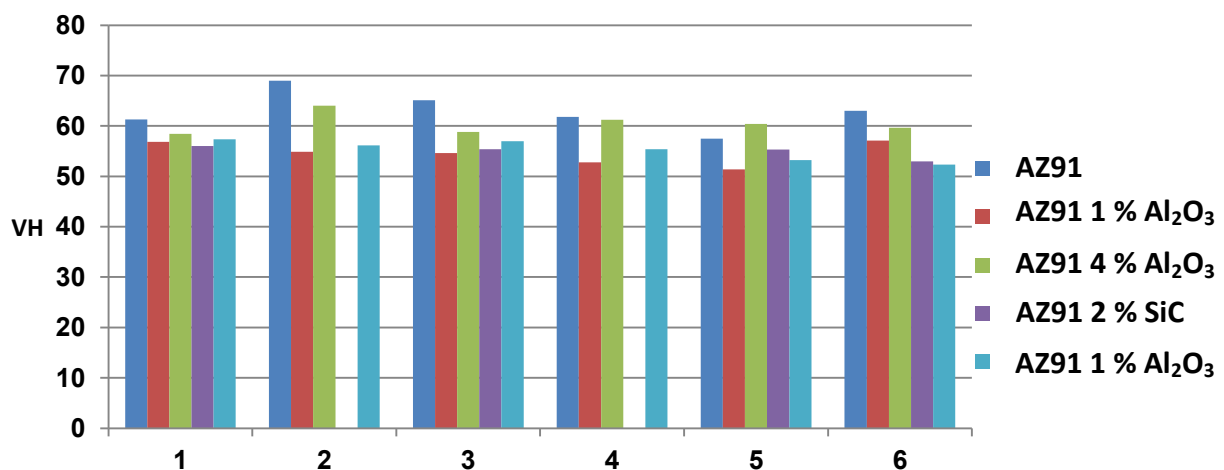


Fig 148 Microhardness measured on samples of Mg AZ91 samples

### 2.4.6.1 Tensile test

Tensile test is a technique used to analyse the influence of the inoculant particles in the tensile strength and ductility of the materials produced. Tensile test was performed on samples of magnesium AZ91 containing  $\text{Al}_2\text{O}_3$  particles at percentages in weight of 1 and 4%, and containing 2% in weight of SiC particles. The strain rate applied during the test is  $0.001\text{s}^{-1}$  and the time between two measurements is set to 0.1 s. The stress – strain curves obtained from the material containing  $\text{Al}_2\text{O}_3$  particles are presented in Fig 149. The material containing 1 % of particles reached a maximum tensile stress of approximately 85 MPa, thus presenting a better tensile behaviour than the samples containing 4% of particles which failed at the beginning of the test. This value is far below the yield strength value of 240 MPa reported for this alloy [161].

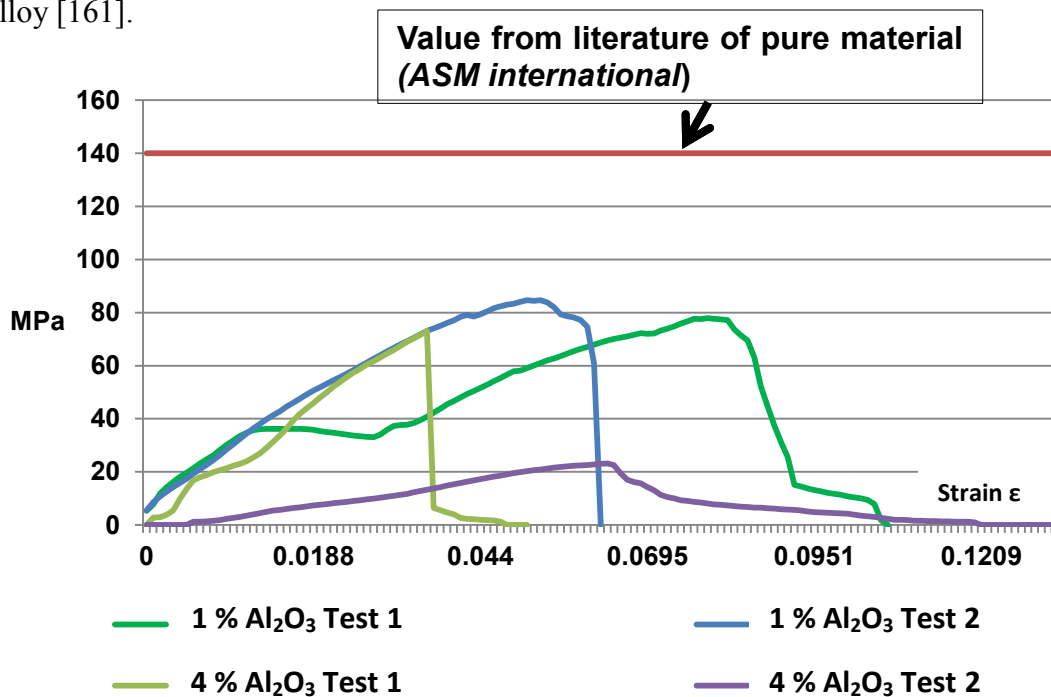


Fig 149 Tensile test Mg AZ91

The stress-strain curves obtained from tensile tests performed on samples of magnesium AZ91+ 2% SiC particles are presented in Fig 150. The maximum tensile strength measured during the test is approximately 100 MPa. This value stands to be approximately 25 % higher than the tensile strength measured on the samples reinforced with  $\text{Al}_2\text{O}_3$  particles. In addition, the material containing SiC particles shows a better ductility and higher strain level than the material reinforced with  $\text{Al}_2\text{O}_3$  particles, and therefore shows a better ductility.

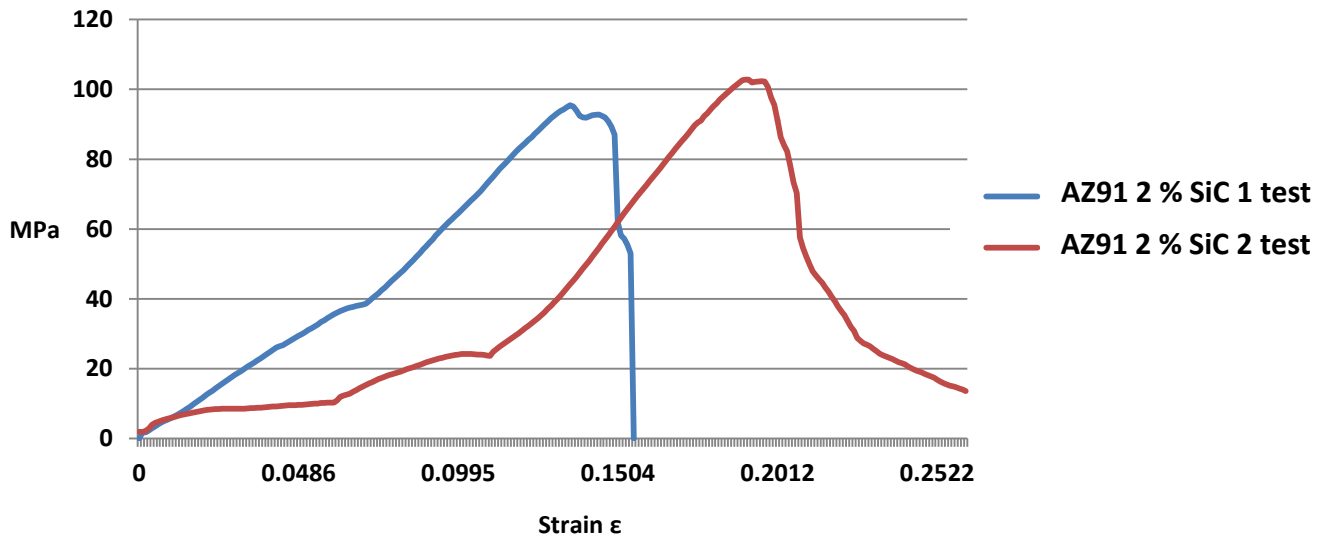


Fig 150 Tensile test on a sample of AZ91 + 2% SiC 0.1-1  $\mu\text{m}$

#### 2.4.7 Discussion on inoculation of magnesium AZ91 using $\text{Al}_2\text{O}_3$ and SiC particles dispersed using a travelling magnetic field (TMF).

The experiments performed using  $\text{Al}_2\text{O}_3$  particles to achieve grain refining in magnesium alloy AZ91 produced several effects in the microstructure of this alloy and also changes in its mechanical properties. The analysis carried out using optical microscopy and SEM shows no signs of  $\text{Al}_2\text{O}_3$  particles within the alloy. The thermodynamic calculations performed demonstrate the great tendency of the particles to react with the magnesium matrix producing different types of reaction products. Conversely, the optical analysis of the specimens produced shows the increase of the area fraction occupied by the  $\beta$  phase in the alloy, composed by  $\text{Mg}_{17}\text{Al}_{12}$ , which is directly related to the amount of particles dispersed. The chemical thermodynamic calculations performed, based on Gibbs energy, shows that as reaction products from the reaction of the particles with magnesium, pure aluminium and particles of magnesium oxide ( $\text{MgO}$ ) are consistently released into the magnesium matrix. The addition of aluminium leads also to changes in the composition of the alloy producing the increase of the  $\beta$  phase. The average grain size of the materials inoculated with  $\text{Al}_2\text{O}_3$  particles decrease with respect to pure magnesium AZ91 by 13%, and 25% in the case of Mg AZ91 1%  $\text{Al}_2\text{O}_3$  and Mg AZ91 4%  $\text{Al}_2\text{O}_3$  respectively. The segregation power of the solute also called the growth restriction factor  $Q$  is critical in the final grain size of alloys. Growth restriction factor  $Q$  calculated for pure magnesium AZ91 is 38.75 while for magnesium AZ91 4%  $\text{Al}_2\text{O}_3$  is 47.36. Empirically, the average grain size can be described as a linear function of  $1/Q$  for magnesium and aluminium alloys [84]. The growth restriction factor  $1/Q$  calculated for pure magnesium AZ91 is 0.0258 whereas for magnesium AZ91 + 4% is 0.0211 presenting grain sizes of 880 and 750  $\mu\text{m}$  respectively. Therefore, the growth restriction factor of the

alloy inoculated with  $\text{Al}_2\text{O}_3$  particles is higher than the one of pure alloy. This could have contributed to the slight grain refinement observed in this material. Particles of MgO, which are considered potential grain refinement of Mg  $\alpha$  grains, are found during SEM analysis. Taking into account that  $\text{Al}_2\text{O}_3$  particles are not detected during the analysis, the grain refinement observed could be related to the increase of solute, and probably to the presence of MgO particles which acted as nucleants for magnesium grains. In order to confirm this, future analysis using TEM should be performed. Pure magnesium AZ91 contains  $\text{Al}_8\text{Mn}_5$  intermetallic particles in its microstructure. The tomography analysis performed shows that the number of  $\text{Al}_8\text{Mn}_5$  intermetallic particles in magnesium AZ91 containing 1% in weight of  $\text{Al}_2\text{O}_3$  particles is higher than in the case of pure material. The size of these intermetallic particles is also found to be smaller. Particles of MgO released by the reaction of the  $\text{Al}_2\text{O}_3$  particles are observed at the centre of AlMn intermetallics, which suggest that they acted as nucleants for these intermetallic particles. Xia and Wang [162] also observed MgO inclusions inside  $\text{Al}_8\text{Mn}_5$  intermetallic particles studying samples of magnesium AZ91. In their studies, the samples were subjected to an intense forced convection produced by mechanical stirring before solidification. In their experiments, magnesium oxide from the surface of the molten alloy was introduced inside the matrix by the strong stirring. The size of the intermetallic particles observed in the Mg AZ91 +1%  $\text{Al}_2\text{O}_3$  particles decreased by 83.9 % with respect to the pure AZ91. Xia also observed a decrease in size of the AlMn particles directly related to the intensity of the mechanical stirring applied. The analysis of the particle dispersion in the specimen of AZ91 1%  $\text{Al}_2\text{O}_3$  shows areas on the lower part of the specimen with high concentration of particles. The density of  $\text{Al}_8\text{Mn}_5$  is higher than the density of MgO and therefore these particles present a higher tendency to sediment at the bottom of the crucible. In the case of magnesium AZ91 containing 4 % in weight of  $\text{Al}_2\text{O}_3$  particles, the AlMn intermetallics detected present a long ‘needle like’ shape, and are found mostly near the  $\beta$  phase. This type of particles could be the result of the coalescence of the intermetallic material nucleating over MgO particles. In this case, the material is inoculated with a higher percentage in weight of  $\text{Al}_2\text{O}_3$  particles. In consequence, it can be predicted that a higher amount of MgO is released into the magnesium matrix. The electromagnetic stirring could have been not enough to disperse efficiently the MgO particles producing agglomerates which served as nucleant surface for intermetallic particles. This type of agglomerate intermetallic particle has a low potential to serve as nucleant for magnesium, and therefore, the grain refinement observed should be related to other mechanisms such as the increase of solute. The tensile test analysis shows that yield strength of the material containing 1% of  $\text{Al}_2\text{O}_3$  particles decreases 62 % with respect to the reported value for this alloy. The material containing 4% of  $\text{Al}_2\text{O}_3$  particles shows extreme fragility breaking at the beginning of the test. In both cases, the low mechanical performance presented by the material can be related to the negative effect produced by the increase of the brittle  $\beta$  phase, as confirmed by other authors such as Matthew [163] . Hardness test shows some areas of high hardness values in magnesium AZ91, but in general the addition of particles produces an increase in porosity in the material,

and in consequence, a decrease of the sample hardness. This is also confirmed by the microhardness analysis. The experiments performed using pure magnesium mixed with 18% of  $\text{Al}_2\text{O}_3$  particles shows the potential of these particles to produce aluminium rich magnesium alloy containing MgO particles produced 'in situ'. The experiment performed inoculating particles of SiC in magnesium AZ91 was successful and particles were found well dispersed within the magnesium matrix. On the other hand, grain refinement was not detected in the material. The mechanical tests demonstrate better results in tensile strength and better ductility of the material reinforced with SiC particles, with respect to the material reinforced with  $\text{Al}_2\text{O}_3$  particles. In this case, the composition of the matrix was not modified by the dissolution of the particles which could have affected negatively the mechanical properties of the material.

## Chapter 4

### Production of composites containing nanoparticles using VB2 and Transel furnaces

This chapter presents the results of the experiments performed using VB2 and Transel furnaces in order to produce nanoparticle-reinforced ceramic matrix composites (NCMMC). The Exomet project proposed the dispersion of nanoparticles of aluminium nitride (AlN) into magnesium Elektron 21. The particles produced by Tomsk University, present a size ranging from 30 to 40 nm. Three objectives are pursued with these experiments; the first is to test the capacity of the electromagnetic stirring to disperse particles of nanometric size; the second is to confirm the stability of the particles; and the third is to reveal any improvement in the mechanical properties of the alloy due to the incorporation of the particles. The samples are produced using two steps, the first consist in the introduction of the particles into the matrix material using Transel furnace. In the second step, the material obtained is re-melted in VB2 furnace and stirred using the travelling magnetic field (TMF) with the objective to enhance the dispersion of the nanoparticles. All the materials presented in this chapter were produced using the casting parameters presented in Table 39.

Max T	Time (max T) min	Cooling rate K/s	T Gradient K/m	TMF	Particles	% Weight
1073 K	60	0.20	666	15 mT	AlN	0.3-1.0

Table 39 Mg EK21 casting parameters used during experiments with Mg EK21



### 3.1 Magnesium Elektron 21 + AlN nanoparticles

Four samples of magnesium alloy EK21 containing different concentrations of aluminium nitride particles (AlN) were produced. Fig 151 presents a sample of both pure magnesium EK21 and magnesium EK21 + 0.3% AlN. The average grain sizes measured in both materials are 0.40 and 1.31 mm respectively. Fig 152 presents samples of both magnesium EK21 +1% AlN and Magnesium EK21 +1% of purified AlN. The average grain size measured in both materials is 1.5 mm. The objective pursued using purified particle is the elimination of any traces of pure aluminium mixed with the particles that could change the composition of the alloy when the particles are introduced in the matrix. All the materials containing AlN particles show an increase in grain size and present an equiaxial grain structure. Table 40 presents a summary of the grain size measurements performed.

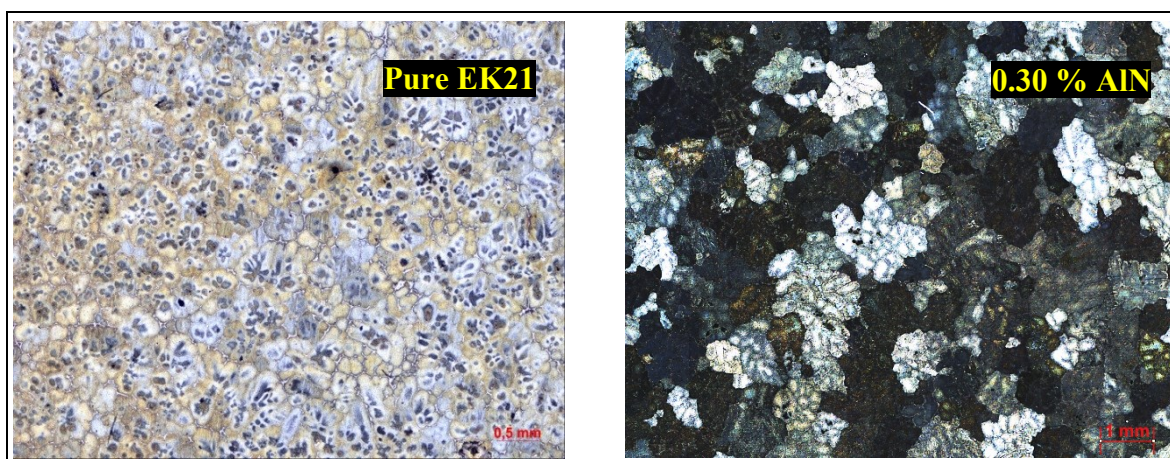


Fig 151 Pure Mg Ek21 and Mg EK21 0.3% AlN particles

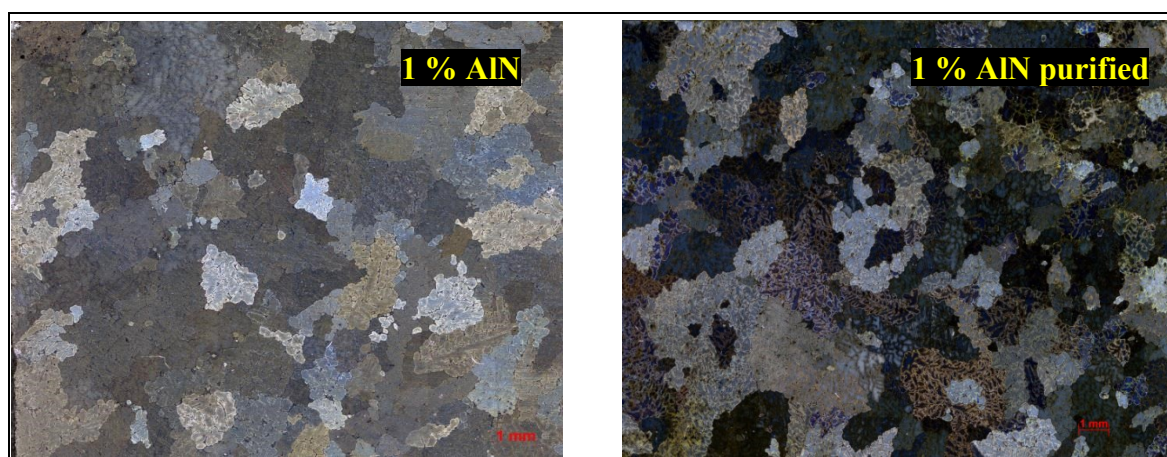


Fig 152 Mg EK21 1% AlN and Mg EK21 1% AlN purified

Measurement	Pure	0.3%	1%	1% purified
Mean grain area (mm <sup>2</sup> )	0.093	1.67	1.08	1.12
Mean grain size (mm)	0.40	1.31	1.54	1.55
Minimum /maximum grain area (mm <sup>2</sup> )	0.03/0.19	0.43/2.9	0.22/2.47	0.2/4.06
Minimum /maximum grain length (mm)	0.23/0.63	0.36/2.9	0.66/2.89	0.62/3.49
Standard deviation (area)	0.043	0.47	0.71	0.87
Standard deviation (grain size)	0.098	0.68	0.58	0.70
Number of grains measured	45	21	35	54

Table 40 Mg EK21 + AlN particles grain size measurements

The evolution of the average grain size measured on the samples of magnesium Elektron 21 containing different percentages of AlN nanoparticles is summarized in Fig 153.

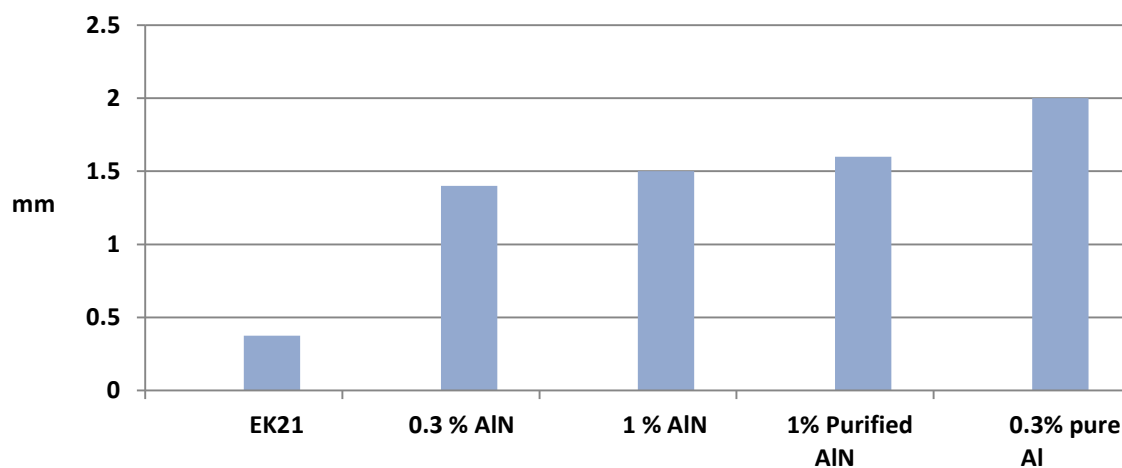


Fig 153 Summary grain size Mg EK21 with different percentages of AlN particles

The analysis performed using optical microscopy reveals many zirconium particles within the grains as shown in Fig 154. The samples also exhibit agglomerates of AlN particles in the intergranular areas, shown in Fig 155.

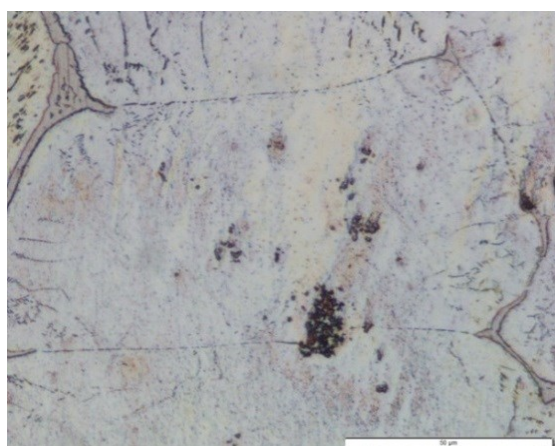


Fig 154 Mg EK21 - 0.3 % scale 1mm

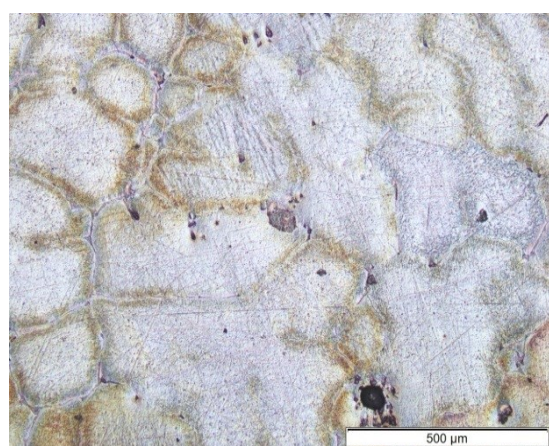


Fig 155 Mg EK21-1% AlN scale 50µm



### 3.1.1 SEM/EDS analysis of magnesium EK21 containing AlN particles

This section presents the results obtained from SEM, EDS and X-ray spectrometry analysis performed on samples of magnesium EK21 containing different amounts of AlN nanoparticles. SEM microscopy, used to reveal the microstructure and detect particle rich areas in the alloy, is used in combination with EDS mapping and X-ray spectrometry in order to confirm the present of the different elements and compounds in the material.

#### Magnesium EK2 with 0.3% in weight of AlN nanoparticles

The EDS mapping of a sample of magnesium EK21 containing 0.3% in weight of AlN particles is presented in Fig 156. The elements were detected in the area presented in the SEM image obtained with secondary electrons. The last element map presented in green colour shows traces of aluminium inside a zirconium rich area. This aluminium is not present in the original composition of the alloy and therefore, its presence should be related to the particles incorporated in the alloy.

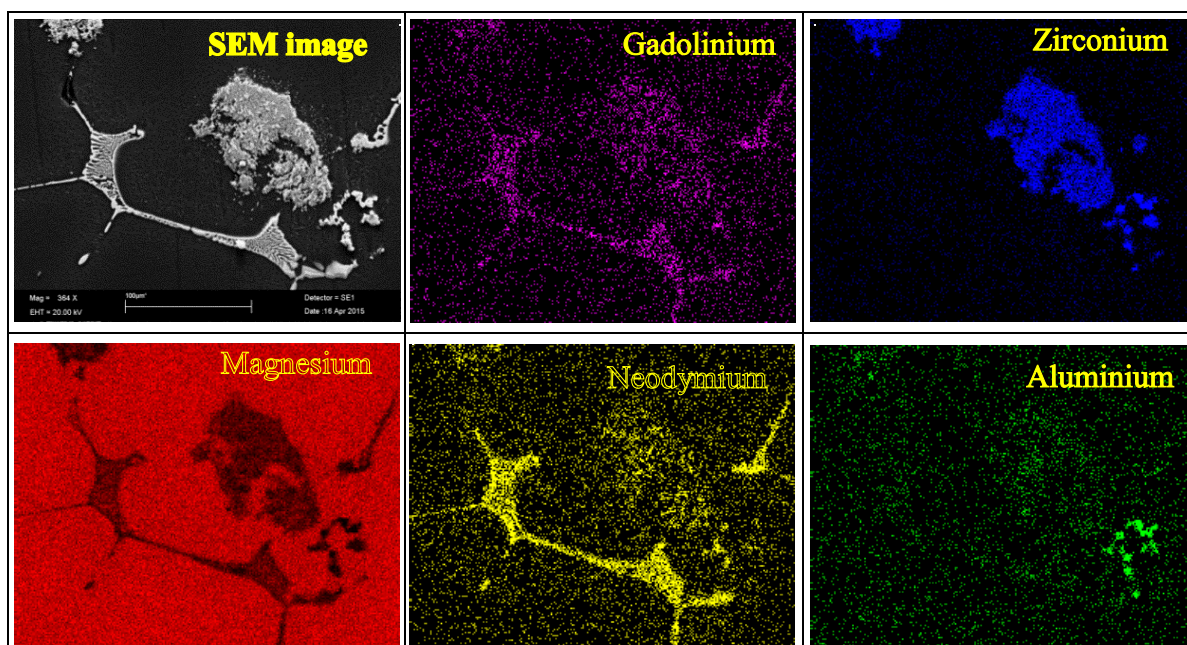


Fig 156 EDS Mg EK21 0.3 % AlN

**Magnesium EK21 with 1% in weight of AlN nanoparticle**

The results of SEM/EDS mapping performed on magnesium EK21 containing 1% in weight of AlN nano particles is presented in Fig 157. In this case, the same elements were detected but aluminium was present in the  $\beta$  phase rich in gadolinium and neodymium.

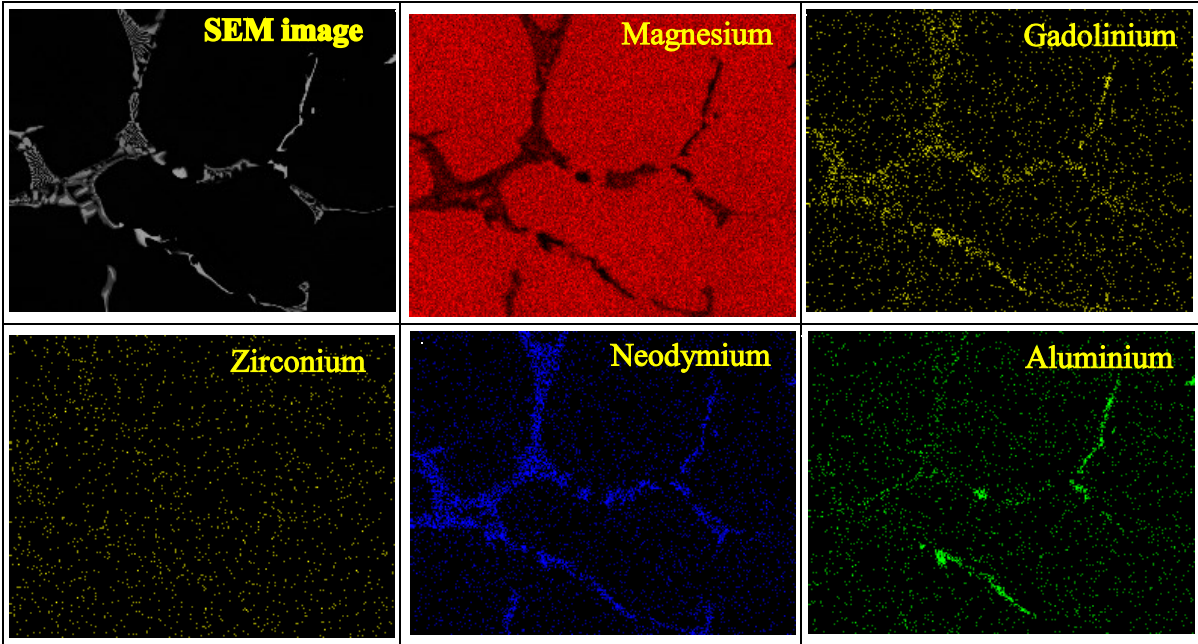


Fig 157 EDS Mg EK21 1% AlN particles

X-ray spectrometry was performed to analyse the eutectic area presented in Fig 158. The X-ray spectrums obtained shows two types of precipitates in the eutectic, a precipitate rich in magnesium and a precipitate rich in aluminium.

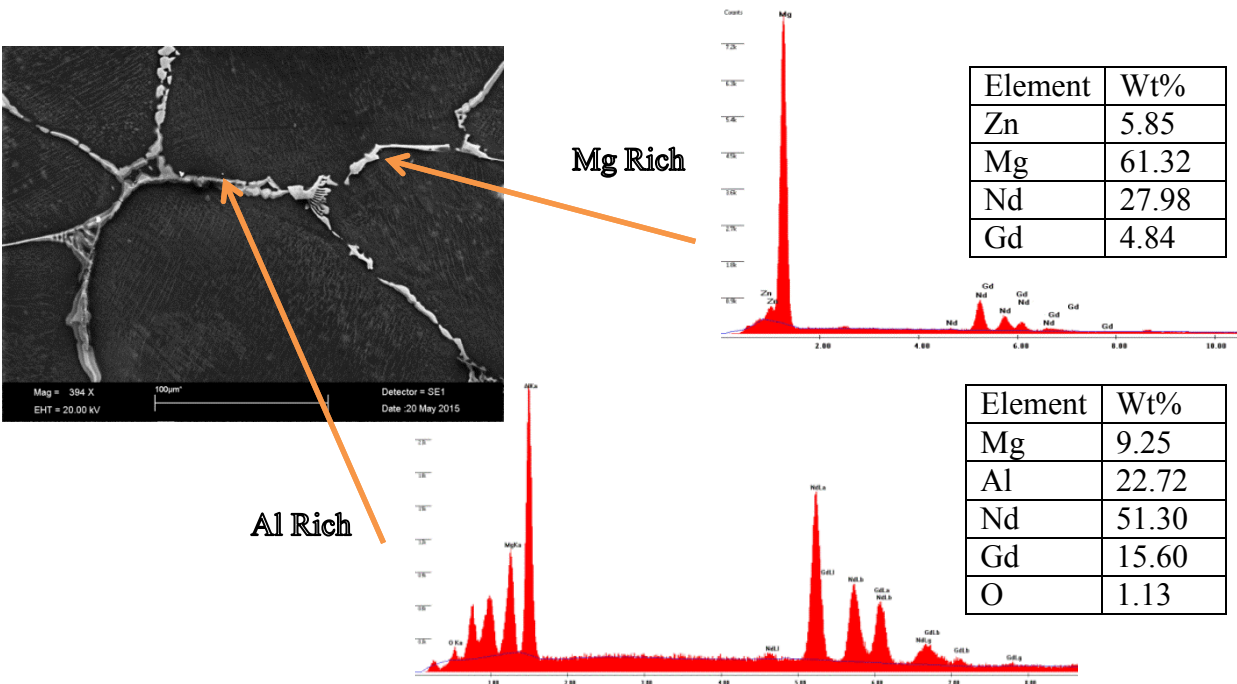


Fig 158 SEM analysis and spectrometry of Mg EK21 1% AlN

EDS analysis presented in Fig 159 was obtained from a zirconium rich area of the material reinforced with 1% of AlN nanoparticles. The analysis shows traces of aluminium next to the zirconium present inside the  $\alpha$  Mg matrix. These particles are identified as AlZr using X-ray spectrometry in Fig 160.

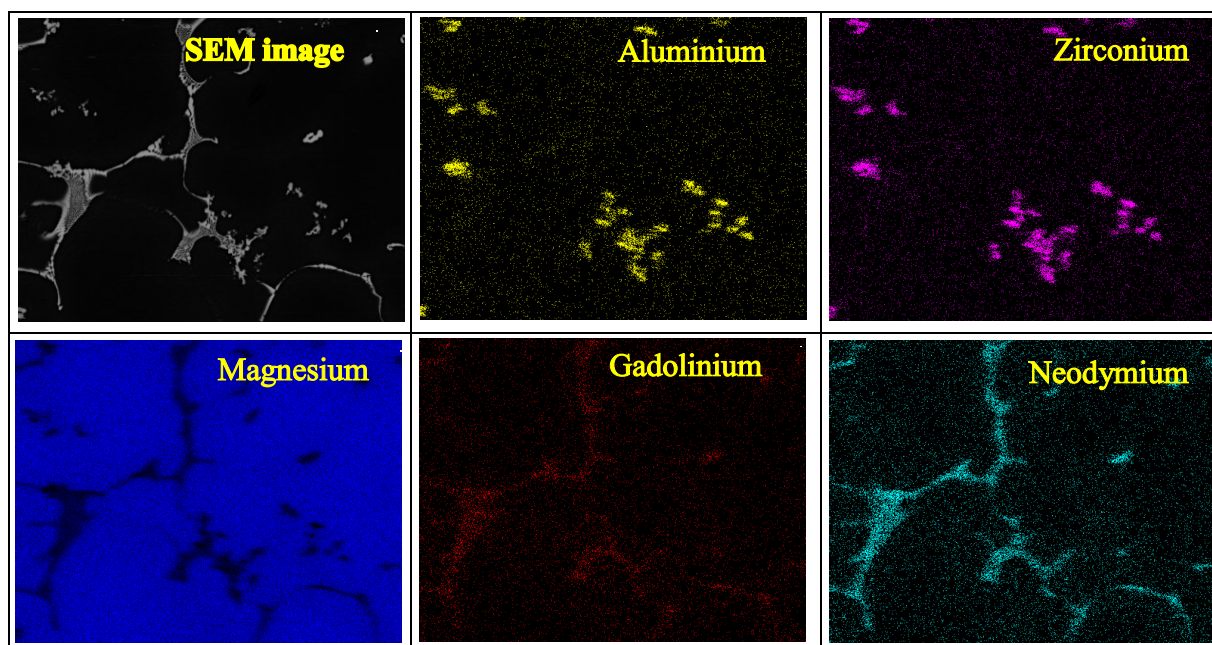


Fig 159 EDS analysis of Mg EK21 1% AlN

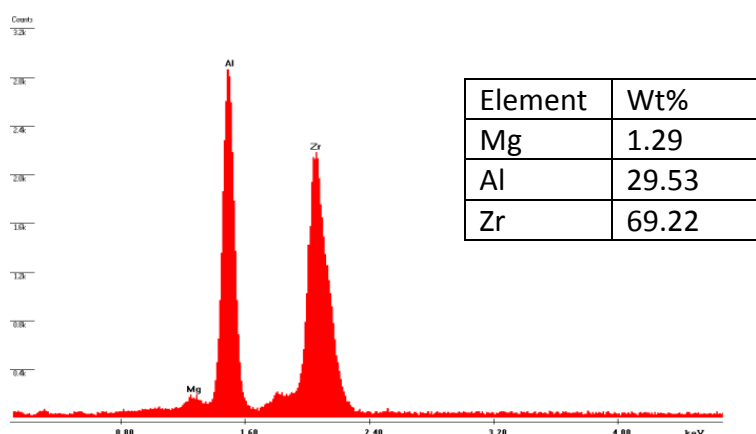


Fig 160 X-ray spectrometry AlZr particle

The SEM/EDS analysis performed on samples of magnesium EK21 0.3% and 1% in weight of AlN nanoparticles, indicates that certain amount of aluminium was released into the magnesium matrix during the process of the material. The aluminium detected in the alloy could have been introduced as impurity within the nanoparticles, or be a reaction product obtained from the reaction between the particles and magnesium.

### 3.1.2 Thermodynamic analysis

The analysis performed using SEM/EDS shows traces of aluminium in the intermetallic phase and forming AlZr intermetallic compound within the magnesium matrix. These results suggest that particles chemically react with the different elements present in the alloy. In order to determine the reactivity of the particles with the magnesium EK21 matrix, the equilibrium reactions between the particles and magnesium are calculated using the thermochemical software FactSage. The first calculation is performed at a temperature of 1073 K adding 1 % in weight of AlN nanoparticles in the alloy composition, and an argon atmosphere at a pressure of 1 bar. Table 41 presents the constituents used to perform the calculations.

Stream Constituents	Zr	AlN	Ar	Mg	Gd	Nd
<b>Amount/gram</b>	0.49	1	10	1	1.2	2.7

Table 41 Constituents used for thermodynamic calculations

The result of the calculation, presented in Table 42, indicates that 36 % of the particles are dissolved releasing and equivalent of 23 % of their weight in pure aluminium. The table also presents intermetallic compounds containing aluminium such as AlGd and AlNd<sub>2</sub> predicted in the equilibrium.

Constituents	Mg <sub>2</sub> Nd_Mg <sub>2</sub> Re_ Mg <sub>2</sub> Nd(s)	AlGd(s)	ZrN_(s)	AlN	AlNd <sub>2</sub> (s)	Nd_Solid- A(s)
<b>Equilibrium gram</b>	3.17	1.4	0.922	0.64	0.359	0.092

Table 42 Constituents at thermodynamical equilibrium

Samples of magnesium Elektron 21 + 1 % AlN were analysed using X-ray diffraction (XRD). The results presented in Fig 161 confirm the presence of AlNd<sub>2</sub>. The other compounds predicted in the equilibrium were not detected in the samples analysed.

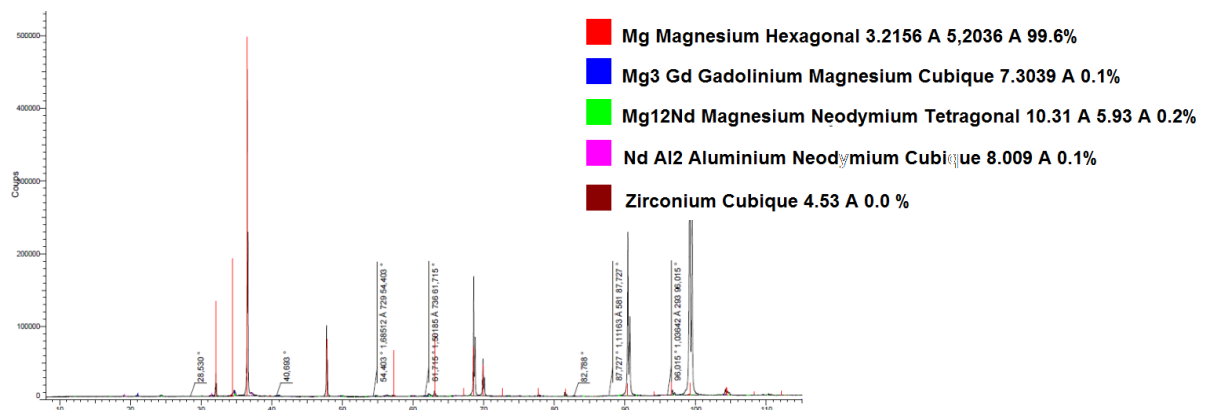


Fig 161 XRD of magnesium EK21 + 1% AlN

A second thermodynamic analysis was performed using the same alloy composition and casting conditions, but in this case the AlN particles were substituted by the equivalent amount of aluminium introduced in the alloy by the dissolution of the particles as calculated in the first thermodynamic analysis. The amount was approximated to 0.3 % in weight of pure aluminium. Table 43 and 44 present the constituents used to perform the calculations and the constituents present at the equilibrium respectively. The results indicate that 100% of the aluminium will be transformed into compounds containing rare earths or zirconium.

Stream Constituents	Zr	Al	Ar	Mg	Gd	Nd
Amount/gram	0.49	0.3	10	1	1.2	2.7

Table 43 Constituents used for thermodynamic calculations

Constituents	Mg <sub>2</sub> Nd	Mg <sub>2</sub> Re	Mg <sub>2</sub> Nd(s)	Al <sub>2</sub> Gd <sub>3</sub> (s)	Al <sub>4</sub> Zr <sub>5</sub> (s)	AlNd <sub>2</sub> (s)
Equilibrium gram		3.22		0.957	0.605	0.35915

Table 44 Constituents at thermodynamical equilibrium

### 3.1.3 X-ray tomography of pure and inoculated magnesium Elektron 21

This section presents the results of the tomography analysis performed on samples of pure and reinforced magnesium EK21. The use of this technique is destined to study the particle dispersion and the microstructure of the alloys. The analysis of the images obtained provide with data useful to calculate the average particle size present in the alloy, and the average interparticle distance.

#### Pure magnesium EK21

Two views obtained from the side and the top of a sample of pure magnesium Elektron 21 e obtained using X-ray tomography are presented in Fig 162 and Fig 163. The images displayed present two types of structures: The first, in grey colour is the intermetallic phase rich in gadolinium and neodymium; the second, visible as bright spots well dispersed within the eutectic phase, are particles of zirconium. Dark areas within the grey structures contain the  $\alpha$  magnesium phase.



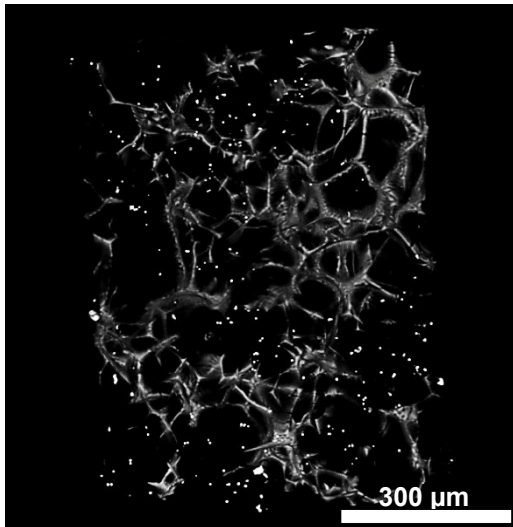


Fig 162 Mg EK21 AlN X-ray side view

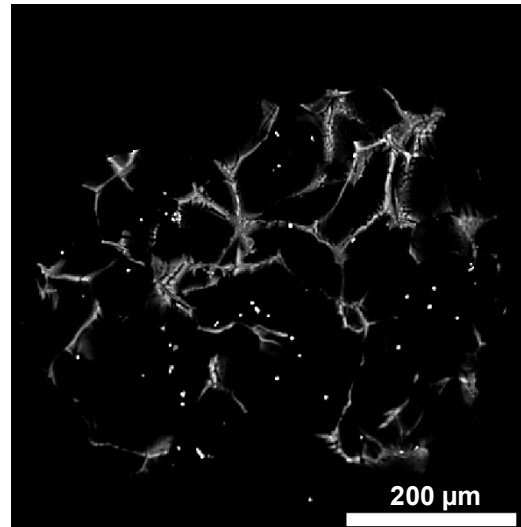


Fig 163 Mg EK21 AlN X-ray top view

### Magnesium EK21 + 1% AlN nanoparticles

The tomography analysis of a sample of magnesium Elektron 21 containing 1% in weight of AlN nanoparticles is presented in Fig 164. In this case, the intermetallic phase presents modifications in its morphology, visible as bright areas (shown in detail in Fig 165) and no traces of single zirconium particles within the alpha magnesium. EDS analysis presented in 3.1.1 showed that these bright areas in the intermetallic phase are rich in aluminium. On the other hand, agglomerates of zirconium particles within the magnesium matrix can be observed within the  $\alpha$  magnesium matrix. A top view of the sample, presented in Fig 166, presents several zirconium agglomerates as the one indicated with an arrow. Within this agglomerates, bright particles were identified as AlZr compounds. Fig 167 presents a detail view of a zirconium rich area in which several particles can be distinguished.

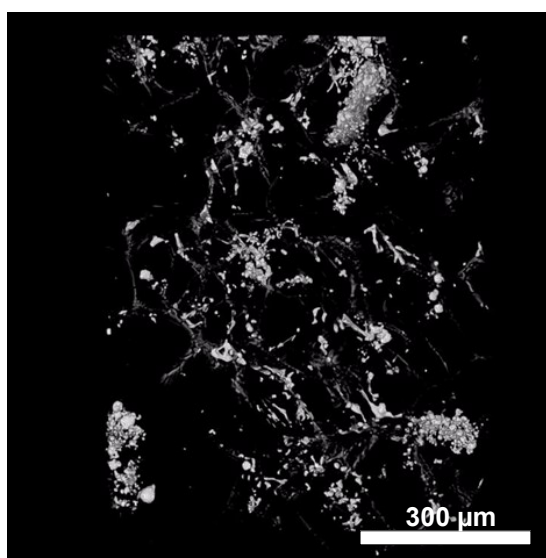


Fig 164 Mg EK21 + 1% AlN tomography

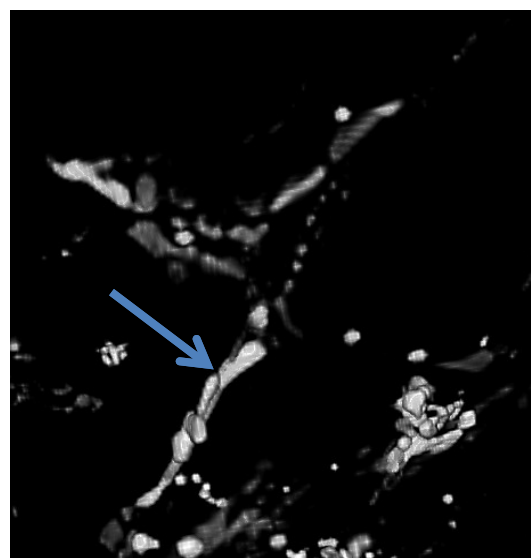


Fig 165 Detail view of  $\beta$  phase

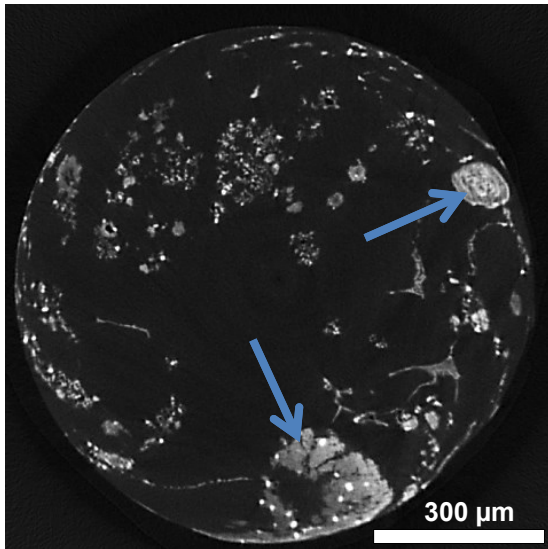


Fig 166 Top view Mg EK21 + 1% AlN

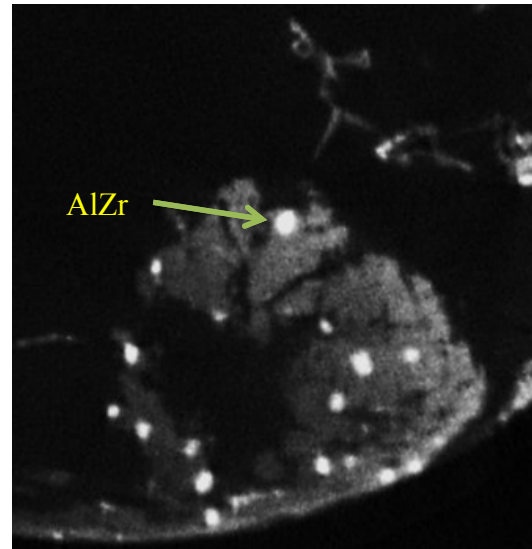


Fig 167 Detail view of zirconium rich area

A second tomography sample is presented in Fig 168. In this case, particles (agglomerates) can be seen dispersed within a single  $\alpha$  magnesium grain. The average interparticle distance and particle average volume calculated for this sample are  $30.29 \mu\text{m}$  and  $178 \mu\text{m}^3$  respectively. Considering the shape of the particles to be fairly approximated as spheres, the average size calculated is  $5.83 \mu\text{m}$ . Fig 169 displays the particle size distribution in which the particle (agglomerate) size most frequently observed is  $14 \mu\text{m}$ .

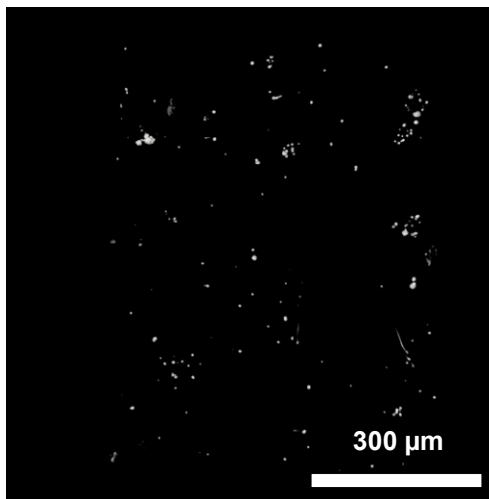


Fig 168 Mg EK21 + 1% AlN particles

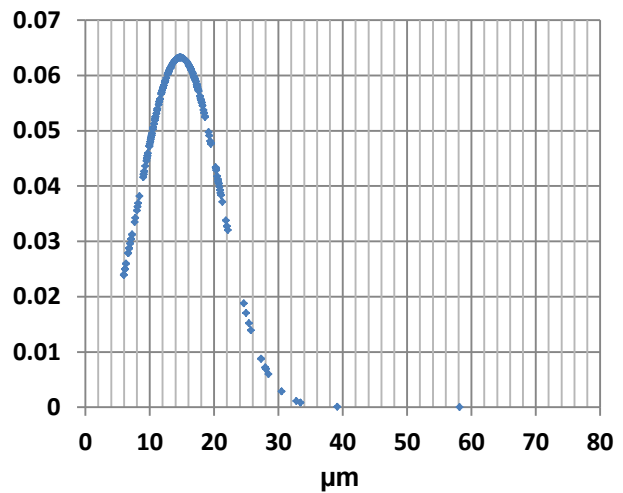


Fig 169 Particle size distribution EK21+1% AlN

### Magnesium EK21 + 0.3 % pure aluminium

The thermodynamic analysis presented in section 3.1.2 shows that approximately 36 % in weight of the particles would be dissolved in contact with the magnesium matrix. The

equivalent percentage in weight of aluminium added to the matrix in the material reinforced with 1% in weight of AlN particles is approximately 0.3 %. According to the Al-Mg phase diagram this amount of aluminium would be totally dissolved into the magnesium matrix. In order to analyse the effects in the microstructure of an equivalent amount of pure aluminium added to magnesium EK21, a sample was produced containing 0.3% in weight of pure aluminium. A sample of volume  $0.10 \text{ mm}^3$  from this material was analysed using X-ray tomography. The images obtained were used to produce a 3D view presented in Fig 170. This image presents the intermetallic gadolinium–neodymium phase in grey colour, and agglomerates of zirconium particles in white within it, indicated with a blue arrow. A detail view of one of this agglomerates revealed several cubic structures identified as AlZr intermetallic compounds. This type of intermetallic particle presents an orthorhombic crystal structure defined as cmcm schematically presented in Fig 171. The average volume of the compounds measured is  $1400 \text{ }\mu\text{m}^3$ . Not traces of aluminium were detected in the intermetallic phase.

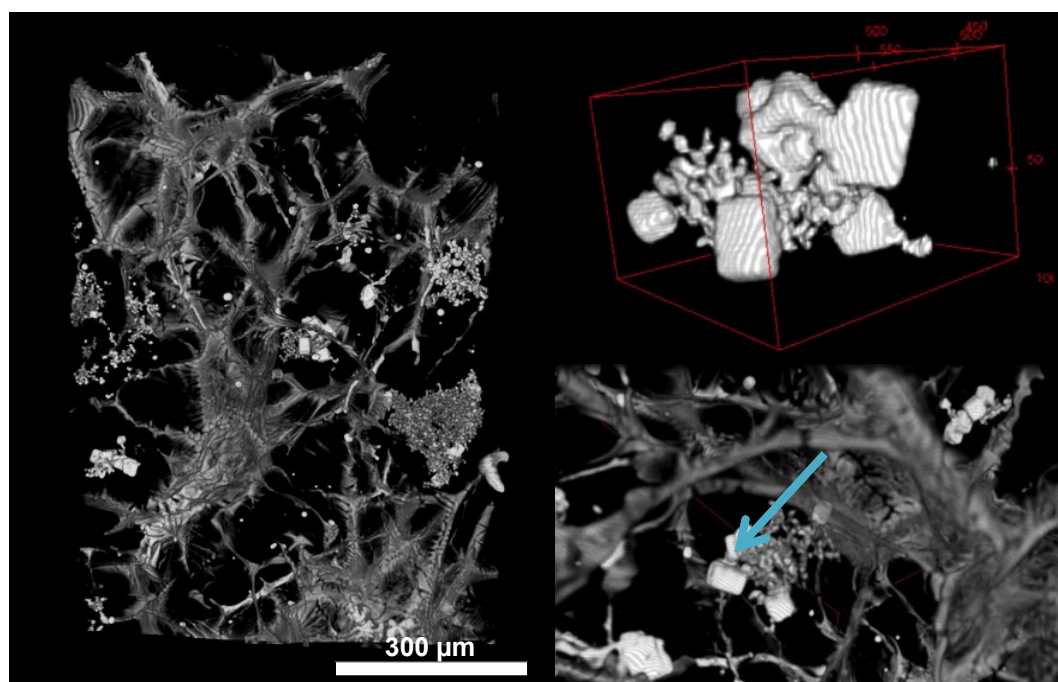


Fig 170 3D tomography of a sample of Mg EK21 0.3% aluminium

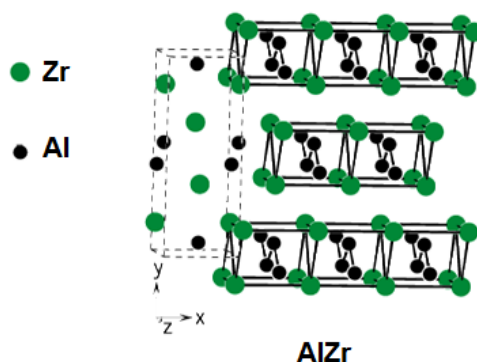


Fig 171 AlZr crystal structure

The tomographic images obtained shows no modifications in the morphology of the intermetallic gadolinium-neodymium phase, as observed in magnesium EK21 containing 1% of nanoparticles. This result suggests that the aluminium rich areas in the eutectic phase detected on samples of magnesium EK21 1% AlN could be related to the presence of AlN particles.

### 3.1.4 Estimation of mechanical reinforcement of magnesium EK21 produced by dispersion of AlN nanoparticles using the classical reinforcement theories

Improvement in the mechanical properties of magnesium EK21 containing AlN nanoparticles can be estimated by calculating the contribution of each of the mechanisms of reinforcement presented in chapter 2. Table 45 presents the parameters used to calculate the contribution of each type of reinforcement mechanism.

$d_pO$ (nm)	$d_pM$ (nm)	$G_m$ (MPa)	B (nm)	$\sigma_y$ (MPa)	$\Delta\alpha$ ( $K^{-1}$ )	$\Delta T$ (K)	$V_p$	$\lambda O$ (nm)	$\lambda$ (nm)
30	14000	16400	0.32	70	$20.63 \times 10^{-6}$	780	2	11	30000

Table 45 Typical values used to calculate the mechanisms of reinforcement

Where  $d_pO$  is the theoretical particle diameter,  $d_pM$  is the particle diameter more often observed in the studies of particle size distribution performed in the alloy of interest here,  $G_m$  is the shear strength of the matrix material in this case magnesium, B is the Burgers vector,  $\sigma_y$  is the yield strength of the monolithic matrix,  $\Delta\alpha$  ( $K^{-1}$ ) is the difference between the coefficient of thermal expansion of the reinforcement and the one for the matrix. The value of  $K^{-1}$  for AlN is  $5.27 \times 10^{-6}$  (40 to 400 °C) while for magnesium it is  $25.9 \times 10^{-6}$  (20° to 100°C).  $\Delta T$  (K) is the temperature difference between the processing and the temperature of the test (1073° – 293° therefore 780),  $V_p$  is the particle volume fraction and  $\lambda O$  is the theoretical interparticle distance calculated for a perfect mixing and  $\lambda$  is the average interparticle distance measured using X-ray tomography. The contribution of each of the reinforcement mechanisms could be predicted by summing all the contributions related to the single strengthening effects. Due to the increase of grain size measured on the materials containing AlN nanoparticles, the contribution due to the Hall Petch reinforcement has been considered negligible. Two approximations are performed in the current case; the first one takes into account a perfect dispersion of the particles with a regular size; the second one is calculated using the data available from tomography on particle size and dispersion. Table 46 presents a summary of the calculus performed using the different strengthening mechanisms responsible for the reinforcement of the alloy.

Reinforcement mechanism	Hall Petch	Orowan	Coefficient of Thermal Expansion $\Delta\sigma_{CTE}$	Load Transfer $\Delta\sigma_{load}$	$\Delta\sigma$
Theoretical	-----	238.6	3.81	0.7	243.11
Tomography data	-----	0.22	0.23	0.7	1.15

Table 46 Contribution of each mechanism of reinforcement

The calculations show that theoretical  $\Delta\sigma$ , which represents the improvement of the yield strength of the reinforced material with respect to the original one, differs extraordinarily with respect to  $\Delta\sigma$  calculated using the data obtained from X-ray tomography. The small value obtained using the real data indicates that no modifications in yield strength should be detected in the material containing particles. However, it should be also considered that the maximum resolution of the tomographic images is 640 nm. Particles smaller than this value, would be undetected during the analysis. In consequence, a certain level of uncertainty should be accepted when considering the influence of the particles in the reinforcement of the matrix.

### 3.1.5 Hardness and microhardness tests

The hardness test performed on samples of magnesium EK21 reinforced with nanoparticles serves to evaluate the influence of the nanoparticles in the resistance of the alloy to deformation, and also to determine the level of porosity present in the alloy. In addition, microhardness test can reveal the presence of nanoparticles within the alpha magnesium which could reinforce the matrix. The hardness curves calculated on samples of magnesium EK21 were produced measuring hardness on 260 points along a vertical cross section, defined from the central axis of the samples, following the procedure explained in chapter 2. The hardness curves obtained from the measurements performed on samples of magnesium EK21 are presented in Fig 172. According to this graph, hardness on the sample reinforced with 1% AlN particles is slightly higher than the one measured on the pure alloy, and the one measured on the material reinforced with 0.3 % in weight of AlN particles. The latest alloy also presented a high level of porosity. Finally, the material containing 0.3% in weight of pure aluminium presents the lowest hardness value with respect to the rest of the materials tested

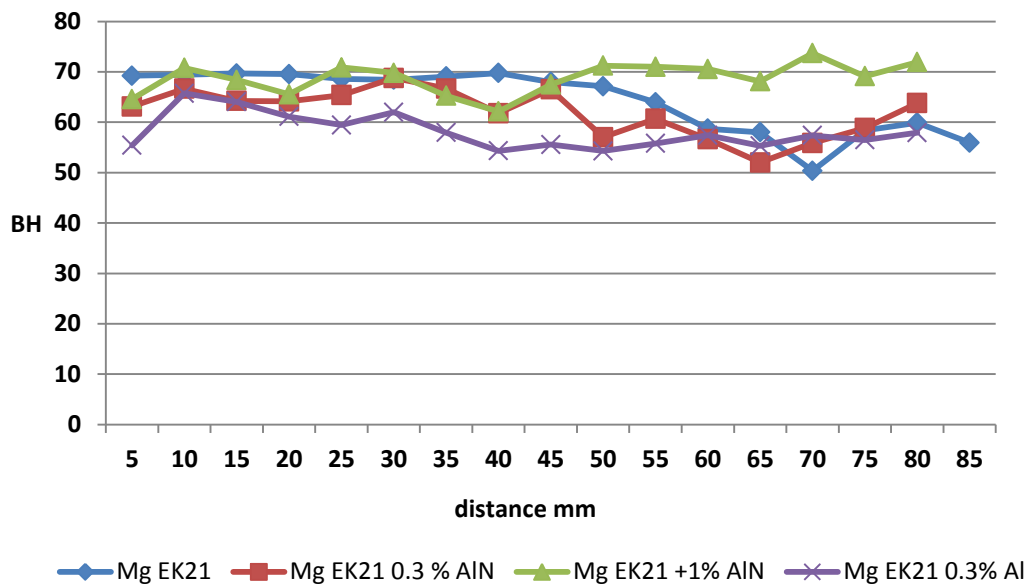


Fig 172 Mg EK21 Hardness measurements

The average microhardness values were calculated using 50 measurements performed on each specimen obtained from VB2. The measurements were taken inside the grains of samples obtained from areas near the central axis and edge of each specimen. The microhardness values obtained were similar in all the materials, but magnesium EK21 +1 % AlN showed a slight highest value on the samples taken from the external area. A summary of the measurement performed is presented in Fig 173.

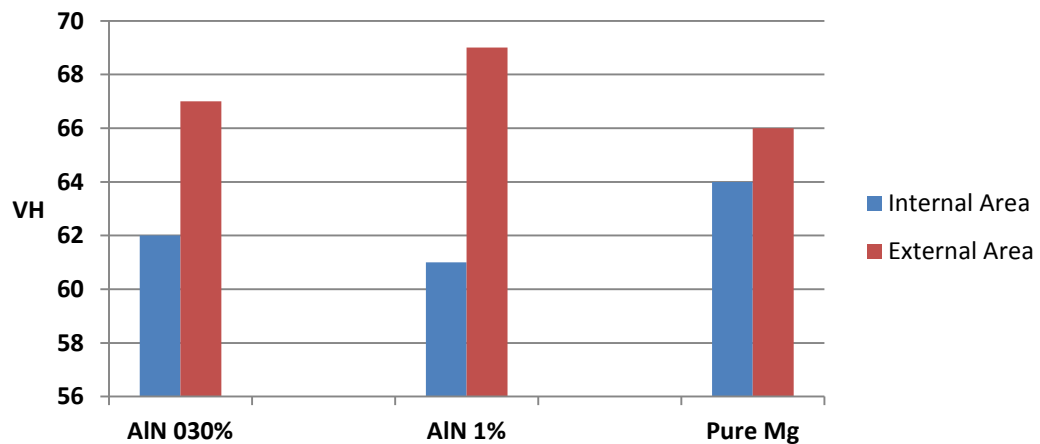


Fig 173 Mg EK21 Microhardness measurements

### 3.1.6 High temperature compression tests

The improvement of the mechanical properties at high temperature of materials reinforced with nanoparticles is an important area of study in the Exomet project. Hot compression test is a mechanical characterization technique used to analyse the behaviour of materials at high



temperatures. The analysis of the data obtained from compression tests performed at high temperature can provide with information such as creep resistance and flow behaviour of a material. Magnesium alloy Elektron 21 is characterised by its good creep resistance at high temperatures. The dispersion of nanoparticles into this alloy could improve this mechanical property by different strengthening mechanisms already explained in chapter 1. This section presents the results of hot compression tests performed on samples of pure magnesium Elektron 21 and magnesium Elektron 21 reinforced with 1% in weight of AlN nanoparticles. The first part of the section is dedicated to study the flow behaviour of samples of pure and reinforced material under compression stress. The tests are performed at a constant temperature of 350 °C. The results obtained from the tests serve to determine the influence of the particles in the creep resistance of the alloy. The second part of the section is dedicated to study the flow behaviour of samples of magnesium Elektron 21 reinforced with nanoparticles under compression stress at temperatures of 350, 400 and 450°C. In this case, the objective pursued with the tests is to determine a constitutive equation useful to describe the flow behaviour of this type of material at different temperatures. The samples tested are cylinders 4.5 mm in height and 3 mm in diameter obtained from a standard specimen obtained from VB2 furnace. Table 47 presents the settings used during the compression tests performed. Detailed information about the compression test machine can be found in section 1.9.7.

<b>Absolute strain to reach</b>	0.1	0.15	0.2	0.25	0.3	0.35	0.4	0.45	0.5
<b>Strain rate (1/s)</b>	0.001	0.0002	0.004	0.001	0.0008	0.002	0.004	0.008	0.01
<b>Time between two measurements (step of 0.1s)</b>	0.2	1	0.5	0.2	0.25	0.1	0.1	0.1	0.1

Table 47 Strain rates applied during hot compression tests

The course of temperature changes during the heating until reaching the temperature of 350°C is presented in Fig 174.

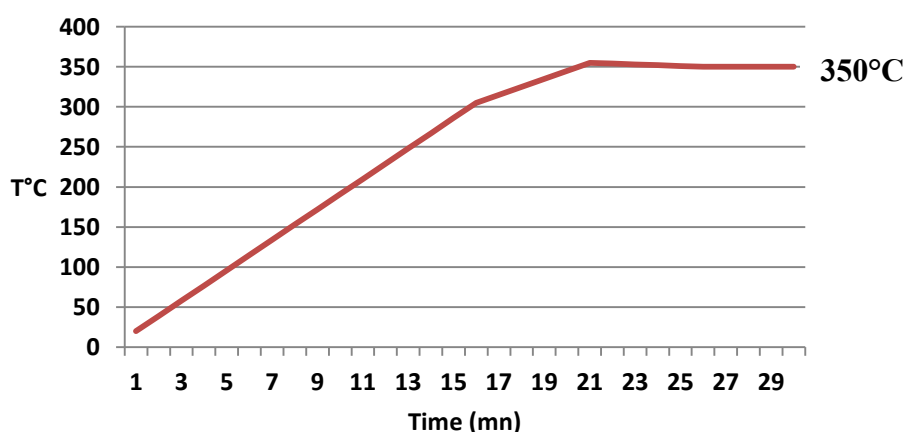


Fig 174 Heating process in hot compression test at 350°C

According to the curve, the material at room temperature is heated until reaching 305°C at a heating rate of 19°C per minute. After reaching this temperature, the heating rate is decreased to 10°C per minute until the temperature reach 355°C. Afterwards, the temperature is decreased at a rate of 1.5 °C per minute until reaching 350°C, and it is stabilized at this temperature. The compression test is performed after 10 minutes from reaching 350°C. The stress-strain curve resulting from the initial loading into the plastic range can be approximated using the power law equation proposed by Norton (35) to describe creep under low stresses [164]. This equation relates flow stress to strain rate when the plastic deformation is so large that the elastic strain can be neglected,

$$\dot{\epsilon} = K\sigma^n, (35)$$

where  $\dot{\epsilon}$  is the steady creep rate,  $\sigma$  is the flow stress required for plastic deformation at the given temperature, K is a constant which depends on the material (Young's modulus, diffusion coefficient, grain size, activation energy, burger vector) and n is the strain hardening exponent which is linked to deformation mechanisms such as dislocation climb, diffusion or grain boundary sliding. The Norton power law equation is used to determine the creep threshold of the materials studied following the heating process presented in Fig 175. The compression curves obtained are depicted in Fig 175.

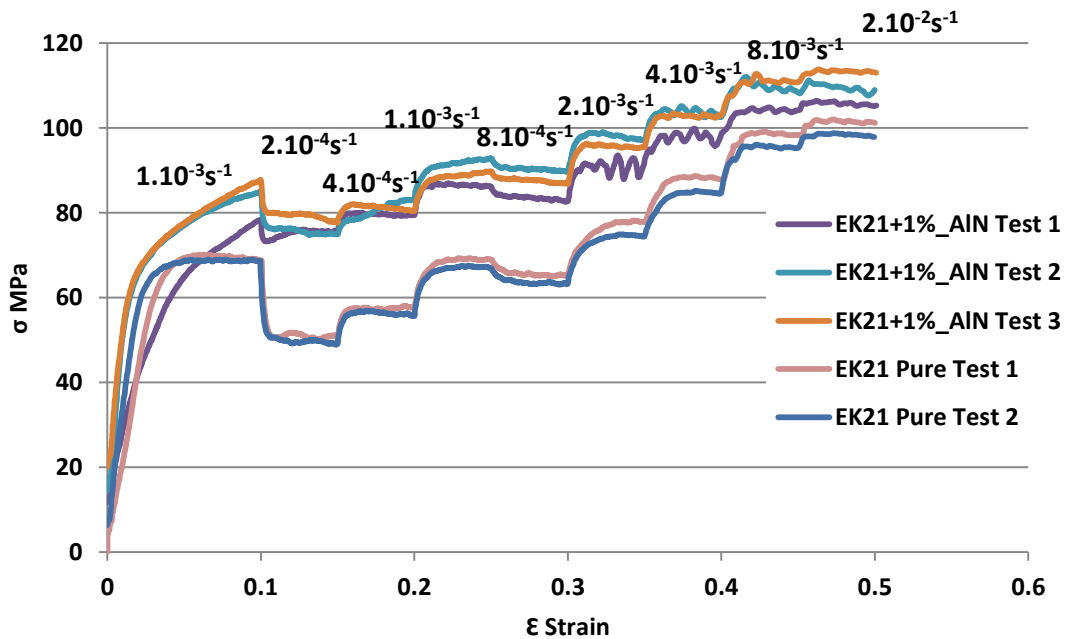


Fig 175 Hot compression test curves Mg EK21 and Mg EK21 + AlN 350°C

It can be observed that on the first part of the curves, the flow stress increases rapidly whereas in the second part it increases at lower rate. The increment of flow stress observed at the beginning of the test is commonly explained by the work hardening, also called strain hardening, produced in an alloy when is subjected to high plastic deformation. This

mechanism of reinforcement is based on the interaction of dislocations present in the material which acts as obstacles to the movements of other dislocations. As the dislocation density increases due to the plastic deformation, the flow stress increases. On the other hand, the second part of the curve is characterised by a plateau. This part of the curve can be explained as the point of equilibrium between work hardening and the relaxation effect also called dynamic recovery [165] produced in the material. The energy stored in the material is lowered by dislocation motion during dynamic recovery according to two primary processes: the annihilation of dislocations and the rearrangement of dislocations into lower energy configurations. The dynamic recovery is facilitated by the high temperature applied during the test which enhances dislocation motion. The test shows that flow stresses on the material reinforced with AlN nanoparticles increases by 20% with respect to the material free of nanoparticles at least in the early time. The results are found to be reproducible in both types of materials. The dynamic recovery also presents a great difference between materials. During dynamic recovery the flow stresses displayed on the first part of the curve of the reinforced material decrease by approximately 12% with respect to the peak value, whereas the unreinforced material presents a difference of approximately 25%. The curves of the EK21-AlN samples present a serrated flow behaviour at the end of the test. This type of behaviour is related to the moving of dislocations which interact with precipitates impeding their motion. The movement of the dislocations affected by their stopping and release due to their pinning with precipitates corresponds to the stress fluctuation depicted as a serration in the stress-strain curve [166]. Plotting the mean value of the flow stresses of each plateau depicted in the curves, which is considered as a constant or steady state flow stress, against the strain rate in a logarithmic scale the graph presented in Fig 176 is obtained. The data displayed is used to find the threshold at which no creep is detected [167].

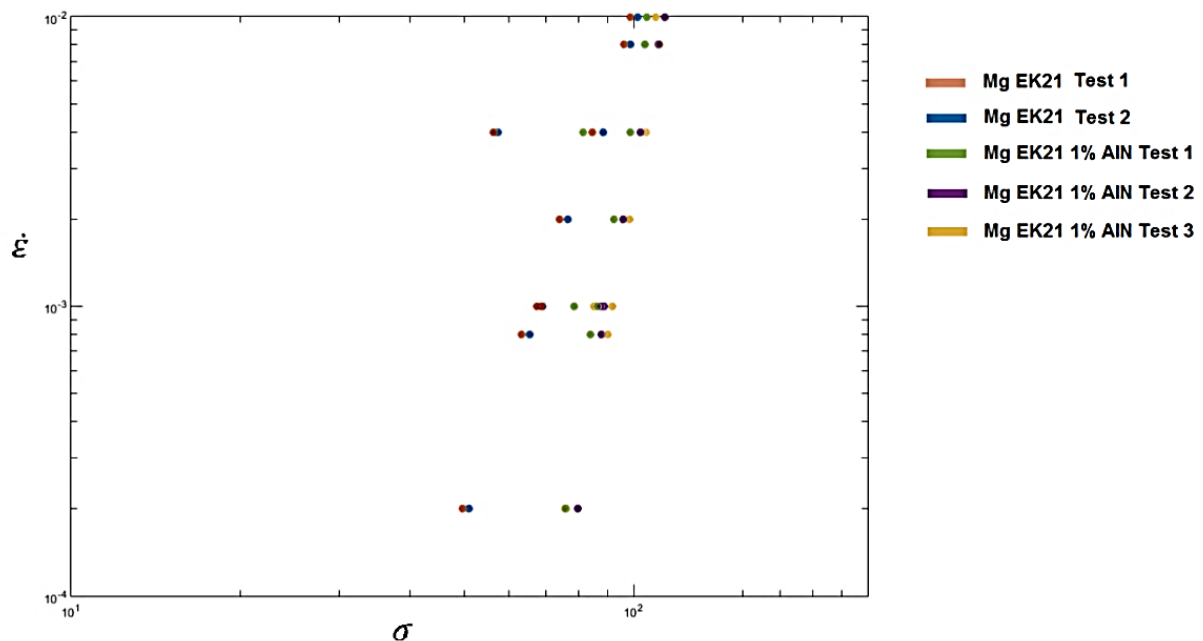


Fig 176 Relationship between strain rate  $\dot{\epsilon}$  vs stress  $\sigma$

In order to determinate this threshold; the data can be fitted using the Norton equation (eq 35) introduced at the beginning of the section. This can be done if the data follow a linear trend, which in the current case is not observed in all of the tests performed. In order to fit this data, a threshold stress parameter  $\sigma_t$  has been added to the Norton equation obtaining the following expression:

$$\dot{\epsilon} = k(\sigma - \sigma_t)^n, (36)$$

The parameter  $\sigma_t$  can be considered as a stress threshold value below which no creep is detected. The calculations performed to fit the curves using this expression, involve the parameter  $n$  fixed to a value of 5. According to different references a  $n$  value ranging from 3 to 7 indicates that climb-controlled dislocation creep is the dominant deformation process [168][169]. The fitted curves are depicted in Fig 177 and a summary of the results is presented in table 48.

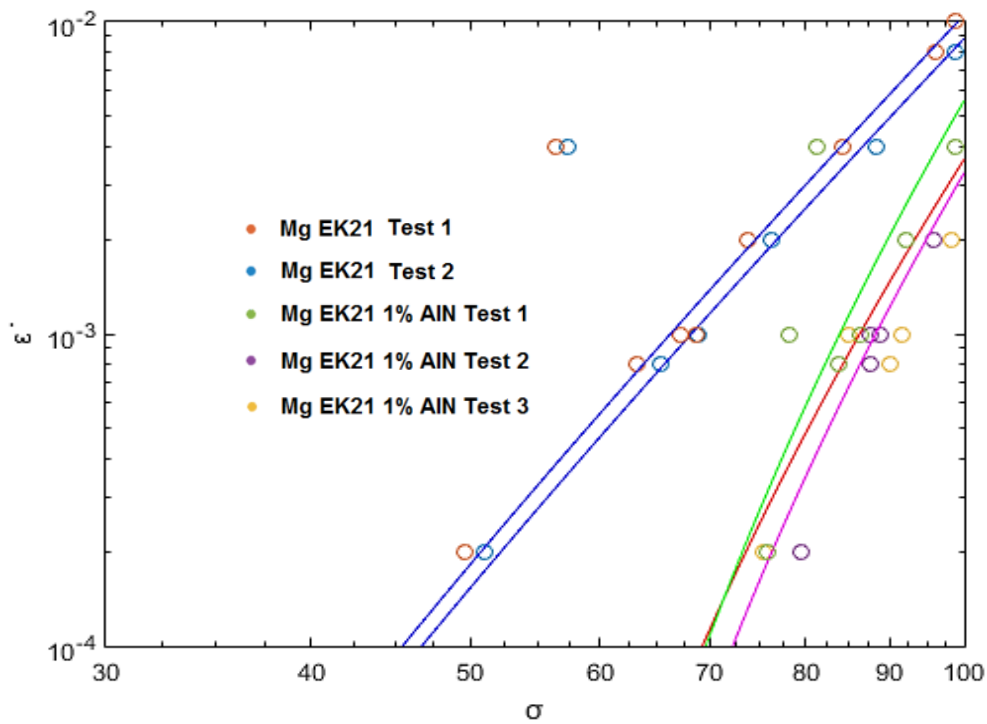


Fig 177 Fitted compression curves

Material	k	$\sigma_t$
Mg EK21test 1	1.49e-12	10
Mg EK21test 2	1.78e-12	10
Mg EK21 1% AlN 1	4.67e-12	40
Mg EK21 1% AlN 2	7.18e-13	45
Mg EK21 1% AlN 3	1.11e-13	45

Table 48 Fitting parameters

The values presented in table 48 shows a significant enhancement in creep properties of the material reinforced with AlN nanoparticles

### **Magnesium Elektron21 + 1% AlN nanoparticles at different temperatures**

The flow stress is the most basic parameter for characterizing plastic deformation properties of metals and alloys, and serves to determine the load and energy needed during their plastic deformation [4]. The Exomet project aims to develop manufacturing technologies to produce materials reinforced with nanoparticles. The manufacturing of these materials could benefit from the knowledge of their flow behaviour obtained using hot compression test. This section presents the results of hot compression tests performed at different temperatures on samples of magnesium Ek21 1% AlN. The correlation between hot deformation parameters such as strain rate, deformation temperature and flow stress can be described by hyperbolic-sine Arrhenius type equation (37) [170].

$$Z = \left( \dot{\epsilon} \exp\left(\frac{Q}{RT}\right) \right) = A[\sinh(\alpha\sigma)]^n, \quad (37)$$

where  $Z$  is the Zener–Hollomon parameter which is used to describe high temperature creep strain of materials [171],  $Q$  is the activation energy of deformation which is the minimum energy required for continuing deformation during hot processes, and it is a useful parameter used to determine the hot workability of a metal,  $R$  is the universal gas constant,  $A$  is a material constant,  $\alpha$  is an adjustable parameter and  $n$  is the stress hardening exponent. The parameters of the Arrhenius equation used to describe the flow behaviour of a material can be obtained using thermomechanical tests such as hot compression tests [105]. Hot deformation process is similar to elevated temperature creep, having the pronounced characteristic of the strain rate being controlled by the thermal activation process, which follows the Arrhenius equation. The flow stress curves obtained from hot compression tests can be used to study the different dynamic softening mechanisms involved in plastic deformation of reinforced materials. There are different forms of Arrhenius-type constitutive equations commonly used to describe the metal flow stresses under specific stress levels. On the other hand, the following expression is commonly applied in a wide range of stress regimes, and therefore it has been selected to describe flow behaviour in the current study:

$$\dot{\epsilon} = A [\sinh(\alpha\sigma)]^n \exp\left(\frac{-Q}{RT}\right). \quad (38)$$

This equation can be also expressed in the following form:

$$\ln(\dot{\epsilon}) = \ln A + n \ln[\sinh(\alpha\sigma)] - \frac{Q}{RT}. \quad (39)$$

The activation energy (Q) can be calculated using the following formula:

$$Q = RS_n \quad (40)$$

where S is the average slope of the lines obtained from the plot of  $\ln[\sinh(\alpha\sigma)]$  against  $1/T$ . The parameter  $n$  can be obtained from the inverse of the slope in the plot of  $\ln |\sigma|$  versus  $\ln |\dot{\epsilon}|$ . With the latter considerations, Eq (40) becomes:

$$Q = R \left( \frac{\partial \ln \sinh \alpha \sigma}{\partial \frac{1}{T}} \right) \left( \frac{\partial \ln \dot{\epsilon}}{\partial \ln \sinh \alpha \sigma} \right)_T \quad (41)$$

The hot compression tests are performed with the objective of measuring the flow stress behaviour presented by magnesium EK21 reinforced with 1% AlN particles at different temperatures. The test was performed in air at temperatures ranging from 350°C to 450 °C. The course of temperature changes during the heating at each testing temperature is presented in Fig 178.

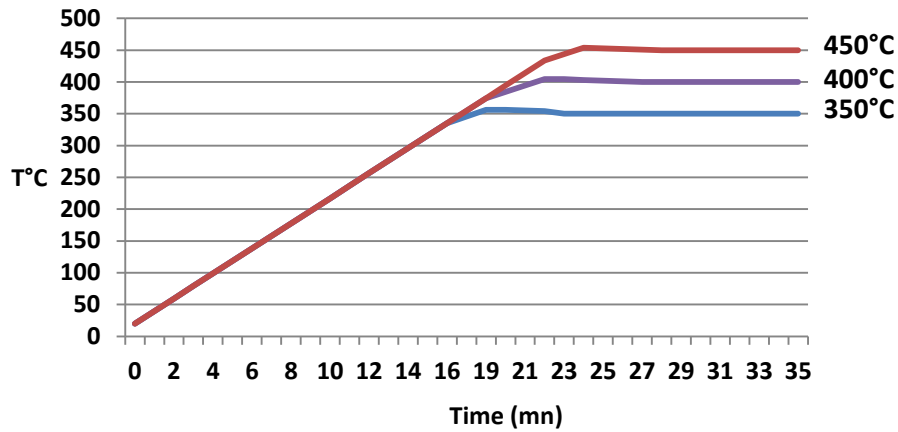


Fig 178 Heating process for hot compression tests

The first material tested at 350°C follows the same heating process presented in Fig 174. In the case of the material tested at 400 °C, the heating rate applied at the beginning of the heating process is 19°C per minute until reaching a temperature of 375°C. After reaching this temperature, the heating rate is decreased to 10°C per minute until the temperature reach 404°C. Afterwards, the temperature is decreased at 1.5°C per minute until reaching 400°C, and it is stabilized at this temperature. The compression test is performed after 10 minutes from reaching 400°C. Finally, the material tested at 450°C is subjected to a heating process applying a heating rate at the beginning of the process of 19°C per minute. Once the temperature reaches 433°C, the heating rate is decreased to 10°C until reaching 453°C. Afterwards, the temperature is decreased at a rate of 1 °C per minute until reaching 450°C, and it is stabilized at this temperature. The compression test is performed after 10 minutes from reaching 450°C. The stress curves of the compression tests of samples of Mg EK21 +



1% AlN nanoparticles performed at different temperatures are presented in Fig 179. The data obtained from the curves is used to obtain the material constants  $n$ ,  $\alpha$  and  $A$  found in the hyperbolic-sine Arrhenius equation.

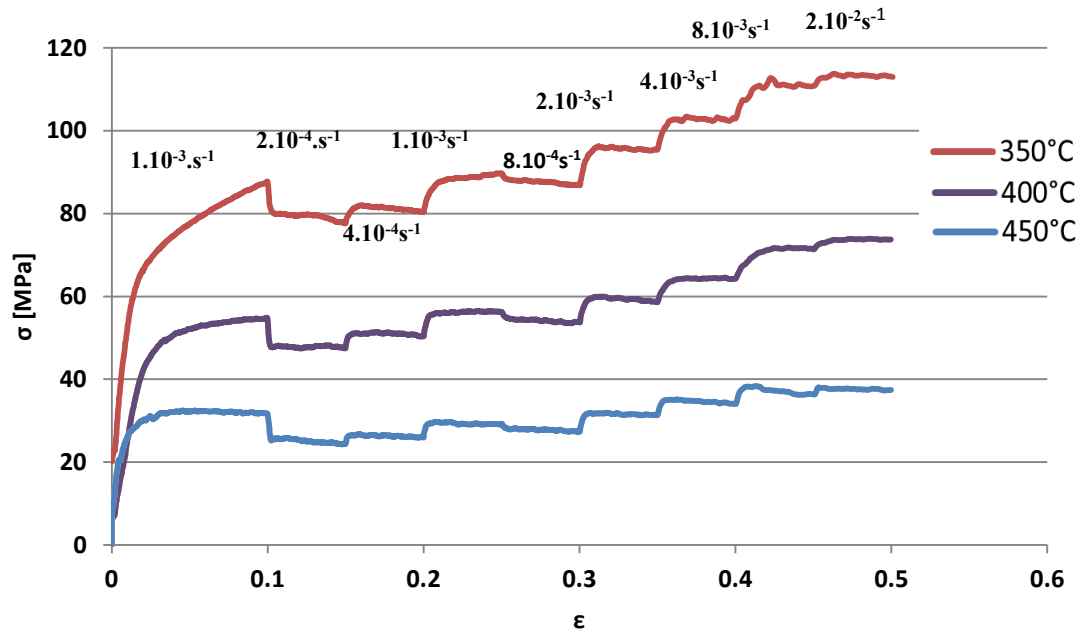


Fig 179 Hot compression test curves of Mg EK21+1% AlN at different temperatures

The curves depicted presents an increasing flow stress when high strain rates are applied, particularly when the test is performed at lower temperatures. Using the data obtained from the curves, the parameter  $n$  can be obtained by plotting  $\ln |\dot{\epsilon}|$  versus  $\ln |\sigma|$  as presented in Fig 180. The parameter  $\sigma$  is the mean flow stress value obtained from each corresponding plateau obtained at different strain rates on each curve. This is considered as a steady state or a constant flow stress value. Using the slope of each curve presented in the graph three values of  $n$  parameter are obtained: 9 for the test performed at 350°C, 6 and 3.2 for the tests performed at 400 and 450°C respectively.

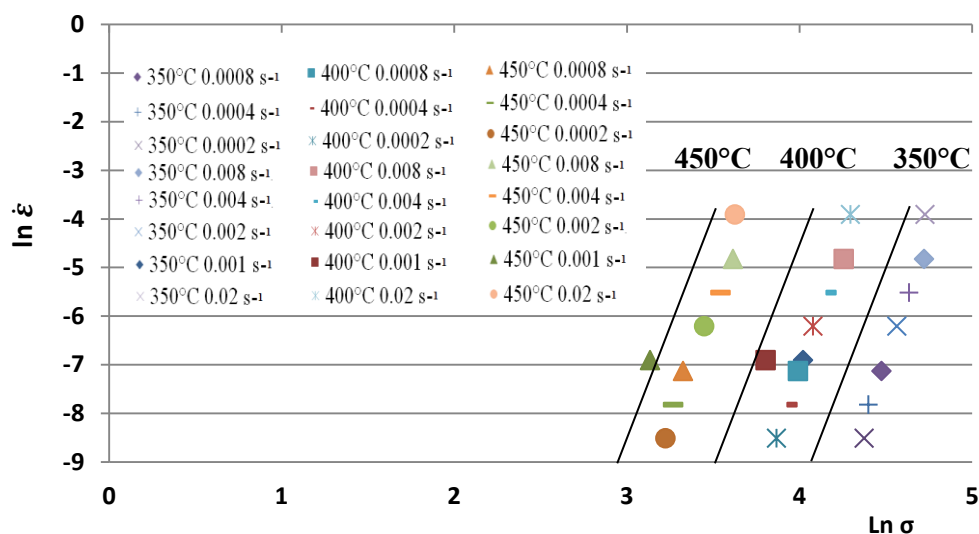


Fig 180 Relationship between  $\ln |\dot{\epsilon}|$  vs  $\ln |\sigma|$

The material constant  $\alpha$  can be calculated dividing the constant  $\beta$  over the average value of  $n$ . This constant is obtained from the average slope of the curves obtained from the plot of  $\ln |\dot{\epsilon}| / |\sigma|$  presented in Fig 181. The  $\beta$  coefficient is found to be 0.183 MPa which means a parameter  $\alpha$  of 0.025 MPa. Finally, the activation energy used to determine the minimum energy required to continue deformation is calculated from the average slope of the curves obtained from the plot of  $\ln (\sinh(\alpha\sigma)) / 1000/T$  presented in Fig 182.

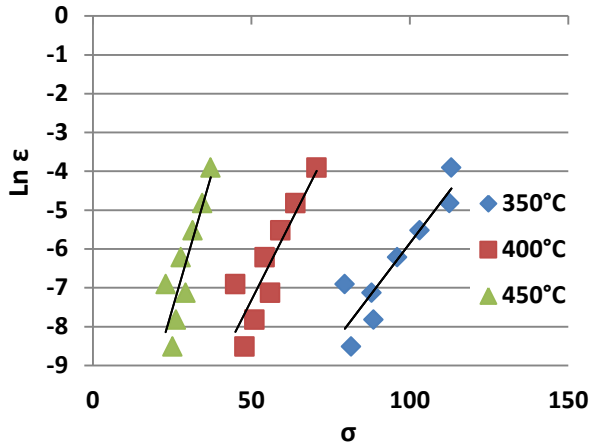


Fig 181 Relationship between  $\ln |\dot{\epsilon}|$  vs  $\sigma$

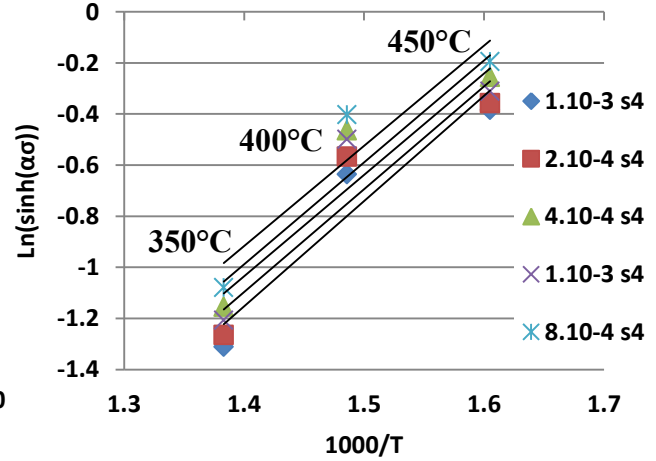


Fig 182  $\ln (\sinh(\alpha\sigma))$  vs  $1000/T$

The average slope measured is 4 which mean and activation energy ( $Q$ ) calculated of 196 KJ/mol. This value is higher than magnesium self diffusion energy (136 kj/mol) [172][173]. An activation energy higher than that for self-diffusion of the matrix materials in composites is commonly found and related to the existence of a creep thershold [174]. The parameter  $A$  can be obtained using the equation (16) applying the different values of  $n$  found during the analysis of the curves presented in Fig 181. Finally, in order to predict flow stresses at different temperatures and strain rates the hyperbolic-sine Arrhenius equation has been applied using the parameters calculated of  $Q$ ,  $n$  and  $A$ . The hyperbolic sine equation has been written as a function of de Zener-Hollomon parameter  $Z$  (temperature compensate strain-rate parameter) developing the following equations [175]:

$$\begin{cases} \dot{\epsilon} = A[\sinh(\alpha\sigma)]^n \exp\left(-\frac{Q}{RT}\right) \\ Z = \dot{\epsilon} \exp\left(\frac{Q}{RT}\right) \end{cases}$$

Therefore  $Z = A[\sinh(\alpha\sigma)]^n$  so  $\sinh(\alpha\sigma) = \left(\frac{Z}{A}\right)^{1/n}$

$$\operatorname{arcsinh}(x) = \ln \left[ x + \sqrt{x^2 + 1} \right]$$

$$\sigma = \frac{1}{\alpha} \ln \left\{ \left( \frac{Z}{A} \right)^{\frac{1}{n}} + \sqrt{\left( \frac{Z}{A} \right)^{\frac{2}{n}} + 1} \right\}. \quad (42)$$

The parameter  $Z$  can be found using the Zener-Hollomon equation applying the calculated activation energy at different temperatures as shown in the following equation:

$$Z = \dot{\epsilon} \exp \frac{196}{RT}, \quad (43)$$

Using the constitutive equation (41) to predict the flow stresses of magnesium EK21 +1% AlN at different strain rates and temperatures, the graph presented in Fig 183 is obtained. The graph displays the stress values predicted using the constitutive equation against different strain rates showing a fairly agreement between the predictions and the experimental results at low strain rates. The results indicates that the proposed constitutive model for high temperature flow stress prediction using the Zener-Hollomon equation and Arrhenius equations, can be used to describe the flow behaviour of magnesium Elektron 21 1% AlN nanoparticles at different strain rates and temperatures.

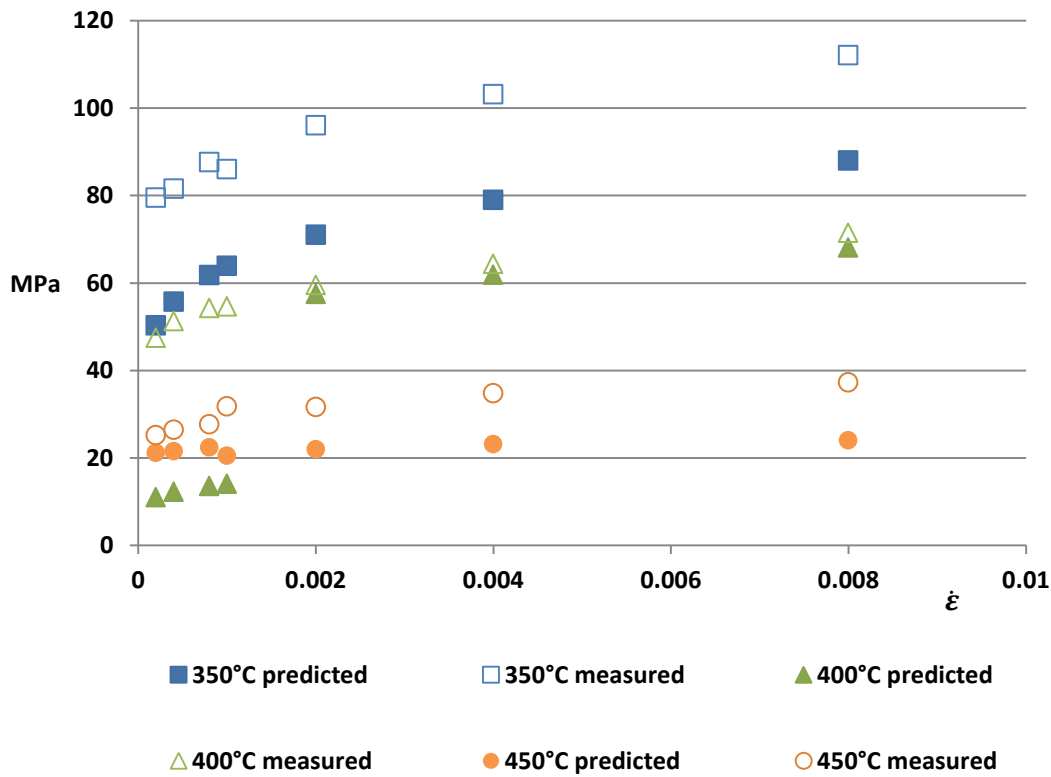


Fig 183 Stress flow vs strain rate 350°C, 400°C and 450°C

### 3.2 Discussion on results from experiments with nanoparticles

The addition of AlN nanoparticles to magnesium EK21 produces measurable changes in the microstructure and mechanical properties of the material. The first effect observed is the increase in grain size with respect to the pure material processed under the same casting conditions. The reinforced material presents an average grain size 200% bigger than the average grain size of pure magnesium EK21. In order to understand if the particles used contain any element that could produce the grain growth, the aluminium nitride powder was analysed using XRD by University de Torino. The results presented in Fig 184, reveal that certain amount of aluminium was present within the nanoparticles as impurity.

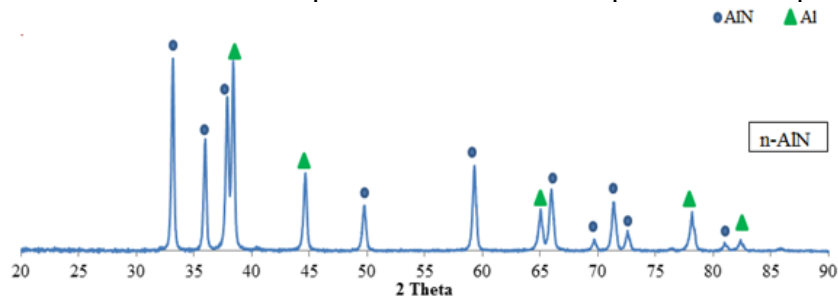


Fig 184 XRD original AlN powder

This aluminium in contact with the liquid magnesium dissolves and changes the composition of the alloy. The aluminium tends to react with the elements present in the alloy such as zirconium. This element is added as grain refiner to magnesium alloys in which a very low or no level of aluminium, manganese silicon or iron is found in their composition [176][177]. The reaction between zirconium and aluminium can produce AlZr compounds which were detected during SEM analysis. Therefore, the presence of aluminium reduces the capacity of zirconium to produce grain refinement. The lattice mismatch between zirconium and magnesium is reported to be less than 1% [178], whereas the lattice mismatch between AlZr and magnesium is approximately 4% which makes this particle a worst candidate to serve as grain refiner of magnesium. In order to eliminate any aluminium impurity within the AlN nanoparticles, the AlN powder was subjected to a process of purification. The particles were heated inside a tubular furnace during several hours under a nitrogen atmosphere. The reaction between the nitrogen and the aluminium resulted in the production of AlN particles eliminating the free aluminium present within the particles. Fig 185 presents the XRD analysis of the purified powder.

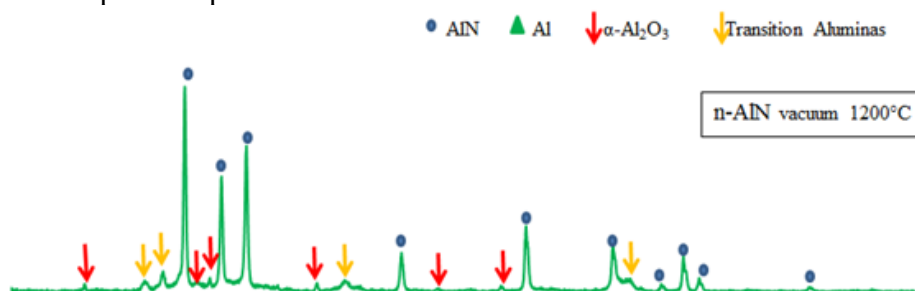


Fig 185 XRD purified AlN powder

The XRD analysis shows some traces of  $\text{Al}_2\text{O}_3$  and transition aluminas. Despite the vacuum performed at the beginning of the process, it is possible that a small amount of oxygen is still present during the purification process. This oxygen reacts with the aluminium producing these compounds. Due to the small amount detected, their presence is considered irrelevant in the results of the experiment. Using the purified particles a sample of reinforced magnesium EK21 was produced. The material obtained presents again a similar grain growth with respect to the material reinforced with the original powder. In order to investigate whether the AlN particles could have reacted with the magnesium matrix, a thermodynamic analysis was performed obtaining the compounds with the highest tendency to be formed. The study of the equilibrium reactions of AlN with pure magnesium shows that an amount equivalent to 0.3 % in weight of aluminium is released in the magnesium matrix, under the casting conditions applied during the experiments. This additional aluminium could be available to react with other elements present in the alloy such as zirconium. According to the thermodynamic calculations, ZrN would be formed in the alloy from the reaction of the AlN particles. The formation of this type of particle on the interphase between AlN particles and Zr is probed in studies performed by the author Xiangju et al. [179]. However, this type of particle was not found during SEM analysis and X-ray spectrometry, instead the particles detected were mostly rich in aluminium and zirconium. The spectrometry analysis performed on samples of magnesium EK21 containing nanoparticles also presented traces of aluminium in the intermetallic phase. The high difference of electronegativity between RE and Al is larger than between RE and Mg. Therefore, rare earth elements preferentially react with Al to form  $\text{Al}_{11}\text{RE}_3$ ,  $\text{Al}_{2.12}\text{RE}_{0.88}$  and  $\text{Al}_2\text{RE}$  compounds [180] [181]. The presence of these compounds in the intermetallic phase could have contributed to the slight increase in hardness detected on Mg Ek21 1% AlN during the mechanical characterization. In order to confirm the effects of aluminium in the material, a sample is produced adding the calculated amount of aluminium dissolved from the specimen reinforced with 1% of AlN particles. The specimen produced shows no traces of aluminium in the intermetallic phase but a considerable amount of AlZr particles are detected in the magnesium matrix. The analysis using X-ray spectrometry during SEM analysis did not show any traces of nitrogen either in the intermetallic phase or within the magnesium matrix. The light atomic mass of this element makes difficult its detection using this technique. On the other hand, TEM analysis combined with X-ray spectrometry performed by Mounib [182] on magnesium EK21 containing AlN nanoparticles of size 30 to 40 nm, shown in Fig 186, demonstrate traces of nitrogen detected from particles found in the eutectic area of the alloy. Considering the Al-Mg phase diagram (presented in **Appendix D. “Materials phase diagram”**), the small amount of aluminium released probably was fully dissolved into the magnesium alloy. This aluminium present in the matrix reacts with the zirconium producing AlZr compounds which are widely found during SEM analysis. Taking into account the great amount of AlZr particles found in the matrix, the different morphology observed of the intermetallic phase in which aluminium was also detected, and considering the TEM analysis performed by Mounib on samples of magnesium EK21 containing the same

type of AlN nanoparticles, it is quite probable that most of the aluminium detected in the intermetallic phase during SEM comes from the actual AlN particles.

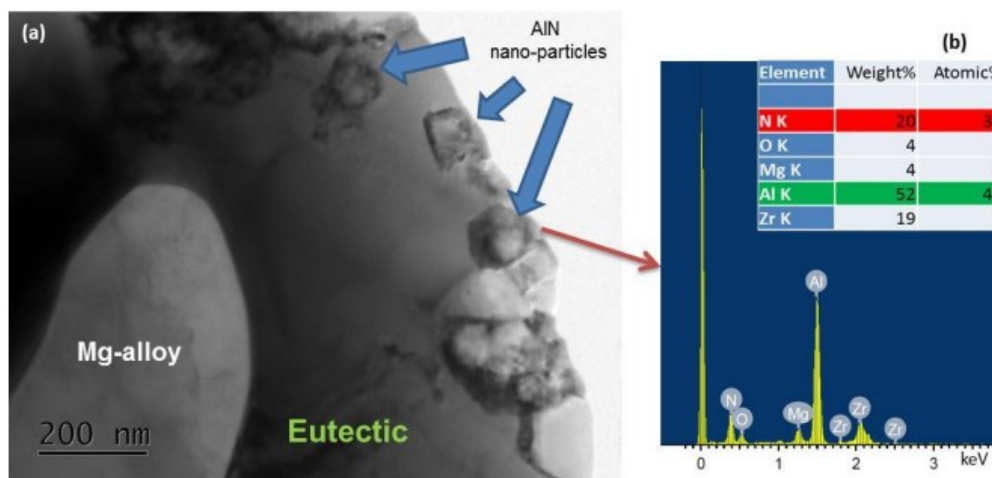


Fig 186 TEM Courtesy of Mounib [179]

The mechanical analysis performed shows a decrease in micro hardness on the alloy containing nanoparticles. This could be attributed to the increase in grain size due to the reaction between the aluminium dissolved and the zirconium particles present in the alloy. The hot compression test performed at 350 °C shows that nanoparticles produced a change in the material creep resistance. The activation energy calculated using the hot compression tests or reinforced magnesium EK21 was higher than the self diffusion energy for magnesium alone. The increase of activation energy during compression tests is mainly due to strong retarding effects of alloying elements on dynamic recrystallization and it is also related to the existence of a creep threshold typical of composites [183]. The compression tests reveal an increase of the flow stress by an average of 26 % at strain rate of 0.1 on the material reinforced with nanoparticles, which could be related to the increase of work hardening due to the interaction between the particles and to the dislocations moving within the material. The test also shows that dynamic recovery is lower in the materials reinforced with nanoparticles. This is a possible evidence of a decrease of the stacking fault energy (SFE) in the alloy. Low SFE promotes the formation of twins in crystalline materials and therefore is desirable for any form of plastic deformation [184]. In addition, this means that the capacity of the material to increase its strength by plastic deformation (also called work hardening) is increased. The increase in strain hardening is usually accompanied with a reduction of ductility but this property was not studied in the current case. The X-ray spectrometry performed during SEM indicates the presence of aluminium in the intermetallic phase which could be related to the presence of particles and rare earth – aluminium compounds. Consequently, it can be considered that grain boundary reinforcement played an important role in the strengthening of the material observed during the hot compression tests. The nanoparticles can hinder the dislocation movement and hinder both grain boundary migration and sliding during high temperature exposure, therefore improving creep resistance. In addition, AlZr compounds such as  $\text{Al}_3\text{Zr}$  have been related to increase creep strength of different alloys such as Mg-Li-Al [185]. Rare earth precipitates were observed on the intermetallic phase. Studies performed



by Matheo Pavesse (Politecnico di Torino) on the same alloy reinforced with 1% of AlN nanoparticles, found that the compounds forming the intermetallic phase are mainly  $\text{Al}_{1.1}\text{Mg}_{0.9}\text{Nd}$  and  $\text{Al}_x(\text{Nd,Gd})_y$   $x-y = 2-3$  or  $2-1$ . The effects of the presence of these compounds in the mechanical performance of the alloy should be assessed, but different studies such as the one performed by Meshinchi [167], have shown that particles of  $\text{Al}_{11}\text{RE}_{11}$  improve the creep resistance of magnesium AZ91. Both types of precipitates containing aluminium with rare earths or zirconium could have contributed to the improvement of creep resistance measured in magnesium EK21 reinforced with AlN nanoparticles. The creep analysis performed shows improvement in the material reinforced with nanoparticles. Taking into account the analysis of the materials and the calculations performed, the improvement detected can be mostly related to the intergranular reinforcement achieved by the rejection of the nanoparticles to the eutectic phase and possibly with the presence of precipitates of aluminium and rare earths.



# General Conclusion

Based on the results the following conclusions can be drawn.

## Aluminium Experiments

- Liquid processes are not suitable for the incorporation of  $\text{Al}_2\text{O}_3$  particles into aluminium matrices using the electromagnetic stirring provided by VB2 furnace. The incapacity to introduce the particles into the aluminium matrix made vanished the efficiency of the particles to produce grain refining, and to improve the mechanical properties of the material. On the other hand, the experiments performed using TMF during the casting of pure aluminium alloy A357 showed that electromagnetic stirring can help to reduce porosity in the material. Nevertheless, the results also showed that electromagnetic stirring can also produce segregation in the alloy.
- The negative results obtained using grain refining particles of  $\text{TiB}_2$  suggest that solute removal could have been the cause of the inefficiency of these particles to produce grain refinement. The solute removal could be related to the effect of the electromagnetic stirring applied during the casting of the material.

## Magnesium Experiments

- The experiments performed mixing magnesium with reinforcement particles showed positive result in the engulfment of both micro and nano particles by the magnesium matrix.
- The dispersion of SiC particles in pure magnesium demonstrated that the travelling magnetic field can be used to control the position of the particles dispersed. The analysis of the dispersion patterns under different vertical orientation of the TMF showed a good agreement between the numerical simulation performed by Greenwich University, and the results obtained from the characterization of the materials.
- The experiments performed using  $\text{Al}_2\text{O}_3$  particles showed that the reactivity of the particles was initially underestimated by the Exomet project.

- Despite the slight grain refinement detected in magnesium AZ91, the efficiency of  $\text{Al}_2\text{O}_3$  particles to serve as grain refiner for magnesium could not be demonstrated. The dissolution of the particles produces changes in the composition of the alloy and the precipitation of different particles such as magnesium oxide within the matrix.
- The mechanical tests showed that the inoculation of  $\text{Al}_2\text{O}_3$  particles produced a decrease in the mechanical properties of the material reducing tensile strength and ductility.
- Besides the negative effects produced by the particles in magnesium AZ91, the reaction of  $\text{Al}_2\text{O}_3$  particles with magnesium could be used to produce an aluminium-magnesium alloy containing MgO particles produced ‘in situ’ as it was demonstrated by the experiments performed using pure magnesium mixed with  $\text{Al}_2\text{O}_3$  particles.
- The experiments performed reinforcing magnesium Elektron 21 showed that some percentage of the particles dissolved releasing aluminium into the magnesium matrix.
- Hot compression tests performed on samples of magnesium Elektron 21 reinforced with nanoparticles showed the enhancement of creep resistance at high temperature.
- Our analysis suggests that the material reinforcement observed was essentially related to grain boundary strengthening produced by the nanoparticles.
- The analysis of the flow stress behaviour of the material reinforced with AlN nanoparticles showed that the hyperbolic-Arrhenius equation can be used to describe the flow stresses of the material.

## Short term outlooks

The difficulty found to disperse  $\text{Al}_2\text{O}_3$  particles into the aluminium matrix during the current study, lead to the development of a system designed to facilitate the introduction of the particles into this metal. The interfacial force presented between the particles and the liquid metal can be overcome by the kinetic energy applied to the particles using a pneumatic injector. A prototype of the system was installed in an induction furnace equipped with a cold crucible. The injector uses a compressed gas to extract and accelerate the particles using the Venturi effect. A description of the pneumatic injector system can be found in ‘**Appendix E. Pneumatic injector**’.

## Mid term outlooks

- In order to enhance grain refiner, modifications should be carried out on VB2 furnace to increase cooling rate.
- The segregation studies of magnesium AZ91 and aluminium A357 samples produced under the influence of TMF should be performed.
- The analyses of magnesium Elektron 21 samples reinforced with nanoparticles showed the presence of different precipitates such as AlZr. The determination of the composition of all the compounds presented in the material should be performed using TEM and other techniques.
- The study of the mechanical properties of magnesium EK21 containing AlN nanoparticles should be continued using tensile strength testing at room and high temperatures.
- The complete study of the deformation patterns using TEM at specified strain should be performed in order to understand the strain hardening mechanisms involved in the reinforcement of magnesium EK21 with AlN nanoparticles.

# Appendix

## Appendix A. Electromagnetic stirring

The multiphase stirring system produces the stirring of a liquid metal by the application of a travelling field. The system uses the configuration of the classical asynchronous motor. This type of AC motor produces torque by electromagnetic induction on the stator winding, as in the typical configuration of the monophas asynchronous motor 50Hz shown in Fig 187. The currents induced in the stator (shown in Fig 188) which is short-circuited or connected to a capacitor, are in the opposite direction. These currents in the rotor create a travelling magnetic field against the stator field with the angular speed of  $\omega/\rho$  producing the movement of the motor.

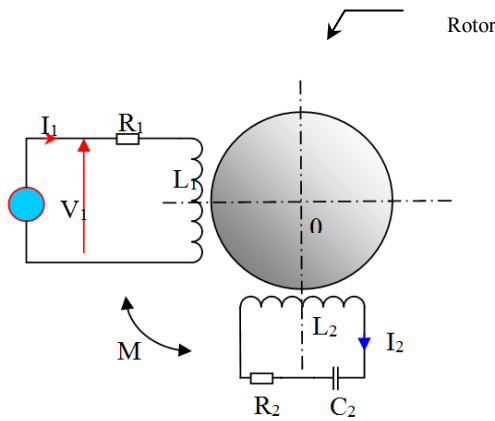


Fig 187 Monophas principle 50 Hz

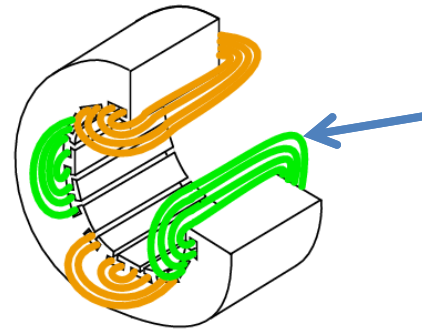


Fig 188 Stator

In a synchronous motor the operating speed is directly proportional to the frequency of the electrical system whereas in the asynchronous motor the operating speed is slightly less. In order to use the asynchronous motor configuration to produce a travelling magnetic field that can be oriented to upwards or downwards direction, this motor is converted into a tubular motor by changing its symmetry of revolution placing it around its vertical axis. The scheme of the electric configuration of an asynchronous motor in which a travelling magnetic field is generated to move its motor shaft is presented in Fig 189. The Bitter coil is feed with the multiphase current provided by the red (at 50Hz) using the same electrical configuration of the asynchronous motor as presented in Fig 190. In this case the travelling magnetic field is used to generate a stirring force (Laplace force) on a conducting liquid.



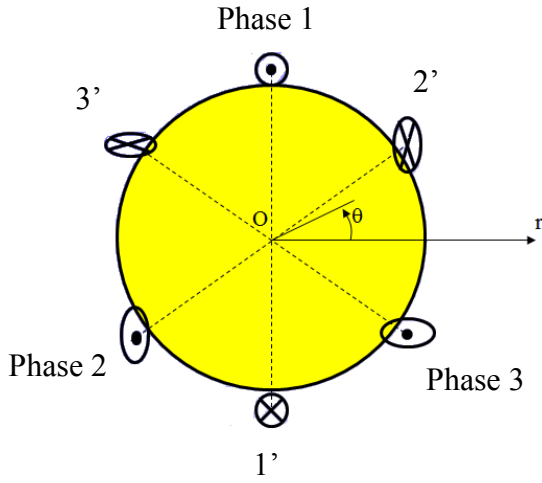


Fig 189 Asynchronous motor phase scheme

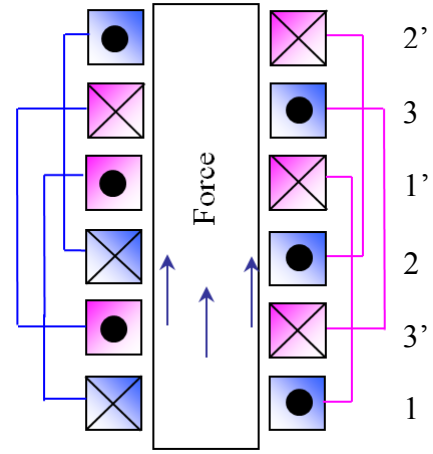


Fig 190 electric setup of the Bitter coil

Each pole of the Bitter coil is characterized by a phase shift of  $2\pi/3$ . The magnetic field applied to the conducting liquid metal is oriented upwards or downwards according to the orientation of the current on the six coils of the Bitter. The force travels along the liquid at the speed of synchronism  $V_s$ :

$$V_s = \lambda f, \quad (44)$$

where  $f$  is the frequency of the current applied, and  $\lambda$  is the wave length of the magnetic field which is calculated as the height of the inductor. Calculus of liquid metal flow speed is based on the calculation of Alfvén speed, which can be calculated using the following formula:

$$U_0 = \frac{B_0}{(\mu_0 \rho)^{1/2}}, \quad (45)$$

where  $B_0$  is the magnetic field,  $\mu_0$  is the magnetic permeability and  $\rho$  is the density of the liquid metal. In the case of aluminium  $\mu = 1.256665 \times 10^{-6} \text{ H m}^{-1}$ ;  $\rho = 2643 \text{ Kg m}^{-3}$ .

## Appendix B. Interparticle distance calculation

This appendix presents the Matlab code use to find the average interparticle distance

```
filename = 'DistanceparticlesEK21.xlsx'; % read file distanceparticlesEK21
A=xlsread (filename);
x=xlsread (filename, 'A:A'); % Separate columns into x,y,z
y=xlsread (filename, 'B:B');
z=xlsread (filename, 'C:C');

pixtolength = 650; %Define the size factor of the images here - what length a pixel covers
d = size(length(A));
mydata_xyz = A;

for j=1:length(A)

    mypoint_xyz = A(j,:);

    %compute the distance from the given point to all of the other test points.
    %Note the use of the transpose (apostrophe) to ensure that it sums in the
    % correct direction

    distance = sqrt(sum( ((mydata_xyz - ones(size(mydata_xyz,1),1)*mypoint_xyz).^2)' ));
    %sort to get the nearest neighbour followed by the next nearest neighbors
    %[sorted_distance, Isort] = sort(distance);

    distance(distance == 0) = inf;
    d(j) = min(distance);
end

dd = d';

d_real = dd.*pixtolength;

XYZD = horzcat(A,dd);

XYZDR = horzcat(XYZD,d_real);

avg_d = mean(d);
avg_d_real = mean(d_real);

fp = fopen('mindist_result.txt','w');
fprintf(fp,'%s\n','Distance to the nearest neighbour in pixels and in used length unit');
fprintf(fp,'%s\n','x y z dist_px dist_length');
fprintf(fp,'%f %f %f %f %f\n',XYZDR);
fclose(fp);
fprintf('Average minimal particle distance in pixels is: %f\n',avg_d);
```

```
fprintf('Average minimal particle distance in the given length unit is: %f\n',avg_d_real);

%print out each one of the points, from closest to farthest
%faceColor=[0.6875 0.8750 0.8984];% Plot a 3D graph
%figure
%tetramesh (DT,'FaceColor',faceColor,'FaceAlpha',0.3);
```

## Appendix C. Particle settling calculation

The main forces related to particle settling are displayed in Fig 191.

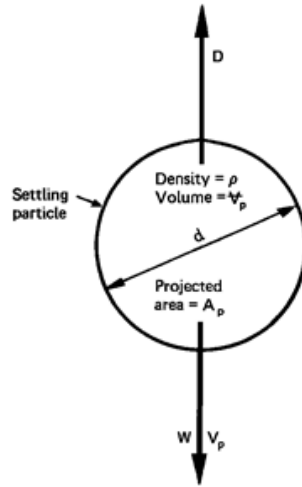


Fig 191 Ideal particle and forces

Where W is the submerged weight of the particle, D is the drag force, V<sub>p</sub> is the terminal velocity (m/s), A<sub>p</sub> is the projected area of the particle normal to the direction of motion, V<sub>p</sub> is the volume of the particle (m<sup>3</sup>), ρ is density (Kg/ m<sup>3</sup>). The following equations are applied on an ideal case with no collision between particles. Equation (46) is used to calculate the terminal velocity of the particle. The value obtained can be used to determine particle settling time:

$$V_s = \sqrt{\frac{4(\rho - \rho_l)gd}{3\rho_l C_d}}, (46)$$

where V<sub>s</sub> is the terminal velocity or settling velocity (m/s), C<sub>d</sub> is the drag coefficient, d is the diameter of the particle (m), ρ is the density of the particle, ρ<sub>l</sub> μ is the density of the fluid (N.s/m<sup>2</sup>) and g is gravity. In practice, it is found that C<sub>D</sub> is a function of the Reynolds Number, R<sub>e</sub>, and, for spherical particles, it can be represented by the following expressions:

$$R_e < 1, C_D = \frac{24}{R_e}, (47)$$

$$1 < R_e < 10^4, C_D = \frac{24}{R_e} + \frac{3}{(R_e)^{1/2}} + 24, (48)$$

$$10^3 < R_e < 10^5, C_D \approx 0.4$$

Substituting the above expression for  $R_e < 1$  (laminar flow) in Equation (46) and noting that  $R_e = \rho V_s d / \mu$ , results in the following equation, known as Stoke's Law:

$$V_s = \frac{g}{18} \frac{(\rho - \rho_l)}{\mu} d^2, (49)$$

At high values of  $R_e$ , where  $C_D \approx 0.4$ , the equivalent expression is:

$$V_s = \sqrt{3.33 \frac{(\rho - \rho_l)}{\rho_l} g d}, (50)$$

where  $\rho$  is the density of the particle,  $\rho_l$  is the density of the molten metal,  $g$  is gravity  $9.98 \text{ m/s}^2$  and  $d$  is the particle size. Mixing  $\text{Al}_2\text{O}_3$  particles size  $4.5 \text{ }\mu\text{m}$  and density  $3.95 \text{ g/cm}^3$  with aluminium in a crucible of  $15 \text{ cm}$  height, the settling time of the particles can be calculated using the developed equation 48. At aluminium melting point temperature ( $660.32^\circ\text{C}$ ) the aluminium density is  $2,375 \text{ g cm}^{-3}$ .  $V_s$  calculated is  $0.010 \text{ m/s}$ . The settling time of the particles inside a crucible of  $15 \text{ cm}$  calculated under ideal conditions (low Reynolds number and laminar-slip settling behavior) is  $25.5 \text{ seconds}$ .

## Appendix D. Materials phase diagram

### 1. Aluminium – magnesium phase diagram

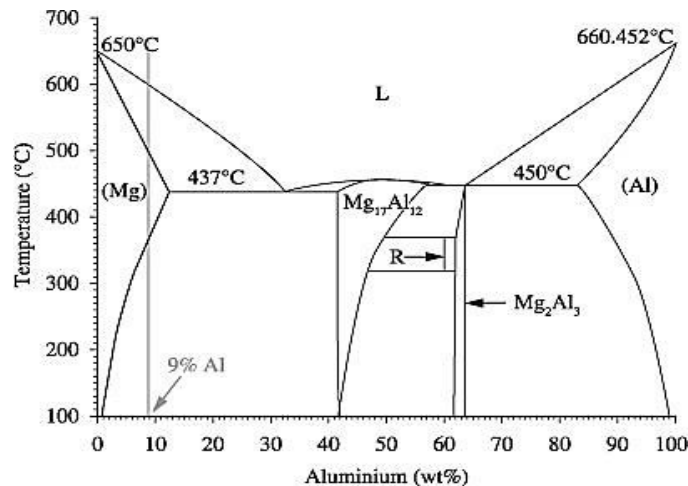


Fig 192 Al-Mg phase diagram

## 2. Aluminium – zirconium phase diagram

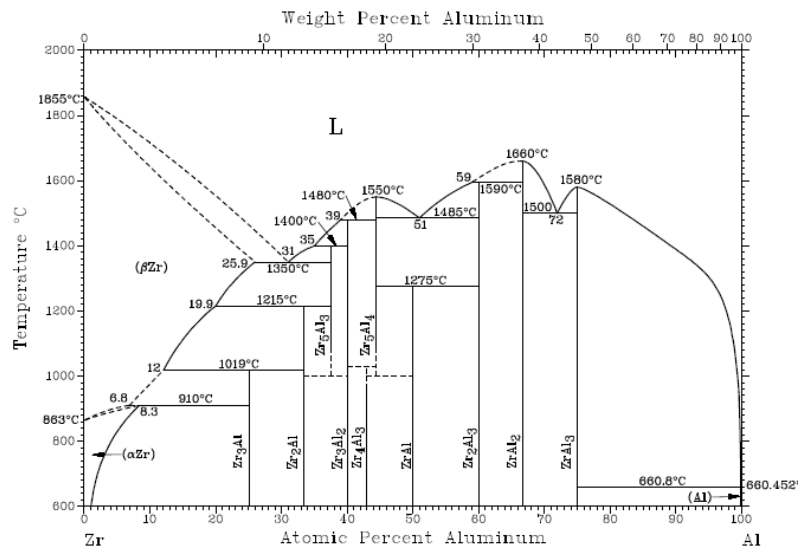


Fig 193 Al-Zr phase diagram

## Appendix E. Pneumatic injector

Fig 194 displays a picture of the pneumatic injector system developed to inject particles into aluminium and magnesium matrices.

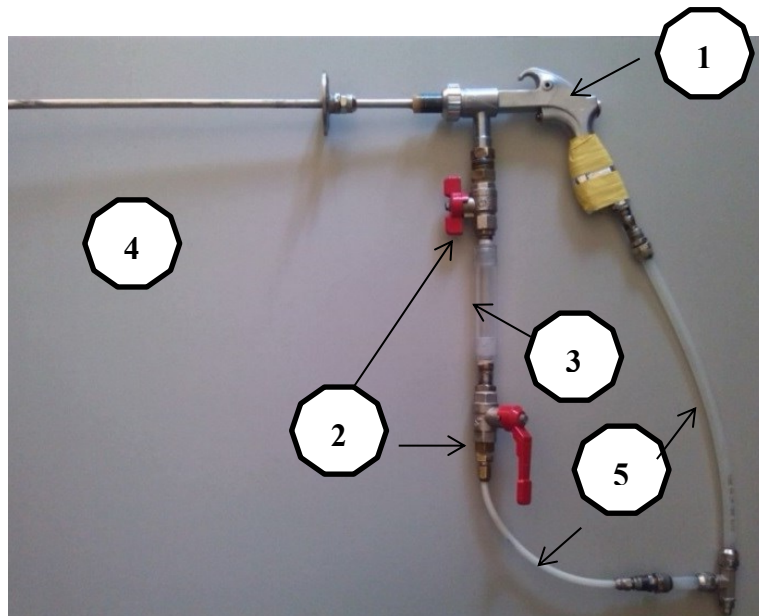


Fig 194 Pneumatic particle injector

**Venturi injector.** This component utilizes the Venturi effect to extract the particles from the particle container to the injection area using the main gas flow **2.Vanes.** They are used to isolate the particle container from the gas flow avoiding the suction of the particles when vacuum is produced inside the furnace. The vanes are in open position to perform the injection. The use of the vanes allows the replacement of the particle container during operations.**3.Particle container.** It is used to store the particles.**4.Injector lance.** It is used to release the gas and particles. It is connected on the top of the furnace and serves to support the injector. The connection with the furnace is carried out using a connector that permits the movement of the tube maintaining the internal pressure of the furnace. Using this system, the distance between the injector and the molten material can be regulated.**5. Gas inlets:** They are used to conduct the gas to the Venturi area. A numerical simulation performed using the program Solidworks was created in order to understand the flow behavior, and to calculate the pressure needed to reach the speed needed to overcome the interfacial force between the particles and the matrix. The numerical simulation presented in Fig 195 was performed applying a gas pressure of 5 bars. The calculated speed of the gas released is 9 m/s. Fig 196 shows a simulation in which particles have been incorporated. The test was performed injecting gas at 5 bars and particles of size 70  $\mu\text{m}$ . Using these parameters the particles reach the speed of 5 m/s at the injector tube.

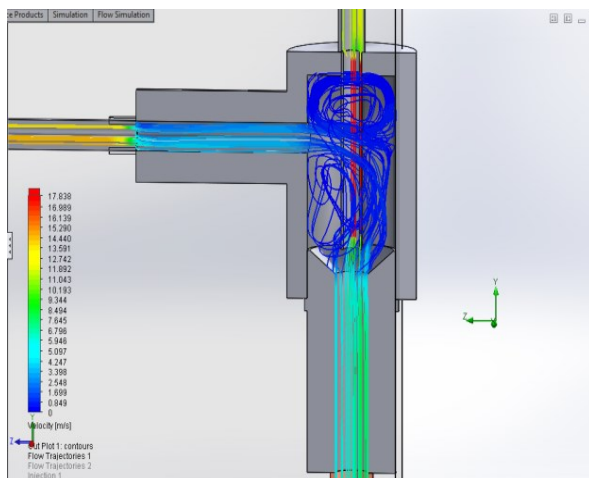


Fig 195 Visualization of the gas flow

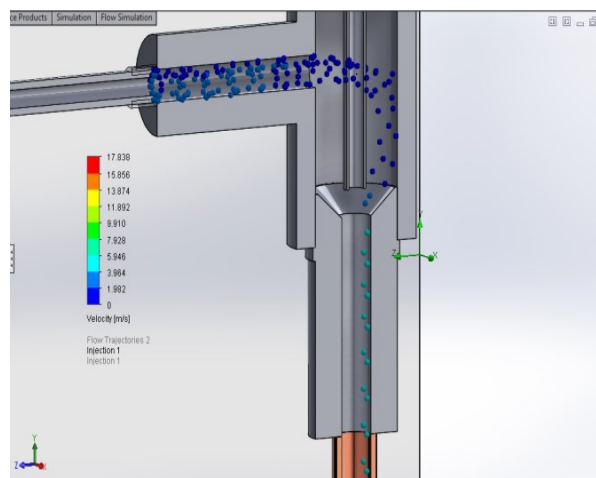


Fig 196 Visualization of the injected particles

## High speed camera test

A water model test bench was used to validate the results obtained from the numerical model. A scheme of the test bench is depicted in Fig 197. The tests were performed using a transparent crucible filled with water, placed inside a transparent container. Microparticles of



$\text{Al}_2\text{O}_3$  were injected at different pressures. Images obtained from the high speed camera were used to determine the speed at the injector lance.

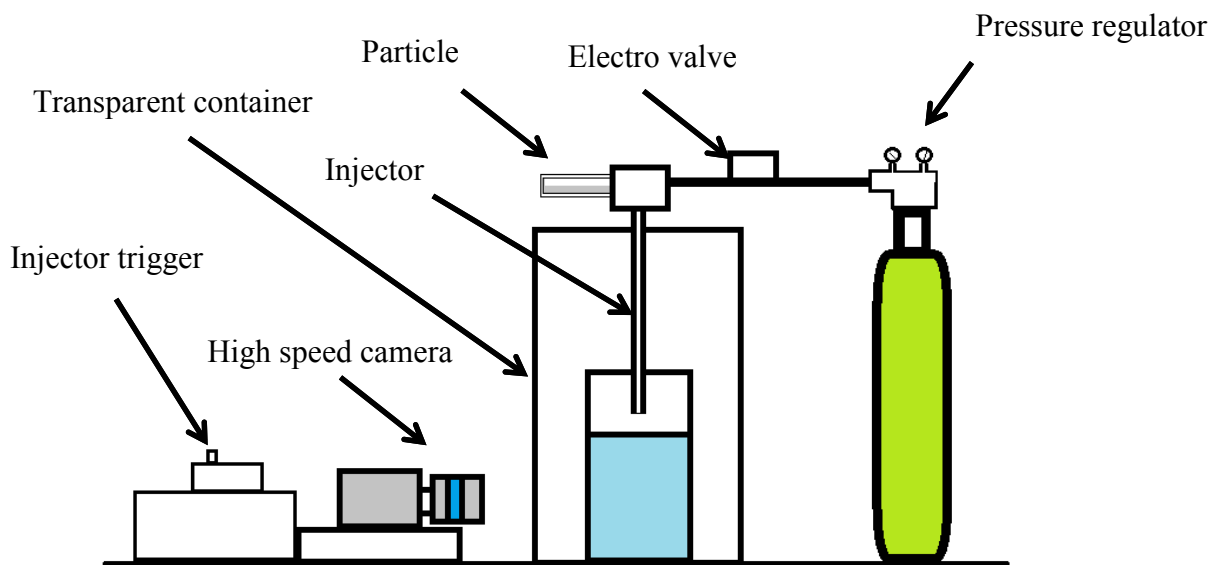
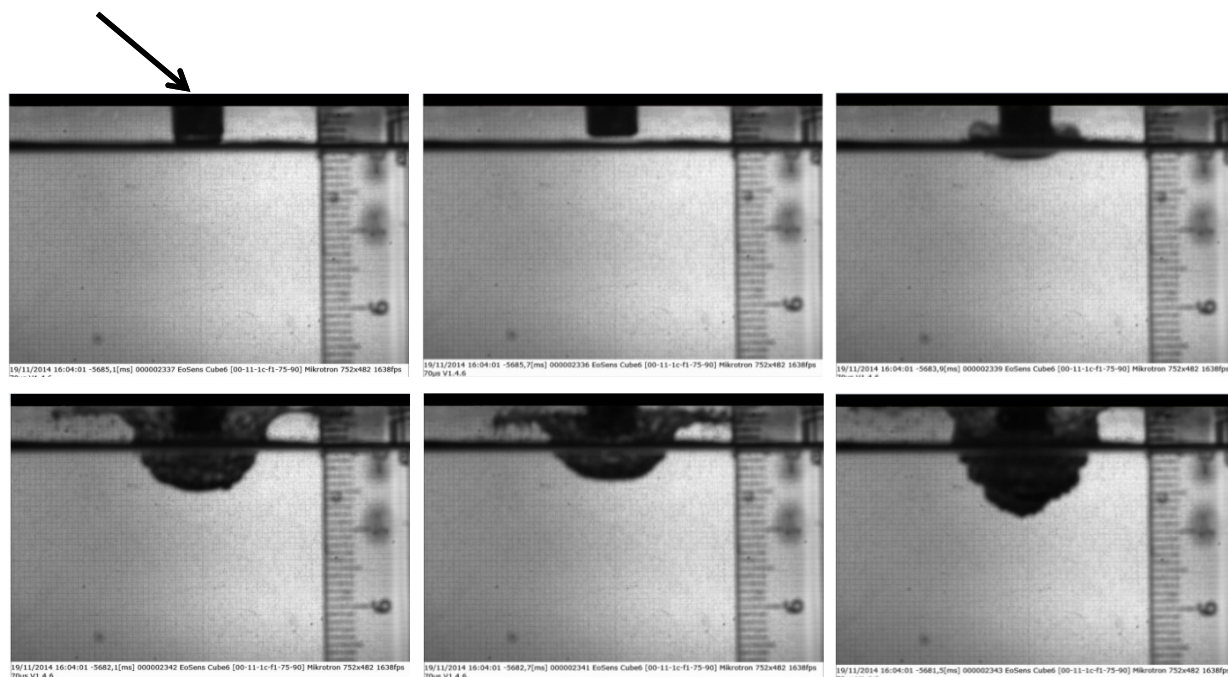


Fig 197 Scheme of water bench

The injection of the particles was tested in two different scenarios, first over the free surface, and second inside the liquid metal. The following images presented in Fig 198 are obtained using a high speed camera. The sequence of photographs is used to measure the velocity of the gas. On the top of the images the injector lance can be seen at approximately 1 mm over the free surface of water. A velocity of 5.26 m/s was calculated at 5 bars of pressure.

Injector lance



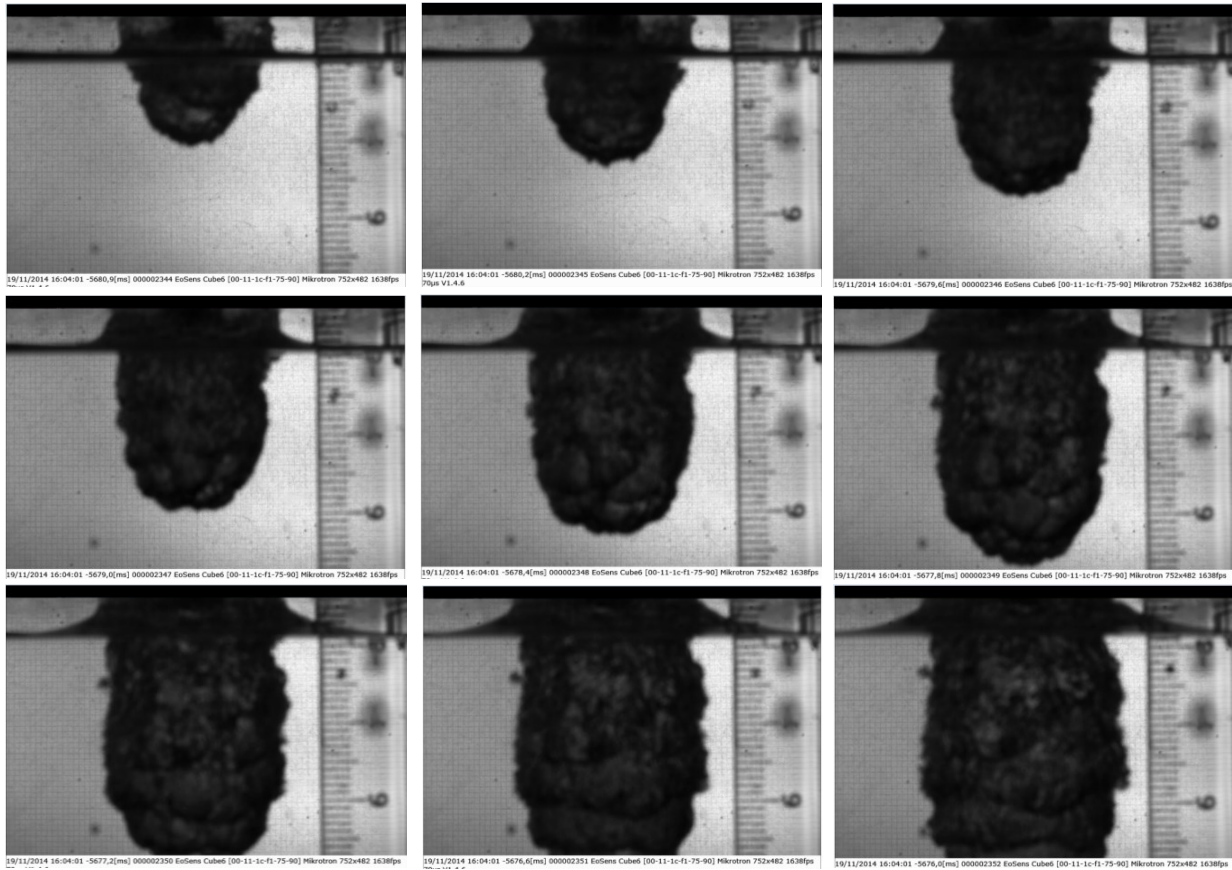


Fig 198 High speed camera sequence of photographs: injection over free surface

The second case studied was the injection of microparticles using a submerged lance. The images presented in Fig 199, show the injection of particles at a pressure of 10 bars. These images were used to calculate the speed of the gas injected as 14.25 m/s.

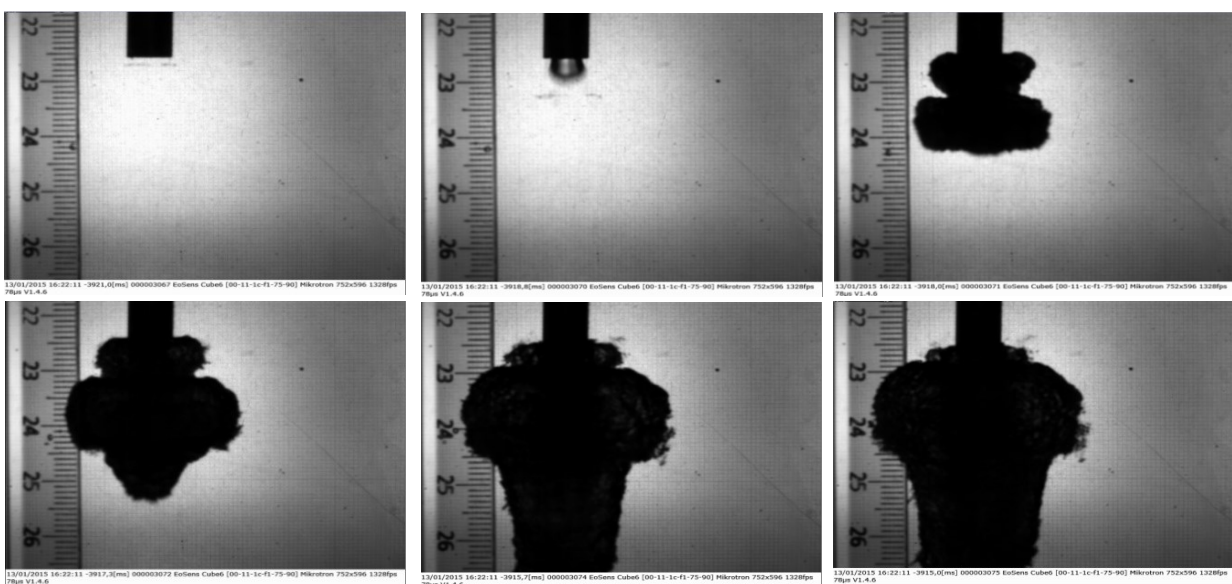


Fig 199 High speed camera sequence of photographs: injection inside water

The injector was installed on the induction furnace 4C as is shown in the scheme presented in Fig 200 and in the picture presented in Fig 201. A detail view of the furnace is presented in Fig 202 and a picture of the furnace in operation is presented in Fig 203.

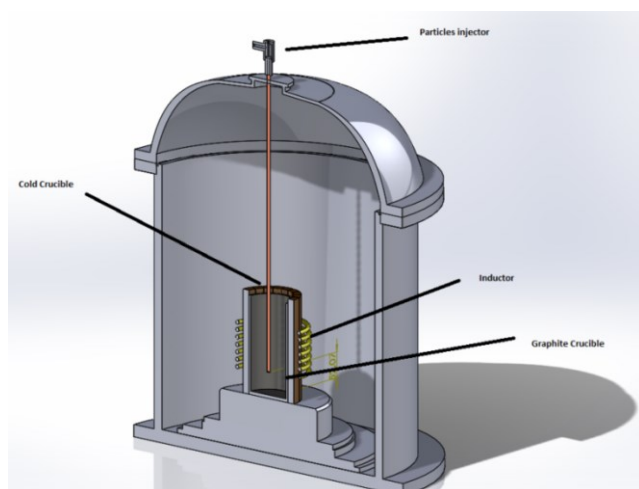


Fig 200 Scheme of furnace with injector



Fig 201 Induction furnace 4C



Fig 202 Detail view of furnace crucible area

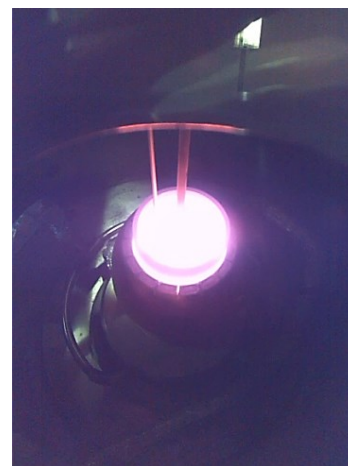


Fig 203 Furnace in operation

The temperature during the experiment is measured using a Fluke Eurotherm system shown in Fig 204. This device is connected to a thermocouple type K placed on the top of the molten material. The injection of the gas is controlled using the electro valve shown in Fig 205. The time employed to open and close the electro valve is controlled using an electronic shutter shown in Fig 206.





Fig 204 Fluke Eurotherm

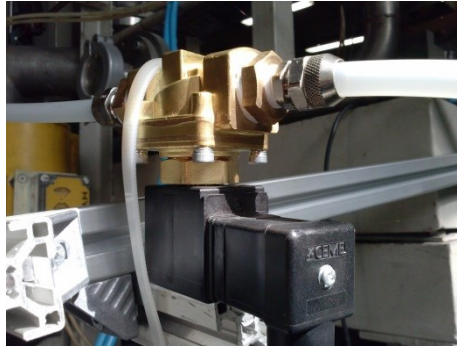


Fig 205 Electro valve



Fig 206 Electronic shutter

Particles of  $\alpha$   $\text{Al}_2\text{O}_3$  were introduced into aluminium A357 using the particles injector at 9 bars of pressure. The test was performed using particles with a size ranging of 20 to 70  $\mu\text{m}$ . The particles used on this experiment are shown in Fig 207 and Fig 208.

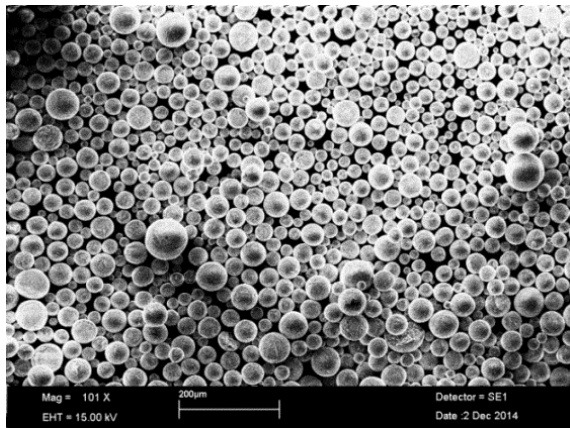


Fig 207  $\text{Al}_2\text{O}_3$  particles

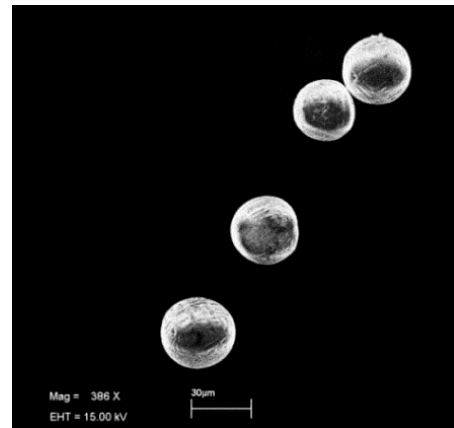


Fig 208 Detail view  $\text{Al}_2\text{O}_3$

The optical analysis of the samples showed that particles were efficiently embedded in the matrix material, but some agglomerates of particles were found. Two areas in which agglomerates of particles were found are shown in Fig 209 and Fig 210. The particles were located mainly inside the eutectic phase and in some cases next to porosity.

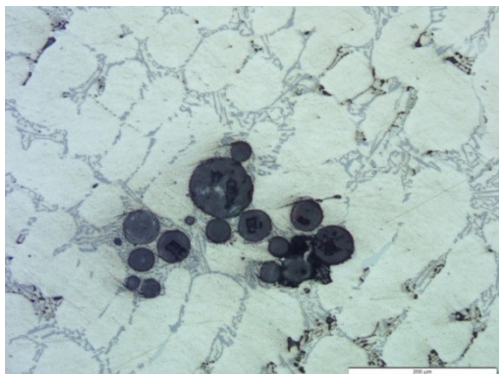


Fig 209 Al<sub>2</sub>O<sub>3</sub> particles detail view 1

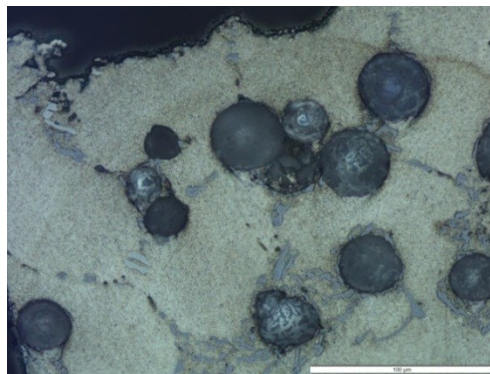


Fig 210 Al<sub>2</sub>O<sub>3</sub> particles detail view 2

The same type of particle was introduced in magnesium AZ91 using the injector system. Fig 211 and Fig 212 present a sample area containing Al<sub>2</sub>O<sub>3</sub> particles. The dispersion of the particles in this case was better than in the case of aluminium matrix and few agglomerates of particles were found.

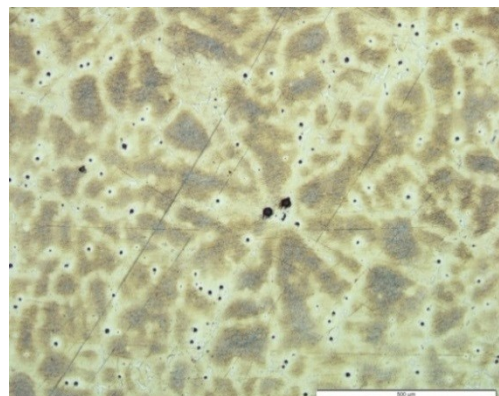


Fig 211 Al<sub>2</sub>O<sub>3</sub> particle

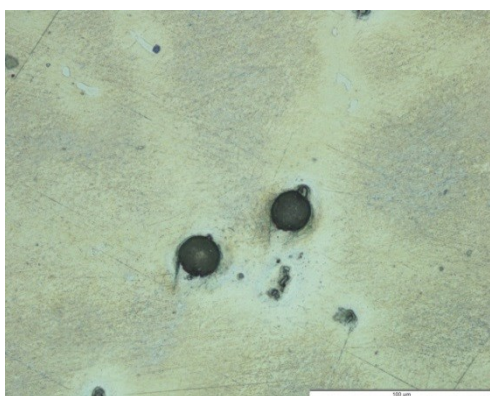


Fig 212 Al<sub>2</sub>O<sub>3</sub> particles detail view

The injector developed showed that applying enough kinetic energy to particles of Al<sub>2</sub>O<sub>3</sub>, it can be possible to introduce them into the melted aluminium. The system has been tested with medium size microparticles and further tests with smaller particles should be performed.

The research leading to these results has been carried out under ExoMet project under the European Community's Seventh Framework Programme, Contract no. FP7-NMP3-LA-2012-280421.

## References

- [1] P. Ning, G. Yongyong, L. Renxing, X. Zangqi, and Z. Qijie, "Mechanism of pulse magneto-oscillation grain refinement on pure Al," *China Foundry*, vol. 8, no. 1, pp. 47–50, 2011.
- [2] W. T. B. Wang, Y. S. Yang, J. Zhou, "Structure refinement of pure Mg under pulsed magnetic field," *Mater. Sci. Technol.*, vol. 27, no. 1, pp. 176–179, 2011.
- [3] J. Szajnar and T. Wróbel, "Exogeneous inoculation of pure Al with use of electromagnetic field," *Arch. Foundry Eng.*, vol. 43, no. 1, pp. 3–8, 2010.
- [4] V. Bojarevics, K. Pericleous, M. Garrido, Y. Fautrelle, and L. Davoust, "Travelling magnetic field mixing for particle dispersion in liquid metal," *Magnetohydrodynamics*, vol. 51, no. 3, pp. 453–460, 2015.
- [5] Organisation for Economic Co-operation and Development OECD, "Green growth and the future of aviation," in *27th Round Table on Sustainable Development*, 2012, no. January, p. 31.
- [6] McCraw-Hill, *McGraw-Hill Concise Encyclopedia of Engineering*. Emerald Group Publishing Limited, 2006.
- [7] C. Zweben, "Advanced by design materials," in *Metal Matrix Composites*, 1987, p. 325.
- [8] ASM International, "Introduction to Aluminum-Silicon Casting Alloys," *Aluminum-Silicon Cast. Alloy. Atlas Microfractographs*, vol. 2, pp. 1–10, 2004.
- [9] "l'Archange jean mermoz," *Aéro Jack*, pp. 19–21, 2014.
- [10] B. N. Chawla and Y. Shen, "Mechanical Behavior of Particle Reinforced Metal Matrix Composites," *Adv. Eng. Mater.*, vol. 3, no. 6, pp. 357–370, 2001.
- [11] I. M. Rajat Banerjee, *Ceramic Nanocomposites*, 1st Ed. Woodhead Publishing, 2013.
- [12] D. Zhang, K. Sugio, K. Sakai, H. Fukushima, and O. Yanagisawa, "Effect of Spatial Distribution of SiC Particles on the Tensile Deformation Behavior of Al-10 vol% SiC Composites," *Mater. Trans.*, vol. 48, no. 2, pp. 171–177, 2007.
- [13] C. Borgonovo and H. Yu, "A6 Nanoparticle Reinforced Al Casting Alloys," no. 9, pp. 1–63.
- [14] A. N. Subra Suresh, Andreas Mortensen, *Fundamentals of Metal matrix Composites*, Revised. Elsevier, 2013.
- [15] M. & M. S. The Minerals, *TMS 2013 142nd Annual Meeting and Exhibition*. John Wiley & Sons, 2013.
- [16] R. J. Moreau, *Magnetohydrodynamics*, 1st ed. Springer Netherlands, 1990.
- [17] A. Hellawell, S. Liu, and S. Z. Lu, "Dendrite Fragmentation and the Effects of Fluid Flow in Castings," *JOM*, vol. 49, no. 3, pp. 18–20, 1997.
- [18] M. Medina, Y. Du Terrail, F. Durand, and Y. Fautrelle, "Channel segregation during solidification and the effects of an alternating traveling magnetic field," *Metall. Mater. Trans. B*, vol. 35, no. 4, pp. 743–754, 2004.
- [19] B. Willers, S. Eckert, U. Michel, I. Haase, and G. Zouhar, "The columnar-to-equiaxed transition in Pb–Sn alloys affected by electromagnetically driven convection," *Mater. Sci. Eng.*, vol. 402, no. 1–2, pp. 55–65, 2005.
- [20] C. Vives, "Hydrodynamic, Thermal and Crystallographic Effects of an Electromagnetically Driven Rotating Flow in Solidifying Aluminum Melts," *Int. J. Heat Mass Transf.*, 1990.

- [21] D. G. McCartney, "Grain refining of aluminium and its alloys using inoculants," *Int. Mater. Rev.*, vol. 34, no. 1, pp. 247–260, 1989.
- [22] J. Megy, "New Process for Grain Refinement of Aluminum," 2000.
- [23] X. Li, A. Gagnoud, J. Wang, X. Li, Y. Fautrelle, Z. Ren, X. Lu, G. Reinhart, and H. Nguyen-Thi, "Effect of a high magnetic field on the microstructures in directionally solidified Zn-Cu peritectic alloys," *Acta Mater.*, vol. 73, no. March 2016, pp. 83–96, 2014.
- [24] P. A. Nikrityuk, K. Eckert, and R. Grundmann, "A numerical study of unidirectional solidification of a binary metal alloy under influence of a rotating magnetic field," *Int. J. Heat Mass Transf.*, vol. 49, no. 7–8, pp. 1501–1515, 2006.
- [25] B. Willersa, S. Eckerta, U. Michelb, I. Haaseb, and G. Zouharb, "The columnar-to-equiaxed transition in Pb-Sn alloys affected," *Mater. Sci. Eng.*, vol. 402, no. 1–2, pp. 55–65, 2005.
- [26] S. Y. Gao, Q. C. Le, and Z. Q. Zhanga, "Grain refinement of AZ31 magnesium alloy by electromagnetic stirring under effect of grain-refiner," *Bull. Mater. Sci.*, vol. 35, no. 4, pp. 651–655, 2012.
- [27] K. Polzin, "Liquid Metal Pump Technologies for Nuclear Surface Power," *Proc. Sp. Nucl. Conf.*, no. March, pp. 363–369, 2007.
- [28] J. C. Kim, J. J. Kim, J. Y. Choi, J. H. Choi, and S. K. Kim, "Control of columnar-to-equiaxed transition in continuous casting of 16% Cr stainless steel," *Metall. Ital.*, vol. 101, no. 8, pp. 43–48, 2009.
- [29] S. Lim and E. Yoon, "The Effect of Electromagnetic Stirring on the Microstructure of Al-7 wt% Si Alloy," *J. Mater. Sci.*, vol. 16, no. 1, pp. 104–109, 1997.
- [30] Z. Shu-cai, L. Hua-ji, R. Jin-song, R. Zheng-de, Z. Jie-xin, and Y. Zhi-li, "Effect of electromagnetic stirring on solidification structure of austenitic stainless steel in horizontal continuous casting," *China Foundry*, vol. 4, no. 3, pp. 8–11, 2007.
- [31] K. Zaidat, "Influence d'un champ magnétique glissant sur la solidification dirigée des alliages métalliques binaires," Th. Sciences et génie des matériaux, Institut National Polytechnique de Grenoble - INP, 2005.
- [32] H. Y. Zhang, L. Bai, K. Y. Ma, and S. Z. Song, "Influences of Electromagnetic Stirring Process Parameters on SiC Particle Distribution in Steel Matrix," *Appl. Mech. Mater.*, vol. 347–350, pp. 1158–1163, 2013.
- [33] H. Li, Y. Wang, and Z. Fan, "Mechanisms of enhanced heterogeneous nucleation during solidification in binary Al – Mg alloys," vol. 60, pp. 1528–1537, 2012.
- [34] J. Grandfield, D. G. Eskin, and I. Bainbridge, *Direct Chill Casting of Light Alloys: Science and Technology*, Illustrate. John Wiley & Sons, 2013.
- [35] K. Kelton and A. Lindsay, *Nucleation in Condensed Matter: Applications in Materials and Biology*, Illustrated. Elsevier, 2010.
- [36] V. Metan, K. Eigenfeld, D. Rabiger, M. Leonhardt, and S. Eckert, "Grain size control in Al-Si alloys by grain refinement and electromagnetic stirring," *J. Alloys Compd.*, vol. 487, no. 1–2, pp. 163–172.
- [37] I. V. Gomez, "Influence des nano-particules d'alumine (Al<sub>2</sub>O<sub>3</sub>) et de di-borure de titane (TiB<sub>2</sub>) sur la microstructure et les propriétés de l'alliage Al-Si<sub>9</sub>-Cu<sub>3</sub>-Fe<sub>1</sub> pour des applications de fonderie à haute pression Iban Vicario Gomez," Th.Physico-Chimie de la Matière Condensée, L'Université Bordeaux, 2011.
- [38] F. Humphreys and M. Ardakani, "Grain bounday migration and Zener pinning in particle-containing copper crystals," *Acta Mater.*, vol. 44, no. 7, pp. 2717–2727, 1996.
- [39] R. Casati and M. Vedani, "Metal Matrix Composites Reinforced by Nano-Particles—A



- Review," *Metals (Basel)*, vol. 4, no. 1, pp. 65–83, 2014.
- [40] H. Z. Ye and X. Y. Liu, "Review of recent studies in magnesium matrix composites," *J. Mater. Sci.*, vol. 9, pp. 6153–6171, 2004.
  - [41] D. Shepelev, J. Klempf, M. Bamberger, and A. Katsman, "Grain refinement and mechanical properties enhancement of AZ91E alloy by addition of ceramic particles," *J. Mater. Sci.*, 2011.
  - [42] S. Kawamori, K. Kuroda, Y. Kasuga, M. Yokouchi, H. Fujiwara, and K. Ameyama, "Effect of alumina content on the mechanical properties of alumina particle dispersion magnesium," *Nippon Kinzoku Gakkaishi/Journal Japan Inst. Met.*, vol. 75, no. 8, pp. 424–431, 2011.
  - [43] M. Paramsothy, J. Chan, R. Kwok, and M. Gupta, "The synergistic ability of Al<sub>2</sub>O<sub>3</sub> nanoparticles to enhance mechanical response of hybrid alloy AZ31/AZ91," *J. Alloys Compd.*, vol. 509, no. 28, pp. 7572–7578, 2011.
  - [44] M. Habibnejad-Korayem, R. Mahmudi, and W. J. Poole, "Enhanced properties of Mg-based nano-composites reinforced with Al<sub>2</sub>O<sub>3</sub> nano-particles," *Mater. Sci. Eng. A*, vol. 519, no. 1–2, pp. 198–203, 2009.
  - [45] A. R. Kennedy and A. E. Karantzalis, "The incorporation and redistribution behaviour of ceramic particles in liquid Al and the relation," *Lloydia (Cincinnati)*, no. July, 1997.
  - [46] S. Bao, K. Tang, A. Kvithyld, T. Engh, and M. Tangstad, "Wetting of pure aluminium on graphite, SiC and Al<sub>2</sub>O<sub>3</sub> in aluminium filtration," *Trans. Nonferrous Met. Soc. China (English Ed.)*, vol. 22, no. 8, pp. 1930–1938, 2012.
  - [47] G. Bracco and B. Holst, *Surface science techniques*, vol. 51, no. 1, 2013.
  - [48] E. Saiz, A. P. Tomsia, and K. Suganuma, "Wetting and strength issues at Al / alumina interfaces," *Journal of the European Ceramic Society*, vol. 23, pp. 2787–2796, 2003.
  - [49] P. Cooper and A. Barber, "Review of the Latest Developments and Best Use of," no. October, pp. 16–17, 2003.
  - [50] C. Borgonovo, "Synthesis of Aluminum-Aluminum Nitride Nanocomposites by Gas-Liquid Reactions," *Metall. Mater. Trans. A*, vol. 47, no. 4, pp. 1818–1827, 2016.
  - [51] P. L. Schaffer, D. N. Miller, and A. K. Dahle, "Crystallography of engulfed and pushed TiB<sub>2</sub> particles in aluminium," *Scr. Mater.*, vol. 57, no. 12, 2007.
  - [52] D. Yadav and R. Bauri, "Friction Stir Processing of Al-TiB<sub>2</sub> In Situ Composite : Effect on Particle Distribution , Microstructure and Properties," vol. 24, no. March, pp. 1116–1124, 2015.
  - [53] P. L. Lü, J. Fuh, and Y.-S. Wong, *Laser-Induced Materials and Processes for Rapid Prototyping*, 1th ed. Springer US, 2001.
  - [54] A. Kumar, M. M. Mahapatra, and P. K. Jha, "Fabrication and Characterizations of Mechanical Properties of Al-4 . 5 % Cu / 10TiC Composite by In-Situ Method," vol. 2012, no. November, pp. 1075–1080, 2012.
  - [55] J. Lelito, P. L. Zak, A. A. Shirzadi, A. L. Greer, W. K. Krajewski, J. S. Suchy, K. Haberl, and P. Schumacher, "Effect of SiC reinforcement particles on the grain density in a magnesium-based metal-matrix composite: Modelling and experiment," *Acta Mater.*, vol. 60, no. 6–7, pp. 2950–2958, 2012.
  - [56] V. Sklenieka and K. Hucharova, "Creep Fracture Processes in Magnesium Metal Matrix Composites," *J. Chem. Inf. Model.*, vol. 53, no. 9, pp. 1689–1699, 2013.
  - [57] H. Dieringa, "Properties of magnesium alloys reinforced with nanoparticles and carbon nanotubes: A review," *J. Mater. Sci.*, vol. 46, no. 2, pp. 289–306, 2011.

- [58] O. Senkov, D. Miracle, and A. Sergey, *Metallic Materials with High Structural Efficiency*. Springer Science & Business Media, 2006.
- [59] Y. Q. Liu, H. T. Cong, W. Wang, C. H. Sun, and H. M. Cheng, "AlN nanoparticle-reinforced nanocrystalline Al matrix composites: Fabrication and mechanical properties," *Mater. Sci. Eng. A*, vol. 505, no. 1–2, pp. 151–156, 2009.
- [60] J. Chen and B. Chong-Gao, "Microstructure and Lattice Parameters of AlN Particle-Reinforced Magnesium Matrix Composites Fabricated by Powder Metallurgy," *Acta Metall. Sin.*, vol. 28, no. 11, pp. 1354–1363, 2015.
- [61] W. Chen and M. C. Chaturvedi, "Depence of Creep Fracture of Inconel 718 on Grain Boundary Precipitates," *Acta Mater.*, vol. 45, pp. 2735–2746, 1997.
- [62] T. H. Courtney, *Mechanical Behavior of Materials: Second Edition*, 2 edition. Waveland Pr Inc, 2005.
- [63] A. Guy, *Essentials of Materials Science*, McGraw- Hill, p153, 1976.
- [64] B. Poquette, "Damping behavior in ferroelectric reinforced metal matrix composites," MsC, Materials Science and Engineering, Virginia, p130, 2005.
- [65] Z. Zhang and D. Chen, "Contribution of Orowan strengthening effect in particulate-reinforced metal matrix nanocomposites," *Mater. Sci. Eng.*, vol. 483–484, no. 148–152, 2008.
- [66] B.K. Agrawal, *Introduction to Engineering Materials*, 21 st. New Delhi: Tata Mc Graw-Hill Education, 1988.
- [67] D. Roylance, "The Dislocation Basis of Yield and Creep," *Modul. Mech. Mater.*, pp. 1–15, 2001.
- [68] R. Casati, *Aluminum Matrix Composites Reinforced with Alumina Nanoparticles*. Springer, 2016.
- [69] N. Hansen, "Hall-Petch relation and boundary strengthening," *Scr. Mater.*, vol. 51, no. 8, pp. 801–806, 2004.
- [70] J. Adamczyk, *Engineering of metallic materials*. Gliwice: Silesian University of Technology, 2004.
- [71] G. Hassold, E. Holm, E. Srolovitz, and J. David, "Scientific Commons: Effects of particle size on inhibited grain growth," *Scr Met. Mater.*, vol. 24, no. c, pp. 11–13, 1990.
- [72] D. C. Van Aken, P. E. Krajewski, G. M. Vyletel, J. E. Allison, and J. W. Jones, "Recrystallization and grain growth phenomena in a particle-reinforced aluminum composite," *Metall. Mater. Trans. A*, vol. 26, no. 6, pp. 1395–1405, 1995.
- [73] G. N. Hassold, E. A. Holm, and D. J. Srolovitz, "Effects of particle size on inhibited grain growth," *Scr. Metall. Mater.*, vol. 24, no. 1, pp. 101–106, 1990.
- [74] M. P. H. Laura C. Stearns, "Particle\_Inhibited Grain growth in Al<sub>2</sub>O<sub>3</sub>-SiC II, Equilibrium and Kinetic Analyses," *J. Am. Ceram. Soc.*, vol. 79, no. 12, pp. 3020–3028, 2005.
- [75] R. K. Everett and R. J. Arsenault, *Metal matrix composites. Mechanisms and properties*. San Diego, CA(US); Academic Press, 1991.
- [76] N. Ramakrishnan, "An analytical study on strengthening of particulate reinforced metal matrix composites," *Acta Mater.*, vol. 44, no. 1, pp. 69–77, Jan. 1996.
- [77] T. Srivatsan, "A review of: 'Metal Matrix Composites: Thermomechanical Behavior,'" *Mater. Manuf. Process.*, vol. 10, no. 1, pp. 122–123, 1995.
- [78] Z. Fan, "Semisolid metal processing," *Int. Mater. Rev.*, vol. 47, no. 2, pp. 49–85, 2002.
- [79] P. Helen, A. Freng, and H. Atkinson, "Semi-Solid Processing of Metallic Materials Semi-Solid Processing of Metallic Materials," *Mater. Sci. Technol.*, vol. 26, no. 12, pp. 1401–1413, 2010.

- [80] A. Dahle and D. StJohn, "Processing from the liquid state," in *Materials Science and Engineering*, Illustratr., vol. II, EOLSS Publications, 2009, p. 432.
- [81] J. J. DeYoreo and P. G. Vekilov, "Principles of Crystal Nucleation and Growth," *Rev. Mineral. Geochemistry*, vol. 54, no. 1, pp. 57–93, 2003.
- [82] W. Becker, R. Doring, "Kinetic treatment of the nucleation in supersaturated vapors," *Naca*, p. 43, 1954.
- [83] M. Volmer and A. Weber, "Keimbildung in übersättigten Gebilden," *Z. Phys. Chem*, vol. 119, p. 277, 1925.
- [84] H. Men and Z. Fan, "Effects of solute content on grain refinement in an isothermal melt," *Acta Mater.*, vol. 59, no. 7, pp. 2704–2712, 2011.
- [85] D. G. McCartney, "Grain refining of aluminium and its alloys using inoculants," *Int. Mater. Rev.*, vol. 34, no. 1, pp. 247–260, 1989.
- [86] J. Campbell, *Castings*, 2th ed. Butterworth-Heinemann, 2003.
- [87] P. Egizabal, "L'Universite Bordeaux I," Th.Physico-Chimie de la Matière Condensée, Universite Bordeaux,p.167, 2007.
- [88] A. Johanson, "Effect of Vanadium on Grain Refinement of Aluminium," MSc Materials Science and Engineering, Norwegian University of Science and Technology, p80, 2013.
- [89] T. Wrobel and J. Szajnar, "The influence of inoculants sort on pure Al structure," *J. Achiev. Mater. Manuf. Eng.*, vol. 50, no. 2, pp. 206–208, 2012.
- [90] A. L. Greer, A. M. Bunn, A. Tronche, P. V. Evans, and D. J. Bristow, "Modelling of inoculation of metallic melts: application to grain refinement of aluminium by Al-Ti-B," *Acta Mater.*, vol. 48, no. 11, pp. 2823–2835, 2000.
- [91] A. Quested and T. Greer, "The effect of the size distribution of inoculant particles on as-cast grain size in aluminium alloys," *Acta Mater.*, vol. 52, no. 13, pp. 3859–3868.
- [92] T. Wrobel, *Structure of Pure Aluminum After Endogenous and Exogenous Inoculation*, vol. 2, no. 1. Intech Open Access Publisher, 2012.
- [93] J. Lelito, Z. Pawe, A. Shirzadi, A. Greer, W. Krajewski, J. Suchy, K. Haberl, and P. Schumacher, "Effect of SiC reinforcement particles on the grain density in a magnesium-based metal-matrix composite: Modelling and experiment," *Acta Mater.*, vol. 60, no. 6–7, pp. 2950–2958, 2012.
- [94] M. Easton and D. StJohn, "A model of grain refinement incorporating alloy constitution and potency of heterogeneous nucleant particles," *Acta Mater.*, vol. 49, no. 10, pp. 1867–1878, 2001.
- [95] A. Bunn, P. Schumacher, M. Kearns, C. Boothroyd, and A. Greer, "Grain refinement by Al–Ti–B alloys in aluminium melts: a study of the mechanisms of poisoning by zirconium," *Mater. Sci. Technol.*, vol. 15, no. October, pp. 1115–1123, 1999.
- [96] F. Ta-Wei and W. R. Wilcox, "Influence of insulation on stability of interface shape and position in the vertical Bridgman-Stockbarger technique," *J. Cryst. Growth*, vol. 48, no. 3, pp. 416–424, 1980.
- [97] R. Naumann and L. Sandor, "Effect of variable thermal conductivity on isotherms in Bridgman growth," *J. Cryst. Growth*, vol. 61, no. 3, pp. 707–710, 1983.
- [98] Z. Zhan-yong, G. Ren-guo, G. Xi-hua, J. Zhanga, X. Suna, and L. Hui-Nan, "Effects of Electromagnetic Stirring, Shearing, and Extrusion on TiB<sub>2</sub> and TiAl<sub>3</sub> Particles in Al-5Ti-1B(wt.%) Alloy," *Mater. Manuf. Process.*, vol. 30, no. 10, pp. 1223–1228, 2015.
- [99] M. Cablea, "Numerical and experimental studies of magnetic field effects on solidification of metallurgical silicon for photovoltaic applications," Th. Matériaux, Grenoble,p.189, 2015.

- [100] V. Bojarevics, K. Pericleous, and R. Brooks, "Dynamic model for metal cleanliness evaluation by melting in cold crucible," *Metall. Mater. Trans. B*, vol. 40, no. 3, pp. 328–336, 2009.
- [101] D. Leenov and A. Kolin, "Magnetohydrodynamic forces experienced by spherical and symmetrically oriented cylindrical particles," *J. Chem. Phys*, vol. 22, no. 4, pp. 683–688, 1954.
- [102] H. Windsheimer, R. Waitz, and P. Wübben, "Inductive melting in cold crucible : technology and - applications," pp. 1–5, 2015.
- [103] J. Kumar, A. G. Abulrub, A. Attridge, and M. A. Williams, "Effect of X-Ray Computed Tomography Scanning Parameters on the Estimated Porosity of Foam Specimens," *Appl. Mech. Mater.*, vol. 110–116, no. Mimat, pp. 808–815, 2012.
- [104] A. Kak and M. Slaney, *Principles of Tomographic Imaging*. Philadelphia, 2001.
- [105] G. Kugler, M. Knap, H. Palkowski, and R. Turk, "Estimation of activation energy for calculating the hot workability properties of metals," *Sci. York*, vol. 43, no. 1, pp. 267–272, 2004.
- [106] M. A. L. D. F. Warne, *Electrical Engineer's Reference Book*, Sixteenth. Newnes.
- [107] Cambridge University Engineering Department, "Materials data book," *Mater. Courses*, pp. 1–41, 2003.
- [108] N. D. Alexopoulos, "Impact properties of the aircraft cast aluminium alloy Al-7Si0.6Mg (A357)," *EPJ Web Conf.*, vol. 6, p. 2002, 2010.
- [109] A. Forn, G. Vaneetveld, J. C. Pierret, S. Menargues, M. T. Baile, M. Campillo, and A. Rassili, "Thixoextrusion of A357 aluminium alloy," *Trans. Nonferrous Met. Soc. China (English Ed.)*, vol. 20, no. SUPPL. 3, pp. 1005–1009, 2010.
- [110] Army US, "High strength-high damping capacity wrought magnesium alloys," Philadelphia, 1975.
- [111] Z. Fan, Y. Wang, M. Xia, and S. Arumuganathar, "Enhanced heterogeneous nucleation in AZ91D alloy by intensive melt shearing," *Acta Mater.*, vol. 57, no. 16, pp. 4891–4901, 2009.
- [112] M. N. Khan, "Solidification study of commercial magnesium alloys," Th M.A.Sc Mechanical and Industrial Engineering, Concordia University, p.95, 2009.
- [113] C. S. Roberts, *Magnesium and its alloys*. John Wiley & Sons, 1960.
- [114] R. T. Xuejun Zhu, Daniel Druyor, "Energy-Saving Melting and Revert Reduction Technology (E-SMARRT)," 2013.
- [115] M. Braszczyńska and N. Kataryna, "Precipitates of  $\gamma$  – Mg 17 Al 12 Phase in AZ91 Alloy," *Magnes. Alloy. - Des. Process. Prop.*, pp. 97–112, 2011.
- [116] A. Kiełbus, "Microstructure and Properties of Elektron 21 Magnesium Alloy," *Magnes. Alloy. - Des. Process. Prop. Frank Czerwinski (Ed.)*, ISBN 978-953-307-520-4, pp. 281–296, 2011.
- [117] R. G. Munro, "Material properties of titanium diboride," *J. Res. Natl. Inst. Stand. Technol.*, vol. 105, no. 5, p. 709, 2000.
- [118] N. Parvin and M. Rahimian, "The characteristics of alumina particle reinforced pure Al matrix composite," *Acta Phys. Pol. A*, vol. 121, no. 1, pp. 108–110, 2012.
- [119] Y. Cai, D. Taplin, M. J. Tan, and W. Zhou, "Nucleation phenomenon in SiC particulate reinforced magnesium composite," *Scr. Mater.*, vol. 41, no. 9, pp. 967–971, 1999.
- [120] M. Paramsothy, J. Chan, R. Kwok, and M. Gupta, "The overall effects of AlN nanoparticle addition to hybrid magnesium alloy AZ91/ZK60A," *J. Nanotechnol.*, vol. 2012, 2012.

- [121] Y. Wang, H. T. Li, and Z. Fan, "Oxidation of aluminium alloy melts and inoculation by oxide particles," *Trans. Indian Inst. Met.*, vol. 65, no. 6, pp. 653–661, 2012.
- [122] C. Song, Q. Han, and Q. Zhai, "Review of grain refinement methods for as-cast microstructure of magnesium alloy," *China Foundry*, vol. 6, no. 2, pp. 93–103, 2009.
- [123] P. Graphite, "Properties and Characteristics of Silicon Carbide," 2002.
- [124] M. E. Levinshtein, S. L. Rumyantsev, and M. S. Shur, *Properties of Advanced Semiconductor Materials*. 2001.
- [125] Z. H. Wang, X. D. Wang, Y. X. Zhao, and W. B. Du, "SiC nanoparticles reinforced magnesium matrix composites fabricated by ultrasonic method," *Trans. Nonferrous Met. Soc. China (English Ed.)*, vol. 20, no. SUPPL. 3, pp. 1029–1032, 2010.
- [126] Hadis Morkos, "General Properties of Nitrides," in *Handbook of Nitrid Semiconductors and Devices*, vol. 1, 2008.
- [127] Suveen Mathaudhu, Alan Luo, Neale Neelameggham, Eric Nyberg, Wim Sillekens, *Essential Readings in Magnesium Technology*. 2014.
- [128] J. W. Martin, *Concise Encyclopedia of the Structure of Materials*. 2006.
- [129] D. Stefanescu, *Science and Engineering of Casting Solidification, Second Edition*. 2008.
- [130] J. G. Kaufman and E. L. Rooy, "Aluminum Alloy Castings: Properties , Processes , and Applications.," *ASM Int.*, p. 340, 2004.
- [131] R. E. and G. Spear, *G.R. Dendrite Cell Size*. Trans. AFS, 1963.
- [132] J. R. Davis, *Aluminum and Aluminum Alloys*, Illustrate. ASM International, 1993, 1993.
- [133] W. D. Griffiths and D. G. McCartney, "The effect of electromagnetic stirring during solidification on the structure of Al-Si alloys," *Mater. Sci. Eng. A*, vol. 216, no. 1–2, pp. 47–60, 1996.
- [134] P. Beeley, *Foundry Technology*, 2nd ed. 2001.
- [135] M. Krupiński, K. Labisz, Z. Rdzawski, and M. Pawlyta, "Cooling rate and chemical composition influence on structure of Al-Si-Cu alloys," *Manuf. Eng.*, vol. 45, no. 1, pp. 13–22, 2011.
- [136] P. Beeley, *Foundry Technology*. 2001.
- [137] K. Fisher, *Fundamentals of solidification*. Trans Tech Publications Ltd, Switzerland, 1992.
- [138] K. Fisher, *Fundamentals of Solidification*. Trans Tech Publications Ltd, Switzerland, 1992.
- [139] K. Zaidat, "Influence d'un champ magnétique glissant sur la solidification dirigée des alliages métalliques binaires," Institut National Polytechnique de Grenoble - INPG, 2005.
- [140] Michael R. Lindeburg, *Mechanical Engineering Reference Manual*. 2013.
- [141] J. Anson, R. Drew, and J. Gruzleski, "The surface tension of molten aluminum and Al-Si-Mg alloy under vacuum and hydrogen atmospheres," *Metall. Mater. Trans. B*, vol. 30, no. 6, pp. 1027–1032, 1999.
- [142] M. Assael, "Reference Data for the Density and Viscosity of Liquid Aluminum and Liquid Iron," *J. Phys. Chem. Ref. Data*, vol. 35, no. 1, p. 285, 2006.
- [143] G. Kaptay, "Interfacial phenomena during melt processing of ceramic particle-reinforced metal matrix composites -- 2. Interfacial force between a spherical particle and an approaching solid/liquid interface," *Solidif. Gravity*, vol. 215, no. May, pp. 467–474, 1996.
- [144] G. Kaptay, "Interfacial Criteria for Producing Metal Matrix Composites and Ceramic Particle Stabilized Metallic Foams," *Mater. Sci. Forum*, vol. 414–415, pp. 419–424,

- 2003.
- [145] J. A. Vreeling, V. Ocelík, Y. T. Pei, D. T. L. Van Agterveld, and J. T. M. De Hosson, "Laser melt injection in aluminum alloys: On the role of the oxide skin," *Acta Mater.*, vol. 48, no. 17, pp. 4225–4233, 2000.
  - [146] S. Rohatgi, M. Tiwari, A. Rathi, and A. Sharma, "Role of Undercooling and Effect of Solute Particles on Grain Refinement of Aluminium Alloys," vol. 61, no. 2, 2015.
  - [147] B. McKay, P. Cizek, P. Schumacher, and K. O'Reilly, "Heterogeneous nucleation in an Al-Ni-Si alloy studied using a metallic glass technique," *Mater. Sci. Eng.*, vol. 304–306, pp. 240–244, 2001.
  - [148] A. Greer and A. Tronche, "Design of grain refiners for aluminium alloys," in *Essential Readings in Light Metals, Cast Shop for Aluminium Production*, 2013, pp. 409–414.
  - [149] T. Quested, "Understanding mechanisms of grain refinement of aluminium alloys by inoculation," *Mater. Sci. Technol.*, vol. 20, no. 11, pp. 1357–1369, 2004.
  - [150] F. Cordelières and S. Bolte, "A guided tour into subcellular colocalization analysis in light microscopy," *J. Microsc.*, vol. 224, no. 3, pp. 213–232, 2009.
  - [151] Y. Wang, M. Xia, Z. Fan, X. Zhou, and G. E. Thompson, "The effect of Al<sub>8</sub>Mn<sub>5</sub> intermetallic particles on grain size of as-cast Mg-Al-Zn AZ91D alloy," *Intermetallics*, vol. 18, no. 8, pp. 1683–1689, 2010.
  - [152] A. Easton, A. Schiffl, J.-Y. Yao, and H. Kaufmann, "Grain refinement of Mg-Al(-Mn) alloys by SiC additions," *Scr. Mater.*, vol. 55, no. 4, pp. 379–382, 2006.
  - [153] J. Liu and P. Wei, "Thermally-Formed Oxide on Magnesium and Magnesium Alloys," pp. 1–15, 2004.
  - [154] A. McLeod and C. Gabryel, "Kinetics of the growth of spinel MgAl<sub>2</sub>O<sub>4</sub>, on alumina particulate in aluminum alloys containing magnesium," *Metall. Trans.*, vol. 23, no. 4, pp. 1279–1283, 1992.
  - [155] Y. Tamura, T. Haitani, and N. Kono, "Liquid Solubility of Manganese and Its Influence on Grain Size of Mg-Al Alloys.pdf," vol. 47, no. 8, pp. 1968–1974, 2006.
  - [156] M. Avedesian and H. Baker, *ASM Specialty Handbook: Magnesium and Magnesium Alloys*. 1999.
  - [157] Y. Tamura, J. Yagi, T. Haitani, T. Motegi, N. Kono, H. Tamehiro, and H. Saito, "Observation of Manganese-Bearing Particles in Molten AZ91 Magnesium Alloy by Rapid Solidification," *Mater. Trans.*, vol. 44, no. 4, pp. 552–557, 2003.
  - [158] C. León, Y. Arroyo, E. Bedolla, E. Aguilar, and R. Drew, "Properties of AlN-Based Magnesium-Matrix Composites Produced by Pressureless Infiltration," *Mater. Sci. Forum*, vol. 509, pp. 105–110, 2006.
  - [159] M. Mounib, H. Dieringa, M. Pavese, C. Badini, and W. Lefebvre, "Reactivity and Microstructure of Al<sub>2</sub>O<sub>3</sub> Reinforced Magnesium Matrix Composites," *Hindawi Publ. Corp.*, p. 6, 2014.
  - [160] A. Olszówka-Myalska, S. McDonald, P. Withers, H. Myalska, and G. Moskal, "Microstructure of In Situ Mg Metal Matrix Composites Based on Silica Nanoparticles," *Solid State Phenom.*, vol. 191, no. March 2016, pp. 189–198, 2012.
  - [161] The American Foundry Society Technical Department, "Magnesium Alloys," *Cast. Source Dir.*, pp. 41–43, 2006.
  - [162] M. Xia, Y. Wang, H. Li, S. Arumuganathar, Y. Zuo, G. Scamans, and Z. Fan, "Refinement of solidification microstructure by Mcast process," in *Magnesium Technology*, 2009, p. 6.
  - [163] M. S. Dargusch, K. Pettersen, K. Nogita, M. D. Nave, and G. L. Dunlop, "The Effect of



- Aluminium Content on the Mechanical Properties and Microstructure of Die Cast Binary Magnesium-Aluminium Alloys," *Mater. Trans.*, vol. 47, no. 4, pp. 977–982, 2006.
- [164] D. Findley, J. Lai, and K. Onaran, "Creep and relaxation of Nonlinear Viscoelastic Materials," *J. Appl. Math. Mech.*, vol. 58, no. 11, pp. 477–528, 1978.
- [165] F. Humphreys and M. Hatherly, *Recrystallization and related annealing phenomena*, Second. Elsevier, 2004.
- [166] W. Qiu, E. Han, and L. Liu, "Serrated Flow Behavior during Compression at Elevated Temperatures in Mg-3Al-1Zn-0.1RE Alloy," *Mater. Sci. Technol.*, vol. 25, no. 4, pp. 441–444, 2009.
- [167] A. Kaveh, "Improving the Properties of Magnesium Alloys for High Temperature Applications," *Magnes. Alloy. - Des. Process. Prop.*, pp. 265–280, 2011.
- [168] H. Somekawa, K. Hirai, H. Watanabe, Y. Takigawa, and K. Higashi, "Dislocation creep behavior in Mg-Al-Zn alloys," *Mater. Sci. Eng. A*, vol. 407, no. 1–2, pp. 53–61, 2005.
- [169] W. Horn-Yu and Y. Jie-Chen, "Dynamic behavior of extruded AZ61 Mg alloy during hot compression," *Mater. Sci. Mech. Eng.*, vol. 535, pp. 68–75, 2012.
- [170] L.-C. Yang, Y.-T. Pan, I.-G. Chen, and D.-Y. Lin, "Constitutive Relationship Modeling and Characterization of Flow Behavior under Hot Working for Fe-Cr-Ni-W-Cu-Co Super-Austenitic Stainless Steel," *Metals (Basel)*, vol. 5, no. 3, pp. 1717–1731, 2015.
- [171] C. Zener and J. Hollomon, "Effect of Strain Rate Upon Plastic Flow of Steel," *J. Appl. Phys.*, vol. 15, no. 1, pp. 22–32, 1944.
- [172] H. Frost and M. Ashby, *Deformation-mechanism maps*, 1st ed. Pergamon Press, 1982.
- [173] M. Barnett, A. Atwell, and G. Beer, "Effect of Grain Size on the Deformation and Dynamic Recrystallization of Mg-3Al-1Zn," *Mater. Sci. Forum*, vol. 467–470, pp. 435–440, 2004.
- [174] A. Venetti, "The compressive Creep Behavior of TiC/AZ91D Magnesium Matrix Composites with interpenetrating Networks," *Prog. Mater. Sci. Technol.*, vol. 23, no. 2, p. 238, 2007.
- [175] S. Wei-Dong, N. Jian-Guo, M. Xiao-Nan, and L. Jian-Qiao, "A constitutive model for particulate-reinforced titanium matrix composites subjected to high strain rates and high temperatures," *Therm. Sci.*, vol. 17, no. 5, pp. 1361–1367, 2013.
- [176] D. StJohn, M. Qian, M. Easton, P. Cao, and Z. Hildebrand, "Grain refinement of magnesium alloys," *Metall. Mater. Trans. A*, vol. 36, no. 7, pp. 1669–1679, 2005.
- [177] K. Kainer, *Magnesium Alloys and Their Applications 2009*, 1st ed. Wiley-VCH, 2000.
- [178] G. Klosch, B. McKay, and P. Schumacher, "Preliminary investigation on the grain refinement behavior of ZrB<sub>2</sub> particles in Mg-Al alloys," in *Essential Readings in Magnesium Technology*, 2014 John Wiley & Sons, Ed. 2014.
- [179] H. Xiangjun, Y. Size, Y. Du, K. Tao, and F. Yudian, "Reaction layer formation at the interface between Ti or Zr and AlN," *Phys. status solidi*, vol. 157, no. 1, pp. 3–209, 1996.
- [180] J. Wang, J. Yang, W. Yaoming, Z. Hongjie, and L. Wang, "Microstructures and mechanical properties of as-cast Mg-5Al-0.4Mn-xNd (x= 0,1,2 and 4) alloys," *Mater. Sci. Eng. A*, vol. 472, no. 1–2, pp. 332–337, 2008.
- [181] L. Wei, G. Dunlop, and H. Westengen, "Development of microstructure in cast Mg-Al-rare earth alloys," *Mater. Sci. Technol.*, vol. 12, no. 9, pp. 741–750, 2013.
- [182] M. Mounib, "composites and aluminum alloys processed under the influence of external fields (Doctoral thesis," Normandie Université, 2015.

- [183] A. Venetti, "in situ reactive infiltration process," in *Progress in Materials Science Research*, N. Publishers, Ed. 2008, p. 99.
- [184] S. Qu, X. H. An, H. J. Yang, C. X. Huang, G. Yang, Q. S. Zang, Z. G. Wang, S. D. Wu, and Z. F. Zhang, "Microstructural evolution and mechanical properties of Cu-Al alloys subjected to equal channel angular pressing," *Acta Mater.*, vol. 57, no. 5, pp. 1586–1601, 2009.
- [185] M. Avedesian and B. Hugh, *ASM Specialty Handbook: Magnesium and Magnesium Alloys*. 1999.